NASA CR-134552
GE R73AEG326

STUDY OF CASING TREATMENT STALL MARGIN IMPROVEMENT PHENOMENA

by

D. C. Prince, Jr.
D. C. Wisler
D. E. Hilvers

GENERAL ELECTRIC COMPANY
AIRCRAFT ENGINE GROUP
CINCINNATI, OHIO 45215

MARCH 1974

prepared for

NATIONAL AERONAUTICS AND SPACE ADMINISTRATION

NASA Lewis Research Center
Contract NAS 3-15707
Everett E. Bailey, Project Manager

1. Report No.	2. Government Accession No.	3. Recipient's Catalog No.
NASA CR-134552		

4. Title and Subtitle	5. Report Date
Study of Casing Treatment Stall Margin Improvement Phenomena	March 1974 6. Performing Organization Code

7. Author(s)	8. Performing Organization Report No.
D. C. Prince, Jr., D. C. Wisler, D.E. Hilvers	R73AEG326 10. Work Unit No.

9. Performing Organization Name and Address	11. Contract or Grant No.
General Electric Company Aircraft Engine Group Cincinnati, Ohio 45215	NAS3-15707 13. Type of Report and Period Covered

12. Sponsoring Agency Name and Address	14. Sponsoring Agency Code
National Aeronautics and Space Administration Washington, D.C. 20546	Contractor Report

15. Supplementary Notes

Program Manager, Everett E. Bailey, Fluid System Components Division
NASA Lewis Research Center
Cleveland, Ohio 44135

16. Abstract

The results of a program of experimental and analytical research in casing treatments over axial compressor rotor blade tips are presented.

Circumferential groove, axial-skewed slot, and blade angle slot treatments were tested. These yielded, for reduction in stalling flow and loss in peak efficiency, 5.8% and 0 points, 15.3% and 2.0 points, and 15.0% and 1.2 points, respectively. These values are consistent with other experience.

The favorable stalling flow situations correlated well with observations of higher-than-normal surface pressures on the rotor blade pressure surfaces in the tip region, and with increased maximum diffusions on the suction surfaces. Annulus wall pressure gradients, especially in the 50-75% chord region, are also increased and blade surface pressure loadings are shifted toward the trailing edge for treated configurations. Rotor blade wakes may be somewhat thinner in the presence of good treatments, particularly under operating conditions close to the baseline stall.

The experimental program was carried out in the General Electric Low Speed Research Compressor, which provides for investigation at low Mach numbers ($M \leq 0.15$) and large geometric scale. The facility is arranged to permit flow visualization. Knitting yarn tufts, viewed in steady and stroboscopic light, showed substantial velocities along circumferential grooves, without systematic components into or out of the grooves. Tuft surveys in the other cavities showed highly random patterns, without correlation to the passage of rotor blades.

Steady-state and transient pressure and velocity measurements can be made in the facility without subminiature instrumentation and ultra-high frequency response. For the program reported these measurements were made with impact tubes, wall static pressure taps, one-dimensional and two-dimensional hot film anemometers, and B&K transient static pressure sensors, as appropriate for the flow patterns suggested by the flow visualization. Results confirmed the random nature of the flow patterns.

17. Key Words (Suggested by Author(s))	18. Distribution Statement
Compressors Compressor Casing Treatment Stall Margin Improvement	Unclassified - Unlimited

19. Security Classif. (of this report)	20. Security Classif. (of this page)	21. No. of Pages	22. Price*
Unclassified	Unclassified	166	

* For sale by the National Technical Information Service, Springfield, Virginia 22151

TABLE OF CONTENTS

LIST OF TABLES

LIST OF ILLUSTRATIONS

LIST OF ILLUSTRATIONS (Continued)

LIST OF ILLUSTRATIONS (Continued)

LIST OF ILLUSTRATIONS (Continued)

LIST OF ILLUSTRATIONS (Continued)

SUMMARY

This report presents the results of a NASA-sponsored General Electric Company investigation into the flow patterns and mechanisms by which porous wall casing treatments over axial flow compressor rotor tips act to postpone the onset of stall and increase the useful operating range. Prior to this program the NASA and cooperating organizations, including General Electric, had a substantial background of empirical results showing that various porous wall treatments were effective at improving stall margins from normal operating lines, but with little understanding about why these treatments were effective and what configurations would give the best results. Almost without exception, the previous experience was obtained on transonic stages and in sizes that made detailed investigation difficult.

The General Electric Company Low Speed Research Compressor (LSRC) is a facility which provided the opportunity to make detailed investigations into the flow patterns in and around treatment cavities, seeking insight into those features of the flow patterns which contribute to the stall margin improvement. Success in the program depended, of course, on showing that the stall margin improvements did not require the presence of compressibility effects, such as cavity resonance, to be effective.

Analytical modelling of the flow patterns in the casing treatment cavities was carried out for use in prediction of the details to be sought in the experimental program. The circumferential groove flow was supposed to be irrotational, with a choice of constant stagnation pressure in a frame relative to the moving blading or in a stationary frame. The measured data seem more nearly consistent with constant stagnation pressure in a frame moving at fractional rotor speed. For flows in slot-type cavities, two types of models were considered, in which the flow is primarily longitudinal or primarily transverse. In the longitudinal type of model, the flow could be driven by the meridional static pressure field or by the static pressure distribution parallel to blade surfaces. In the transverse flow type of model the flow is driven by momentum interchange across the cavity face from the free stream. Some features of each type of model were observed, but in too random a pattern for ready correlation with the modelling.

The experimental phase of the NASA/GE Casing treatment program included the testing of eight different casing treatment configurations in three basic types: circumferential grooves, axial-skewed slots, and blade angle slots. Each configuration showed at least some improvement in stall margin. The basic circumferential groove treatment yielded 5.8% reduction in stalling flow with no sacrifice in efficiency. The axial-skewed slot treatment (with a mid-length baffle) yielded 15.3% reduction in stalling flow with 2.0 points sacrifice in efficiency. The blade angle slot treatment, with slots 70% wider than the maximum blade tip thickness, yielded 15.0% reduction in stalling flow with 1.2 points sacrifice in efficiency. These values are consistent with previous casing treatment experience. A more detailed summary of the casing treatment results is presented as Table IV.

The LSRC facility provides for visual observation of flow patterns by means of knitting yarn tufts. It was expected that flow patterns would be found with a dominant blade passing frequency and that these could be seen by illuminating the tufts with stroboscopic flashes. No patterns at blade passing frequency were observed for any configuration. Some concern was felt that the tufts might not respond to that high a frequency. The tufts showed that the circumferential grooves carried substantial circumferential velocity with little or no transverse or radial components. The circumferential velocities were inhibited only slightly when twelve baffles were introduced. The axial-skewed slots showed an average

pattern of flow into a cavity at its aft or downstream end and out at its forward or upstream end. Superimposed on this average pattern was a highly random situation, which often obscured the average pattern. The flow is apparently driven by the time-average pressure gradient through the rotor and increases considerably when removal of a mid-cavity baffle increases the driving pressure difference. The blade angle slots had a similar average pattern, nearly obscured by a high level random behavior.

More detailed and quantitative measurements of cavity flows were made with steady-state total and static pressures, hot film anemometers for steady-state and transient velocities, and B&K pressure sensors for transient pressures. These measurements confirmed the existence of large circumferential velocities in circumferential grooves, and random flow patterns in all other cavities.

Static pressures were measured on the blade surfaces. These showed that the circumferential groove configuration improved pressure recovery in the 50-75% chord region, so that some of the pressure loading is shifted away from the leading edge, relative to the baseline solid wall. The maximum suction surface pressure rise before stall was greater in the presence of treatment. Observations with axial-skewed and blade angle slot cavities showed extremely high static pressures on the pressure surfaces, close to the blade tip. These pressures were even higher than the freestream relative total pressure. The high static pressure level persisted to some degree over as much as 20% of the span. Thus, the beneficial effect of these cavities may result from the generation of a high level of static pressure on the pressure surface, which in turn generates a high velocity off the pressure surface into the wake and serves as an energizing mechanism for the marginally stable suction surface boundary layer.

Annulus wall boundary layers were surveyed using hot film anemometry, which also permitted investigation of rotor blade wakes. The circumferential groove treatment has little influence on the wall boundary layers. The axial-skewed and blade angle slot treatments have little influence on the boundary layers in the flow range where the baseline configuration operates stably, but yield substantial reduction in boundary layer momentum defect close to stall. Some reduction in rotor blade wake thickness is found in the presence of treatment.

Vector diagram analyses show modest flow shifts and modest increases in limiting blade element loadings in the presence of casing treatments.

PROGRAM BACKGROUND

Introduction

During the years 1968 to 1970, several experimental programs were conducted by the NASA in-house, and by contractors with NASA support, to demonstrate that operational flexibility for transonic fan stages could be improved substantially by introducing porous casings over rotor tips, as compared with solid casings. The program described in Reference 1, for example, showed 7% improvement in stall margin for 0.02 sacrifice in efficiency. At about the end of 1969, for the first time, some configurations (References 2 and 3) showed significant improvements in stall margin with only slight sacrifices in stage efficiency.

Based on the experience as of March 1970, NASA sponsored a modification to the testing program at General Electric under Contract NAS3-11157 (Reference 4) to make an independent evaluation of the most promising configurations. Four treatment types were included in this program: circumferential grooves, blade angle slots, axial-skewed slots, and honeycomb cavities. The circumferential groove configurations were especially attractive in that they provided substantial (3%) improvement in stall margin with no measurable efficiency sacrifice. The other configurations provided more stall margin improvement (approximately 6%) at 100% speed with 0.01 to 0.02 sacrifice in efficiency. Although these latter configurations performed almost equally well, the trade-offs among them with respect to cost-effectiveness in application and susceptibility to further development received little exploration. With regard to manufacturing cost, for example, the honeycomb configurations appear to be the most difficult to manufacture, while the blade angle slots should be relatively easy.

The various experimental programs (References 1 - 4) had shown that the geometric parameters associated with the configuration designs could be quite critical. Only a few configurations of each type, chosen somewhat arbitrarily, had been investigated. It seemed likely that a detailed investigation into the mechanisms and principles behind the beneficial influences of casing treatment would lead to a substantial further improvement in the observed performance. The present program was undertaken to make a detailed investigation into the mechanisms of the casing treatment influence.

Empirical Background

The state-of-the-art with respect to casing treatment at the beginning of the present program could best be expressed by a series of empirical observations. The following list is a digest of information contained in References 1 - 7.

1. Most of the rotors on which casing treatment seemed beneficial encountered instability in the form of a rotating stall initiated at a critically loaded rotor tip. In one case, reported in Reference 1, the stall began at the part-span shroud during tests with undistorted inlet. Most of that investigation was carried out with tip radial distortion, so as to transfer the critical loading to the tip, which provided the favorable environment for observing casing treatment benefits.

2. All of the stages on which attractive casing treatment results had been found were transonic. Transonic stages tend to be designed with little or no camber in the tip region. They tend to have heavy leading edge loadings as compared with subsonic designs. At high speed, the heavy leading edge loading results from having a subsonic region on the pressure surface behind a leading edge shock and a highly supersonic region in the flow-induction portion of the suction surface. At lower speeds, the heavy loading of the transonic design comes from excessive positive incidence due to the small camber and to unfavorable matching of the density-annulus-area combinations between leading and trailing edge regions. Thus the pressure distribution patterns from transonic rotors might be peculiarly amenable to stability enhancement through the use of casing treatment.

3. Recirculation in grooves, slots, or plenums may serve to stabilize or delay rotating stall. Some of the early casing treatment tests indicated large recirculation and substantial efficiency sacrifice as compared with solid casings. It seems likely that in those cases the recirculation may have damped out those discontinuities in the operating region which are referred to as stalls. The test programs reported in References 1 and 4 showed conflicting influences of recirculation. Rotors were tested in both programs with honeycomb cell treatment over the rotor tips, and with a plenum chamber available in the form of a manifold around the outside of the honeycomb. In the test program of Reference 1, a substantial improvement in stall margin was obtained with the honeycomb cells open to the plenum, regardless of the plenum size. The benefit disappeared when the honeycomb cells were blocked off at the back. In the test program of Reference 4, the stall margin improvement as compared with a plain casing was slightly greater with the backs of the honeycomb cells blocked off than with them open to a plenum chamber. When the treatment cavities were slots that could permit substantial recirculation driven by the fore-and-aft pressure gradient, introduction of partitions across the cavities would inhibit recirculation, without apparently interfering with the benefit in stall margin improvement.

4. The most successful casing treatments have 65-75% open area in the nominal casing surface. Perforated plates with 10-30% open area have not been effective. Circumferential grooves with 50% open area were much less effective than those with 65% open area or more. In the blade angle slot case of Reference 4, there was a substantial loss in benefit from casing treatment when one-half of the cavities were filled up. This comment on open area refers to the nominal axial extent of the treatment, and is independent of any conclusions about the value of treating leading and trailing edge regions.

5. Treatment over the 20% of the meridionally projected rotor chord from either the leading or the trailing edge is ineffective. Most, if not all, of the benefits come from treating the center 60% of the chord projection. Filling the cavities over the leading and trailing edges resulted in efficiency improvements with little change, or even some gain, in stall margin for the circumferential groove and axial-skewed slot configurations of Reference 2. Treatment in the leading edge region alone was investigated in the testing for Reference 5, and was found ineffective.

6. Some tip treatments have been observed which lead to increased blade tip loading and pressure rise as compared with a solid casing, as if the diffusion process were improved. The overall pressure rise of the stage may still appear to remain

constant during throttling of a stage in which the tip region picks up load, if the strengthened tip results in transferring the throttle response to a hub region with a drooping characteristic. For other tip treatments, stable operation may be maintained to higher incidence angles than with plain casings, but without increased pressure rise in the extended operating region. Under these circumstances the loss does increase at the high incidence. The increases in incidence angle for stable operation in the tests of Reference 4 are illustrated in Figure 1a. That test series also demonstrated increases in the stalling diffusion factor as a result of the casing treatment, as is shown on Figure 1b. The diffusion factors were calculated from vector diagrams and, consequently, are measures of the work input, but not of the pressure rise. The static pressure rise coefficients did not increase significantly as a result of casing treatment: this result is shown on Figure 1c.

7. Several investigations have looked for favorable influences of resonant cavities tuned to blade passing frequency. No such investigations have identified a significant selective effect which can be attributed to resonance.

8. Some of the favorable effects of casing treatments can be attributed to radial shifts in the flow distribution, which may provide relief from limiting blade loadings.

9. Casing treatments may tend to reduce disparities among flows in successive blade passages. When a full stall is caused by an extreme flow condition in one passage, suppression of that extreme may delay the stall.

10. The severity and frequency of rotating stall cells may be reduced by casing treatment.

11. Vortex generators may improve annulus wall boundary layer profiles (Reference 7), enhancing stability, improving stall margins, and suppressing flow separation losses.

Hypotheses on Mechanisms

A specific objective of the NAS 3-15707 Casing Treatment program was to explore the relevance of a series of possible mechanisms which had been suggested as possible explanations for the manner in which casing treatment works to extend stable operating ranges. None of the mechanisms on the original list had been found adequate to explain all the observed results. It was thought that different types of treatment might require different explanations for the success. It also seemed possible that different types of rotor design might respond differently to the various treatments.

The mechanisms* which seemed worthy of exploration fell into a number of groups:

1. Suppression of incipient separation - inherently two-dimensional cascade effects

   "If a critical corner boundary layer develops on the suction surface near the blade tip, flow out of a cavity may impinge on the boundary layer, energizing it and delaying separation."

*Proposed mechanisms are quoted as they came from a "brainstorm session" and may lack coherence under critical examination.

"Flow into a cavity may serve as a bleed, removing low energy fluid from a critical corner boundary layer between a blade suction surface and the annulus wall, delaying separation."

"Flow into or out of a cavity may dissipate an incipient vortex generation."

"Casing treatments may increase the effective turbulence for flow close to the annulus wall, leading to energized boundary layers and increased flow stability."

"Airfoils with extreme leading edge loading may be particularly susceptible to boundary layer instability in the mid-chord region, and therefore are special candidates to respond to artificial stabilizing devices."

"Where a critical circulation time delay determines the sensitivity of a particular rotor to circumferential distortion, a stabilizing treatment may increase the time delay enough to avoid a stall."

"The several flow passages between the rotor blades may have substantially different flow characteristics, resulting from manufacturing tolerance or foreign object damage, which make the rotor vulnerable to onset of a rotating stall, and the casing treatment may promote establishment of a preferred, stable pattern in place of an indeterminate, sensitive flow pattern."

These statements about the influence of a casing treatment on the stability of a compressor rotor share the common premise that stalling starts with an instability in the two-dimensional or quasi-two-dimensional flow around the blade tip airfoils. Under these circumstances a small amount of properly directed extra leakage flow could serve to promote stability, and in some cases might even smooth out the free stream flow enough to more than compensate for the entropy increase of the leakage flow. It should be observed that the boundary layer growth toward separation on a surface may not be distinguishable from a boundary layer approaching the stagnation point of the vortex, shed with the approach of a rotating stall cell.

Various investigators (e.g., Reference 8) in the early 1950's explored details of the rotating stall flow phenomena, and noticed that the passage of a rotating stall cell involves the shedding of an "unstart vortex" when an individual airfoil first encounters the cell moving with respect to the airfoil cascade, followed by shedding a "start vortex" during recovery after passage of the stall cell. Also during the 1950's the former NACA joined with the Douglas Aircraft Company (Reference 9) in demonstrating the existence and behavior of a "floor vortex". This vortex may originate on an airfield runway and extend into the inlet of an aircraft gas turbine engine, acting as a vacuum cleaner for any foreign objects on the runway. The demonstration also showed that the floor vortex was unstable and could easily be blown away by a screen of low intensity air jets.

Considering the logic of flow patterns in and around casing treatment cavities, it was natural to expect that the suction surface pressure would be lower than the cavity pressure, even if the cavity pressure fluctuated somewhat following the blade-to-blade pressure field, and that there would be a flow induced from the cavity into any region of vortex generation or boundary layer separation on the suction surface. Since transonic blades tend to be designed with little camber and definite positive incidence to stay within a narrow low loss operating range, they could be peculiarly sensitive to separation effects that could be stabilized by treatment. Near stall at high speed, there may be an extreme adverse pressure gradient on the suction surface, in the transition through a shock system from a high supersonic velocity to a subsonic velocity. The boundary layer subjected to this gradient would be susceptible to separation, and could be stabilized by the treatment.

2. Meridional boundary layer control

"The flow barriers between casing treatment cavities may interfere with a tendency toward flow reversal in the annulus wall boundary layer."

"The pressure field in and around casing treatment cavities may lead to wall force components, entering into any control volume analysis, which augment the axial forces from the blades."

The meridional boundary layer control mechanisms, in contrast to the incipient two-dimensional boundary layer separation mechanisms, disregard considerations of stability of the two-dimensional flow around a blade. Attention is given instead to the pressure difference across a flow barrier which produces a force component in the axial direction. There was no clue as to whether the extrapolation of a continuous pressure rise in the free stream to a compartmented wall, such as the circumferential groove treatment, would appear as a discontinuous pressure rise across the barrier between compartments, with nearly uniform static pressure in the compartment, or in some other manner. It seemed probable that pressure gradients in small compartments would be small compared to those in the free stream. Then the pressure differences would be across the barriers, and in the circumferential groove configuration would constitute force components entirely in the axial direction, pushing in the normal flow direction. Shear forces on a solid wall, in contrast, tend to push against the normal flow direction.

Breakdown of an annulus wall boundary layer with increasing back pressure is a possible mechanism for a stall. Since a compressor blade row must support the static pressure rise more or less uniformly along its span, the wall boundary layer must also support the full rise. This pressure rise reacts against the axial component of blade force and is opposed by the small axial component of the shear stress on the casing. As stall is approached, the casing boundary layer presumably thickens and measurements have shown that stall occurs when the displacement thickness of the annulus boundary layer reaches a value near 20% of the blade staggered spacing. Data of this type have been given by Smith (Reference 10) for stages in multistage environments. The 20% value also seems representative for single rotors that stall at the tip.

The theory of the meridional boundary layer control is that the casing treatment may allow the wall shear stress term in a control volume analysis to become favorable, delaying the wall boundary layer thickening process. This would happen if the tip clearance flow, with its axial backward flow component, were captured by the cavity and its backward momentum were absorbed there.

3. Compliant wall absorption of pressure disturbances

"The separation surface between an essentially stagnant cavity and the free-stream flow is compliant to local disturbances, serving as a damper on them where a solid wall would act as an amplifier."

"A mean flow velocity in the circumferential grooves reduces tip leakage and sets up a situation equivalent to a reduced effective clearance."

"The presence of a casing treatment cavity acts as a suppressor on large scale circumferential static pressure variations and, therefore, serves to suppress the development of rotating stall cells."

It is clear that a small "blob" of high pressure fluid impinging on a solid wall will have its velocity component perpendicular to that wall brought suddenly to rest, resulting in an amplification of the high pressure. The same high pressure blob impinging on the separation surface between the freestream and a stagnant cavity will find that the contents of the cavity give way. The high pressure disturbance is then reflected as a low pressure disturbance, a tranquilizer for flow separation.

If the roles of rotating blade and stationary wall are interchanged, so that the wall is considered to be a belt moving past the blade tip from the pressure surface to the suction surface, both wall friction drag and pressure difference contribute to the induction of flow through the leakage space. The circumferential groove configuration presents the possibility that an average flow component moving in the same direction as the rotating blade may reduce the shear force adding to the pressure difference, and thus reduce the leakage flow. Operation of this mechanism requires that the cavity flow and the freestream flow have separate identities, so that the flow in the cavity is not really an increased leakage flow.

When an axial flow compressor stage is throttled toward stall, the approach to a discontinuity in the flow behavior is sometimes marked by a small amplitude velocity or pressure disturbance traveling in the direction of rotor travel at fractional rotor speed. Presumably this is a rotating stall of insufficient amplitude to destroy the stability of the compressor operation. The amplitude of the disturbance may grow with further throttling until a noticeable discontinuity in operation does appear. The effect of some casing treatment schemes could be to attenuate the amplitude of the traveling disturbance so that it does not build up to the point of discontinuity until later in the throttling process. Circumferential communication of flow or pressure signals in a plenum chamber or manifold is a possible means for this sort of small disturbance attenuation. This may explain the occasional beneficial effects of treatment cavities communicating with a plenum chamber.

Flow modelling

An extensive program of analytical flow modelling for flow patterns in and around the casing treatment cavities was carried out as a part of the NAS3-15707 Casing Treatment program. It was expected that analytical predictions for these flows would be valuable guides, assisting in the choice of physical parameters to be measured, and the instrument ranges to be used. Many of the model results have been used to good advantage in evaluating the experimental data from the program.

Analytical modelling investigations carried out during the program included:

a. Potential flow analysis of the rotor tip cascade, treated as a two-dimensional incompressible, inviscid flow problem;

b. Two-dimensional, incompressible, inviscid flow in a circumferential groove cavity assuming constant total pressure relative to the moving blade row;

c. Two-dimensional, incompressible, inviscid flow in a circumferential groove cavity assuming constant total pressure in the stationary coordinate system;

d. Two-dimensional, incompressible, inviscid flow in a blade angle slot cavity;

e. Laminar viscous flow in a circumferential groove cavity;

f. Roller bearing flow (two-dimensional, incompressible, non-viscous, with total pressure gradient) in the mouth of an axial-skewed slot.

Details of the analyses and results are presented in the following text:

Potential flow analysis of the rotor tip cascade - The General Electric Company Compressible Fluxplot computer program (Reference 11) has been available for some years. It is a straightforward procedure (using a numerical finite difference field solution for the two-dimensional stream function, similar to the approach described in Chapter IV, PP 126-130, of Reference 12) for estimating surface pressure distributions in subsonic airfoil cascades provided viscous flow effects are not dominant. In the Casing Treatment program it was expected that the blade-to-blade pressure field would be applied to the cavity faces, and would serve as the driving force for flows in the cavities. The Fluxplot procedure was especially well suited for obtaining the pressure distributions on cross sections parallel to the cascade axis, which were desired as boundary conditions for circumferential groove cavity flows.

The rotor tip section cascade analyzed has the following geometric properties:

Camber	= 23.12 degrees
Stagger	= 43.39 degrees
Maximum Thickness Ratio, t/c	= 0.045
Solidity, c/s	= 1.314

The airfoil shape consists of a modified NACA 65-series thickness distribution on a circular-arc mean line. The blade-to-blade flow field analysis was done for two inlet air angles: (a) $\beta_1 = 55.25°$, corresponding to design-point conditions, and (b) $\beta_1 = 63.08°$, corresponding to the measured operating condition just prior to onset of rotating stall.

The calculation procedure requires specifying the cascade exit air angle β_2, and this was set at $\beta_2 = 38.00°$, corresponding approximately to the Carter's Rule deviation angle. This value of exit air angle was kept the same for both values of inlet air angle analyzed.

The resulting static pressure fields obtained from the blade-to-blade flow calculations are shown in Figures 2 and 3. Figure 2 shows the blade surface static pressure distributions, in terms of static pressure coefficient, for both inlet angles. Figure 3 shows blade-to-blade static pressure traces, as would be seen by a circumferential groove over the rotor tip, at several axial locations and for both inlet angles. Area average relative tangential velocities, including an estimated average for the tip leakage region, for the near stall condition are 55.3%, 44.4%, and 38.8% of the upstream velocity at 30% chord, 50% chord, and 70% chord, respectively.

The static pressure fields shown in Figure 3 were used as boundary condition information for preliminary modelling of circumferential groove flow fields. Of course, the enclosed results do not reflect the effects of tip clearance, blade and endwall boundary layers, and/or secondary flows on the tip section flow field, but are probably representative of the maximum static pressure gradients that can be expected along a groove or other casing treatment cavity opening.

Circumferential groove cavity flow with constant total pressure relative to the moving blade row - An incompressible, inviscid, two-dimensional flow model for the flow in a circumferential groove casing treatment cavity, with constant total pressure relative to a moving blade row, was synthesized using an analogy to the classical "wavy-wall problem" (see, for example, Reference 13). Results of the analysis of this flow model showed that the blade-to-blade rotor tip static pressure gradients could induce significant radial flows in and out of the groove and could produce a radial outflow or suction effect over the blade tip region. The magnitude of the induced flow velocities was found to increase with groove depth and reach an asymptotic maximum for groove depths of approximately 25% of the rotor blade tip tangential spacing. Extension of the results to compressible flows by applying linearized theory showed that compressibility rendered the induced velocity magnitudes more sensitive to groove depth, and that deeper grooves were required to achieve the same relative effect as the incompressible flow case. It was deduced that high speed compressor stages would see a greater effect of groove depth increases on stall limit improvement than low speed stages, and that the induced tip region suction could conceivably improve performance as well. Details of this analysis follow.

A schematic of a typical compressor stage with a casing treatment of the circumferential groove type over the rotor tip is shown in Figure 4. The flow field in the tip region of the rotor is characterized by large gradients in pressure from blade to blade, a result of the blade pressure distributions and loadings.

The circumferential groove configurations which have been the most successful have been those which did not have grooves too near the leading or trailing edges and those whose groove depth was appreciably larger than the groove axial width. It can, therefore, be speculated that the blade-to-blade flow imposes strong circumferential pressure gradients on the flow in the groove, inducing a primarily two-dimensional flow in and out of the groove in the radial/circumferential plane. This type of flow geometry is qualitatively illustrated in Figure 5. The axial pressure gradients are assumed to be small in comparison with the circumferential ones.

The average flow in the groove is assumed to be in the direction of rotor rotation, traveling at some fraction of rotor speed. The groove average flow velocity is assumed to be equal to the average absolute tangential velocity as determined by the rotor tip section at that axial location. An alternative is to assume that only a fraction of this tangential velocity is recovered in transferring from the flowpath to just inside the groove, due to equilibrium between viscous mixing which may occur at the interface and skin friction drag on the groove walls. As a first approximation, the flow in the groove is assumed to be inviscid, at least as far as induced radial flows are concerned. The effects of viscosity are, therefore, assumed to affect only the average swirl level in the groove.

Consider the blade-to-blade pressure distribution at one axial location corresponding to the location of a casing groove. If we transfer to a coordinate system fixed to the rotor, then, relative to the rotating frame, the blade-to-blade pressure distribution is stationary in time. The groove flow pattern repeats itself every blade pitch, and the net flow in/out of the groove is zero. A bounding streamline is, therefore, formed at the groove mouth which is stationary in time relative to the moving rotor coordinate system.

Figure 5 shows a section of a groove, in the radial/circumferential plane, with the rotor moving in the negative X (positive θ) direction. Relative to the rotor, since the average groove flow velocity is some fraction of rotor speed, the average flow is in the positive X (negative θ) direction.

Let U_t be the rotor tip speed, and let U_m be the groove flow average tangential velocity, in the absolute reference frame. In the rotating frame, the average flow velocity in the groove is

$$V_\infty = U_t - U_m \tag{1}$$

Since the groove mouth bounding streamline is stationary with time in the rotating frame, it can be treated as a solid wall whose shape is some waveform to be determined. The flow in the rotating system is, therefore, analogous to flow through a channel formed by one straight wall and one "wavy" wall, and having a mean or average velocity V_∞. The straight wall corresponds to the groove bottom, and the "wavy" wall corresponds to the groove mouth bounding streamline. We can, therefore, apply the classical solution of the flow past a wave-shaped wall to the present problem. In our case, however, we will be solving for the wave-shape of the "wall" from a prescribed "wall" (blade-to-blade) pressure distribution, rather than the inverse. This application of the wavy wall model implies the corollary, that total pressure of the field relative to the moving blade is constant.

A small perturbation solution for the two-dimensional, inviscid flow past a wave-shaped wall is presented by Shapiro, Reference 13. Also given in Reference 13 is the solution for the flow between a wave-shaped wall and a parallel straight wall. For a wall whose shape is described by a cosine wave-form the flow field solution is as follows:

$$\varphi(x, y) = \frac{V_\infty}{\beta} \frac{h}{1-e^{-4\pi\beta H/\ell}} \left(\sin\frac{2\pi x}{\ell}\right) e^{-2\pi\beta y/\ell} \left[1 + e^{4\pi\beta(y-H)/\ell}\right] \tag{2}$$

Where φ = Velocity potential of perturbation flow

β = Compressibility parameter, $\beta^2 = 1 - M^2_\infty$

V_∞ = Average mean velocity (in the relative frame)

h = Half-amplitude of wave-shaped wall

H = Mean distance between walls

ℓ = Wavelength of wave-shaped wall

x = Coordinate along wall axis

y = Coordinate normal to wall axis

and the wall shape is given by

$$y_w = h \cos\frac{2\pi x}{\ell} \tag{3}$$

The above variables are also defined in Figure 5. From Equation (2), the x- and y- components of velocity, u and v, and the pressure coefficient C_P can be found. They are as follows:

$$\left.\begin{aligned} u &= \frac{\partial\varphi}{\partial x} + V_\infty ; && \text{(a)} \\ v &= \frac{\partial\varphi}{\partial y} ; && \text{(b)} \\ C_P &\cong -\frac{2}{V_\infty}\frac{\partial\varphi}{\partial x}, && \text{(c)} \end{aligned}\right\} \tag{4}$$

where

$$\frac{\partial\varphi}{\partial x} = \frac{2\pi V_\infty h}{\ell\beta}\left(\cos\frac{2\pi x}{\ell}\right)\left[\frac{e^{2\pi\beta(H-y)/\ell} + e^{-2\pi\beta(H-y)/\ell}}{e^{2\pi\beta H/\ell} - e^{-2\pi\beta H/\ell}}\right], \tag{5}$$

and

$$\frac{\partial \varphi}{\partial y} = - \frac{2\pi V_\infty h}{\ell} \left(\sin \frac{2\pi x}{\ell}\right) \left[\frac{e^{2\pi\beta (H-y)/\ell} - e^{-2\pi\beta (H-y)/\ell}}{e^{2\pi\beta H/\ell} - e^{-2\pi\beta H/\ell}}\right]. \tag{6}$$

For the circumferential groove flow problem, we assume we know pressure C_P on the groove mouth bounding streamline, which corresponds to the wave-shaped wall. Evaluating Equations (4c, 5) at $y \approx 0$ yields a relation for wall shape amplitude as a function of pressure coefficient, as follows:

$$h \cos \frac{2\pi x}{\ell} = - \frac{\beta}{4\pi} C_P \tanh \frac{2\pi\beta H}{\ell}. \tag{7}$$

The distance between walls H corresponds to the groove depth, while the wavelength corresponds to the rotor tip tangential blade spacing or pitch. Thus, for a cosine pressure distribution, the bounding streamline shape at the groove mouth is a negative cosine wave, whose amplitude is given by Equation (7).

For sine-wave wall shape, a simple phase shift of $3\pi/2$ radians yields the following solution:

$$\varphi(x, y) = - \frac{V_\infty h}{\beta} \left(\cos \frac{2\pi x}{\ell}\right) \left[\frac{e^{2\pi\beta (H-y)/\ell} + e^{-2\pi\beta (H-y)/\ell}}{e^{2\pi\beta H/\ell} - e^{-2\pi\beta H/\ell}}\right]. \tag{8}$$

Then,

$$\frac{\partial \varphi}{\partial x} = \frac{2\pi h V_\infty}{\beta \ell} \left(\sin \frac{2\pi x}{\ell}\right) \left[\frac{e^{2\pi\beta (H-y)/\ell} + e^{-2\pi\beta (H-y)/\ell}}{e^{2\pi\beta H/\ell} - e^{-2\pi\beta H/\ell}}\right]; \tag{9}$$

$$\frac{\partial \varphi}{\partial y} = \frac{2\pi h V_\infty}{\ell} \left(\cos \frac{2\pi x}{\ell}\right) \left[\frac{e^{2\pi\beta (H-y)/\ell} - e^{-2\pi\beta (H-y)/\ell}}{e^{2\pi\beta H/\ell} - e^{-2\pi\beta H/\ell}}\right], \tag{10}$$

where

$$y_w = h \sin \frac{2\pi x}{\ell}.$$

A typical blade-to-blade pressure distribution is neither sine- nor cosine-shaped, but we can synthesize the actual pressure distributions with a Fourier series representation. Since the above problem formulation is based on a linear governing equation, i.e.,

$$\beta^2 \frac{\partial^2 \varphi}{\partial x^2} + \frac{\partial^2 \varphi}{\partial y^2} = 0, \tag{11}$$

then solutions for the individual harmonics of the Fourier series representation can be summed to give the total solution for the actual pressure distribution.

Consider the case where the blade-to-blade pressure distribution is a sine wave, as shown in Figure 6. This is a reasonable approximation to an actual distribution for examining qualitative trends. Equations (4, 8 - 10) indicate that, for $C_P \sim \sin(2\pi x/\ell)$ at the groove mouth,

$$\frac{\partial \varphi}{\partial x} \sim -\sin\frac{2\pi x}{\ell};$$

$$\frac{\partial \varphi}{\partial y} \sim -\cos\frac{2\pi x}{\ell};$$

$$\varphi \sim \cos\frac{2\pi x}{\ell};$$

$$y_w \sim -\sin\frac{2\pi x}{\ell}.$$

Thus the above variables have the qualitative variations with x as shown in Figure 6. Of particular interest is the radial velocity component $v = \partial\varphi/\partial y$, which indicates the amount of radial inflow/outflow at the groove mouth. Since the blade tip is located at $x/\ell = 1/2$ in Figure 6, the results show that, over the region surrounding the blade tip, the radial flow is outward, i.e., into the groove. Thus the induced flow in the groove effectively applies suction to the rotor tip. Note that the bounding streamline shape is a mirror image of the pressure distribution, so that the groove flow cross-sectional area expands where the pressure is high and velocity is low, and it contracts where the pressure is low and velocity is high.

It is also of interest to examine the radial variation of flow properties from the groove mouth ($y/\ell = 0$) to the groove bottom ($y/\ell = H/\ell$), and the effects of groove depth on the flow properties at the groove mouth. From Equations (5, 6) or (9, 10), it can be seen that the induced velocities vary exponentially with y/ℓ, the distance into the groove. Typical variations of velocity amplitudes with radial distance y/ℓ are shown in Figure 7 for a sine-wave groove mouth pressure distribution.

The induced flow velocities at the groove mouth for a sine-wave pressure distribution are obtained from Equations (9, 10) by taking the limit as $y \to 0$:

$$\left[\frac{\partial \varphi}{\partial x}\right]_{y=o} = \frac{2\pi V_\infty h}{\beta \ell}\left(\sin\frac{2\pi x}{\ell}\right)\left[\frac{\cosh(2\pi\beta H/\ell)}{\sinh(2\pi\beta H/\ell)}\right]; \quad \text{(a)}$$

$$\left[\frac{\partial \varphi}{\partial y}\right]_{y=o} = \frac{2\pi V_\infty h}{\ell}\left(\cos\frac{2\pi x}{\ell}\right), \quad \text{(b)} \qquad (12)$$

and so

$$\left[C_P\right]_{y=o} = -\frac{4\pi h}{\ell\beta}\left(\sin\frac{2\pi x}{\ell}\right)\left[\frac{\cosh(2\pi\beta H/\ell)}{\sinh(2\pi\beta H/\ell)}\right]. \quad \text{(c)}$$

The bounding streamline half-amplitude at the groove mouth then becomes, for a sine-wave pressure distribution,

$$h = -\frac{\beta}{4\pi}\left[C_P\right]_o \tanh\left(2\pi\beta H/\ell\right); \qquad \text{(a)}$$

where

$$\left[C_P\right]_{y=o} = \left[C_P\right]_o \sin\frac{2\pi x}{\ell}. \qquad \text{(b)} \qquad (13)$$

From Equations (12, 13) it is seen that the bounding streamline half-amplitude h and the radial velocity at the groove mouth increase with increasing groove aspect ratio H/ℓ. In the limit as H becomes infinitely large, the induced velocities approach a maximum given by

$$\left[\frac{\partial\varphi}{\partial x}\right]_{y=o} \longrightarrow \frac{2\pi V_\infty h}{\beta\ell}\left(\sin\frac{2\pi x}{\ell}\right) = \left(u - V_\infty\right)_{MAX};$$

$$\left[\frac{\partial\varphi}{\partial y}\right]_{y=o} \longrightarrow \frac{2\pi V_\infty h}{\ell}\left(\cos\frac{2\pi x}{\ell}\right) = v_{MAX};$$

$$h = \frac{\beta}{4\pi}\left[C_P\right]_o = h_{MAX}.$$

Thus the ratio of velocity amplitude for a given value of H/ℓ to that for H approaching infinity becomes

$$\left(\frac{v}{v_{MAX}}\right)_{y=o} = \frac{h}{h_{MAX}} = \tanh\frac{2\pi\beta H}{\ell}. \qquad (14)$$

Figure 8 shows the variation of v/v_{max} with H/ℓ and M_∞ implied by Equation (14). It can be observed that the radial velocity amplitude rapidly approaches its maximum value with increasing groove depth for incompressible ($M_\infty = 0$) flow. For $M_\infty > 0$, the rate of increase of v/V_∞ with H/ℓ is reduced as M_∞ increases. Thus, deeper grooves are required to achieve maximum effect for the compressible case; Figure 8 also shows a representative cross-plot giving the Mach number effect on the groove depth required for constant relative effectiveness.

The preceding analysis was used to predict the circumferential groove flow for the NAS3-15707 LSRC configuration. The blade-to-blade flow field, predicted by the General Electric Compressible Fluxplot Computer Program, and presented in Figure 2, was used for the circumferential pressure distributions to be imposed on the casing grooves. The circumferential groove configuration to be tested consists of five grooves over the rotor tip, located over the middle 60% of the chord length. The groove depth is 28.7% of the blade

spacing. The grooves located at 30% and 50% of chord length were analyzed by the method presented herein. A Fourier analysis of the pressure distribution (blade-to-blade) was made to determine the various sine and cosine harmonic components. The induced flow velocities and streamline shapes for each component were then computed. The components were then summed to obtain the total induced flow field.

Results for the groove at 30% chord are presented in Figure 9. These results imply that an approaching blade treats the flow in the groove something like a snow plow: the high static pressure in front of the blade calls for a low relative velocity, which in turn calls for a large streamtube area to pass the flow. Thus much of the flow is squeezed out of the groove like snow spilling around the plow. Under the blade tip the pressure is dropping. The flow (relative frame still) accelerates, and occupies less stream tube area. Flow is drawn into the groove with quite large radial velocity to satisfy continuity with the changing longitudinal velocity. It is interesting to observe that this model implies a very large fluctuation in the absolute frame longitudinal velocity, from 10% to 80% of the blade speed at the groove face, which should be easy to measure experimentally.

Results for the groove at 50% chord are presented in Figure 10. The calculations were carried out, not only for the experimental groove depth, but also for half this depth and twice this depth. The pressure loading predicted across the blade at this axial position is less than at 30% chord, and the range of longitudinal velocity predicted in the groove is correspondingly less. The groove depth may be seen to have a significant, but quantitatively small, effect on the predicted velocities. Figure 11 is a cross-plot of Figure 10 at two positions relative to the blade, showing the influence of groove depth.

The preceding analytical study suggests that the blade-to-blade rotor tip pressure field can induce significant radial flows when circumferential grooves are present. The study has neglected the effects of viscous damping on the groove flows, which could be of considerable importance. It has also been assumed that the groove flow pattern consists of a small perturbation from an average groove flow in the circumferential direction. An additional restrictive assumption was made that the groove flow was two-dimensional in the radial/circumferential plane. These assumptions imply that the analysis is restricted to cases where the groove axial width w is substantially smaller than the depth H, i.e., $w/H << 1$, and that the perturbation velocities are much smaller than the mean velocity in the groove:

$$\frac{v}{V_\infty} << 1$$

These conditions are quite unrealistic unless V_∞ has substantial magnitude in comparison to the blade speed U_t. (See equation 4.) Since $U_m = U_t - V_\infty$, this implies that the groove mean flow velocity U_m in the absolute reference frame should be substantially less than rotor speed U_t. It seems reasonable to expect that this is the case for typical grooved casing treatment configurations, since rotor tip sections generally operate with absolute swirl levels much less than rotor speed, and the action of viscosity will be to reduce these levels even further.

It remains to determine how the induced groove cavity flow would affect the compressor flowpath in terms of performance and stall limit. It is certainly possible that a mutual interaction can occur, e.g., the induced cavity flow can alter the rotor tip region flow and blade-to-blade pressure field, which in turn can change the induced flow in the groove, etc. It is beyond the scope of the present study to analyze these possible interactions, but the

results suggest that the induced groove flow can apply effective suction to the blade tip boundary layers, possibly delaying separation and stabilizing the flow in the tip region. It can then be speculated that the magnitude of the induced flow velocities corresponds in some monotonic fashion to the observed magnitude in stall margin improvement. It is interesting that the variation in stall margin improvement with groove depth presented in Figure 12 based on data from Reference 5, has a similar trend to the variation of radial velocity with groove depth shown in Figure 11.

Based on the analysis presented herein, it was concluded that the blade-to-blade rotor tip static pressure distributions could induce significant radial inflow and outflow in circumferential groove cavities. The flow over the rotor blade tip region has a radially outward (into the groove) component, and this suggests that the induced groove flow produces effective suction on the rotor tip blade surfaces.

It was further concluded that the magnitude of the induced suction velocities was dependent on groove depth, varying as the hyperbolic-tangent of the groove depth/pitch ratio. For incompressible flow, the induced suction velocity magnitude increases with groove depth, reaching 90% of its asymptotic maximum when the groove depth is about 25% of the blade pitch. The effect of compressibility in the groove flow is to reduce the rate at which the induced suction velocity approaches its maximum value. It was therefore deduced that high-speed compressor stages would be more sensitive to changes in groove depth, and would require deeper grooves to achieve maximum effect, compared to low-speed stages.

Because the induced groove flow effectively produced suction at the blade tip, it was tentatively concluded that circumferential grooves could conceivably improve the tip region performance through reducing boundary layer losses, in addition to delaying the onset of rotating stall.

Irrotational model in the absolute frame for the flow in circumferential groove and blade angle slot casing treatment cavities - Analysis methods from the theory of two-dimensional incompressible, inviscid, irrotational flows have also been adapted to the prediction of flow patterns with constant absolute frame total pressures, in two kinds of casing treatment cavities for casings over axial flow compressor rotor tips. Static pressure on the cavity face serves as a boundary condition for the solutions; this static pressure is obtained from a two-dimensional cascade analysis of a rotor tip section. An assumption is needed in each case for a unique total pressure for the cavity flow. The total pressure for the circumferential groove flow is taken from the absolute flow component in the free stream parallel to the groove. The solution predicts that a substantial amount of this flow actually enters the groove. The total pressure for the blade angle slot flow is taken from the absolute flow across the slot face, with allowance for loss as this flow negotiates a 90° deflection entering the cavity. Quite large velocities entering and leaving the cavities are predicted, which could exercise a modifying influence on blade surface boundary layers and on tip clearance region flow.

A possible model for the flow in a circumferential groove cavity is a two-dimensional incompressible potential flow, with a static pressure impressed on the cavity face by the flow field of the rotor tip and a total pressure appropriate for driving the flow by momentum interchange with the mean absolute tangential velocity of the external flow. A similar flow pattern also seems applicable to the blade angle slot configuration; the flow would enter the slot at the downstream end with the static pressure there, and some small recovery of the velocity head across the slot.

Several distinctive features of the circumferential groove flow pattern can be identified before any detailed analysis is carried out:

1. The static pressure boundary condition on the cavity face has just one maximum, reached close to the pressure surface of the rotor blading passing outside of the groove. The lowest velocity in the groove, for the flow at uniform total pressure, must be found at the static pressure maximum.

2. The locale of the static pressure maximum moves along the groove more rapidly than the flow velocity. Ahead of the advancing pressure maximum the flow will be moving faster than at the maximum. To satisfy continuity makeup flow must be drawn into the groove in this region. Behind the pressure maximum flow must leave the groove.

3. Flow along the bottom of the groove must be uniformly in the direction of rotor rotation. For reversal there would have to be a stagnation point, and a static pressure higher than at the groove face. But actually pressures on the groove bottom must represent an average of the face pressure over some distance, and therefore must be lower than the maximum face pressure.

Two-dimensional incompressible flows with constant total pressure can be described by complex velocity potentials, combining a potential function ϕ which expresses the constancy of total pressure, and a stream function ψ which satisfies continuity. (Note that this potential function should not be confused with the potential function used in the previous section.)

Given two Euler equations and a Continuity equation in velocity components u and v and static pressure p,

$$u \frac{\partial u}{\partial x} = v \frac{\partial u}{\partial y} + \frac{1}{\rho} \frac{\partial p}{\partial x} = o , \tag{15a}$$

$$u \frac{\partial v}{\partial y} + v \frac{\partial v}{\partial y} + \frac{1}{\rho} \frac{\partial p}{\partial y} = o , \tag{15b}$$

$$\frac{\partial u}{\partial x} + \frac{\partial v}{\partial y} = 0 , \tag{16}$$

and if

$$\frac{\partial u}{\partial y} = \frac{\partial v}{\partial x} , \tag{17}$$

as is implied by the potential function definition

$$u = \frac{\partial \phi}{\partial x}, \tag{18a}$$

$$v = \frac{\partial \phi}{\partial y}, \tag{18b}$$

equations (15a) and (15b) will reduce to

$$\frac{u^2 + v^2}{2} + \frac{p}{\rho} = c \quad . \tag{19}$$

Similarly equation (16) is automatically satisfied if

$$u = \frac{\partial \psi}{\partial y} \quad , \tag{20a}$$

$$v = \frac{\partial \psi}{\partial x} \quad . \tag{20b}$$

Equations (18a) and (20a), constitute one Cauchy-Riemann Equation, and (18b) and (20b) a second Cauchy-Riemann Equation for the existence of the complex velocity potential

$$\begin{aligned} W &= \phi + i\psi \\ &= f(x + i\,y) \quad . \end{aligned} \tag{21}$$

Substituting equations (18) into (16) and (20) into (17), it is apparent that ϕ and ψ both satisfy Laplace's Equation

$$\frac{\partial^2 \phi}{\partial x^2} + \frac{\partial^2 \phi}{\partial y^2} = 0 \quad ; \tag{22}$$

$$\frac{\partial^2 \psi}{\partial x^2} + \frac{\partial^2 \psi}{\partial y^2} = 0 \quad . \tag{23}$$

Any standard method for solving Laplace's Equation with appropriate boundary conditions may be useful.

From complex function theory we learn that if any function, W for example, is analytic in z, its derivative $\frac{dW}{dz}$ also is, and the logarithm of that derivative, $\ln\left(\frac{dW}{dz}\right)$, also is. The real and imaginary parts of those functions also satisfy Laplace's Equation, and may be developed to satisfy boundary conditions by standard methods.

In terms of velocity components

$$\begin{aligned} \ln \frac{dW}{dz} &= \ln \left| \frac{\partial \phi}{\partial x} + i \frac{\partial \psi}{\partial x} \right| \left(\text{or } \ln \left| \frac{\partial \phi}{\partial y} + i \frac{\partial \psi}{\partial y} \right| \text{ etc.} \right) \\ &= \ln \left| u - i\,v \right| \\ &= 1/2 \ln \left| u^2 + v^2 \right| - \tan^{-1} \frac{v}{u} \quad . \end{aligned} \tag{24}$$

Thus a logarithmic function of the velocity magnitude should satisfy Laplace's Equation.

For the purpose of the circumferential groove flow pattern, the groove may be represented as a rectangle, as in the sketch, with height equal to the period from one blade to the next. Then the boundary conditions are:

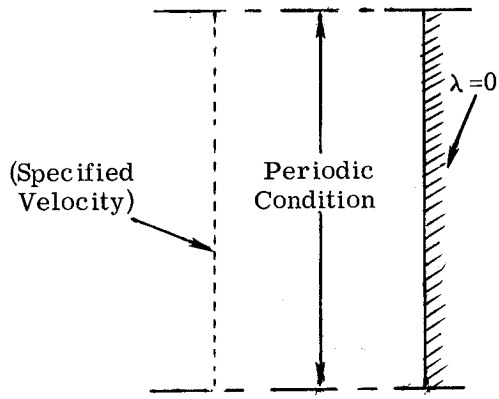

(a) the logarithmic velocity function specified arbitrarily on the left hand side of the rectangle;

(b) the groove bottom defines a constant flow direction--the gradient of flow angle is perpendicular to the groove bottom, so the gradient of velocity function must lie along the groove bottom, giving a vanishing derivative perpendicular to the groove bottom.

(c) the velocity function should be periodic, with identical values at corresponding points on top and bottom of the rectangle.

The General Electric FLUXPLOT computer program (Reference 11) provides for solving Laplace's Equation with these boundary conditions, and therefore is a means for obtaining the velocity function. Complete evaluation of the complex velocity potential from the velocity function, or at least mapping the streamlines, requires construction of the conjugate to the logarithmic velocity function, and then exponentiation and integration. A simple auxiliary program to carry out these operations has been written. It takes advantage of the built-in calculation of derivatives of the first function satisfying Laplace's Equation. Cauchy-Riemann Equations identify these as derivatives of the conjugate function, the flow angle function, which may then be integrated away from the rectangle edge where the flow angle is known. Then the velocity components are obtained and integrated to form the stream function as in Equation (20).

The analysis has been used to predict the flow pattern in a circumferential groove along the line $\frac{x}{s} = 0.5$ in Figure 2. Three cases have been considered. The first, with results shown as Figure 13, supposes the total pressure in the groove to be based on the circumferential average static pressure, with a velocity head taken from the circumferential average of the absolute velocity component along the groove. The figure shows contours of constant resultant velocity and contours of constant flow inclination from the groove bottom. The figure also shows streamlines, identifying the maximum and minimum stream functions. The difference between maximum and minimum is 0.157, indicating that 15% of the average groove flow is drawn in fresh from the free stream in each blade passage. Thus a substantial macroscopic momentum transfer between free stream and groove may occur, which will undoubtedly be supplemented by turbulent momentum transfer across streamlines.

Two additional cases, presented as Figures 14 and 15, consider that the total pressure in the groove is based on 80% recovery of the velocity head of the absolute tangential velocity, and 60% recovery of that velocity head. The macroscopic momentum transfer is 25% of the average groove flow for Figure 14 and 44% for Figure 15. Thus, the analysis encourages the idea that the groove flow level may be maintained at a level close to the absolute free stream velocity, even in the face of laminar or turbulent shear forces from the groove walls.

In fact, the total pressure of Figure 13 is not even an upper bound to the possibility: there may be some recovery of the axial component of momentum for the flow entering the groove.

These sample calculations were made for a groove geometry similar to that planned for the NAS3-15707 experimental program. The groove depth is 21.4% of the blade spacing. The implication of a shallower groove depth would be a relatively greater penetration of the free stream pressure variation to the bottom of the groove. Following inviscid reasoning, there is no obvious reason why the larger variation between maximum and minimum pressure on the groove bottom should be harmful. If the effect, however, is one of maintaining a smooth flow pattern when the total pressure near the bottom is degraded by wall shear, the smoothing effect of groove depth may be important in determining the favorable influence of the cavity.

If the flow pattern in the circumferential groove, as predicted by the uniform total pressure inviscid model, is relevant to the real fluid behavior of this configuration, the critical geometrical parameters should be those defined in the model. Clearly there is just one such parameter, the ratio of groove depth to blade spacing. The ratio of groove width to groove depth does not enter the picture.

Table I takes a look at the ratio of groove depth to blade spacing for some of the examples reported in the literature.

The successful treatment examples have generally had groove depths greater than 14% of the blade spacing. In only one case has a groove depth less than 7% of the blade spacing shown significant stall margin improvement.

As suggested earlier, the basic method of analysis has also been adapted to predicting the flow in a blade angle slot. Referring again to Figure 2, the static pressure over the pressure surface region is nearly constant. When a particular slot is exposed to this pressure distribution, there is little or no driving force to support a longitudinal flow in the slot. As soon as the blade tip passes over the slot, leaving it exposed to the suction surface region, there is a quite large pressure difference between the ends of the slot. The absolute flow direction is nearly perpendicular to the blade angle slot. Some flow may, however, be presumed to enter the slot at the downstream end, at the static pressure there and with some small recovery of the velocity head across the groove.

Figure 16 has been prepared for a blade angle slot, with a baffle in its middle, so that the actual cavity extends from $\frac{x}{s} = 0.5$ to $\frac{x}{s} = 0.8$ (Figure 8). Twenty-five percent recovery of the velocity head across the downstream end of the slot has been assumed, defining the groove total pressure. The reference velocity for the calculations is the upstream relative velocity to the cascade, which happens in this case to be the absolute velocity across the slot at its downstream end also.

The analysis for the blade angle slot is complicated somewhat, relative to the circumferential groove, by the presence of stagnation points at the inside corners of the cavity and 90° changes of the flow inclination from the slot bottom. These stagnation points are singularities of the logarithmic complex velocity. The singularities have been incorporated into the analysis by choosing small radius circular boundaries near the corners, and adjusting the velocity level on this boundary until the numerical analysis gives a velocity doubling for a circle at double the boundary radius, as is required by the analytical representation of a stagnation point pattern.

The results of Figure 16 predict a mean longitudinal velocity along the slot equal to some 30% of the relative velocity upstream of the rotor tip cascade, and a mean radial velocity into 25% of the slot length at the downstream end equal to 35% of the relative velocity upstream (this, is, of course, defined by the assumed recovery). This level of velocity into the slot, if it represents suction of a blade surface boundary layer about to separate, could have substantial stabilizing influence on that boundary layer. The slot flow level would be expected to drop off rapidly as the blade moves away, damped by wall shear as well as the reduced driving force. Consequently, the slot could act as a wall suction device over the small fraction of a blade pitch when it is needed, without maintaining objectionable leakage effects over the remainder of the period.

Figure 17 has been prepared for the same geometry as Figure 16, while assuming that only 5% of the absolute velocity head across the downstream end of the slot is recovered. This recovery assumption is believed to be quite pessimistic. The mean radial velocity into the downstream end of the slot is still almost 25% of the cascade upstream relative velocity, and the mean velocity along the slot is still about 20% of the upstream velocity.

It should be observed that the description of the flow in the upstream half (with respect to the freestream) of the slot would be equally rational for a total pressure corresponding to zero recovery. The static pressure difference along the slot is large enough to provide for substantial velocity at the upstream end, whatever the recovery. If one supposes that the actual effect of the loss associated with flow taking one 90° deflection from the freestream into the slot, and a second 90° deflection from the depthwise direction to the longitudinal direction in the slot, actually takes place over 25% or so of the slot length, then the effective recovery may actually be negative without destroying the realism of this flow model.

This analysis may be summarized in the following conclusions:

1. This inviscid flow model predicts flows in circumferential grooves which are closely connected with the absolute flow outside of the groove. Substantial amounts of the freestream flow entering and leaving the groove in each blade passage supply the driving force for the groove flow.

2. This inviscid flow model predicts rather large flow into a blade angle slot at the downstream end and out at the upstream end, when the slot is exposed to the suction surface pressure distribution. The driving force is largely removed when the slot is exposed to the pressure surface pressure distribution.

3. The flow patterns of these predictions provide guidance in designing experiments to measure casing treatment influences in axial flow compressors.

Viscous flow in circumferential grooves - Experiments with circumferential grooves have shown that the stage response may be quite sensitive to the groove geometry. In particular, configurations with groove depths three or more times the width are substantially more effective than those with depths equal to the width. In the previous section it was pointed out that inviscid models suggest that the ratio of groove depth to blade spacing should be the significant parameter, and that the ratio of groove depth to groove width is irrelevant. If, however, an extended model is developed to include wall shear forces there is a possibility that wall shear forces may alter the flow patterns near the groove face enough to explain groove depth influences.

Considering further the impact of wall shear forces, these may result from strictly turbulent flow in and around the grooves. If, however, the flow is fully turbulent in the groove, the velocity profiles would be concentrated within a distance corresponding to 25% of the groove width (0.9 V_{max} for a 1/7 power profile) from the walls. On this basis the presence of the groove bottom would certainly be felt for that distance from the bottom, and to a lesser degree out to one-half the groove width, but should not be noticeable at the groove face for any depth greater than the width.

Wall shear forces could also be felt through laminar flow in the groove. This section presents some analysis and discussion of implications on the hypothesis of such a laminar flow.

The classical theory of Poiseuille investigates the Navier-Stokes Equations for fluid motion including viscosity, with a restrictive assumption of parallel flow. All velocity components perpendicular to a reference direction (the x direction in the first sketch) are disregarded. The velocity component u in the reference direction may vary over a cross-section perpendicular to the flow direction, but may not vary in the flow direction. With these restrictions the Navier-Stokes Equations reduce to:

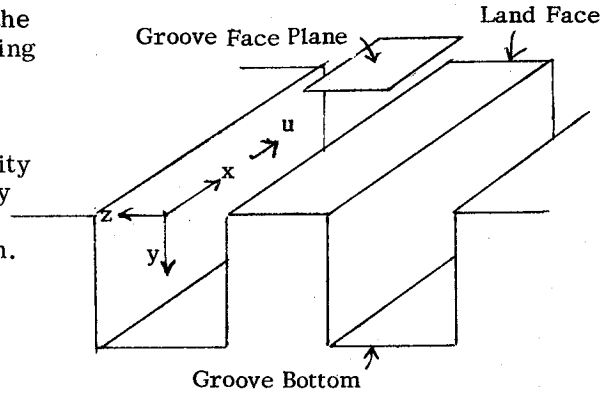

$$\frac{\partial p}{\partial x} = \nu \left(\frac{\partial^2 u}{\partial y^2} + \frac{\partial^2 u}{\partial z^2} \right) \qquad (25)$$

The Poiseuille theory may be applied to the circumferential groove problem if it is assumed that the flow in the groove is driven by the mean absolute tangential velocity outside of the groove, at the nominal blade tip clearance above the groove face. For this first approximation estimate, it is convenient to suppose that pressure gradients from the field of the moving rotor, which may actually be large, average out to zero and contribute only second order effects to the wall shear forces. Then the pressure gradient terms in equation (25) may be neglected and the problem requires solution of Laplace's Equation, subject to the boundary conditions (second sketch):

1. Zero velocity on the groove walls and the land face,
2. Freestream velocity at the clearance distance from the groove and land face.
3. Zero velocity gradient normal to symmetry planes on the groove and land centerlines.

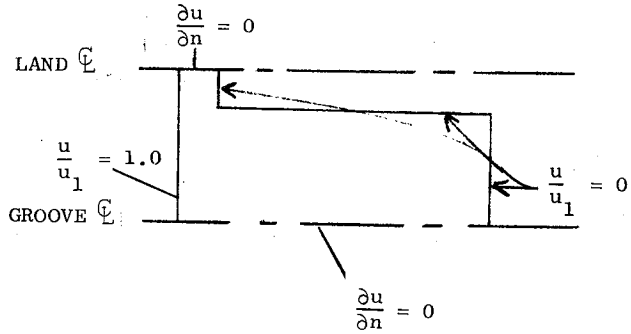

An additional refinement in this analysis considers that the effective viscosity outside the groove face may be much higher than that inside the groove. This

would be the situation if the flow inside the groove is truly laminar, while a turbulent transition outside the groove to the freestream is approximated by an eddy viscosity. The situation may be simulated by postulating an interface between regions with different viscosities at which the shear forces are balanced by requiring velocity gradients in inverse proportion to the viscosities.

Solutions to this problem have been obtained for a groove depth equal to three times the groove width. This is the geometry chosen for the experimental program. Results are presented in Figures 18a - 18c for external viscosities equal to the groove viscosity, four times and twenty times the groove viscosity, respectively. The reference dimension, D, is the depth of the grooves in the experimental configuration. Although the different viscosities significantly alter the velocity contour lines, it should be observed that the penetration of the flow into the groove is not greatly influenced by the assumption on freestream viscosity (or shear force due to momentum transfer). This can be seen by noting the position of the $u/u_1 = 0.1$ velocity contour in Figures 18a - 18c at the groove centerline, $Z/D = 0$. This occurs at a value of $y/D = 0.22$ for the freestream eddy viscosity equal to the groove viscosity, at $y/D = 0.26$ for four times the groove viscosity, and $y/D = 0.27$ for twenty times the groove viscosity. Solutions have also been obtained for a groove depth equal to the width, with freestream viscosity equal to and four times the groove viscosity. The results are presented as Figures 19a - 19b. By comparing the velocity contour lines in Figure 18a with those in Figure 19a and the contour in Figure 18b with those in Figure 19b one can draw two major conclusions. First, all of the significant velocities would be confined to the 30% of the groove width nearest the face. Secondly, varying the groove depth to width ratio from 3 to 1 has a minimal displacement effect on the location of the velocity contour lines. Thus the flow pattern characteristics are not suitable for explaining the observed effect of depth on stall margin and efficiency.

Based on results observed during the experimental program, it seemed appropriate to investigate a Poiseuille-type solution in which variable eddy viscosities are hypothesized along the cavity walls. Figure 20 presents the result. The variable eddy viscosity along the side walls of the groove has been simulated by specifying that the velocity shear gradient at 6% of the cavity width from the wall should be 1/4 of the shear gradient at 3% of the cavity width (i.e., the shear stresses are equal for a four to one viscosity ratio), and the shear gradient at 9% of the cavity width is 1/4 of that at 6% width. Similarly the shear gradient at 3.75% of the cavity depth from the bottom is specified to be 1/4 of that at 1.25% of the cavity depth, and the shear gradient at 6.25% depth is 1/4 of that at 3.75% depth. The results show that this simulation does indeed set up a turbulent-type profile transverse to the cavity. Depthwise in the cavity this model allows substantial velocity magnitudes to penetrate farther into the cavity than any of the more strictly laminar models. The 10% velocity contour still only penetrates to half the cavity depth (1.5 cavity widths), where the experiments showed roughly 50% velocity penetrating to 90% of the cavity depth. The model results could be slanted in the direction of the experimental results by exaggerating the magnitude of the viscosity gradient at the bottom of the cavity, and the depth extent over which this gradient is applied.

One function of the analyses discussed in this section is to suggest particular features to be investigated during an experimental program. The cavities in the experimental hardware for the NAS3-15707 program are large enough to permit some detail in the investigation of the viscous-flow-type phenomena which are the subject of this discussion. Although the present analyses are confined to flows with lengthwise uniformity along the groove, the experimental program may identify viscous flow influences with lengthwise variation. There may, for example, be viscous flow patterns tied to the blade-to-blade pressure field, which appear periodically time-varying to a stationary observer.

a. Lengthwise Uniformity - The critical measurement in this area is the time average velocity profile in the groove. Profile variations are possible across the groove width and through the groove depth. The simplest measurements will be time averaged static pressures on the groove walls and groove bottom, and a depthwise total pressure traverse on the groove centerline, assuming average flow in the direction of rotation. If the groove flow is turbulent this traverse will show little or no variation over the distance range beyond 25% of the groove width from the bottom. If the groove flow is laminar, all significant velocities should be confined to the 30% of the groove width nearest the face. Somewhere between the laminar and turbulent situations, a velocity profile which is linear with depth into the groove would be more appropriate as a basis for an influence of depth on the stage performance. Hot film anemomenter traverses, depthwise, should also indicate what velocity profiles may contribute to the performance.

b. Time Variations - It is expected that the flow in the bottom of the groove is subject to a static pressure field varying with time at blade passing frequency. If the effective total pressure of this flow is degraded, due to wall shear forces, it could approach the level of maximum static pressure. An observer observing just after passage of a pressure peak should see the local pressure forces trying to accelerate the flow in the reverse direction. If this is contrary to the average flow in the groove, disturbed flow conditions at the interface between directions should be present. A depthwise traverse of time-varying velocities, by hot-film anemometers, should indicate whether a transition from a flow predominantly in one direction to an oscillating flow may be significant to the configuration behavior.

Roller bearing flow in the mouth of an axial-skewed slot - One flow pattern suggested for an axial-skewed slot cavity to provide a surface reaction different from a solid wall is the "roller bearing" flow. In this pattern the freestream flow is visualized as driving obliquely across the cavity mouth. There is momentum exchange across the cavity mouth between the freestream flow and the cavity flow. If the wall surface friction drag of the cavity opposes longitudinal circulation more effectively then the tranverse circulation, the remaining flow pattern will be one in which the velocity components are primarily in a transverse cross section plane of the cavity. This is the roller bearing flow model, a model in which the roller axis lies along the cavity mouth. The flow moves along with the freestream flow in the cavity-freestream interface, into the cavity along the down-rotation wall and across the cavity and outward along the up-rotation wall.

One feature of the General Electric Compressible Fluxplot Computer program which makes it useful for modelling the roller bearing flow is that it can calculate some flows with a gradient of total pressure perpendicular to streamlines. If the roller bearing flow concept is relevant, the flow is expected to have a solid body rotation core and there will be a gradient of total pressure, with low total and static pressure on the core axis.

The application of the Fluxplot computation to the axial-skewed slot takes a cross-section of the cavity. A small diameter core boundary is simulated. The center is located arbitrarily opposite the lip of the down-rotation wall. Although no precise criteria have been formulated for choosing this core location, it is believed that the entrainment effect of the freestream driver calls for a concentration of circulation in this region, or perhaps farther out toward the open face.

Figure 21 presents the results of a streamline calculation for this flow model. This is a flow which satisfies continuity by having a nearly symmetrical distribution of inward velocities on the down-rotation side of the cavity and outward velocities on the up-rotation side of the cavity. Toward the cavity bottom from the core, the mean velocity near either wall decreases as some of the flow has made the transition from the inward flow side to the outward flow side. At $\frac{x}{D} = -0.65$ the velocity has dropped to half its level on the wall opposite the core. At $\frac{x}{D} = -1.50$ the maximum velocity is less 10% of the wall velocity at $\frac{x}{D} = 0$. Correspondingly, the static pressure in the bottom half of the cavity is high, representing recovery of the kinetic energy of the velocity of the flow entering the cavity. Similarly, the flow entrained along the open face is drawn away from the outward flow wall so that the velocity is made to decelerate away from the cavity mouth. At 25% of the distance from the core to the end of the outward flow wall the velocity has dropped to half. With a real fluid having some viscosity a separation point may be expected, perhaps at about the center of this open surface.

A particular impression given by Figure 21, as a model of a possible flow pattern, is that the flow characteristics would be substantially the same if the cavity depth were no greater than the width.

The analysis of this flow model has been restricted to flow with constant total pressure on streamlines. A truly realistic model should include quantitative evaluation of the momentum interchanges, between free stream and cavity flow, and through shear between cavity and wall. Inclusion of this quantitative evaluation in the model was not justified, since there was no experimental evidence that this type of flow pattern actually occurred.

Specific Experimental Objectives

The advance consideration of the possible mechanisms behind the beneficial influence of casing treatments also emphasized the abstract nature of the concepts. It seemed important to reduce the concepts to specific questions on which concrete answers could reasonably be expected from an experimental program. Six main questions were identified to guide the program:

1. Does the influence of the casing treatment alter the blade loading, as measured by either a blade surface pressure distribution or a momentum balance measurement across the blade row?

2. Can an incipient separation be identified in the blade tip region which is suppressed or delayed in the presence of one or more of the casing treatments?

3. Can radial velocity components (velocity components into and out of the treatment cavities) be identified which are large enough to account for a qualitative difference in the blade tip flow pattern?

4. Can velocity components exist along a cavity with magnitudes comparable to velocity components in the free stream? If so, are they beneficial or would it be desirable to suppress them through the use of suitable baffling?

5. Can significant pressure gradients transverse to a cavity be identified?

6. Can any significant departure of individual passage work inputs and resulting pressure rises from the average be identified? If so, do they change in the presence of casing treatment?

EXPERIMENTAL RESOURCES

Low Speed Research Compressor Facility

The General Electric Low Speed Research Compressor (LSRC) is designed to provide quantitative and qualitative aerodynamic data on axial flow compressor stages. It is ideally suited for the exploration of phenomena in which viscous effects, characterized by Reynolds number, play a predominant role but where compressibility effects, characterized by Mach number or density ratio, are relatively unimportant. Since many compressor flow problems are in this category (secondary flows, wall boundary layer breakdowns, leakage effects, etc.), this facility has been used extensively during its 13 years of existence.

Even though the blade tip speed employed is low (60 meters per second maximum), the large tip diameter (152.5 cm) allows testing with blade chord Reynolds numbers of about 400,000. This is sufficiently high to be above any critical value known for compressor stages and, in fact, is higher than many smaller engines encounter during altitude operation. The large diameter also makes possible the study of small scale phenomena, such as secondary flows, without the need for extreme miniaturization of instrumentation.

A cross sectional drawing of the LSRC is shown in Figure 22. Significant axial positions are indicated by plane locations. Plane 0.0 marks the flow measuring plane of the calibrated bellmouth, plane 0.5 marks the inlet to the IGV's, plane 1.0 marks the inlet to the rotor, plane 1.5 marks the rotor discharge and the stator inlet, plane 2.0 marks the discharge plane of the stator. The discharge of the LSRC is covered with a large movable plate for throttling the flow. The throttle annulus area varies linearly from wide open as the throttle position numbers vary from 0 to 422. A photograph of the final buildup is shown in Figure 23.

The rig is driven from the floor below by a 300 kilowatt (400 HP) stream turbine. Input power is obtained from a strain-gage-type torque meter and an electronic pulse counter speed indicator that reads to the nearest 1/10th rpm. Flow is measured at the bellmouth, which has been calibrated in place over a range of speeds from detailed total pressure and static pressure surveys. This calibration includes a mushroom-shaped high solidity inlet screen enclosure and flow straightener assembly (at top of Figure 13) used for performance tests. The screen surface area is 16 times the rotor tip circle area and has a porosity of 25 percent.

Fluid density is deduced from measurements of barometric pressure, ambient temperature, and air moisture content. A first order approximation of the small compressibility effects encountered at the low speeds used is included in performance computations when precise efficiencies are being sought.

In order to keep operation simple and inexpensive, pressures are read on vertical or inclined water manometers. Since it may take an hour or more with the usual two-man test crew to record all desired pressures for one throttle setting, variations in ambient density due to barometer and room temperature variations may be significant. Possible errors are avoided by making frequent slight adjustments to the speed so as to keep a reference gage pressure in the discharge constant. This approach is justified by the similarity laws for low Mach number flow, which say that all gage pressures in the vehicle should remain in the same ratio, independent of speed, except for negligible effects due to the slight Reynolds number variations that result from this procedure. In order to compute accurate efficiency, the torque, speed, and ambient conditions are all read simultaneously two or more times during the pressure data logging process and the results are averaged.

Test Compressor

The test compressor selected for the Casing Treatment program was a 0.7 radius ratio single stage compressor which had previously been tested as a four stage assembly, with results reported in Reference 10. The four stage assembly had been tested extensively, including various perturbations on stagger and solidity. Tuft explorations and performance measurements had shown that the design was subject to stalling of the rotor tip. It was, therefore, expected to be a good showcase for stabilizing influence of casing treatments on the rotor tip flow.

The stage consists of inlet guide vanes, rotor, and stator. These assemblies are shown in Figure 24. An instrumented rotor blade is shown in Figure 25. Blade design geometry for the blading is given in Table II.

Instrumentation Common to All Configurations

The following instrumentation was used for all configurations:

a) Overall

Wet and dry bulb ambient temperature

Barometer

Electronic (digital readout) tachometer

Strain gage torquemeter

b) Flow measurement plane (plane 0.0 - see Figure 22)

Eleven hub static pressures - equally spaced - with provision for manifolding

Eleven casing static pressures - equally spaced - with provision for manifolding

One 12 element total pressure rake - with provision for manifolding

c) IGV inlet measurement plane (plane 0.5 - see Figure 22) as in (b) above

Flow angle (visual alignment of knitting yarn tuft) and stream static pressure traverse probes

d) Rotor inlet measurement plane (plane 1.0 - see Figure 22)

Eleven rotor hub static pressures - equally spaced

Eleven rotor casing static pressures - equally spaced

One 12 element total pressure rake (7%, 13%, 20%, 27%, 33%, 43%, 53%, 63%, 73%, 80%, 87%, 93% span from hub)

One flow angle (visual alignment of knitting yarn tuft) and stream static pressure traverse probes

e) Rotor exit measurement plane (plane 1.5 - see Figure 22) as in d) above

f) Stator exit measurement plane (plane 2.0 - see Figure 22) as in d) above

g) Rotor blade surface static pressures

Two rotor blades were fitted with blade surface static pressure taps. The suction surface tap installation is shown on Figure 25. Pressure lines (one for each group of three taps at the same chordwise position) are carried through the blade mounting trunnion, inward along the rotor disk to the shaft, and then to a rotating stepping switch, which allows the pressures to be read by a single Cetra transducer. Normally two of the three rows of pressure taps are sealed with pressure sensitive tape to allow the pressures on the third row to be read individually. Pressure taps were located at 14 chordwise positions on the suction surface (5, 15, 25, 35, 45, 55, 60, 65, 70, 75, 80, 85, 90, 95% chord) and at 8 chordwise positions on the pressure surface (5, 15, 25, 40, 55, 70, 80, 95% chord). Rows of taps were located at 2.8%, 8.3%, and 16.7% of the span from the casing.

Manifolding of the hub static pressures, the casing static pressures, and the total pressure rake proved to be satisfactory at the flow measurement and IGV inlet measurement planes.

Casing Treatment Configurations and Special Instrumentation

Transparent removable casing windows are used over the rotor for the various casing treatment configurations. Testing with plain casing windows provided a baseline for comparison. The four casing treatment configurations consist of circumferential grooves, axial-skewed slots, wide blade angle slots (slot width approximately 1.7 times blade maximum thickness), and narrow blade angle slots (slot width approximately 0.80 times blade maximum thickness). All four configurations were centered over the rotor tip and covered approximately 70% of the axial projection of the rotor tip section. Photographs of the various treatment configurations, including some of the special instrumentation, are shown in Figures 26 - 33.

1. Baseline Casing - The window for the baseline configuration is shown in Figure 26. This window covers the rotor inlet and rotor exit measurement planes. Eleven (11) static pressure taps, equally spaced circumferentially, were installed at each of these measurement planes. Nineteen (19) additional pressure taps were located over the rotor tip at locations to allow convenient comparison with taps on the circumferential grooves. Three (3) installation holes were provided for transient static pressure sensors (B & K microphone) at locations corresponding to the first, third, and fifth grooves of the circumferential groove configuration.

2. Circumferential Groove Configurations - The basic circumferential groove configuration is shown on Figure 27. The treatment covers the central 73% of the rotor tip axial projection, located in the center. Cavity widths are 0.89 cm; land widths are 0.38 cm, giving 75% open area for the actual axial extent of the treatment. The cavity depth is three times the width, 28.7% of the rotor tip blade spacing.

In addition to circumferentially spaced static pressure taps at the rotor inlet and exit measurement planes, static pressure taps were located on the centerlines of all cavity bottoms, on the surfaces of all lands, on both side walls of lands near the cavity face, and on the casing surface upstream and downstream of the treatment region.

Traversible total pressure probes were provided at 30% of the cavity width from each wall of each cavity.

Installation holes were provided for B & K transient static pressure sensors in grooves 2 and 4, on the centerline of the bottom of the groove and on both walls near the face.

Hot film anemometers (HFA) were installed in grooves 1, 3 and 5. Two "diagonal X" array HFA's were used in groove 3, located at 30% of the cavity width from each wall. A typical "diagonal X" HFA installation is shown on Figure 28. The "diagonal X" HFA is suited to the measurement of a velocity vector with a dominant circumferential component and with perturbation components into and out of the cavity. Single-parallel-element HFA's were used on the centerlines of grooves 1 and 5, to measure the dominant circumferential velocity component.

A variant on the basic circumferential groove configuration was produced by filling two grooves (Figure 29). The windows were reversible, so this configuration was tested with the open grooves on the forward side and on the aft side.

Another variant was produced by inserting mylar sheet baffles between each of the twelve window segments.

There was some speculation during the design activity about the value of circumferential groove configurations with tapered lands so that large open area could be maintained on the cavity faces, with enhanced mechanical integrity. A configuration with a slanted land, so that the momentum of flow out of the cavity would be in the free stream flow direction, was also considered. These variants were, however, considered to be beyond the scope of the program before the effectiveness of treatment at low Mach number was demonstrated.

3. Axial-Skewed Slot Treatment Configuration - The axial-skewed slot treatment configuration is shown on Figure 30. The cavity extent is 73% of the axial projection of the rotor tip. Cavity width is 0.89 cm. Land thickness is 0.38 cm. The cavity is skewed in the direction of rotation at 60° from the radial direction. The cavity depth is three times the width, measured along the short wall from the tip, the down-rotation wall as seen by the rotor. On this basis the long or up-rotation wall is five times the cavity width. The open area is 70% of the total surface area within the treatment extent.

   The basic axial-skewed slot configuration includes a thin mylar sheet baffle dividing the cavity into two identical, forward and aft, cavities. The configuration was also tested with the baffles removed.

Static pressures, in addition to rotor inlet and exit measurement planes, were installed at five locations on a cavity cross-section and at four axial positions. Cross section locations included the cavity bottom, near the free stream surface on short and long walls, and in the centers of the short and long walls. The location in the center of the long wall is almost opposite the lip of the short wall; these two locations together measure a cavity mouth pressure. Axial locations are at 85% of the cavity width from each end of each cavity. Additional static taps are located at the center of the cavity bottoms. Static pressures were also measured on the annulus surface before and after the treatment, opposite the cavity and opposite the land.

Installation holes for B & K transient static pressure sensors were located at the same axial locations as the steady-state static pressure taps, and in the center of the long wall and on the bottom: 8 locations altogether.

"Perpendicular X" array hot film anemomenters were installed to measure steady state and transient velocities near the cavity mouth and near the cavity bottom. These instruments are suited to evaluating flow patterns that are primarily in the plane of the cavity including components lengthwise and in and out. Figure 31 shows a typical installation.

4. Blade Angle Slot Treatment Configurations - The two blade angle slot configurations, the wide slots shown on Figure 32 and the narrow slots shown on Figure 33, are similar in principle. The slot angles are 53.5° from the axial direction, where the rotor blade tip stagger is 43.4°. This provided a flexibility so that the influence of the treatment could be correlated with a lengthwise velocity component in the cavity. If the lengthwise component turned out to be negligible, the actual angle was unlikely to be critical. If significant lengthwise velocities were measured, the rotor stagger could be altered to align with the slot and the test repeated.

   The slot widths were chosen to augment previous information (References 2 and 4) concerning what dimensions relative to the blade tip thickness are effective. Previous experience had been primarily with slot widths nearly the same as the tip thickness. For this program two thicknesses were selected: the narrow slots are 80% of the maximum tip thickness; the wide slots are 1.7 times the maximum tip thickness. The wide slots provide clearance space communication in case clearance space velocities are an important part of the treatment influence. The narrow slots insure that there will not be clearance space communication.

   Slot depths are three times the wide slot width. All slots are partitioned at the center.

   The wide blade angle slots have static pressures installed on the annulus surface before and after the treatment region, opposite the cavity and opposite the land. There are also pressures measured on the land surface, at mid-depth on both cavity walls and on the cavity bottom, spaced axially at 80% of the cavity width from each end of each individual cavity. Finally, static pressures are located at the centers of the individual cavity bottoms.

Installation holes for B & K transient static pressure sensors are provided on the land surface and the cavity bottom, at the forward end of the forward cavity and the aft end of the aft cavity. These are axial positions at which similar measurements were made on the baseline casing.

Static pressure taps in the narrow blade angle slot windows are at the same locations as on the wide slot windows, omitting taps at mid-depth, and at the centers of the individual cavity bottoms.

Provision was made for measuring total pressure with traversible probes at the center of the narrow blade angle slot cavities.

Test Procedures

The test program was carried out in two phases, with procedures in each phase adapted to profit by experience.

The Quick-Look series of tests was designed to obtain a rapid overview of the influence of casing treatment schemes on efficiency and stall margin. Approximate performance, with accuracy appropriate for comparison between configurations, was obtained from static and total pressure at the flow measuring plane, casing static pressures at rotor inlet and stator exit measurement planes, and torque input. Knitting yarn tufts were installed in representative cavities of all configurations. Observations of the tufts were designed to identify flow patterns which could be measured quantitatively in the Performance Test phase of the program. The observation technique included stroboscopic illumination synchronized with the passage of rotor blades. This technique promised to reveal flow patterns driven by the blade-to-blade pressure field, provided the tufts had sufficient response to follow blade passing frequency.

Normal rotative speed was chosen to obtain 12.7 cm H_2O (5 inches H_2O) as the value for $1/2\ \rho U_t^2$, based on measurements of the inlet temperature and barometric pressure for the day. Nominal speed was set at the nearest integral rpm, and data recorded only when speed was within 1 rpm of the nominal. For a nominal speed of 575 rpm this represents a precision of $\pm$ 0.2%. The particular choice of speed facilitated on-the-spot conversion between pressures in inches of H_2O and normalized pressure coefficients. The Reynolds number varied $\pm$ 2% by this procedure, which is considered to be insignificant for Reynolds number effects.

In the Performance Test series the primary thrust was toward measurement of flow pattern details, both those details contributing to precise performance evaluation and those measuring treatment cavity flow patterns quantitatively. Measurements were taken at a restricted group of flow levels selected from the range covered during Quick-Look testing. A standard series of throttle settings was chosen for convenience in making comparisons between treatment configurations. Below is a summary presentation of characteristics of these throttle settings. This listing is also included as Table III.

Description	Throttle Setting	Nominal Flow Coefficient	Remarks
Standard Operating Line	422	0.493	80% of peak static pressure coefficient
Peak Efficiency	170	0.46	Some variation in location of peak between configurations
High Operation Limit	145	0.438	95% of peak static pressure coefficient, edge of region of cascade flow breakdown
Baseline Near-Stall	115	0.406	Near-peak static pressure coefficient
Circumferential Groove Near-Stall	105	0.388	Near peak static pressure coefficient
Slot Treatment Near-Stall	92	0.362	Stability beyond this flow affected by instrumentation and Reynolds number

The most clearly defined throttle setting in the series is that close to stall with the baseline (untreated) casing, throttle 115. At this setting the compressor stage operation is stable, but local flow patterns show signs of breaking down, especially in the tip region.

The "standard operating line", throttle setting 422, point has as its primary definition a static pressure rise of 80% of the peak rise. A test point near peak efficiency, or slightly on the open throttle side of peak efficiency, was desired. It was feared that peak efficiency would not be well defined, which led to specification in terms of pressure rise. The choice of points has been satisfactory for comparison studies.

The "high operation limit", throttle setting 145, test point was chosen somewhat arbitrarily to lie between the standard operating line and the near-stall untreated casing point. This point is usually at the edge of the region in which treatment affects local pressure rise characteristics.

Peak efficiency usually occurs about midway between the standard operating line and the high operation limit.

The "circumferential groove near stall", throttle setting 105, test point was conveniently located for the double purpose of searching for characteristic features of the stability limit with this configuration and for worthwhile extrapolation of any trends observed through the test series defined by the untreated casing.

The "slot treatment near stall", throttle setting 92, test point was arrived at after some experimentation and search for a throttle setting at which stable operation was not disturbed by use of instrumentation or variations in speed.

Reliance in the Performance Test series was placed on standardized LSRC measurement and data reduction techniques, developed over the 13-year history of the facility, for overall performance evaluation. The standardized technique, for example, traverses movable

stator vane rings past a fixed 12 element total pressure rake and through ten equally spaced positions covering a vane spacing. During the course of the performance testing, it became apparent that inlet guide vane wakes in the mid-annulus region occupied just about 10% of the blade spacing and that the wake sometimes fell entirely between standard stator positions. It was outside the scope of the Casing Treatment program to develop revisions of the standard techniques that would avoid vulnerability to missing thin wakes. In practice, data comparisons from the Quick-Look method of testing proved to be quite satisfactory. Another weakness in the standard technique appears to be a possible reason for failure to obtain repetitive results: this is measurement of the inlet temperature, used to establish the reference velocity head. Previous experience had shown uniform inlet temperature throughout the large inlet chamber from which the compressor air is drawn so that operator convenience could determine the location of the temperature measurement. The Casing Treatment program experience suggests that some temperature stratification may be possible, particularly during periods of cold weather outdoors, and that a modification of the temperature measuring standards may be needed.

Specialized measurement techniques, using hot film anemometers for velocity and B & K microphones for time-varying static pressure measurement, were specified for examination of flow pattern details in this Casing Treatment program. The experience during the program showed that it would have been beneficial to put more effort into developing special calibration techniques to suit the needs of the program.

A 1.27 cm (0.5 inch) jet, fed from a 7.6 cm x 15.2 cm (3 inch x 6 inch) cylindrical plenum chamber, served for calibration of hot film anemometers at the appropriate velocity levels immediately before and after use on test. Amplifier gains could be set for voltage outputs for convenient readout on a digital voltmeter or an oscilloscope screen. It appears, however, that the jet diameter was marginal for calibration of the instruments with sensing elements 2.5 mm (0.1 inch) long. With amplifier gains set for correspondence between the HFA reading and total and static pressures in the calibration jet, the HFA's gave substantially higher velocities than the pressure measurements in the test vehicle. The calibration jet was also used to determine the sensitivity of angle measurements with two-element, X-array HFA's. Typically the amplifier gains were set to give a convenient velocity calibration at zero angle, where the outputs A and B of the two elements are equal. Then the signal measurements are repeated at specified angles (pitch angle for a "diagonal X", yaw angle for a "perpendicular X") at which the ratio of the difference between signals to their sum measures the angle. For small angles the calibrations showed that the sum of the signals is insensitive to angle. It appears that the electronic circuitry associated with HFA readout can be arranged to give direct readout of the signal output function (A-B)/(A+B). This arrangement was not made for the present program.

The B & K microphone was chosen as a suitably sensitive sensor for measuring pressure fluctuations in the range of peak-to-peak amplitudes from 0.2 cm H_2O to 5 cm H_2O at frequencies from blade passing at 500 Hz to 10 times blade passing. Calibration of the B & K microphone is carried out conventionally using a 124 db Pistonphone. For application to the unsteady pressure measurement problem the 124 db signal is to be interpreted as a sinusoidal pressure variation over a peak-to-peak range of 9.14 cm H_2O (3.6 inches H_2O). B & K traces taken later in the program made use of variable amplifier gain to produce a signal amplitude of 2.54 cm H_2O/volt (1 inch H_2O/volt), so that the oscilloscope display could be interpreted directly as 2.54 cm H_2O/division (1 inch H_2O/division), or 0.2 x $(1/2\ \rho\ U_t^2)$/per division. With gains for each channel in use set to deliver the same scale sensitivity, interpretation of the display was much simpler than on the earlier tests.

EXPERIMENTAL RESULTS

Overall Performance

The study of overall performance of the test stage in the General Electric LSRC Casing Treatment Study was designed to answer several questions:

1. Can an influence of porous wall casing treatment on compressor performance, and especially on the limit to the stable operating range set by stall, be found in a vehicle where compressibility effects are insignificant?

2. Assuming an affirmative answer to question 1, can definite influences of the treatment on pressure rise, work input, and efficiency, as well as stall limit changes, be identified?

3. Can special features be found in the measurements associated with overall performance evaluation which will show how treatment schemes work to extend stability limits?

4. Can mechanisms causing efficiency loss be separated from mechanisms extending the stable operating range?

The first question was quickly answered affirmatively: there is no doubt that the stable operating range of an axial compressor stage limited by loading of the rotor tip section is extended by casing treatment, at approximately Mach number 0.11 (and also at one-half of this nominal Mach number level).

An overall comparison of the stall characteristics of the various configurations emphasizing salient features is presented in Table IV. Table IV also presents a summary of some salient performance characteristics for the various configurations. Eight different treatment configurations, of three basic types, were included in the series. Qualitative behaviors are similar to those reported previously, for example in References 2 and 4. A conventional circumferential groove treatment gave a 5% improvement in stalling flow with a nominal sacrifice in peak efficiency. An axial-skewed slot configuration gave a 15% improvement in stalling flow with three points sacrifice in peak efficiency. A blade angle slot configuration gave 15% improvement in stalling flow with two points sacrifice in peak efficiency. Exploration of circumferential groove variants showed that grooves over the entire center 73% of the blade axial projection contributed to the stalling flow improvement, and that still more improvement could be achieved by inserting a few partitions to restrict the flow in the grooves. Exploration of variants on the axial-skewed slots showed that removal of the mid-length baffles produced a nominal improvement in stalling flow with serious efficiency loss. The performance comparison among blade angle slot configurations shows that a cavity width substantially greater than the blade thickness gives more favorable performance than a cavity width which is less than the blade thickness.

Performance characteristic curves for the test compressor stage have been prepared on two bases; one method uses static pressure rise from the rotor inlet measurement plane to the stator exit measurement plane, as measured on the casing; the second method uses average total pressures at the same two measurement planes. The first method had the great advantage of measurement simplicity, so that many data points could be taken and

evaluated for statistical consistency. While the total pressure method was considered to be a better measure of the absolute performance level, at least in principle, it turned out to be more vulnerable to uncertainty and variability in inlet temperature, which is believed to be responsible for some data scatter. The two methods gave almost identical results through much of the operating region. The correspondence is, however, rather fortuitous. The casing static pressure rise is higher than the hub static pressure rise, apparently because meridional streamline curvatures reduce the radial pressure gradient at the rotor inlet measurement plane and raise the gradient at the stator exit measurement plane. The total pressure rise is affected by a low effective annulus area at the stator exit (e.g., thick rotor blade wakes persisting through the stator) which gets progressively lower with increasing throttling.

Figure 34 presents the overall performance of the baseline configuration on a casing static pressure basis. Figure 35 gives the performance on an average total pressure basis. Static pressure data were available from the original "quick look" series of tests, from a repeat "short point" series, and from a detailed "full point" series. All of these are consistent within the experimental resolution of the test setup. Measured work input for the "short point" and "full point" series was slightly higher than for the "quick look" series, but the difference is not considered to be significant. Work input and efficiency comparisons with other configurations have been made using the "quick look" work data. Solid lines through the test points on Figure 35 are used as background curves on subsequent figures and as comparison standards for performance of the various treatment configurations.

Figures 36 - 38 present pressure-flow characteristic curves based on casing static pressure rise for the nine configurations on which detailed performance investigations were made. Figure 36 contains the primary information: the comparative performances of each of the basic treatment types with the baseline. Figure 37 compares the variants of the circumferential groove configuration. Differences among these, except for stalling flow, are slight. Putting baffles in the grooves makes them slightly more effective at stabilizing flow near stall and also makes them absorb a little more work. Figure 38 compares the variants on the axial-skewed slot system: the cavities with and without baffles. Removing the partition from the center of the cavity seems to allow considerably increased recirculation, with extra work absorption to match, and does not improve flow stability. Therefore, this open cavity configuration may be given low priority for interest in application in any future investigation.

Figures 39 - 41 present overall performance based on total pressures, in the same pattern as Figures 36 - 38. The same pattern of behavior may be seen, except that a near-linear relation between flow and pressure is maintained to lower flows. In the throttling regime around the baseline near-stall, rotor blade wakes seem to be thickening rapidly so that increasing total pressures may be measured without corresponding static pressure increases. With additional throttling, to the near-stall regime for slotted configurations, static pressures drop rapidly, total pressures stop rising and begin to drop slowly.

Data on static pressure rise and work input have been subjected to statistical analysis and curve-fitting, in an effort to improve the reliability of performance change evaluation, especially with respect to efficiency. The results are presented as Figure 42, and are summarized in Tables V and VI. An arbitrary reference flow coefficient, 0.46, is used for curve-fitting. Peak efficiencies are ususally found near this flow coefficient. During individual test series work-input data typically fell within a scatter band defined by +0.1% of the normalizing reference, $1/2\ (\rho\ U_t^2)$. On a similar basis static pressure rise data were dispersed over a +0.2% band. Since, however, some shifts occurred between series, as between the Quick Look Series and the Performance Series on Baseline and Baffled Axial-Skewed Slot Configurations, it is felt that confidence levels for comparative efficiency evaluation should be set at +0.3% of the normalizing reference.

Table V compares work input among the configurations, at the flow level representative of peak efficiency as determined from the curve fits, and at three standard throttle settings in the Performance Test Series. Confidence in the representative character of data at these throttle settings was supported by study of the statistical results. The baseline configuration and the three open circumferential groove configurations exhibited substantially the same work input. The baffled circumferential groove configuration, the two blade-angle slot configurations, and the baffled axial skewed slot configuration showed progressively increasing work inputs, in steps about equal to the experimental resolution. Among the slotted configurations, the work input is roughly proportional to the freedom of flow to recirculate axially. The unbaffled axial-skewed slots allowed considerably greater freedom for recirculation, and required considerably greater work input.

The comparison among static pressure rises, given in Table VI, shows minor variations among the configurations at the standard operating line (throttle 422) and high operation limit (throttle 145). For the condition close to the baseline stalling flow (throttle 115) the baseline configuration and the circumferential groove configuration with only the first three grooves open have less pressure rise than the others. This is apparently a symptom of the approach to stall. There is somewhat more variation among the pressure rises for various configurations in the curve fits of Figure 42. The curve-fit variation includes some difference among bellmouth airflows measured at fixed throttle settings. Figure 42 shows a tendency for those configurations, where the treatment has extended the stable operating range, to show high pressure rise near stall. A slightly different comparison would show that the configurations with extended flow ranges also have extended ranges with a linear pressure-flow characteristic, such as is often predicted by idealized vector diagram calculations.

Radial profiles of total and static pressure are presented on Figures 43 and 44 and profiles of flow angle on Figure 45. These profiles show that the various casing treatments have very little influence on the radial profiles on the standard operating line. A comparison among the profiles at the baseline near-stall condition, however, shows much more variation. The circumferential groove treatment (Figure 43) shows a small tendency toward a higher total pressure than the baseline in the outer 30% of the annulus, which might be ignored in a simple two configuration comparison. All three slot configurations (the axial-skewed slot configuration in Figure 43 and the two blade angle slot configurations on Figure 44) show substantially higher total pressure than the baseline in this outer 30% of the annulus. This high total pressure represents a flow shift, such that total pressures in the hub region should be reduced. Some reduction in the hub region does appear, but the mean dynamic pressure appears to increase, suggesting that the extra tip loading has come partly at the expense of increased rotor wake blockage.

Results of the absolute air angle surveys (Figure 45) are presented for reference. Internal consistency among the measurements was disappointing. Analysis of these data is not expected to contribute to understanding the casing treatment influences, since air angle measurements do not contribute to stall margin or efficiency evaluation. The flow angle survey at the rotor inlet measurement plane was omitted for several of the test conditions because the distribution did not exhibit significant variation.

Tuft Investigation

Extensive flow visualization with tufts was conducted on the rotor blade surfaces and in the treatment cavities. The results are presented in Figures 46 - 52. In each figure the photographs are mounted such that the axis of the compressor lies along a vertical line (flow from top to bottom) and the rotation is to the right.

The photographs in Figure 46, taken through the baseline windows, show tufts on the rotor blades for various throttle settings. Each column of photographs, moving from left to right, shows the tufts at different positions on the suction surface of the rotor. Each row of photographs, from top to bottom, shows a different throttle setting with the near stall throttle along the top row and the wide open throttle along the bottom row. When the tuft on the blade surface is exposed to full free stream velocity flow, it lies near a cylindrical intersection with the blade surface as shown in Figure 46a, suggesting a meridional streamline direction. When the tuft is in a region of very thick boundary layer or separated flow, its motion will be dominated by the centrifugal force of the rotating blade and the tuft will point almost radially outward; see Figure 46d. In regions of a thickening boundary layer or partially separated flow, the direction of the tuft will lie somewhere between the directions indicated in Figures 46a and 46d.

Using the criterion discussed above, it is seen in Figure 46 that the start of the thickened boundary layer region moves toward the trailing edge as the compressor is unloaded from near stall to wide open throttle. This can be seen by comparing Figures 46c, g, k, and o.

Photographs of tufts on the rotor blades were also taken through the circumferential grooved windows; see Figure 47. Although visibility is somewhat obscured by the grooves, the photographs show the same qualitative picture as was presented for the baseline case in Figure 46.

Detailed tuft surveys of the flow in the circumferential groove were made. The results for the near-stall throttle setting are presented in Figure 48. Stroboscopic illumination permits examination of tuft indications at arbitrary positions with respect to the rotor blade tips. There was no apparent pattern to the tuft indications to show a periodic flow pattern carried along with the rotor blades. The tufts may not, however, have a sufficiently high frequency response to detect patterns with the period of the passing rotor blades. Analytical models for the effect of the rotor blade pressure field on the cavity flow had predicted that a conspicuous pattern would be found. In Figure 48 the support stems show light, extending out of the focal plane of the camera. The tufts show dark. Thus the flow in the grooves is clearly left to right; this is also the direction of the rotor blade motion. Some tufts, when immersed close to the groove face, but still inside the groove, may have been pulled out of the groove into contact with the blades. Under these conditions a fluctuating tug was transmitted to the support stem. There were also slight indications of flow transverse to the grooves.

Presenting a realistic report on the tuft surveys of flow in the axial-skewed slots is quite challenging. Frequently individual tufts would hold a particular direction for a substantial fraction of a second, perhaps 1/4 - 1/2 sec, and then shift to another direction for a similar length of time. The observer might conclude that a particular direction was predominant at a particular location, but could not easily supply documentary evidence to support the conclusion. A series of photographs of the tufts was taken to illustrate the situation. These are presented as Figures 49 and 50. The support stems for the dark tufts show light in these photographs. Three throttle settings, two axial positions, and two depths are represented in each cavity, forward and aft. For each condition several flash photographs, timed to give fixed synchronization with blade passage, were taken in an effort to illustrate the random nature of the flow directions. The best defined flow pattern is illustrated by the four photographs in Figure 49c. For both forward and aft cavities, the flow comes into the slot at the downstream rotor discharge end, goes up the bottom end of the slot and comes out at the upstream end of the slot. The four photographs in Figure 49c, which were taken at intervals of several minutes, show the same flow pattern. As the compressor is throttled to the near stall position, the motion within the slot cavity exhibits increasingly random fluctuations; see Figures 49a and 50a. Fluctuations up to 30° from the average direction are common. An extreme example is shown in the second photograph of Figure 49a, where the upper tuft in the lower (aft) cavity has been caught at 135° from the usual direction. A greater variety of flow directions is evident in photographs of tufts located near the slot mouth, Figures 50a - c. For example, 180° swings may be seen for flow at the aft end of the aft cavity in Figure 50a. A larger sample of photographic records, perhaps a minimum of ten for each condition, would be required for objective statistical analysis to estimate the average flow direction. A regularity of the pattern, controlled by passage of a blade tip, could have been detected by varying the synchronization of the stroboscopic illumination with the passing blades. There was no evidence of this sort of regularity.

Randomly timed flash photographs of the tufts in the wide blade angle slots are presented in Figures 51 - 52. Figure 51 also gives a schematic view of the tufted slots. Odd numbered tufts are on the up-rotation side of the cavities, even numbered tufts on the down-rotation side. Letters F and A identify forward and aft cavities separated by the baffle. Although the tufts cannot be distinguished from their support stems by the color in these photographs, the relative breadths are distinctive. The tufts show as broad lines. The stems start as fine lines, and become blurred as they extend out of the region of sharp focus.

Tuft locations 1 and 2, at the forward end of each cavity, show a predominant flow direction out of the cavity. These locations were particularly vulnerable to loss of the tuft when its end, flowing out of the cavity into the main stream, was "picked up" by the passing rotor blades. At the other locations the flow patterns were irregular and quite confused: a typical example is that defined by tufts 5F and 6F. Since 6F points counter to rotation, parallel to the baffle, in both throttle settings and both immersions, while 5F points more or less parallel to the slot land in a forward direction, these two tufts suggest an eddy vortex with radial axis located in the aft end of the cavity. Tuft 4F contrasts with tuft 6F in that it usually indicates a direction at least 90° away, and generally in a forward direction. Tuft 2F often lies nearly in opposition to tuft 4F, showing flow aft along the land. Occasionally tuft 2F shows flow forward along the land and occasionally flow radial from the free stream into the cavity. Tuft 3F shows flow forward along the land 3/4 of the time, aft the rest of the time. The flow generally seemed to show at least one reversal along either land and sometimes two reversals. No attempt was made during this survey to determine whether the flow pattern was repeated in successive cavities.

No photographs are available for tufts in the narrow blade angle slot windows since photographic clarity was obscured by the small width of the slot. From visual tuft surveys at open throttles, the flow was observed to enter the downstream end of the slot, go up the bottom wall and exit from the upstream end of the slot. At near-stall throttle settings the flow was observed to enter radially at the middle of the groove and split into two directions near the bottom wall. Part of the flow turned upstream along the bottom wall, exiting from the upstream end of the slot, and part turned downstream, exiting from the downstream end of the slot.

In the advance planning and during the flow modelling, the investigation was heavily influenced by the hypothesis that the cavity flow in the blade angle slot configuration would respond to a nearly uniform pressure along the blade tip pressure surface, and to the severe pressure gradient along the suction surface. Based on this hypothesis, it was expected that the tuft observations would always show flow in the slot from the downstream end to the upstream end, and that the periodic driving force would somehow be visible. Since no response to a periodic driving force was observed, enthusiasm for this hypothesis was largely dissipated. To the extent that the cavity flow is a response to a time average meridional pressure field rather than the special orientation of the blade, this experiment suggests that all more-or-less axially oriented cavities may be equivalent.

Annulus Wall and Cavity Static Pressures - Time Average

Analysis of time-averaged (or steady-state) static pressures in the outside diameter annulus wall and inside the various cavities is one obvious way to investigate flow patterns in the cavities and their impact on the rotor behavior.

The distributions of static pressure over the rotor tip for the baseline, solid-wall configuration, at three standard throttle settings, are given in Figure 53. At the standard operating line throttle setting, (422), the forward 20% of the rotor axial projection serves for flow induction. The static pressure rise is confined to the remaining 80% of the rotor axial projection, and is distributed nearly linearly. At the high operation limit throttle setting (145) the initiation of the steady pressure rise has moved forward to 10% of the axial projection. There is an early linear pressure rise with a gradient 30% greater than at the more open throttle. There is a break in the gradient at mid-chord, such that the average gradient over the pressure rise region is no greater than that at the open throttle. At the near-stall throttle setting (115) the start of the initial pressure rise moves close to the leading edge; the initial gradient is 50% greater than the uniform gradient at the open throttle, but this gradient breaks at one-third chord and the average gradient is about the same as that for the open throttle. Table VII has been prepared to make annulus wall pressure gradients readily available for comparative study.

Distributions of static pressure in and around the cavities of the basic circumferential groove configuration (five open grooves) are shown in Figure 54. Symbols, keyed to schematics of the cavity cross-section at the bottom of the figure, indicate measurement locations for the various pressures. The dashed lines are drawn through those pressures actually measured on the annulus boundary. In almost every case where pressures have been measured on both walls of a groove, these pressures are the same. The solid lines have been drawn to emphasize this. Pressures on the groove bottom appear to be greater than those across the groove face by an amount consistent with simple radial equilibrium of the flow in the groove. Efforts at identifying flow components (by tuft survey) other than a dominant circumferential flow are discussed elsewhere in this report. Some such compo-

nents have been identified, but they do not contradict the dominance of the mean circumferential flow.

At open throttle settings the static pressures on the land surface are close to the cavity pressure on the downstream side which suggests that there may be some circulating flow, in each groove, such that the land surface pressure represents some recovery of dynamic pressure of the axial flow component in the normal downstream direction. Under this reasoning the cavity pressure is that level required for flow trying to exit from the upstream wall to overcome the impingement of flow into the upstream.

Near stall the land surface pressures fall nearly midway between the cavity pressure on either side, which suggests a somewhat greater extension of a cavity flow circulation into the main stream.

The overall distribution of pressures across the lands between grooves for the standard operating line throttle setting (422) gives a profile very similar to the baseline. The pressure rise starts at the land between the first and second grooves and progresses linearly over the rest of the chord. At throttle settings nearer stall the circumferential groove configuration contrasts with the baseline configuration in having only a slight reduction in the gradient over the aft half of the rotor tip as compared with the forward half. Annulus wall pressure gradients for the circumferential groove configurations are included in the tabulation of Table VII. In comparison with the baseline configuration, this tabulation suggests that the groove configuration makes a substantial increase in adverse wall pressure gradient possible, as if the groove serves as an annulus wall boundary layer bleed, managing to energize this bleed flow and/or shed it further into the main stream. In conjunction with the increased maximum wall pressure gradient, the start of the pressure rise may be delayed, or the initial gradient may be relieved, depending on the position of the particular test point on the pressure-flow characteristic. Close to stall, the circumferential groove configuration exhibits larger wall gradients on both the steep initial rise and the gentler subsequent rise, than any found on the baseline.

Figure 55 shows available wall and cavity pressure data for the baffled circumferential groove configuration. The effective annulus wall pressure gradient for the two more open throttle settings (Table VII) is even greater than was observed with the open circumferential grooves. On the standard operating line (throttle 422) this gradient is so effective as to result in a depression of the static pressures around the first groove, as compared with the open grooves. The extremely high wall pressure leads, near stall, to observation of pressures in and around the last groove well above the rotor exit interstage static pressure. Apparently the flow pattern in the cavity must be quite complex to produce the large observed pressure difference between annulus surface and cavity bottom, and between the two sides of each cavity.

Figures 56 and 57 show the wall and cavity pressures for the circumferential groove variants with two grooves filled. Wall and cavity pressures for the variant with the first three grooves open match those with all grooves open over the flow range above baseline stall. As this configuration is throttled toward its stall the adverse gradient in the plain wall region settles out to the limit demonstrated by the baseline configuration. When the three open grooves are over the aft portion of the rotor, the gradient sustained in the forward half is like the baseline, while the treatment in the aft region maintains the stability of the gradient there for some additional throttling.

Annulus wall and cavity static pressures for the baffled axial-skewed slot configuration, the basic configuration of this type, are presented in Figure 58. To a first approximation it appears that longitudinal pressure variations in the cavity are negligible, and that the pressures just inside the lip of the short or downrotation cavity wall and the pressures at the center of the long wall may be combined and considered as a "cavity mouth pressure". Then the static pressure rises from the cavity mouth to the cavity bottom as if there is substantial average flow through the cavity mouth, which is brought to rest in the cavity bottom. The effective annulus wall pressures which govern the behavior of the mainstream are presumably suitably weighted averages of the cavity mouth pressure and the "long wall face pressure", just beyond the break from the land surface into the cavity. Cavity mouth pressures have been connected by long-short-short-long dash lines to assist in following the development of these pressures. The history of these respective pressures during throttling is substantially different for the forward cavity and the aft cavity. In the forward cavity the cavity mouth pressure is very responsive to throttling; this may really be response to leading edge blade loading, such that heavy leading edge loading results in pumping flow into the cavity. The long wall face pressure for the forward cavity recognizes the light loading situation at open throttle. (It should be observed, however, that the leading edge region has not been completely unloaded at this throttle setting.) In fact, since all the pressures throughout the cavity are nearly the same, a stagnant flow condition may be inferred.

At the next throttle setting, the high operation limit (throttle 145), the relation among the pressures, low at the cavity mouth and high both on the wall face and in the depth of the cavity, is that appropriate for the "roller bearing" flow model, as developed and presented in the discussion of flow modelling. No other evidence of roller bearing flow has been seen.* With additional throttling the long wall face pressure rises slowly, while all pressures in the cavity rise more rapidly. This situation may represent unsteady pressure bearing on the cavity contents. In the aft cavity the long wall face pressure is always higher than the cavity mouth pressure, sometimes approaching the cavity bottom pressure. This is also consistent with the roller bearing flow model, and surprising if mainstream flow over the land separates at the long face corner and reattaches along the face. Study of the cavity pressures for this configuration suggests that the decision to limit pressure measurements to locations with fore-and-aft symmetry was unfortunate, since longitudinal circulation could have given lower pressures on the fore-and-aft center line than at the cavity ends. Some such pressure depression is suggested by the pressure at the center of the cavity bottom; the cavity bottom is presumably a region where nearly all kinetic energy of the flow has been converted to pressure, so the pressure depression at the center due to lengthwise flow will not be large. Annulus wall pressure gradients for the baffled axial-skewed slot configuration have been included in Table VII, even though the relevance of the concept for this configuration has not been established.

---

*The discussion of tuft observations for flow in circumferential grooves gives some evidence of helical flow. The helical flow concept (longitudinal velocity substantially larger than the circulatory velocity) overlaps somewhat with the roller bearing concept (the circulatory flow velocity components larger than the longitudinal velocity).

The annulus wall and cavity pressures for the unbaffled axial-skewed slot configuration are presented in Figure 59. These pressures clearly show the tendency to have high static pressures at the fore and aft ends of the cavity and low pressure at the center, as was postulated for the baffled slots. This configuration also shows that the static pressures in the cavity bottom are much higher than those at the cavity mouth, indicating substantial flow into the downstream end of the cavity and recovery of the kinetic energy as the flow is decelerated near the bottom. At the two highly throttled conditions it is the wall pressure in front of the cavity rather than the wall pressure in front of the land which conforms to the upstream pressure. Perhaps the land pressure responds to the heavy leading edge loading in the regime close to stall, while flow out of the cavity at its upstream end serves as an insulator between the wall pressure in front of the cavity and the blade surface pressure. All cavity pressures are high compared to long wall face pressures, to a greater degree than was observed for the baffled cavities.

Annulus wall and cavity static pressures for the wide blade angle slot configuration are presented in Figure 60 and for the narrow blade angle slot configuration in Figure 61. To at least a first approximation, the wall and cavity pressures for these two configurations are the same. Based on cavity flow surveys, an attempt was made to measure total pressure in the narrow slots. The measurements failed to show any total pressure significantly different from the static pressure. The tuft flow surveys for the wide blade angle slots showed that the flow was highly erratic. Therefore, no attempt was made to measure velocities. A high static pressure at the bottom of the cavity near the forward end is a typical measurement for both wide and narrow cavities and for both forward and aft cavities in each configuration. If the general nature of the flow pattern is that of the predicted flow model, a flow entering the cavity at the aft end at a stagnation pressure slightly above the land static pressure there and exiting from the forward end at a higher velocity appropriate to the low land static pressure there, this type of pressure field would result. It is probably to be expected that corner effects and flow separation effects for adverse pressure gradients along walls should prevent the appearance of true stagnation pressure in the lengthwise corners. The effective annulus wall pressure gradients, both initial and final, given in Table VII are substantially greater than those observed in the baseline and circumferential groove testing. For comparable test points the blade angle slot configurations show much lower pressure on the lands at a corresponding location than the pressure on the land between grooves 1 and 2. The high effective surface gradient usually appears aft of this point. At the near-stall point for these configurations the same high gradient is pushed forward to the leading edge region.

Blade Surface Static Pressures

Measurement of rotor blade aerodynamic loading, and of the influence of casing treatment on that loading, has been one of the more rewarding areas of investigation in the LSRC casing treatment program.

The blade aerodynamic loading was measured by surface static pressure taps (Figure 25) embedded in a rotor blade at three spanwise locations. Fourteen taps are located on the suction surface at each spanwise location and eight taps are on the pressure surface. Pressure lines are led along the blade surface to the rotor hub, then inward along the rotor disk to the shaft, where they are connected through a Scannivalve stepping switch to a Cetra transducer. The electrical output (and the stepping switch control signal) are carried out through slip rings to the control room, where the output signal is read on a digital voltmeter. A single pressure line is used to read the three taps at spanwise locations for a particular chordwise location; normally two of the three taps will be sealed with tape while the third is being read.

Figure 62 presents blade surface static pressure data for the baseline configuration at the three standard throttle settings and the three spanwise locations. The spanwise pressure variation is quite small, except at the leading edge of the suction surface; larger relative flow angles are to be expected in the annulus wall boundary layer, which should appear in the surface pressures as increased leading edge pressure loading. Interpretation of the overall test data in the form of vector diagrams suggests that the relative air angle for the standard operating line test point is about 58°, which may be compared to the 55° value used in the cascade prediction (Figure 2). Similar analysis for the near-stall point gives 67° as the relative air angle, slightly short of the 64° level proposed in the cascade prediction. The "high operation limit" test point on this basis has 63° as the relative air angle. The measured pressure distributions seem to exhibit a substantial unloading of the leading edge in comparison with the cascade prediction for a similar relative upstream flow angle. For similar loading distributions there is apparently a 5° offset between the predicted and measured upstream flow angles. At the near-stall test point the measured pressure surface pressure falls below the prediction, consistent with the observation that the pressure rise characteristic of the rotor droops as it approaches stall.

Blade surface static pressures for the basic circumferential groove configuration (grooves 1-5 open) are presented on Figure 63. Dashed background curves give the distributions for the baseline configuration at the same spanwise location and throttle setting for comparison, except at the treated near-stall condition, where the baseline near-stall is repeated. The discussion of the baseline distributions is generally applicable to the circumferential groove configuration also. There apparently are systematic differences between the distributions for the two configurations, although the magnitude of the systematic differences is hardly greater than the random variations with spanwise position for either configuration alone. The minimum pressure on the suction surface with the circumferential groove configuration at the standard operating line test point is not as low as with the baseline configuration. The circumferential groove configuration has higher pressure surface pressures near the trailing edge than the baseline configuration at all throttle settings. It is believed that the minimum suction surface pressure with the circumferential groove configuration is not as low as with the baseline configuration for near-stall throttle settings as well, but this is hard to determine with assurance when the lowest pressure is a minimum defined by a single tap.

Some blade surface pressures were measured for the three other circumferential groove configurations (baffled grooves 1-5, open grooves 1-3, open grooves 3-5). The distributions of these pressures seemed identical with the distributions shown in Figure 62 or Figure 63 within the resolution of the testing technique.

Blade surface pressures for the baffled axial-skewed slot treatment configuration are presented on Figure 64. In the interest of testing economy, the surface pressures were measured at only two spanwise positions. The character of these distributions is in sharp contrast to the character of the distributions from the baseline and circumferential groove testing. The pressures measured on the pressure surface close to the blade tip are much higher than those measured at 16.7% span from the tip. Several of these pressures are actually higher than the total pressure relative to the blading in the free stream. (This is not believed to be defective instrumentation, since subsequent circumferential groove testing gave no unusual results.) The highest surface pressures appear in about the right location to be consequences of flow into the aft cavity at its downstream end, at about the absolute total pressure at rotor exit, which then passes along the cavity bottom and exits from the cavity upstream end with little loss in absolute total pressure and substantial velocity counter to rotor rotation. This type of flow would have total pressure relative to the rotor high enough to produce the observed surface static pressures. A second high pressure peak for the near-stall throttle setting could well result from a similar flow pattern in the forward cavity, with strength critically dependent on the degree of leading edge loading. The suction surface pressure on the near-blade-tip section in the trailing edge region is also substantially higher than the surface pressure farther down the span or than the pressure from the baseline test.

On the standard operating line and high operation limit test points there seems to be a substantial relief of the suction surface leading edge loading, carrying the observation about the circumferential groove situation a step further. Elsewhere in this report, results are presented to show that the casing static pressure between the rotor and the following stator is substantially higher for slot configurations than for the baseline, even though the static pressure rise along the casing for the rotor-stator combination is close to the same. Since it does not seem likely that the two-dimensional flow pattern and pressure rise characteristic of the stator is altered by the presence of rotor tip casing treatment, an alternate hypothesis is suggested: that there is enough radial component to the flow into the downstream end of the aft cavity so that the casing sees substantial recovery of dynamic pressure, from the end of the cavity to the stator leading edge plane. At the 16.7% span location the pressure distributions on both surfaces look like those from the circumferential groove test.

Blade surface static pressures with the wide blade angle slot treatment are presented on Figure 65 and those with the narrow blade angle slot treatment are presented on Figure 66. These configurations show characteristics similar to the axial-skewed slot configuration.

Both configurations show surprisingly high static pressures on the pressure surface near the blade tip, though not quite so high as the axial-skewed slot. It does not seem as if any flow out of the cavity could have any absolute tangential momentum in the counter-rotation direction. If, however, any such flow forces a place for itself in the boundary layer it may demand increased deflection of the rotor through-flow, such that increased pressure surface pressure relative to the baseline (approaching relative total pressure) is needed. As in the case of the axial-skewed slots, the circulatory pattern of flow into the cavities seems to produce some dynamic pressure recovery visible along the casing surface between the cavity end and the stator leading edge without influence on the static pressure rise of the rotor-stator combination.

Some examination of the blade surface pressures suggested the possibility that some general statements could be made about the casing treatment influences. Table VIII was prepared for detailed examination of blade surface diffusions. The tabulation presents the difference between the maximum and the minimum pressure observed on each surface at the spanwise position. Two positive observations may be made:

1. All treatment configurations show a much greater pressure rise on the pressure surface along the section at 2.8% span from the tip than the baseline. The surface pressure measured near the leading edge with any treatment configuration is usually close to that measured during the baseline test. The maximum surface pressure for treatment configuration tests is substantially above that for the baseline (but the cascade surface diffusion concept (reference 11) may not be relevant for the slotted configurations). The pressure rise along the pressure surface at 16.7% span from the tip also appears to be greater for treatment configurations than for the baseline, but the effect is obscured by the lack of data resolution.

2. Suction surface pressure rises are about the same at the same throttle setting and spanwise location for all configurations. In the presence of treatment, however, the maximum pressure rise on the surface before stall increases greatly. This should be expected if the overall cascade pressure rise remains about constant, implying little change in the pressure on the suction surface in the trailing edge region, while the minimum pressure in the leading edge region follows the increasingly high incidence as the stall flow level is reduced.

Cavity Velocity Measurements

Velocity measurements have been made by using hot film anenometers (HFA's) and total and static pressures in the circumferential grooves, by HFA's in the axial-skewed slots, and by total and static pressures in the narrow blade angle slots.

Radial profiles of the average circumferential velocity in the grooves as seen by the HFA's are presented on Figure 67, and as seen by total and static pressures on Figure 68. Also shown on Figures 67 and 68 are mean absolute circumferential velocities obtained from the cascade predictions. Measurements obtained in the two ways are similar, at least qualitatively. Some differences are observed between the forward and aft sides of grooves, but these do not appear to be systematic. Many of the measured circumferential velocities near the groove faces, particularly those measured by total and static pressures, are close to the predictions for the free stream from cascade analyses. To this extent momentum inter-

change between the freestream and the cavity is confirmed as the driving mechanism for the cavity flow. Elsewhere in this report comparisons between the predictions and the measured blade surface pressures show that the leading edge loading from the predictions is too high. Allowance for this effect would improve the correspondence between freestream and cavity velocity. There is no evidence of significant recovery of the axial component of the velocity outside of the cavity.

Velocity levels appear to drop linearly from the groove face toward the groove bottom. Groove bottom velocities range from 1/3 of the groove face velocity up to 2/3 of the groove face velocity. According to analytical speculation before the experiment, it was expected that:

(1) laminar viscous flow in the groove might be predominant, in which case measured velocity would be less than 10% of the face velocity over 75% of the cavity depth;

or

(2) turbulent flow in the groove might be predominant, in which case cavity velocities would be greater than 90% of the face velocity for at least 75% of the cavity depth.

The experimental results fall in between these two expectations. Where the velocity varies linearly with depth, it suggests a laminar viscous model for flow between infinite parallel planes, with one plane moving relative to the other. The groove configuration could be equivalent to the infinite plane model if shear forces at the land surfaces are small compared to depthwise shear forces. Significant land surface shear forces ought to appear as concavity in the depthwise velocity profile. When a linear velocity profile approaches a fixed wall with a slip velocity, or with a turbulent-type transition profile, some sort of profile to an effective eddy viscosity is implied. The corners between the land surfaces and the groove bottom could provide the environment for transition from a high eddy viscosity through most of the groove depth to a lower viscosity near the groove bottom.

Some typical variations in the groove velocity in response to passage of the rotor blades are shown on Figure 69. Maximum flow inclination indicated by the X-array anemometer signal is 23° into the groove and is found along the aft wall just ahead of the blade. The inward velocity component at this inclination is approximately 10% of blade speed. The compensating outward flow appears to be distributed over almost the entire space between blades, along the forward groove wall. The ± 15% fluctuations in magnitude (upper traces) may be contrasted with predictions based on constant total pressure relative to the moving rotor. These call for a component fluctuation between 50% and 130% of the mean absolute velocity in the groove. The resultant magnitude increases from the suction surface to the pressure surface. The alternative predictions based on constant absolute total pressure, call for a fluctuating component equal to about 10% of the mean absolute tangential velocity, with the resultant magnitude decreasing from the suction surface to the pressure surface. Thus, the measurements fall somewhere between the two models. The actual fluctuations from one revolution to another are large enough in comparison to the fluctuations at blade passing frequency to make the blade passing frequency effect seem unlikely as a dominant factor in the casing treatment influence.

Responses of the longitudinal velocity components in grooves 1 and 5 to blade passage were also investigated. Fluctuation amplitudes in groove 1, toward the rotor leading edge, were similar to those in groove 3 (but superposed on a lower mean level), with a fairly well defined wave pattern at the blade passing frequency. The fluctuations in groove 5, toward the trailing edge were quite erratic, with little or no evidence of systematic response to the blade passage.

The discussion of the tuft survey of velocities in the axial-skewed slots described the erratic nature of the flow pattern and the failure to correlate the flow pattern with the passage of rotor blades. HFA measurements were also made in the effort to confirm the preference for flow into the aft ends of the cavities and out of the forward ends of the cavities. Figure 70 presents some typical results. For these photographs the X-array anemometer has been rotated for a null balance between the signals from the two elements, and the angle of the probe-indicated mean flow direction has been recorded. With this procedure the upper trace in each oscillogram is the A+B signal which has been calibrated to give the velocity component parallel to the null axis of the instrument. The lower trace is the A-B signal measuring the transverse velocity component. For many of the oscillograms, but not all, the RMS output of the A+B signal was recorded, and is indicated on the figure. The statistical record of each location is limited to a sample of one. In contrast to the photographs presenting tuft survey results, this null balance procedure should suppress departures from an average direction lasting less than ten seconds or so. Those angles which have been recorded show little enough consistency among themselves, and with the tuft survey photographs at a similar throttle setting, to suggest that a more sophisticated sampling procedure would be required for real definition of the flow patterns. The photographs show substantial velocity into the aft end of the forward cavity and a smaller velocity outward along the forward end of the aft cavity. In at least two cases the transition from one metastable flow pattern to another seems to take place during the time period of the photograph. In some of the cases the velocity level indicated by a digital readout is clearly different from that shown on the oscillogram, another suggestion of jumping between patterns. The HFA measurements confirm the erratic nature of the flow patterns, previously found in tuft surveys.

Total and static pressures in the narrow blade angle slots indicate low velocities in comparison with characteristic through-flow velocities in the main stream, or in comparison with blade speed.

Annulus Wall and Cavity Static Pressures - Variations with Time

Static pressure variations with time at various locations over the rotor tips and in cavities have been studied, searching especially for systematic variations at blade passing frequency which would connect cavity flows with any stabilizing influence of casing treatment on blade flow.

Figure 71 shows photographs of oscillograph traces taken on the baseline casing, at three axial positions, corresponding to the centerlines of circumferential grooves 1, 3, and 5. These photographs were taken by superposing records of five separate revolutions on the oscilloscope screen. The time sweep is triggered by a one/revolution signal, so that all sweeps show characteristics of the same blades. Successive sweeps were performed at random times, typically a second or so apart. Where variations are seen between sweeps, they are believed to be representative of random time variations.

Pressure amplitudes given by the time-varying pressure traces are summarized in Table IX, which also compares them with blade loadings measured by taps on the moving rotor blades. The amplitudes measured by the two methods at the 20% chord location are about the same. At 50% and 80% chord the blade surface pressures show larger blade loading than the casing pressures. This is understandable if the growth of the blade surface and/or corner boundary layers toward the trailing edge improves pressure communication through the tip clearance relative to the cascade pressure field. The discussion of blade surface pressures commented on the small spanwise variation in the surface pressures measured for this configuration.

Table IX also includes pressure fluctuation amplitudes taken from cascade predictions (Figure 3). The experimental amplitudes agree reasonably well with the predictions. The cascade prediction method gives wave shapes resembling a rip-saw tooth: a near linear rise in pressure over the passage width, followed by a sharp pressure drop across the blade thickness. This shape is sometimes observed, at 51% chord at IGV positions 0 and 8 at high back pressures for example, but more often the shape is distorted. Comparing the high back pressure, 51% chord trace at IGV position 4 with the traces at positions 0 and 8 shows little difference in the extreme amplitudes, but a conspicuous difference in the shape. The flat top to the pressure wake is difficult to understand unless it represents a thick wake of flow stagnated relative to the rotor blade. It is possible that the low flow region in an IGV wake could also appear as a low flow relative to the rotor, and that the stagnant constant pressure region could exist.

Another conspicuous characteristic of the oscillogram traces is the "dip" in the upper trace (Trace No. 1) at about 1/4 blade spacing from the suction surface. This dip appears to be present at all IGV positions and throttle settings, at almost the same relative position on the trace. It is, therefore, primarily a rotor blade characteristic, perhaps a vortex shed from a local boundary layer in the corner between the leading edge suction surface and the annulus wall. The amplitude of the dip appears to be influenced strongly by the relative position of the IGV wake.

Time varying static pressures were also measured during testing of the basic circumferential groove configuration on the bottom surface of grooves 2 and 4 and on both sidewalls of each groove near the cavity face. Results are shown on Figure 72. Unfortunately the calibration scales used for the traces may be confusing. Pressure fluctuation amplitudes from this figure are summarized in Table X. In each case the pressure fluctuation amplitude on the aft side of the groove is substantially larger than the amplitude on the forward side. The fluctuation amplitude on the bottom of the groove is much smaller than the amplitude on either side near the groove face. Table X also provides amplitudes from blade surface pressure measurements for comparison. In the majority of the situations examined the pressure difference from the pressure surface to the suction surface of the blade is greatest at the leading edge and diminishes toward the trailing edge. It is the fluctuation amplitude on the aft side of the groove which corresponds most closely to the blade surface pressure difference. The maximum amplitude in the cavity is reduced from the corresponding blade surface amplitude, usually by 25-30%. A possible explanation for this fluctuating pressure pattern appears to involve a helical pattern, with net flow into the groove along the aft wall driven by the pressure field of the passing blade. This type of flow pattern was suggested by tuft indications of transverse flow. The pressure fluctuation amplitude is damped along the streamline trajectory so that smaller amplitudes are seen along the forward wall where the net flow is outward. If the helical pattern is concentrated in the outer half of the groove, the fluctuation amplitude in the groove bottom region could naturally be much smaller than near the face. It is appropriate to observe that the constant-total-pressure-in-relative-

frame model predicts the pressure fluctuation on the cavity bottom to be about 60% of that on the face, while the constant-total-pressure-in-absolute-frame model predicts the bottom fluctuation to be about 30% of the face fluctuation.

Figure 73 shows the influence of the position of the inlet guide vane wake relative to the pressure sensor on the wave shape. The photograph for IGV position 0 is repeated from Figure 72. The variations with wake position are less conspicuous than on the baseline configuration casing, but may be seen by comparing the near-linear pressure rise along the aft-wall at position 2 with the sudden rise to half-amplitude at position 0, or by comparing the simple cross-cut saw tooth shape on the groove bottom at position 2 with the more complex shape at position 8. All of the wave shapes are markedly repetitive from blade to blade and with time on the same blade.

Quantitative comparisons of the pressure fluctuation amplitudes and wave shapes on the baseline casing surface and in the circumferential groove cavities have been made and are presented on Figure 74. In these comparisons the signal seen near the aft cavity face of groove number 2 is quite similar to that imposed on the baseline casing (and presumably the face of groove 3) farther downstream at 50% chord. Since this amplitude is much reduced on the forward cavity wall, even though the driving amplitude applied may be larger, it appears that the cavity may seem to absorb imposed pressure fluctuations while the solid wall reflects them.

Time varying static pressures measured in the cavities of the axial-skewed slot treatment are presented on Figure 75. Comparisons may be made: (1) between forward and aft ends of one cavity at the same depth; (2) between mid-depth (two-thirds cavity width inside the mouth) and bottom of a cavity; (3) between forward and aft cavities; and (4) at any location for varying throttle settings. Only minor differences are to be seen in these comparisons, such as slightly smaller fluctuation amplitudes on the cavity bottom than near the mouth and somewhat more scatter on repetition of the traces near stall. A conspicuous signal at about five times blade passing frequency may be seen superposed on the fundamental passing frequency. This frequency is not believed to be significant to the influence of the cavity on compressor behavior. The pressure fluctuation amplitude at blade passing frequency in the forward axial-skewed slot cavity is about the same as that measured on the baseline casing at 21% chord. To the extent that "eyeball" filtering of the high frequency signal is valid, the basic wave pattern appears more nearly sinusoidal than the patterns from the baseline and circumferential groove configurations. The pressure fluctuation in the aft cavity is somewhat larger than anything observed in corresponding regions from either the baseline or the circumferential groove configuration.

The results of measuring the time varying pressures in the wide blade angle slots, and on the land surfaces between the slots, are presented on Figure 76. The land surface pressure wave pattern for the forward cavity conforms more closely to the rip-saw tooth shape of the advance prediction than any of the others experienced during the program. It is somewhat surprising to see that the amplitude of this land surface pressure fluctuation doubles in throttling from the standard operating line (throttle 422) to the near-stall-baseline (throttle 115) and then does not increase any more with additional throttling. Even the larger amplitude is only half the amplitude observed in baseline testing (Figure 71) at the same axial position. At the same time the fluctuation amplitude on the cavity bottom is as large as or larger than the amplitude on the land surface. It would be more logical to expect an amplitude on the land surface comparable to that measured during baseline testing and a substantial attenuation from there to the cavity bottom. As in the case of the axial-skewed slot treatment, a conspicuous frequency component at about five times blade passing frequency is not believed to be significant.

Fluctuation amplitudes in the aft cavity region are small and irregular, both on the land surface and on the cavity bottom. This conforms to observations on baseline and circumferential groove configurations and is different from the observations on the axial-skewed slot treatment.

Annulus Wall Boundary Layer Surveys

Boundary layer surveys have been made on the annulus wall at the measurement planes before and after the rotor to determine whether casing treatment influences the wall boundary layer profile. The results appear to show statistically different velocity profiles for different throttle settings on the various treatment configurations. All configurations show thicker boundary layers at the rotor inlet plane with increasing throttling. The slot configurations, which allow substantial reverse flow in the rotor tip region, tend to have thicker inlet wall boundary layers than the baseline and groove configurations. At the rotor discharge plane, the recirculation effect seems to give a real boundary layer bleed system, particularly at near-stall throttle settings.

The annulus wall boundary layer profiles are presented on Figure 77 for the baseline and three treatment configurations. Measurements were made with a "perpendicular X" two-element hot film anemometer, which has two mutually perpendicular elements, perpendicular to the stem axis. The most satisfactory operating procedure was to rotate the anemometer for null balance of the signals from the two elements, and then to record the flow angle and the resultant velocity. It was also possible to set the anemometer at a fixed angle, and to rely on calibration data for angular displacement from the setting angle.

The presentation of Figure 77 is based on relating the local velocity magnitude to the freestream magnitude. Overall performance data showed little difference among flow and energy levels at fixed throttle setting among the various configurations. Consequently, it was felt that differences in the freestream velocity measured for the configurations were probably not realistic and a representative average for all configurations could be used to advantage. These representative freestream velocities are higher than can be deduced from total and static pressure measurements at the same planes, 8-12% higher at the rotor inlet and 2-5% higher at the rotor exit. It is presently believed that HFA calibration procedures may require development for realistic application to this type of environment.

Reference one-seventh-power velocity profiles have been presented on Figure 77 for assistance in comparing the various data. The thickness of the reference profile has been chosen arbitrarily at 1/10 of the annulus height at the rotor inlet plane and 1/15 at the rotor exit plane. These reference profiles appear consistent with the character of the data.

A series of specific observations may be made on the data presented on Figure 77:

1. For the rotor inlet station on the baseline case, boundary layer momentum defect increases with increasing throttling.

2. For the rotor inlet station with the circumferential groove treatment, momentum defect increases with increasing throttling. The momentum defect level with the circumferential groove treatment is slightly lower than with the baseline casing.

3. For the rotor inlet station with the axial-skewed slot treatment, the momentum defect level is substantially greater than with the baseline or circumferential groove treatment casing. The momentum defect level rises slightly from standard operating line to baseline near-stall, and does not increase any more through the extended operating range permitted by the treatment.

4. For the rotor inlet station with the wide blade angle slot treatment, the momentum defect level on the standard operating line is approximately the same as with the baseline casing. This momentum defect level rises rapidly with throttling to the baseline-near-stall setting, where it is slightly greater than with the baseline casing, and then does not rise further through the extended operating region.

5. For the rotor exit station with the baseline casing, the momentum defect level is nearly independent of throttling (but this result is confused by the measurement of freestream velocity near stall).

6. For the rotor exit station with the circumferential groove casing, the momentum defect level and profile shape are independent of throttling. Differences from the baseline case are insignificant.

7. For the rotor exit station with the axial-skewed treatment, there is an appreciable momentum deficit quite far into the stream. Throughout the normal operating range this momentum deficit is greater than with baseline or circumferential groove configurations. Close to the configuration stall limit there is a dramatic reduction in the momentum deficit, as if recirculation in the treatment cavity is quite effective as a boundary layer bleed device.

8. For the rotor exit station with the wide blade angle slot treatment, in the normal operating range, the momentum deficit at a moderate distance from the wall is increased relative to the baseline and circumferential groove configurations; the penetration of this deficit into the stream is less than with the axial-skewed slot configuration. This configuration also shows a dramatic decrease in momentum deficit close to its stall.

Even though the differences among the velocities are apparent on Figure 77, there is no pattern to identify these differences with the influence of treatment on the compressor performance, and especially on stall margin improvements. The advance planning had anticipated that the baseline configuration might show an increasing momentum defect in the profile at the rotor exit with throttling toward stall. If this had happened, and if the treatment results had shown substantially less defect at the near-stall flow for the baseline, this type of annulus boundary layer modification would have been a strong candidate as one of the important mechanisms for the casing treatment influence. The near-stall condition of the axial-skewed slot and blade angle slot configurations does show substantial reduction in the momentum defect of the profile. In the neighborhood of the baseline stall flow there is little difference among the profiles.

The annulus wall boundary layer survey also provided opportunity for examining the influence of the casing treatment on rotor blade wake profiles, including the uniformity from one blade to the next. Figures 78 - 80 show comparisons among these profiles for the baseline and open circumferential groove configurations.

For these photographs the "perpendicular X array" hot film anemometer was oriented in the approximate absolute flow direction. The zero output baseline for the "A + B", resultant velocity signal appears at the bottom of each photograph, and signal outputs for five (or ten) randomly timed sweeps appear at the top. Characteristically the absolute resultant velocity did not change significantly with passage of a wake. Since the HFA orientation was close to the flow direction, all signals for the "A-B", transverse component trace are close to the zero output baseline for that channel. The passage of a wake is identified by a substantial component perpendicular to the average direction, where the slow moving wake flow appears nearly tangential in the absolute frame.

Figure 78 shows traces taken at 17% span from the tip, presumably far enough away from the annulus wall so that local flows in the treatment cavities should not disturb the free stream flow. At the standard operating line (throttle 422) flow setting, there is little difference between the traces for the baseline and treated configurations. As the flow is reduced with increasing throttle restriction, the blade wakes for the baseline case become more prominent, and the disparity between the wakes of adjacent blades becomes larger. The wakes for the treated configuration also grow, but less rapidly. At the flow setting corresponding to baseline near stall the rotor blade wakes for the treated configuration are conspicuously less prominent than those for the baseline situation. The wake profiles for these two configurations show similar enlargements for the flow settings close to the respective stalls.

At radial positions closer to the annulus wall, Figures 79 and 80, the blade wake situations become considerably more complex. Wake disturbances appear to be as large as, or larger, with the treated casing as with the baseline. The treatment may, however, have enforced some periodic regularity where the baseline showed strictly random time variations. It is particularly interesting to observe that the wake effect appears earlier with respect to the timing trace near the tip than farther into the stream, that the wake flow has a high absolute velocity level and therefore a low relative flow velocity, and that two separate regions of high absolute flow angle are frequently present for each passing blade.

In the test planning for the program it was hoped that these wake profiles would be well enough defined so that they could be interpreted as velocity profiles in the relative flow, with definite displacement and momentum thicknesses. It has not proved feasible to analyze the complex traces in this manner within the scope of the program.

Vector Diagram Analysis

Blade element characteristics have been suggested as indications of the ways in which casing treatments influence the stage performance. It was thought, for example, that critical limitations on loading parameters, such as static pressure rise coefficient and diffusion factor, might be raised by effective treatments. Vector diagram analyses were carried out for the experimental data from the open circumferential groove treatment and the axial-skewed slot treatment, looking for a pattern to the change in blade element characteristics. No attempt was made to include the baseline configuration in the vector diagram analysis and comparisons. Since the work input and pressure rises for the baseline are very nearly the same as for the open circumferential groove it was expected that the results for the treated configuration would also apply to the baseline.

Primary input to the vector diagram analysis, in addition to the stage geometry, consists of static pressures measured on the casings before and after blade rows, and the stagnation pressure profiles before and after the rotor and after the stator. The absolute air angle profiles before and after the rotor are also used, as measures of the tangential momentum change and work input. These angle profiles are not sensitive enough, however, to reflect differences in work input between configurations.

A clear difference between the two treated configurations was observed in the profiles of the axial velocity component between the rotor and the stator. Figure 81 presents these profiles, with a tabulation of the effective area coefficients resulting from integrating the profiles. At the open throttle condition, the axial velocity profiles are similar. The casing static pressure is higher for the axial-skewed slot treatment, which implies a lower velocity level and leads to the 2% higher area coefficient. As the stages are throttled, the axial-skewed slot treatment picks up total pressure in the tip region, signaling a small outward flow shift and a tilting of the profiles. The indicated effective area coefficient remains about 2% higher with the axial-skewed slot treatment, a continued consequence of high casing static pressures. It should be observed that the high casing static pressure level is not preserved through the stator. Instead the high casing static pressure between rotor and stator with the axial-skewed treatment may be local consequences of radial flow components.

Loading parameters for the two configurations are compared in Figure 82 for the rotor, and on Figure 83 for the stator. The calculation of the rotor diffusion factors reflects inability to detect a systematic shift in angle profiles consistent with the overall work inputs. The same angle profiles were used for both configurations. The diffusion factor calculation has little dependence on the measured pressures, which are conspicuously different. These pressures are reflected directly in the static pressure rise coefficients, where the contrast is even more conspicuous than in the axial velocity profiles. As has been observed previously, the axial-skewed slot configuration shows much more difference from the circumferential groove configuration in casing static pressure between rotor and stator than in overall static pressure rise. The relative positions of the static pressure rise data on Figure 83 for the stator as compared with Figure 82 for the rotor confirm this. If Figure 82 is examined for trends in loading parameters with increasing incidence, the impression appears that high incidence always results in a deterioration of pressure rise effectiveness. In the open throttle region pressure rise is nearly linear with incidence. At high incidence angles the pressure rise drops below a linear extrapolation, reaches a maximum, and starts to drop absolutely before breaking down. The more effective treatment maintains linearity of the pressure rise characteristic to higher incidences, and apparently also slows the rate of deterioration.

The vector diagram analysis also yields data on blade element stream deflections and loss coefficients. These are presented on Figure 82 for the rotor. The stream deflection data suggest that the flow angle measurements at near-stall throttle settings may have been too large near the hub and too small near the casing. Over the entire span the rotor loss coefficients rise sharply near stall, because the rotor exit total pressure profiles near stall showed pressure rises that failed to increase in proportion to the tangential momentum.

DISCUSSION

A series of questions was established at the beginning of the experimental program to serve as a guideline for the investigation. Experimental data were obtained which were suitable for discussing, if not answering, these questions.

1. Does the influence of the casing treatment alter the blade loading, as measured by either a blade surface pressure distribution or a momentum balance measurement across the blade row?

The blade surface pressure distributions were changed in the presence of casing treatment at those flow-levels/throttle-settings where comparative data were obtained. In contrast the overall pressure rises and discharge total pressure profiles on the "standard operating line" did not change in the presence of the treatment. The responses of the circumferential groove treatments differed from those of the slot treatments. The circumferential groove treatment did not change the span-wise distribution of blade loadings. The circumferential groove treatment did seem to shift the blade loading from the leading edge toward the trailing edge at all throttle settings. All of the slot treatments, axial-skewed, wide blade angle and narrow blade angle, produced startlingly high blade surface pressures on the pressure surface close to the blade tip. For the design with preswirl induced by inlet guide vanes, the tangential velocity of the freestream air relative to the moving blades is substantially less than blade speed. Any flow coming out of the blade angle slots does so with no swirl, so that the relative tangential velocity is equal to the blade speed. The high surface static pressures may, therefore, be the consequence of accelerating cavity exit flow to the freestream tangential velocity. Flow out of the axial-skewed slot cavities has swirl velocity opposite to the blade speed, so that even higher acceleration in bringing the flow into the freestream might be expected. The increase in blade pressure loading at 17% span from the blade tip with the slot-type treatment was much smaller than that at the blade tip, but did appear to be significant.

The resolution among measured flow angles was not fine enough to detect differences between treatments. It is clear, however, that work input at a given throttle setting was increased in the presence of slot-type treatments and was not increased by groove treatments.

2. Can incipient separation be identified in the blade tip region which is suppressed or delayed in the presence of one or more of the casing treatments?

Hot film anemometer traces of the rotor blade wakes were taken at the standard throttle settings during the testing of the baseline and open circumferential groove configurations. Interpretation of the results was difficult. The results at 17% span from the tip obtained from the circumferential groove test at the baseline-near-stall throttle setting show a distinctly thinner blade wake than the baseline results. Closer to the blade tip both configurations show thick wakes. No convincing difference favoring the treated configuration has been found. Since these measurements were unrewarding, they were not repeated for the axial-skewed slot configuration. In view of the difference in the character of the blade surface pressures, rotor blade wake comparisons from the axial-skewed slot configuration would probably have been valuable.

3. Can radial velocity components (velocity components into and out of the treatment cavity) be identified which are large enough to account for qualitative differences in the blade tip flow patterns?

Some conspicuous velocity components into and out of the cavities were identified for each of the cavity configurations. It is, however, difficult to connect these velocities with the blade tip flow patterns.

In the experiments with the circumferential groove treatment, evidence on radial velocity comes from tuft observations and from HFA measurements. Since the HFA measurements in grooves 1 and 3 show a periodic pattern at blade passing frequency, and the tuft observations do not correlate with blade passage, it is probable that the tufts have too much inertia to respond to passing frequency. The HFA data for groove 3 show flow into the cavity along the aft wall as the blade tip approaches the sensor. The magnitude of the inflow is highly variable, with peaks sometimes as high as 15% of blade speed and sometimes no more than 5% of blade speed. The HFA data for groove 1 show large percentage variations in the longitudinal velocity. Some substantial radial velocities must therefore be required to satisfy continuity. Evidence of radial flow from tuft observations comes from occasional "tugs" felt through the tuft support stem as the tuft is moved close to the cavity face. Since a substantial portion of the improvement in stable flow range before stall with circumferential grooves is lost when grooves 4 and 5 are filled, and since the HFA velocity measurements in groove 5 show longitudinal levels nearly independent of blade position, it seems unlikely that radial velocities could be very important to the stabilizing influence of the configuration.

Flow components into and out of the axial-skewed slot and blade angle slot cavities are apparently required to account for the free stream flow patterns over the rotor blading. At least the most obvious explanation for the high static pressures on the blade pressure surfaces near the tip depends on interaction with a cavity flow. Tuft and HFA observations of the flow in the axial-skewed slot cavities suggest a predominant, but by no means uniform or continuous, circulating flow into the cavity at its aft end and out at the forward end. This flow is presumably driven by the meridional pressure field: its velocity components show no evidence of correlation with blade passage. Tuft observations of the flow in blade angle slot cavities show predominant flow out of all these cavities at the forward ends. Elsewhere in the cavities the flow patterns are erratic. A significant follow-on experiment would involve both types of slot cavities with additional baffles, to determine whether the stalling flow coefficient and the blade surface pressures respond in the same way to the cavity extent. It is, of course, expected that additional baffles would reduce the excess power input.

4. Can velocity components exist along a cavity with magnitudes comparable to velocity components in the freestream? If so, are they beneficial, or would it be desirable to suppress them through the use of suitable baffling?

The velocity component along the circumferential groove cavity is comparable to the freestream velocity. In fact, the measured velocity near the cavity face is consistent with a prediction that the mean absolute tangential velocity of the freestream should also be found in the cavity. Apparently this cavity velocity is beneficial, at least in part, since introduction of baffling resulted in efficiency loss. On the other hand, the baffled grooves were more effective than the open grooves at improving stall margin.

Results on velocity components along slot-type cavities are inconclusive. Removing the baffles from the axial-skewed slots certainly increased the work input. There must, therefore, have been a significant increase in the longitudinal flow, which hurt efficiency without helping stall margin very much. Some longitudinal velocity is required to satisfy continuity in respect to the flow out of these cavities at their forward ends. The measurement of dynamic pressure in the narrow blade angle slot cavities did not show significant velocity levels. Tuft observations suggest that the single baffles in the cavities are enough to suppress harmful recirculation without destroying the beneficial influence. The compliant wall hypothesis seems to have gained credibility as a result of failure to measure systematic flow patterns. A supplementary investigation, in which the blade wakes of the existing axial-skewed slot configuration are measured and followed by a test with additional baffling to measure blade surface pressures, blade wakes, and stalling behavior, seems indicated as a way to separate compliant wall effects from cavity-blowing-on blade effects.

5. Can significant pressure gradients transverse to a cavity be identified?

Most of the data from circumferential groove, axial-skewed slot, and wide blade angle slot cavities indicate no transverse pressure gradients. Where transverse pressure gradients were observed, the effect seems to be data resolution.

6. Can any significant departure of individual passage work inputs, and resulting pressure rises from the average, be identified? If so, do they change in the presence of casing treatment?

The test procedure does not seem to have been suited to answering this question. During the test program variations in time-varying wave form from repetition to repetition, and variations with relative inlet guide vane position, masked the variations from blade-to-blade. It does not appear that significant variations attributable to treatment can be identified.

A series of observations was reported earlier in this report under the heading "empirical background", to represent the state of knowledge on casing treatment effects. It is appropriate at this time to reconsider these in the light of NAS3-15707 program results:

1. Rotating stall at rotor tip does seem to be the stall inception symptom. Inception was postponed with most treatment configurations.

2. The program showed conclusively that stall margin improvements are not confined to transonic rotors. Low Mach number pressure distributions do seem to be changed by treatment. A separate investigation would be required to consider whether there is relatively more change at transonic Mach numbers.

3. Extra recirculation by removing baffles from axial-skewed slots did lower stalling flow coefficient, or at least reduce sensitivity to stalling induced by rotor blade instrumentation. Testing of either axial-skewed or blade angle slots with additional compartmentation would be significant. Some recirculating flow is apparently required to account for high blade pressure surface pressures. The influence of the cavity on pressure surface pressure might have been less for a design without preswirl, in which case the treatment might have been less effective.

4. Investigation confirms effectiveness of treatments with more than 60% open area. There was no effort to determine whether the open area could be reduced somewhat without destroying effectiveness. Neither was there any effort to determine whether tapered lands (e.g., between circumferential grooves) would preserve the beneficial effect of large open area and enhance mechanical integrity.

5. The investigation confirms the effectiveness of configurations that are untreated in leading edge and trailing edge regions. The investigation also showed substantial loss in effectiveness of circumferential grooves if either the 20-45% chord region or the 55-80% chord region, from the leading edge, was left untreated.

6. The diffusion process is apparently improved. All treatment configurations show greater static pressure rise than the baseline at the baseline-near-stall throttle setting.

7. Blade passing frequency effects of any kind were hard to find. Frequencies substantially higher than blade passing frequency were sometimes observed on transient pressure traces (Figures 75 and 76). Efforts at establishing a pattern to these frequencies with change of rotor speed were unrewarding. There is, therefore, still no evidence of a significant selective effect which can be attributed to resonance.

8. Some radial shifts in flow distribution were observed, particularly in the experiments with the axial-skewed slot treatment. The nature of the shift should have lowered the pressure rise demanded of the tip section at a given flow level somewhat. This effect was masked by the change in the split between rotor and stator pressure rise (an apparent increase in reaction). Limiting blade element loadings appear to increase with the treatment.

9. This test program did not identify any disparities among flows in successive blade passages.

10. Although rotating stall cells may have been identified close to stall by tuft observations, they were not conspicuous enough for recording with the transient pressure or velocity instrumentation. There was, therefore, no way to measure a change in stall cell frequency. Overall pressure rises at given flow levels near the stall condition for the circumferential groove configuration were higher with slot treatments than with groove treatments. If a depressed pressure rise for the groove treatment is actually a time average of a rotating stall situation, the increased pressure rise would be equivalent to suppression of the stall cells.

Since a significant proportion of the program effort was put into flow modelling to predict the flow patterns in and around the treatment cavities, it is appropriate to review the extent to which the predicted flow patterns were actually observed. Predictions were made for the ideal pressure distributions around the rotor tip airfoils, for the primarily circumferential inviscid flow in circumferential grooves, for the viscous flow in circumferential grooves, for longitudinal flow in blade angle slots, and for transverse flow in blade angle and axial-skewed slots.

The cascade analysis of the rotor tip section was undertaken to obtain boundary condition data for analysis of cavity flows. The results of the analysis, however, with their comparison to the experimental results, suggested opportunity for a special investigation, which could only receive a skeleton treatment within the scope of the NAS3-15707 program. Early vector diagram analysis predictions were made to match stage characteristics from a previous test on the stage which was to be used for the experimental program. These predictions showed that peak efficiency occurred at approximately 0° incidence on the rotor tip and that the stage stalled at approximately +8° incidence. The cascade predictions were, therefore run for these two incidence angles. These predictions gave a moderate leading edge pressure loading at 0° incidence which agreed with advance expectations. The leading edge loading increased rapidly with positive incidence, also in agreement with advance expectation. It was expected that real fluid flow would produce local boundary layer separations in the leading edge regions, which would alter the effective airfoil shape and alleviate the severe loading there. It was a surprise to find that the blade surface pressures showed the leading edge region to be almost unloaded at the "standard operating line" throttle setting, and that the vector diagram analysis of this data taken at this throttle setting showed substantially positive incidence. The scope of the investigation would apparently require substantial expansion to cover full reconciliation of the experimental freestream cascade behaviour with the predictions.

The flow modelling predictions for flow in circumferential grooves all supposed that this flow would somehow be driven by momentum interchange with the circumferential component of the absolute flow outside the cavity. Some response to the blade-to-blade static pressure field was also expected. The measurements, both by total and static pressure and by hot film anemometry, show mean levels comparable to the mean absolute flow outside the cavity (definition of the flow outside the cavity is subject to some uncertainty in interpretation of the vector diagram analysis). The differences between the measured cavity velocity level and the freestream level are presumably an effect of the cavity wall shear drag. The influence of the blade-to-blade pressure field is small on the flow in the farthest-aft groove, which makes its substantial contribution to the beneficial effect of the treated casing on stall margin. In the center groove (Figure 69) the velocity increases slowly and decreases rapidly in the period of passage of a rotor blade. This is consistent with acceleration under the force of the static pressure field between blades and acceleration over the blade tip (a feature of constant relative frame total pressure) and inconsistent with constant total pressure in a stationary frame. The fluctuation amplitude, however, is not great enough to satisfy the reference frame moving with the full rotor speed.

The flow modelling effort for the blade angle slots led to an expectation of a rather large longitudinal flow when the slot is near a blade suction surface, little flow when near a pressure surface. Tuft observations failed to identify any velocity response to the passage of a blade. Measurements of total and static pressure failed to detect a significant velocity level in the narrow slots. On the other hand, the longitudinal flow model predicts rather low radial velocities into the cavity at the downstream end and need higher radial velocities out of the cavity at the upstream end. Something like the outward velocity situation is required to explain the high pressure surface pressures measured in the presence of any of the slot-type cavities.

Although no evidence of the roller-bearing-type of flow pattern was detected in tuft observations, or hot film anemometer measurements, the static pressure distributions in the baffled axial-skewed slots do suggest this pattern. Recovery of the kinetic energy of a substantial velocity is required to explain the high static pressures on the bottoms of these cavities, as compared with the cavity mouths. Fore- and aft-symmetry could explain the near-constancy of pressure measurements made at the same depth, but is not very likely. Longitudinal uniformity of transverse flow seems a simple way to explain this result.

CONCLUDING REMARKS

1. Porous wall casing treatments do improve stall margins for operation at low (≈ 0.1) Mach number. Although compressibility may have some impact on the effectiveness of treatment (evaluation of this was not within the scope of this investigation), it clearly is not an essential input to understanding the phenomena.

2. Radial velocity components in circumferential groove configurations do not seen adequate to alter flow patterns. The velocity level of the longitudinal flow circulating in the grooves does seem to influence blade boundary layer stability.

3. Circumferential velocity components in circumferential groove configurations are comparable to freestream flow velocities. High absolute circumferential velocities (low relative to the moving blade) are helpful for efficiency. Low absolute circumferential velocities (as obtained with baffles in the grooves) are helpful for stability.

4. The use of at least one baffle to inhibit longitudinal flow in an axial-skewed slot cavity reduces efficiency loss due to recirculation significantly without harming the stall margin benefits. Although this feature was not tested in blade angle slots, similar results are expected.

5. The width of blade angle slots makes a small but significant difference to their influence. Slots somewhat wider than blade tips give more stall margin improvement than narrow slots, with about the same effect on efficiency. Since longitudinal velocities in blade angle slots are not large, and since no systematic response to blade passing frequency was identified, it seems likely that the orientation angle is not important to the influence of these cavities.

6. Blade loadings, as measured by blade surface pressures, are changed significantly in the presence of casing treatment. Circumferential groove treatments appear to improve pressure recoveries in the 50-75% chord region, which has the effect of shifting some pressure loading from the leading edge region toward the trailing edge. Pressure surface pressures, those close to the tip particularly, are raised in the presence of slot treatments. If the flow off the trailing edge from this region of high surface pressure has indeed been energized, it may have a stabilizing influence on the suction surface flow as well.

7. Radial velocity components out of slot configurations are apparently required to account for observed blade surface pressures. The test program did not investigate the correlation between influence on blade surface pressure and influence on stage stability.

8. Except possibly for radial velocity components out of the forward ends of cavities in the slot configurations, the flows in the cavities are highly erratic. Correlations of these flows with systematic influences on stage efficiency and stage stability seen unlikely.

9. Rotor blade wakes appear to undergo significant modification, as measured by momentum thickness and/or momentum defect, by regularity, and by concentration near the annulus wall, by the presence of treatment. Data taken were not detailed enough for generalized observations about the modifications.

10. The beneficial effects of casing treatments in this investigation were obtained without conspicuous suppression of variations in loadings from blade to blade or in flow patterns from blade passage to blade passage.

11. Additional tests which would contribute to understanding of casing treatment influences and to design standards include circumferential grooves with slanted lands and with tapered lands, axial-skewed slots and blade angle slots with more baffles, shallower axial-skewed slots, and axial-skewed and/or blade angle slots with vector diagrams adjusted for much lower mean circumferential velocities.

REFERENCES

1. Bailey, E.E., and Voit, C.H., "Some Observations of Effects of Porous Casing on Operating Range of a Single Axial Flow Compressor Rotor", NASA TM X-2120, October 1970.

2. Osborn, W.M., Lewis, G.E., Heidelberg, W., "Effect of Several Porous Casing Treatments on Stall Limit and on Overall Performance of an Axial Flow Compressor Rotor", NASA TN D-6537, November 1971.

3. Moore, R.D., Kovich, G., Blade, R.J., "Effect of Casing Treatment on Overall and Blade Element Performance of a Compressor Rotor", NASA TN D-6538, November 1971.

4. Tesch, W.A., "Evaluation of Range and Distortion Tolerance for High Mach Number Transonic Fan Stages: Task IV Stage Data and Performance Report for Casing Treatment Investigations", NASA CR 72862, May 1971.

5. Bailey, E.E., "Effects of Grooved Casing Treatment on the Flow Range Capability of a Single-Stage Axial-Flow Compressor", NASA TM X-2459, January 1972.

6. NASA-Lewis Research Center Technical Staff, Aircraft Propulsion, Proceedings of Conference, NASA SP259, November 18, 1970.

7. Brent, J.A., "Single Stage Experimental Evaluation of Compressor Blading with Slots and Vortex Generators", NASA CR-72793, March 1972.

8. Kriebel, A.R., Seidel, B.S., and Schwind, R.G., "Stall Propagation in a Cascade of Airfoils", NACA TN 4134, June 1958.

9. Rodert, L.A., and Garrett, F.B., "Ingestion of Foreign Objects into Turbine Engines by Vortices", NACA TN 3330, 1955.

10. Smith, L.H., Jr., "Casing Boundary Layers in Multistage Axial Flow Compressors, Contribution to Flow Research in Blading", L.S. Dzung, Editor, Elsevier Publishing, Amsterdam, Netherlands, 1970.

11. Prince, D.C., Jr., "Evaluation of Compressibility Effects by the Compressible Fluxplot Computer Program", GE R66FPD270, 1966.

12. Johnsen, I.A., and Bullock, R.O., Ed's., "Aerodynamic Design of Axial Flow Compressors (Revised)", NASA SP-36, 1965.

13. Shapiro, A.H., "The Dynamics and Thermodynamics of Compressible Fluid Flow", Ronald Press, New York, c. 1953.

TABLE I

CRITICAL PROPORTIONS OF CIRCUMFERENTIAL GROOVES

REFERENCE	CONFIGURATION NOTES	GROOVE DEPTH BLADE SPACING	STALL MARGIN IMPROVEMENT 100%N/90%N	REMARKS
TM X-2459*	Grooves 1 - 9	0.038	0.015/	Ineffective
		0.113	0.037/	Reduced effectiveness
		0.287	0.057/	Typical
	Grooves 2 - 6	0.038	0.040/	Reduced effectiveness
		0.113	0.058/	Typical
TN D-6537**		0.287	0.135/0.093	Unusually effective
CR 72862***	Grooves 3 - 9	0.144	0.051/0.025	Typical (?)
	3 - 7	0.288	0.065/0.030	Typical
	3 - 7	0.072	0.043/0	Ineffective

*Reference 5

**Reference 2

***Reference 4

TABLE II

BLADE GEOMETRY FOR LOW SPEED RESEARCH COMPRESSOR CASING TREATMENT PHENOMENA INVESTIGATION

	Inlet Guide Vanes			Rotor			Stator		
Number of Blades	40			54			53		
Radius Ratio	0.7	0.85	1.0	0.7	0.85	1.0	0.7	0.85	1.0
Chord - cm	12.60	15.30	18.00	--	11.63	--	--	11.72	--
- in.	4.95	6.01	7.07	--	4.583	--	--	4.609	--
Camber (deg.)	21.5	32.6	34.5	41.7	32.3	23.1	32.6	29.4	31.6
Stagger (deg.)	13.2	20.5	21.9	16.4	34.1	43.4	29.9	39.9	41.5
Max thickness/ chord	0.1	0.1	0.1	0.13	0.088	0.045	0.040	0.080	0.120
Solidity	1.5	1.5	1.5	1.88	1.55	1.31	1.85	1.53	1.30
Aspect Ratio $\left(\frac{\text{Span}}{\text{Chord}}\right)$	--	1.5	--	--	1.96	--	--	1.94	--
Mean Line	A4K6*			Circular Arc			Circular Arc		
Profile	63 Series			65 Series			65 Series		

*Dunavant, J.C., Cascade Investigation of a related Series of 6-Percent-Thick-Guide-Vane Profiles and Design Charts, NACA TN3959 May 1957

TABLE III

STANDARD THROTTLE SETTINGS FOR PERFORMANCE TESTING

Description	Throttle Setting	Nominal Flow Coefficient	Remarks
Standard Operating Line	422	0.493	80% of peak static pressure coefficient
Peak Efficiency	170	0.46	Some variation in location of peak between configurations
High Operation Limit	145	0.438	95% of peak static pressure coefficient edge of region of cascade flow breakdown
Baseline Near-Stall	115	0.406	Near-peak static pressure coefficient
Circumferential Groove Near-Stall	105	0.388	Near peak static pressure coefficient
Slot Treatment Near-Stall	92	0.362	Stability beyond this flow affected by instrumentation and Reynolds number

TABLE IV

OVERALL STALL CHARACTERISTIC COMPARISON AMONG EIGHT CASING TREATMENT CONFIGURATIONS

		Circumferential Grooves				Axial-Skewed Slots		Wide Blade Angle Slots	Narrow Blade Angle Slots
	Baseline	1-5 Open	1-5 Baffled	1-3 Open	3-5 Open	Baffled	Unbaffled	Baffled	Baffled
Stalling Throttle	112.2	100.5	88.2	106.8	105.5	83.5 (88.8)	82.5 (89.0)	84.5 (90.8)	90.2 (92.7)
Flow Coefficient at Stall	0.404	0.380	0.353	0.387	0.386	0.342	0.336	0.343	0.362
Pressure Coefficient at Stall	0.619	0.638	0.653	0.622	0.634	0.624	0.610	0.640	0.650
At Throttle 115 (Near Baseline Stall)									
Flow Coefficient	0.406	0.406	0.406	0.406	0.405	0.404	0.409	0.406	0.405
Pressure Coefficient	0.617	0.627	0.633	0.616	0.622	0.646	0.640	0.635	0.630
At Peak Efficiency									
Peak Efficiency	0.941	0.941	0.928	0.932	0.942	0.923	0.855	0.927	0.928
Flow Coefficient	0.475	0.460	0.480	0.475	0.475	0.445	0.475	0.494	0.494
Pressure Coefficient	0.537	0.548	0.555	0.532	0.530	0.602	0.538	0.505	0.501
At Peak Pressure Coefficient (if different from stall)									
Flow Coefficient	---	---	---	---	---	0.385	0.385	0.370	---
Pressure Coefficient	---	---	---	---	---	0.664	0.652	0.651	---
% Change in Stalling Flow From Baseline	---	-5.8	-12.5	-4.1	-4.3	-15.3	-16.7	-15.0	-10.3
% Change in Pressure Rise At Baseline Stall Throttle from Baseline	---	+1.8	+2.8	-0.1	+1.0	+4.9	+3.9	+3.1	+2.2
% Change in Peak Pressure Rise from Baseline	---	+3.7	+6.0	+1.0	+2.9	+7.8	+5.8	+5.7	+5.2
Change in Peak Efficiency from Baseline	---	0	-0.013	-0.009	+0.001	-0.018	-0.086	-0.014	-0.013

Note: Stalling throttle indications in parentheses show stability limits with inter-blade row total pressure rakes in place. Stalling characteristic limits are quoted with rakes removed.

TABLE V

LSRC CASING TREATMENT PROGRAM - WORK INPUT COMPARISON

Configuration	$\left(\psi_{C_F} - \psi_{Mod}\right)_{\phi = 0.46}$	Throttle 422		Throttle 145		Throttle 115	
		ϕ	$\psi - \psi_{Mod}$	ϕ	$\psi - \psi_{Mod}$	ϕ	$\psi - \psi_{Mod}$
Baseline							
● Quick-Look	0	0.4951	0.0013	0.4388	-0.0002	0.4041	-0.0001
● Repeat in performance test	0.0034	0.4923	-0.0013	0.4385	0.0030	0.4042	0.0004
Circumferential Groove							
● Grooves 1-5 open	0.0015	0.4933	0.0047	0.4370	0.0008	0.4062	0.0070
● Grooves 1-5 baffled	0.0064	0.4924	0.0028	0.4377	0.0087	0.4056	0.0052
● Grooves 1-3 open	0.0022	0.4907	-0.0015	0.4365	-0.0023	0.4022	0.0002
● Grooves 3-5 open	0.0012	0.4925	0.0002	0.4364	-0.0021	0.4041	0.0011
Axial-skewed Slots							
● Slots baffled - Quick Look Performance	0.0227	0.4967	0.0182	0.4410	0.0257	0.4092	0.0346
● Slots baffled perf.	0.0258	0.4941	0.0197	0.4393	0.0328	0.4061	0.0389
● Slots open perf.	0.0566	0.4922	0.0362	0.4402	0.0651	0.4091	0.0791
Blade Angle Slots							
● Wide	0.0194	0.4956	0.0150	0.4404	0.0262	0.4079	0.0302
● Narrow	0.0141	0.4947	0.0107	0.4384	0.0196	0.4065	0.0273

Note: Comparison based on Curve Fit Model for Baseline Configuration (Quick-Look)

$$\psi_{Mod} = 0.59955 - 1.64558\ (\phi - 0.46) - 1.85901\ (\phi - 0.46)^2$$

Data from Performance Test Series unless otherwise specified

TABLE VI

LSRC CASING TREATMENT PROGRAM - CASING STATIC PRESSURE RISE COMPARISON

Configuration	Throttle 422				Throttle 145				Throttle 115			
	ϕ	$p_{1.0}$	$p_{2.0}$	ψ_s'	ϕ	$p_{1.0}$	$p_{2.0}$	ψ_s'	ϕ	$p_{1.0}$	$p_{2.0}$	ψ_s'
Baseline	0.4923	-0.362	0.144	0.506	0.4385	-0.282	0.313	0.595	0.4042	-0.236	0.383	0.619
Circumferential Grooves												
Grooves 1-5 open	0.4933	-0.361	0.144	0.505	0.4370	-0.281	0.313	0.594	0.4062	-0.241	0.391	0.632
Grooves 1-5 baffled	0.4924	-0.362	0.140	0.502	0.4377	-0.283	0.312	0.595	0.4056	-0.241	0.387	0.628
Grooves 1-3 open	0.4907	-0.359	0.143	0.502	0.4365	-0.280	0.312	0.592	0.4022	-0.233	0.384	0.617
Grooves 3-5 open	0.4925	-0.366	0.142	0.508	0.4364	-0.285	0.311	0.596	0.4041	-0.239	0.386	0.625
Axial-skewed Slots												
Slots baffled	0.4918	-0.360	0.141	0.501	0.4372	-0.283	0.309	0.592	0.4041	-0.241	0.383	0.624
Slots open	0.4922	-0.358	0.140	0.498	0.4402	-0.285	0.308	0.593	0.4091	-0.244	0.384	0.628
Blade Angle Slots												
Wide	0.4937	-0.362	0.142	0.504	0.4387	-0.283	0.314	0.597	0.4064	-0.241	0.390	0.631
Narrow	0.4924	-0.361	0.142	0.503	0.4368	-0.281	0.313	0.594	0.4050	-0.238	0.388	0.626

Note: Data from Performance Test Series

TABLE VII

ANNULUS WALL PRESSURE GRADIENT

Configuration	Throttle 422 Standard Operating Line		Throttle 145 High Operating Limit		Throttle 115 Near-Stall Baseline		Throttle 105 Near-Stall Open Circumferential Groove		Throttle 92 Near-Stall Slot Configurations	
	Initial Gradient	Final Gradient	Initial Gradient	Final Gradient	Initial Gradient	Final Gradient	Initial Gradient	Final Gradient	Initial Gradient	Final Gradient
Baseline	0.39	0.39	0.50	0.24	0.58	0.24	---	---	---	---
Circumferential Grooves										
1-5 Open	0.42	0.42	0.45	0.31	0.52	0.27	0.72	0.28	---	---
1-5 Baffled	0.60	0.60	NA	NA	0.60	0.60	NA	NA	0.75	0.46
1-3 Open	0.42	0.42	0.45	0.31	0.63	0.28	0.69*	0.23*	---	---
3-5 Open	0.39	0.39	0.47	0.27	0.60	0.21	0.65*	0.19*	---	---
Axial-Skewed Slots										
Baffled	0.35	0.92	0.52	0.74	0.52	0.52	0.60	0.47	0.86	0.31
Unbaffled	---**	---	---	---	---	---	---	---	---	---
Blade Angle Slot										
Wide	0.62	0.62	0.56	0.56	0.63	0.47	0.67	0.37	0.56	0.17
Narrow	0.67	0.67	0.57	0.57	0.63	0.63	0.92	0.44	0.74	0.31

NB Wall pressure gradient definition: $\dfrac{d\left(\frac{p}{1/2\ \rho U_t^2}\right)}{d\left(\frac{X}{L}\right)}$, where L is axial projection of blade tip.

* Near-stall results for groove configurations with only three open grooves are given at throttle 108.

** Annulus wall gradients for the unbaffled axial-skewed slot configuration do not appear relevant.

TABLE VIII

INFLUENCE OF CASING TREATMENT ON BLADE SURFACE DIFFUSION

	Standard Operating Line			High Operating Limit			Baseline - Near Stall			Circumferential Groove Near Stall			Slot Treatment Near Stall		
	Cascade Overall	Pressure Surface	Suction Surface	Cascade Overall	Pressure Surface	Suction Surface	Cascade Overall	Pressure Surface	Suction Surface	Cascade Overall	Pressure Surface	Suction Surface	Cadcade Overall	Pressure Surface	Suction Surface
Baseline															
2.8% Span	0.485	0.283	0.655	0.553	0.049	0.906	0.560	0.066	1.259						
16.7% Span	0.465	0.400	0.572	0.542	0.182	0.798	0.563	0.124	0.843						
Circumferential Groove															
2.8% Span	0.507	0.409	0.643	0.562	0.275	0.909	0.568	0.155	1.232	0.551	0.124	1.544			
16.7% Span	0.479	0.427	0.572	0.552	0.191	0.794	0.567	0.130	0.883	0.555	0.106	0.995			
Axial Skewed Slots															
2.8% Span	0.498	0.547	0.691	0.589	0.441	0.841	0.704	0.353	1.254	0.627	0.230	1.402	0.623	0.278	1.874
16.7% Span	0.500	0.413	0.571	0.580	0.217	0.745	0.620	0.162	0.848	0.627	0.140	0.902	0.607	0.077	1.382
Wide Blade Angle Slots															
2.8% Span	0.488	0.362	0.654	0.581	0.272	0.866	0.688	0.301	1.261	0.601	0.188	1.420	0.598	0.157	1.858
16.7% Span	0.488	0.404	0.566	0.572	0.208	0.761	0.606	0.162	0.854	0.604	0.139	0.911	0.584	0.095	1.443
Narrow Blade Angle Slots															
2.8% Span	0.545	0.375	0.770	0.625	0.286	0.953	0.656	0.302	1.305	0.590	0.345	1.499	0.596	0.426	1.781
16.7% Span	0.511	0.429	0.581	0.604	0.228	0.804	0.636	0.183	0.898	0.594	0.144	0.873	0.582	0.113	1.223

Note: Diffusion rates are measured from minimum to maximum pressure on the surface (from rotor inlet plane to rotor exit plane on casing for cascade overall) and referred to $1.2\,\rho W_1^2$.

TABLE IX

COMPARISON BETWEEN BLADE LOADINGS MEASURED BY SURFACE PRESSURES AND BLADE LOADINGS MEASURED BY TIME-VARYING CASING PRESSURES BASELINE CONFIGURATION

Throttle Setting	Position (% Chord)	Blade Surface Pressure Amplitude	Casing (B & K) Pressure Amplitude	Analytical Prediction
Std Operating Line (422) $\phi = 0.493$	21	0.38	0.44	0.41*
	51	0.40	0.35	0.29*
	81	0.27	0.18	0.12*
High Operation Limit (145) $\phi = 0.438$	21	0.50	0.50	0.54
	51	0.37	0.29	0.26
	81	0.20	0.13	0.08
Near Stall (115) $\phi = 0.404$	21	0.50	0.44	
	51	0.30	0.24	
	81	0.16	0.11	

Note = Pressure amplitudes are normalized by $1/2\ \rho U_t^2$.

*Analytical prediction is for $\varphi \approx 0.47$ locally at the rotor tip, equivalent to 0.55 for the stage average.

TABLE X

SUMMARY OF FLUCTUATING PRESSURE AMPLITUDES FROM CIRCUMFERENTIAL GROOVE TESTING

Throttle Setting	Position	Projected % Chord	Groove Pressure Amplitude (B&K)	Blade Surface Pressure Amplitude
Std Operating Line (422) $\phi = 0.493$	#2 groove aft	42	0.34	0.41
	#2 groove fwd	31	0.20	0.41
	#2 groove bot	36	0.13	
	#4 groove aft	73	0.18	0.35
	#4 groove fwd	62	0.15	0.40
	#4 groove bot	67	0.10	
High Operation Limit (145) $\phi = 0.437$	#2 groove aft	42	0.34	0.41
	#2 groove fwd	31	0.18	0.44
	#2 groove bot	36	0.10	
	#4 groove aft	73	0.17	0.27
	#4 groove fwd	62	0.14	0.32
	#4 groove bot	67	0.06	
Near Stall Baseline (115) $\phi = 0.406$	#2 groove aft	42	0.31	0.39
	#2 groove fwd	31	0.17	0.43
	#2 groove bot	36	0.10	
	#4 groove aft	73	0.12	0.20
	#4 groove fwd	62	0.09	0.25
	#4 groove bot	67	0.05	
Near Stall Circumferential Groove (105) $\phi = 0.387$	#2 groove aft	42	0.26	0.34
	#2 groove fwd	31	0.13	0.40
	#2 groove bot	36	0.08	
	#4 groove aft	73	0.09	0.18
	#4 groove fwd	62	0.08	0.22
	#4 groove bot	67	0.03	

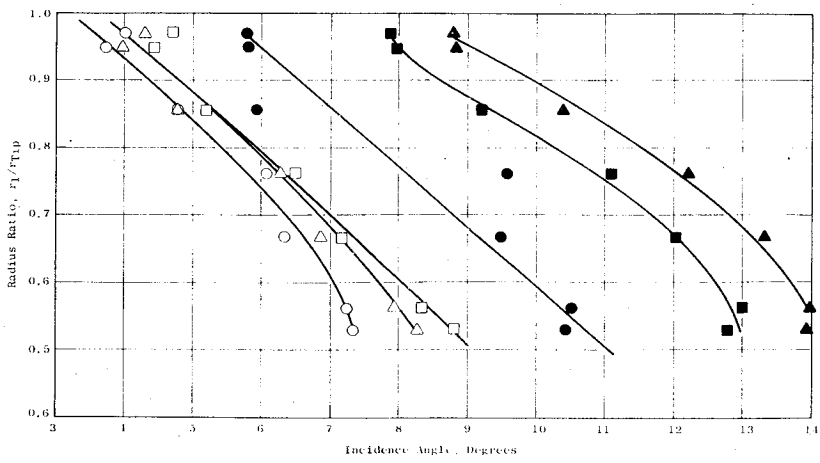

a. Increase in Incidence Angle Range from Design to Stall

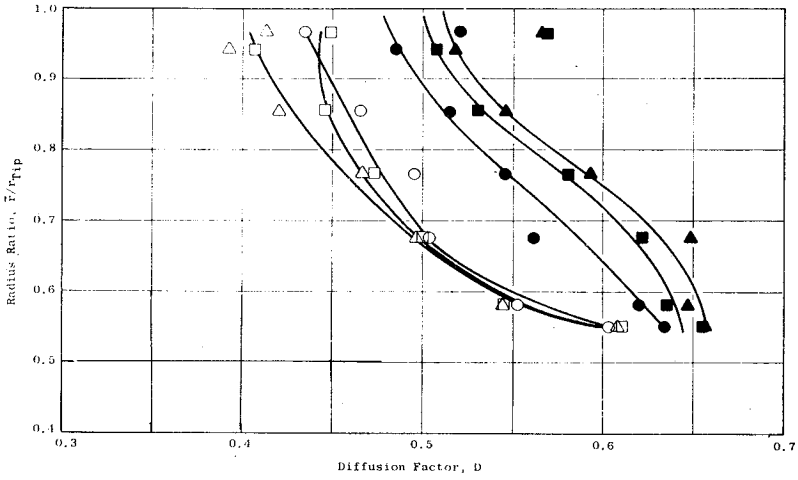

b. Increase in Stalling Diffusion Factor

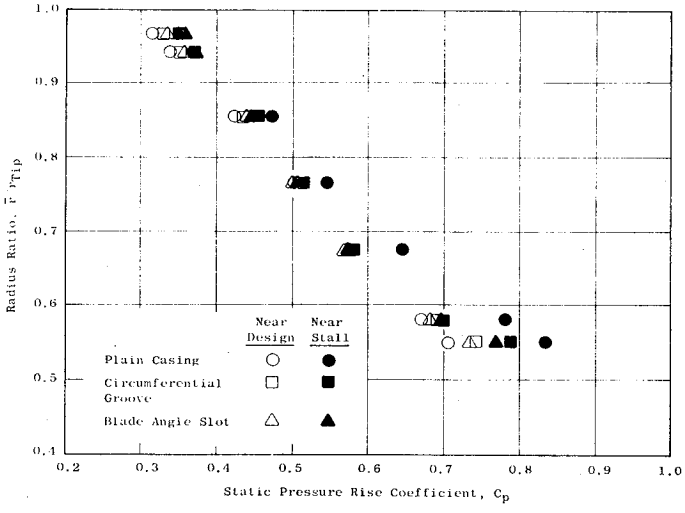

c. Increase in Maximum Static Pressure

Figure 1 Influence of Casing Treatment on Blade Element Performance

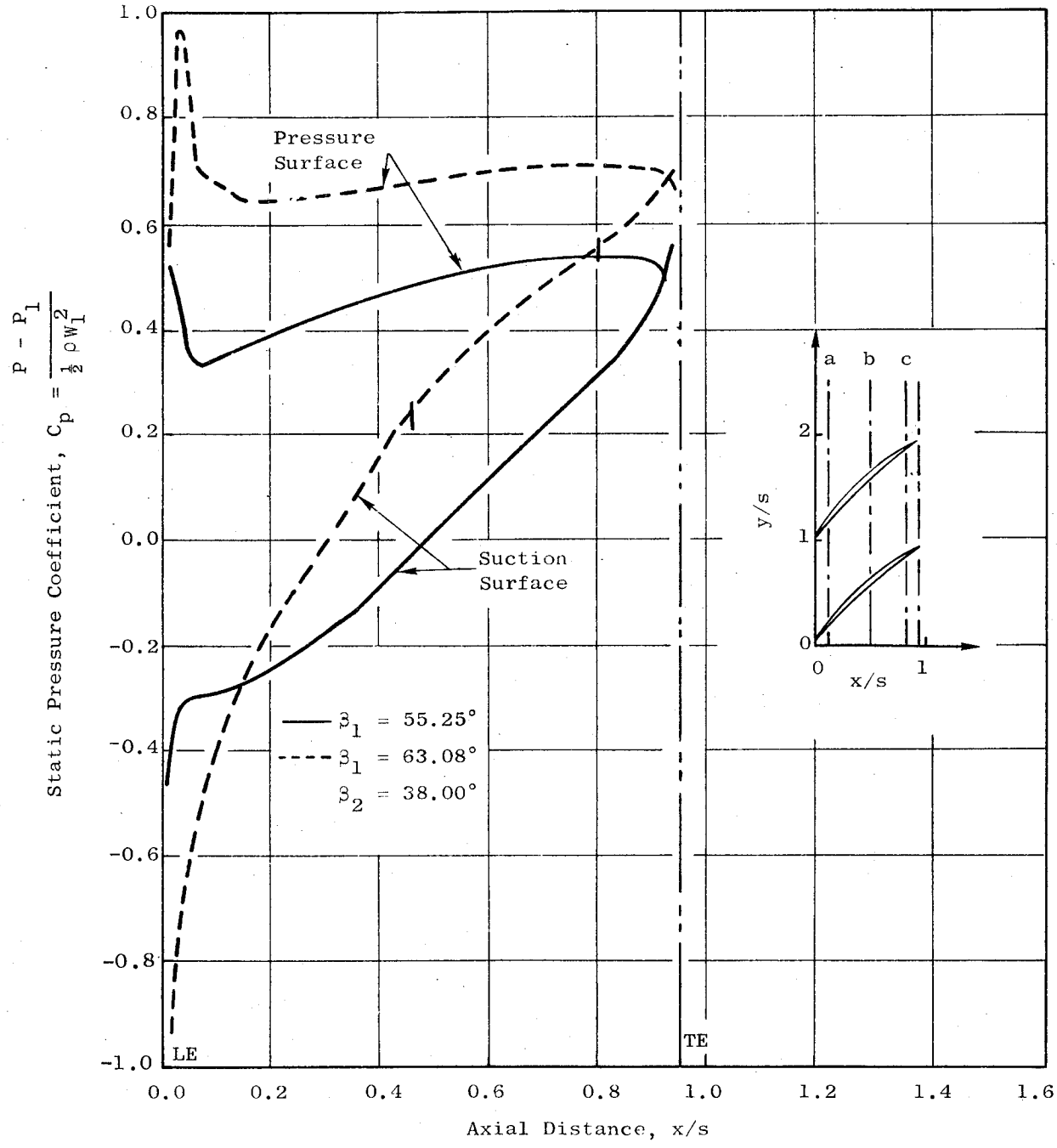

Figure 2 Blade Surface Static Pressure Distribution as Predicted by Fluxplot Analysis

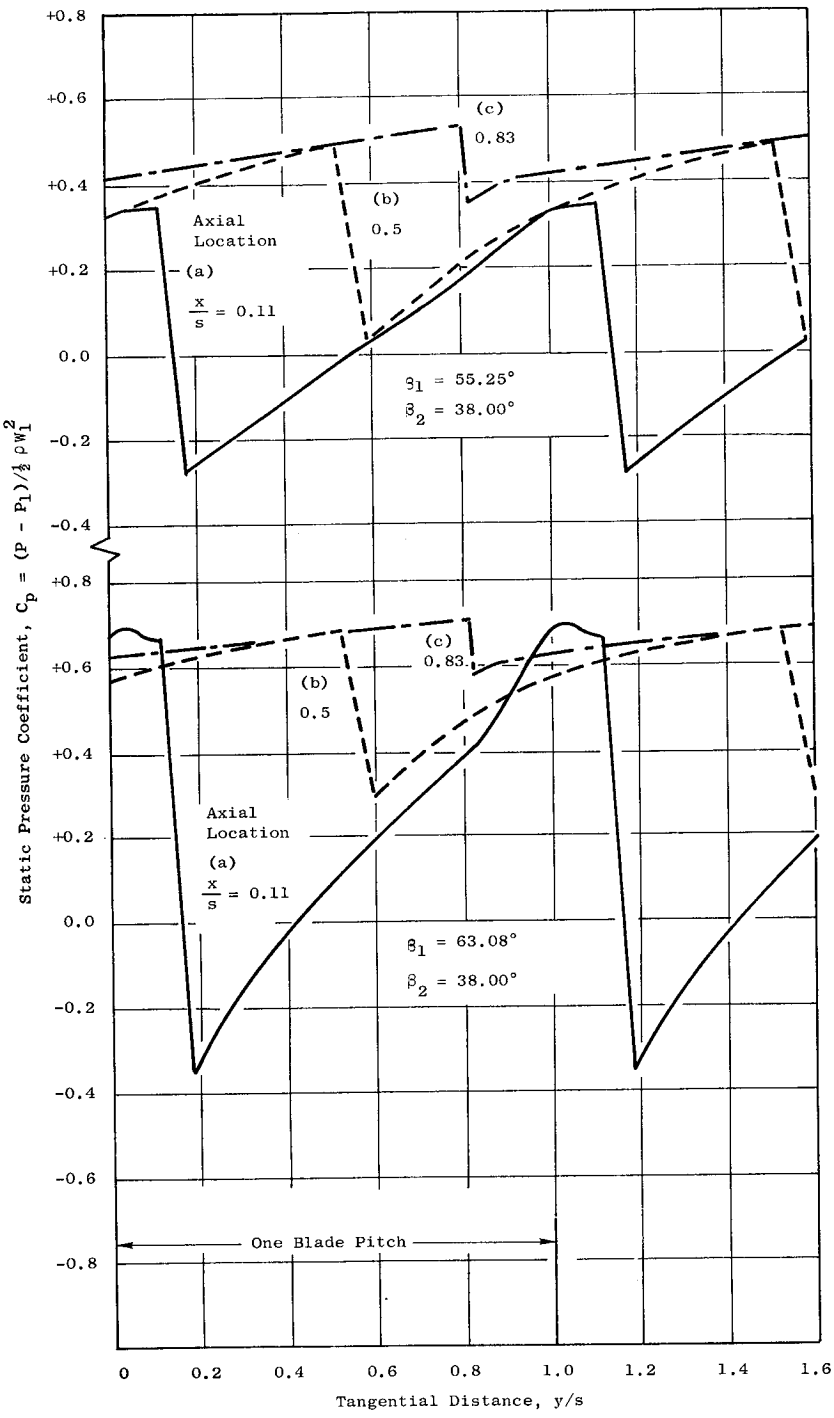

Figure 3 Flow Field Flux Plot Analysis Blade-to-Blade Static Pressure Distributions.

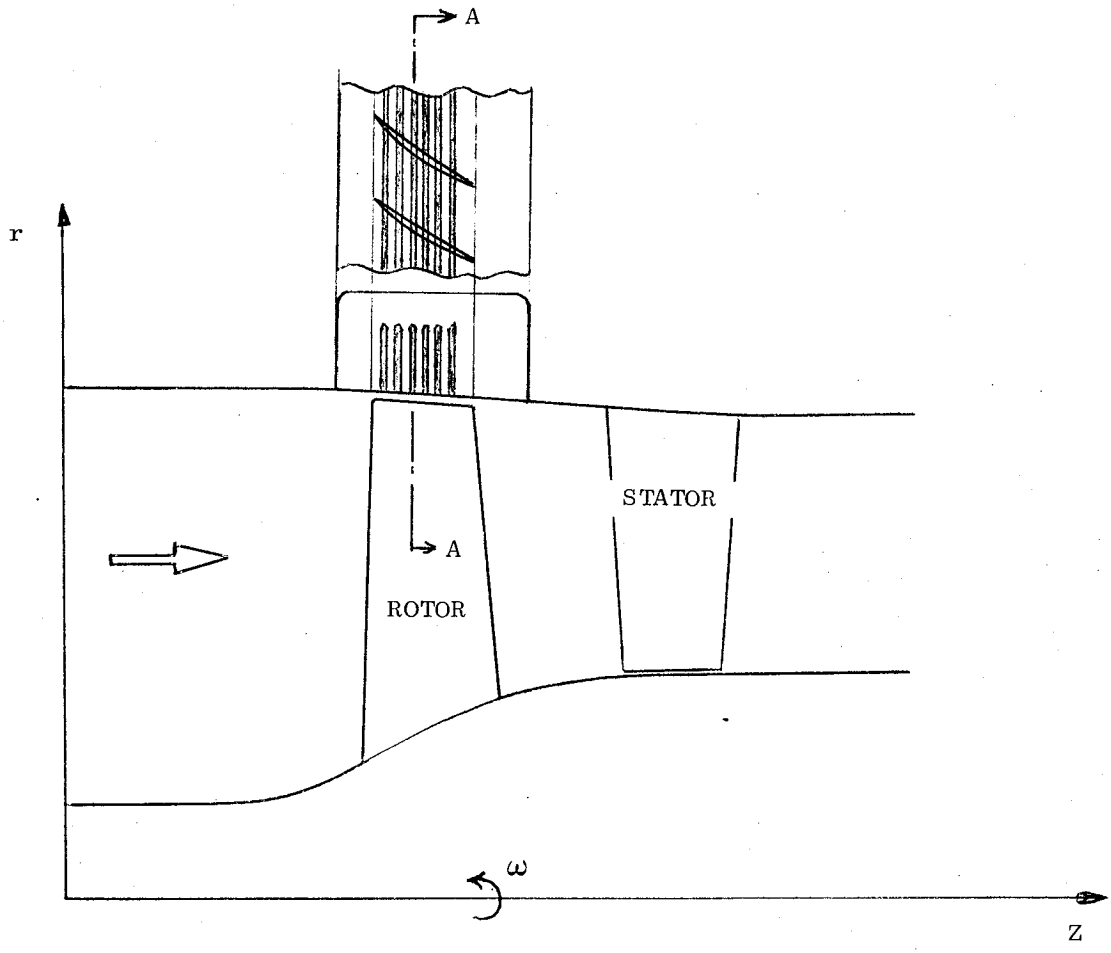

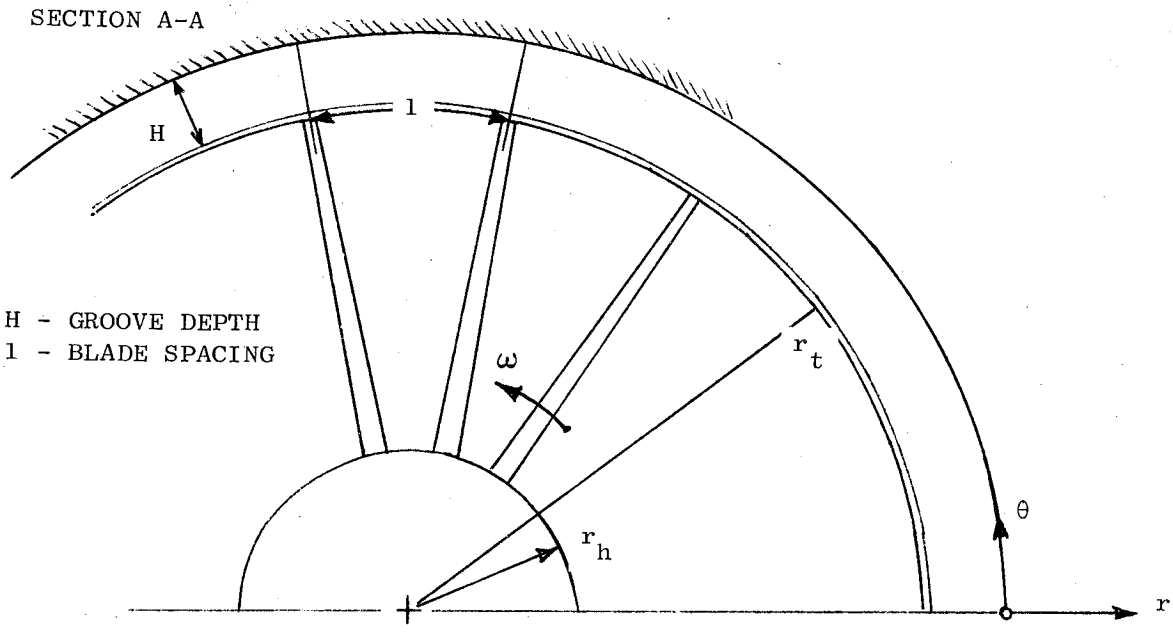

Figure 4 Circumferential Groove Casing Treatment Model

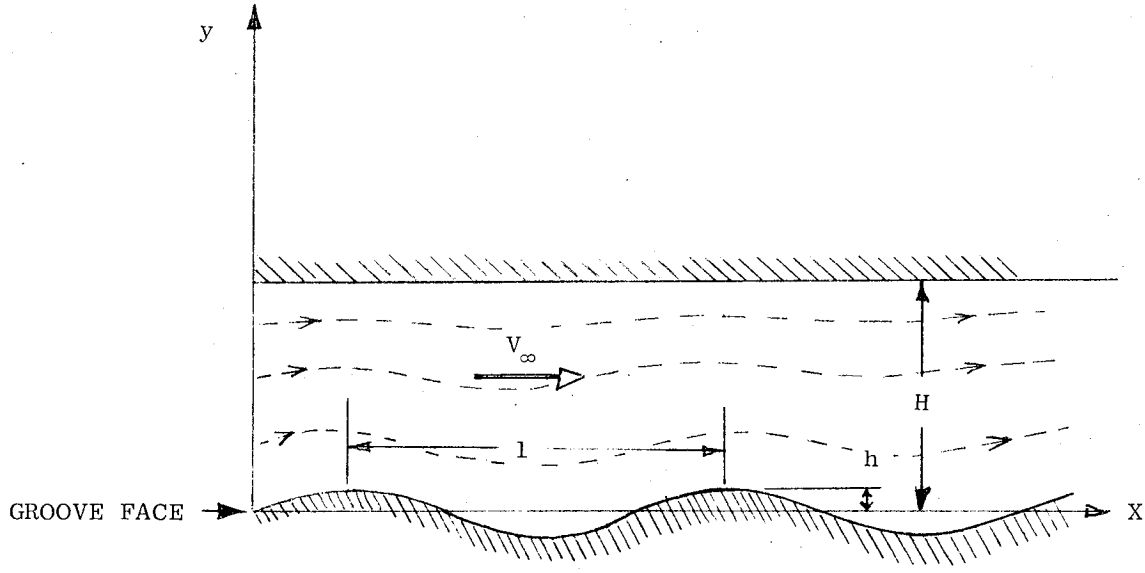

Figure 5 Wavy Wall Model for Circumferential Groove Casing Treatment Flow

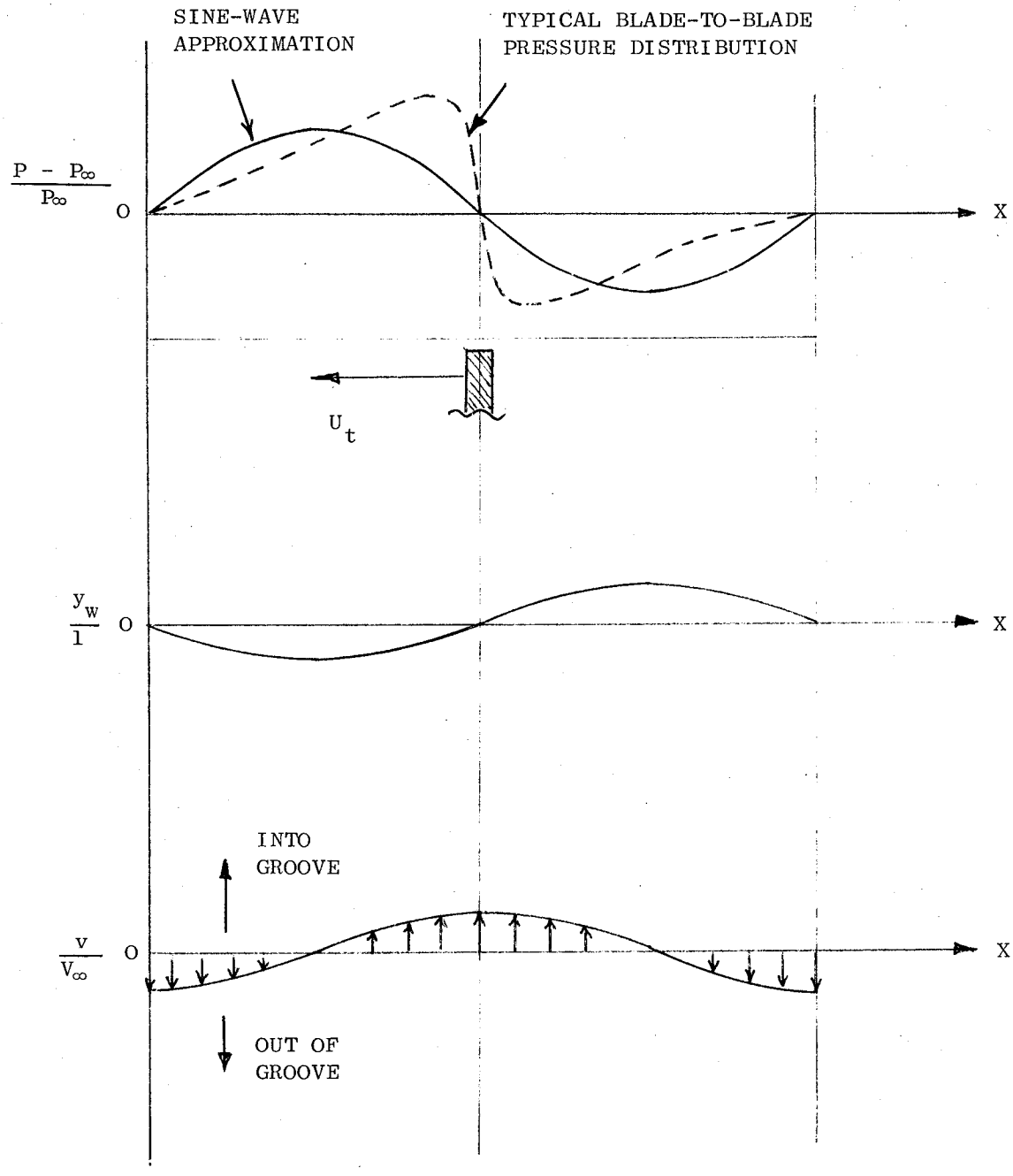

Figure 6 Blade-to-Blade Pressure and Velocity Component Distributions, Sine-Wave Approximation

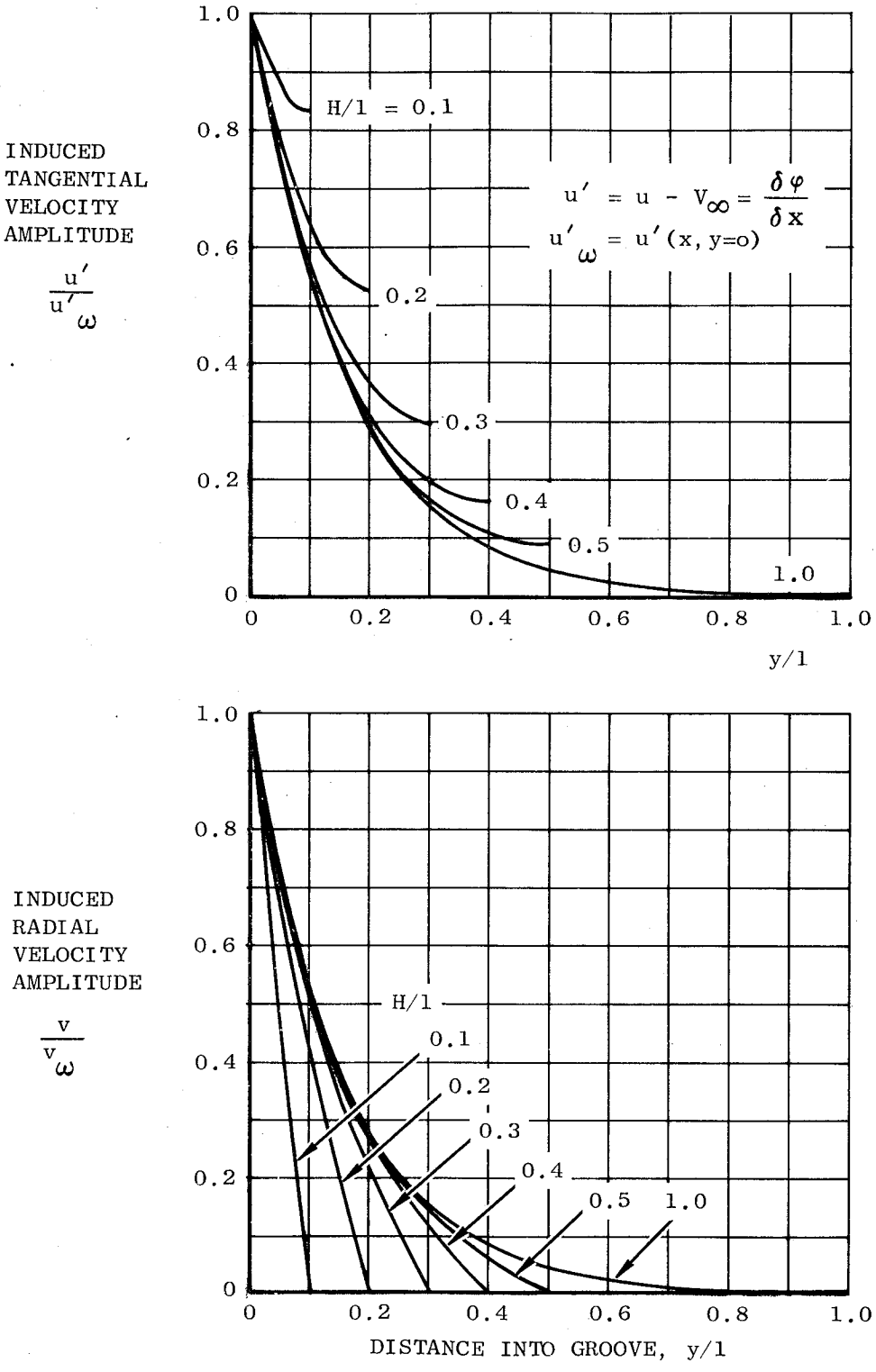

Figure 7 Predictions of Induced Velocity Component Amplitudes, Constant Relative Total Pressure (Wavy Wall) Model for Circumferential Groove Casing Treatment Flow

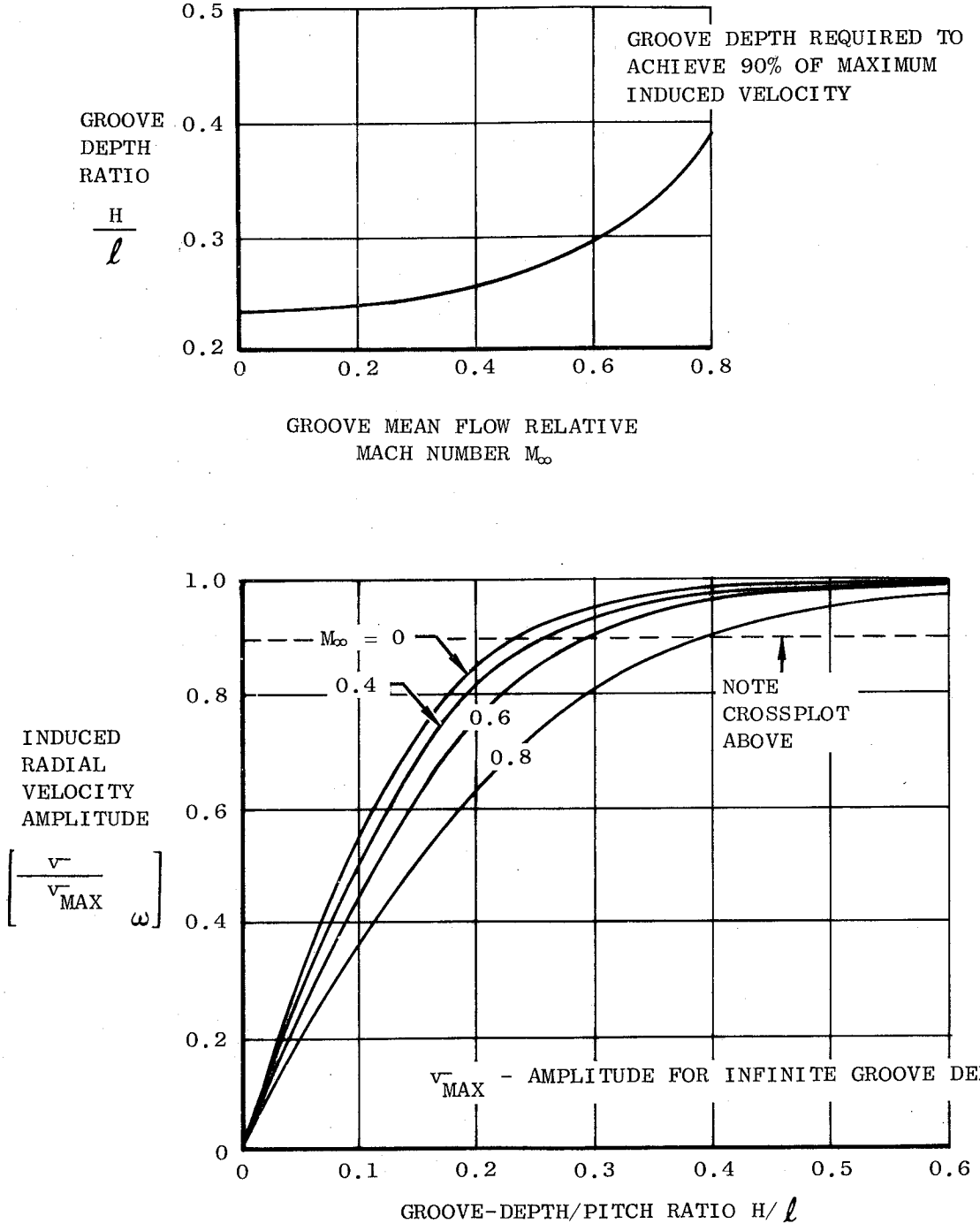

Figure 8 Predicted Effect of Groove-Depth-to-Blade-Pitch Ratio on Induced Flow Velocity, Constant Relative Total Pressure (Wavy Wall) Model for Circumferential Groove Casing Treatment Flow

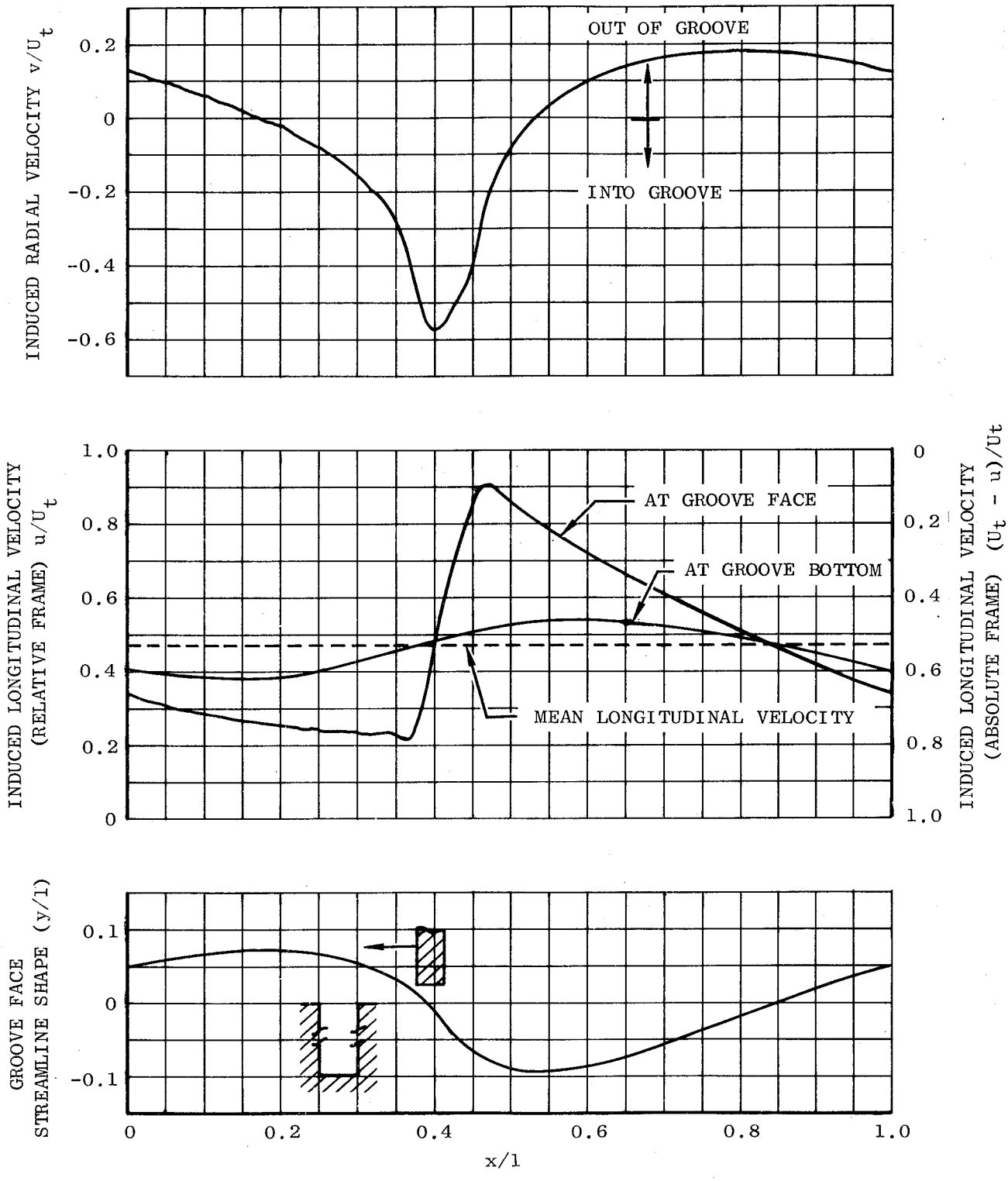

Figure 9 Induced Flow Prediction for Circumferential Groove over Rotor Tip - 30% Chord Position

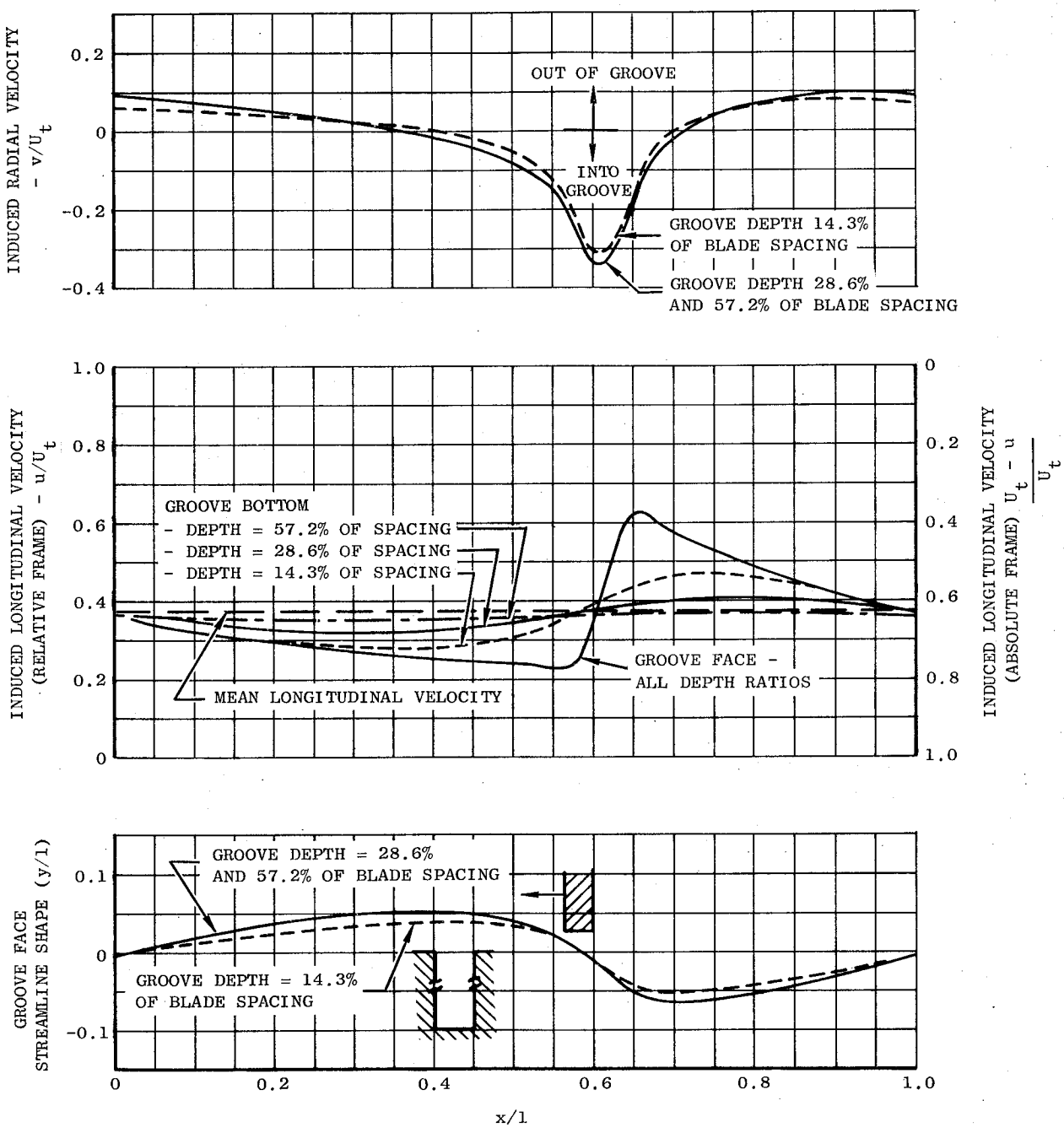

Figure 10 Induced Flow Prediction for Circumferential Groove over Rotor Tip - 50% Chord Position

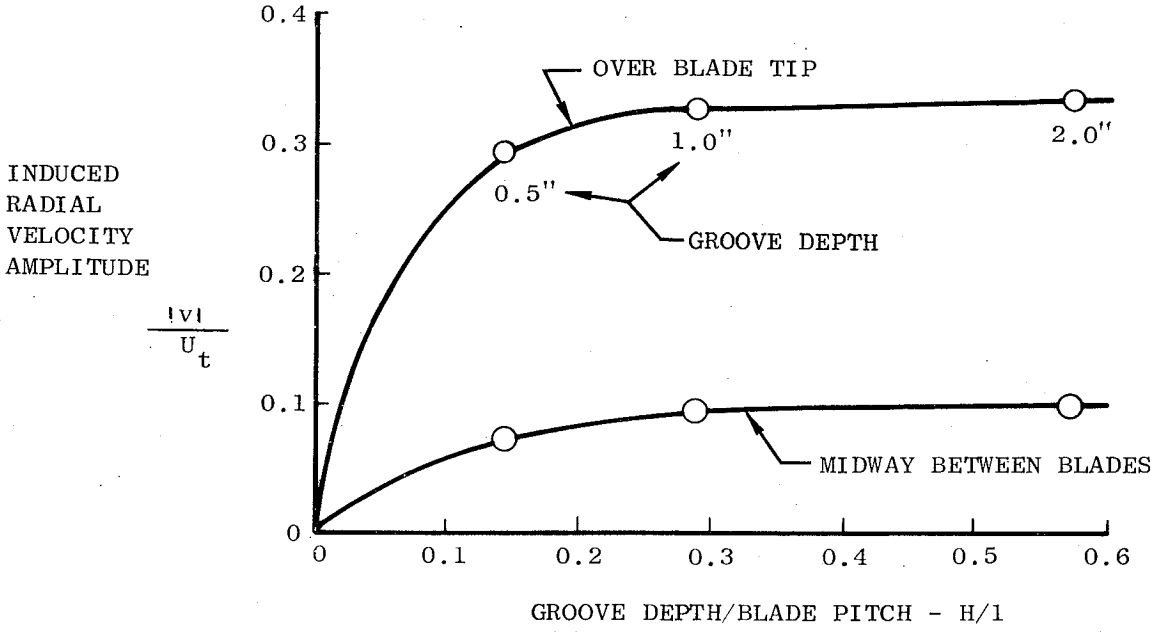

Figure 11 Predictions for LSRC Rotor Induced Velocity Amplitude at Near-Stall Flow

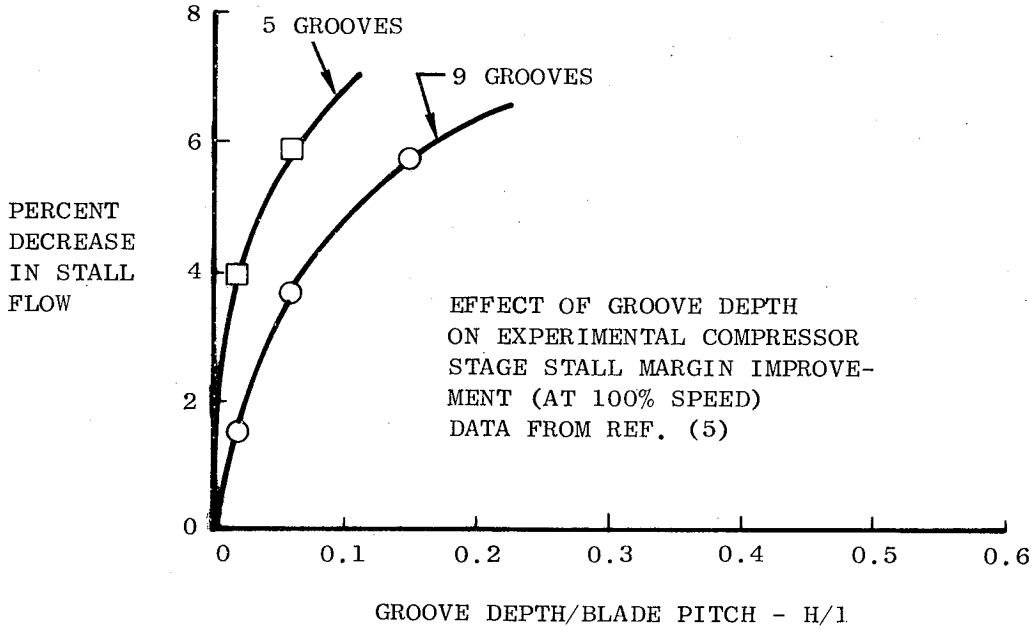

Figure 12 Effect of Groove Depth on Experimental Compressor Stage Stall Margin Improvement (100% Speed)

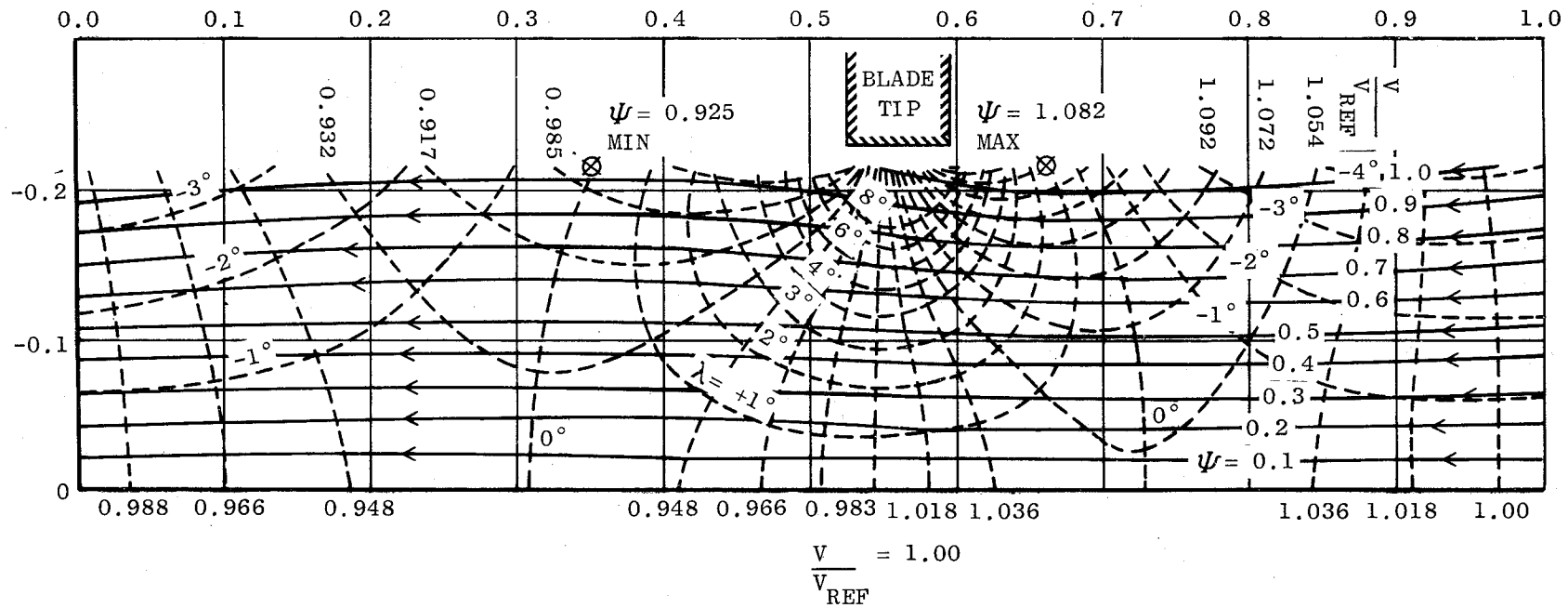

Figure 13 Potential Flow Model in a Circumferential Groove, Mean Velocity Based on Free Stream Absolute Tangential Velocity

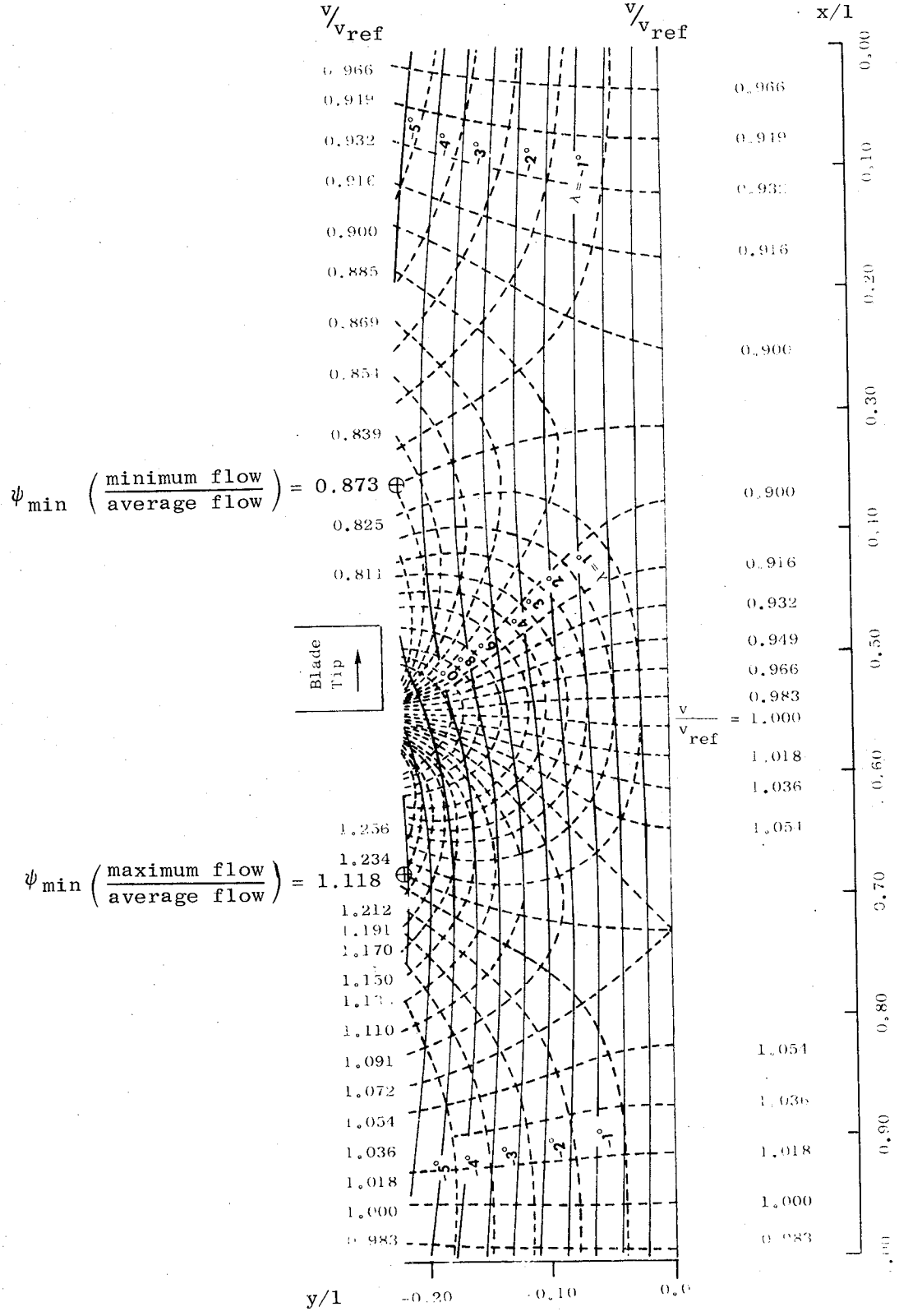

Figure 14 Potential Flow Model in a Circumferential Groove, Mean Velocity Based on 80% of Free Stream Absolute Tangential Velocity

Figure 15 Potential Flow Model in a Circumferential Groove, Mean Velocity
Based on 60% of Free Stream Absolute Tangential Velocity

CAVITY LENGTH = 53% OF BLADE SPACING
CAVITY DEPTH = 28.6% OF BLADE SPACING

ALL VELOCITIES ARE REFERRED TO RELATIVE VELOCITY UPSTREAM OF ROTOR CASCADE

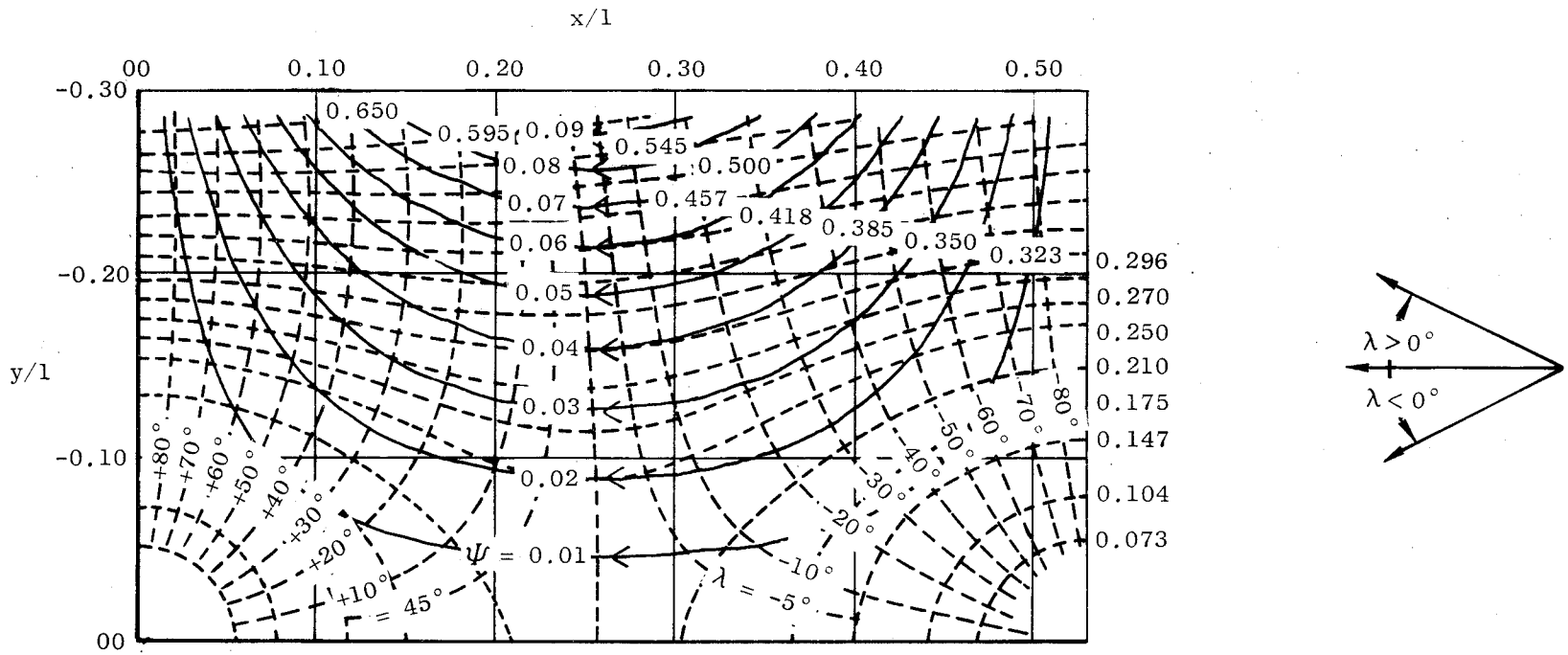

Figure 16 Inviscid Flow Model in the Blade Angle Slot, 25% Recovery of the Absolute Velocity Head Entering the Slot

CAVITY LENGTH = 53% OF BLADE SPACING
CAVITY DEPTH = 28.6% OF BLADE SPACING

ALL VELOCITIES ARE REFERRED TO RELATIVE VELOCITY UPSTREAM OF ROTOR CASCADE

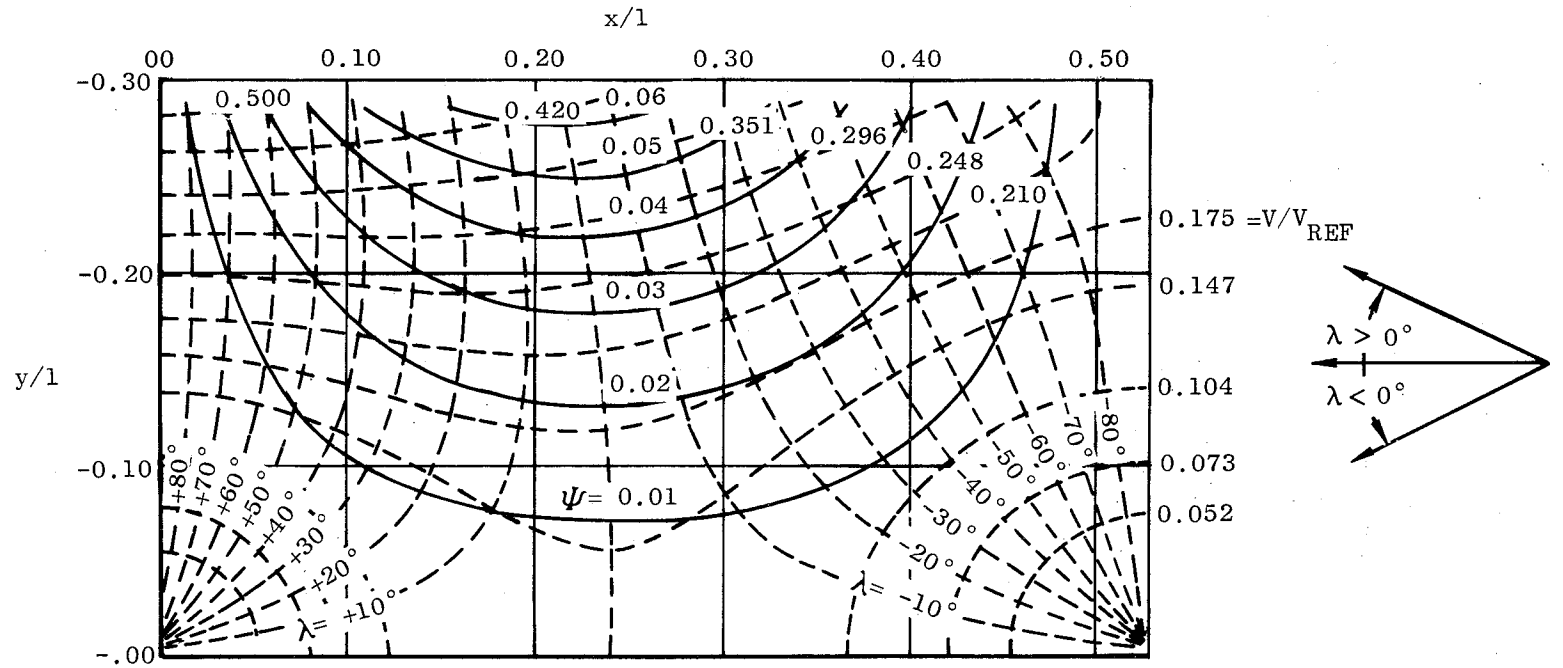

Figure 17 Inviscid Flow Model in the Blade Angle Slot, 5% Recovery of the Absolute Velocity Head Entering the Slot

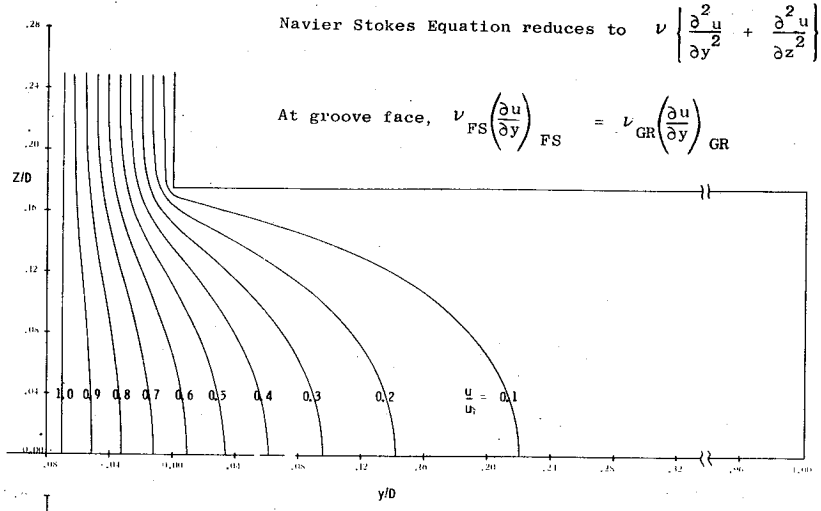

a. Free Stream Eddy Viscosity = Groove Viscosity

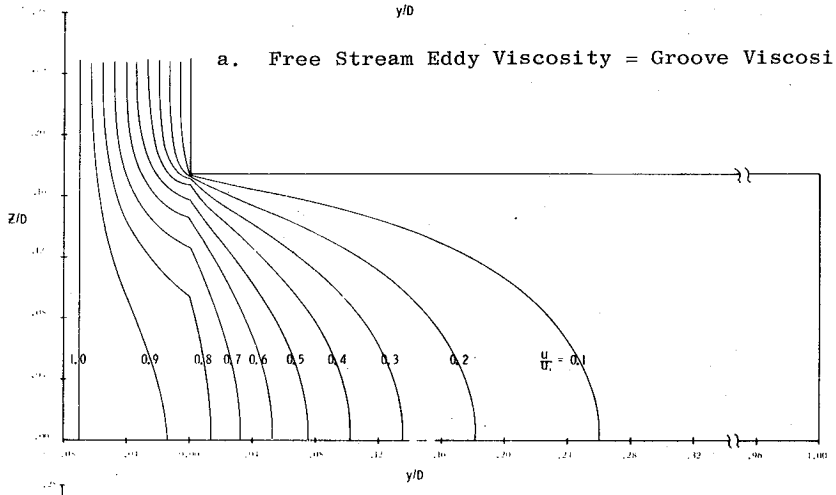

b. Free Stream Eddy Viscosity = 4 x Groove Viscosity

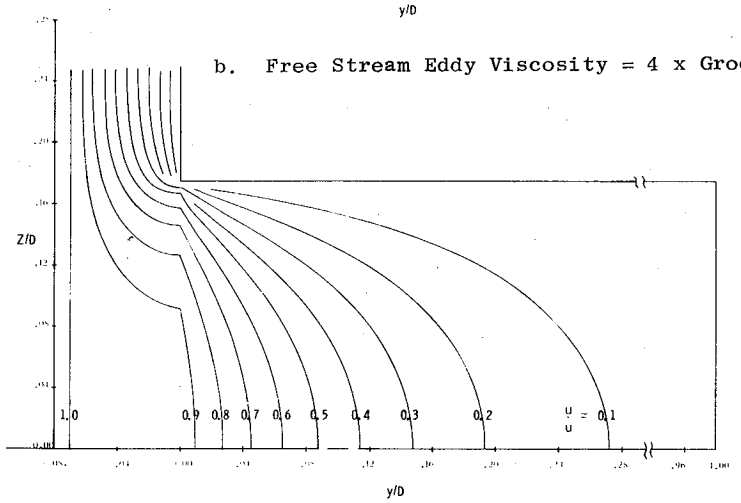

c. Free Stream Eddy Viscosity = 20 x Groove Viscosity

Figure 18 Laminar Viscous Flow Model in the Circumferential Groove, Groove Depth = 3X Groove Width

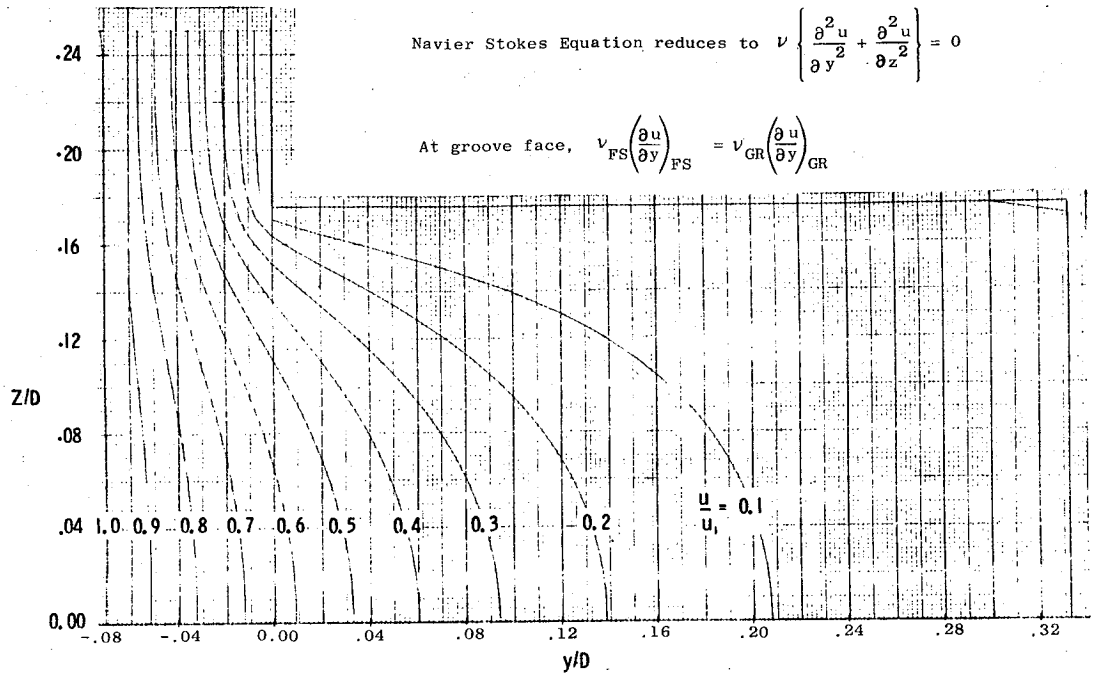

a. Free Stream Viscosity = Groove Viscosity

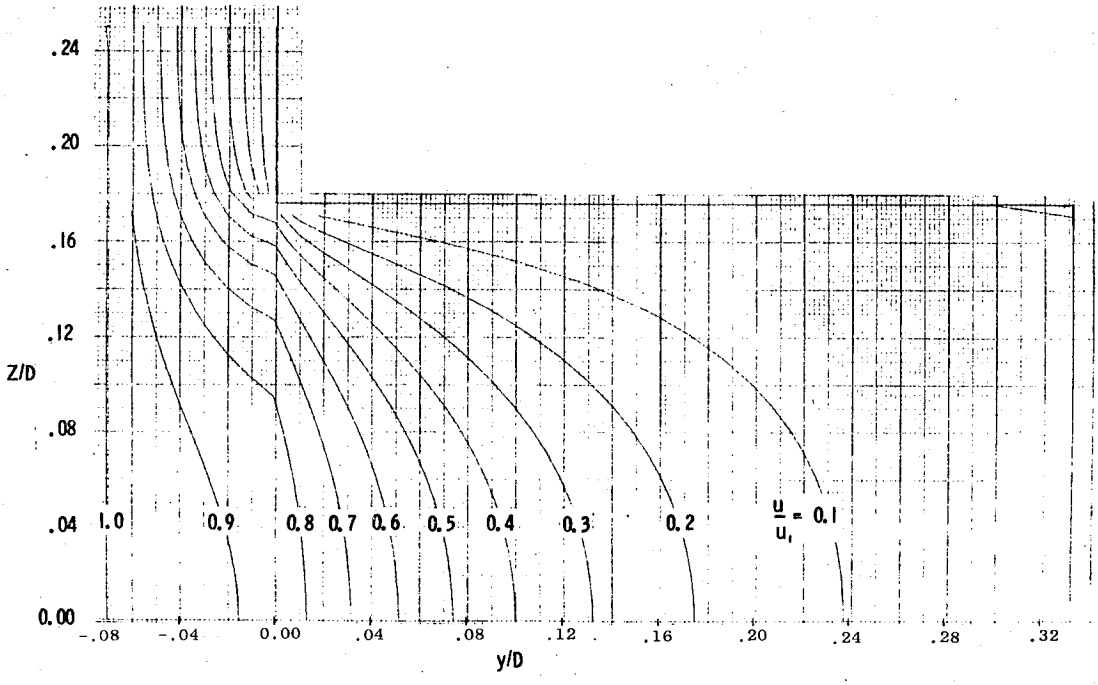

b. Free Stream Viscosity = 4 x Groove Viscosity

Figure 19 Laminar Viscous Flow Model in the Circumferential Groove, Groove Depth = Groove Width

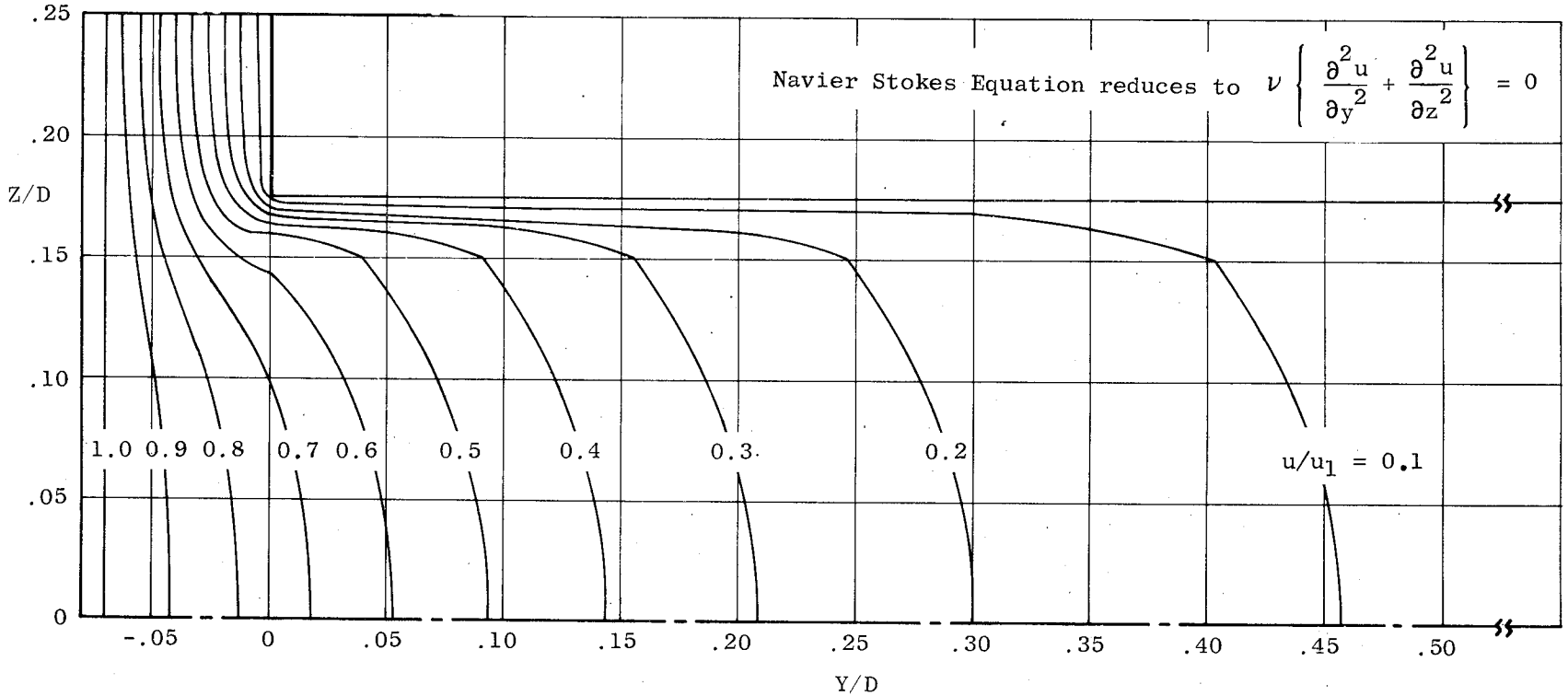

Figure 20 Viscous Flow Model in the Circumferential Groove, Variable Eddy Viscosity Near Cavity Walls; Groove Depth = 3X Groove Width

FOLDOUT FRAME

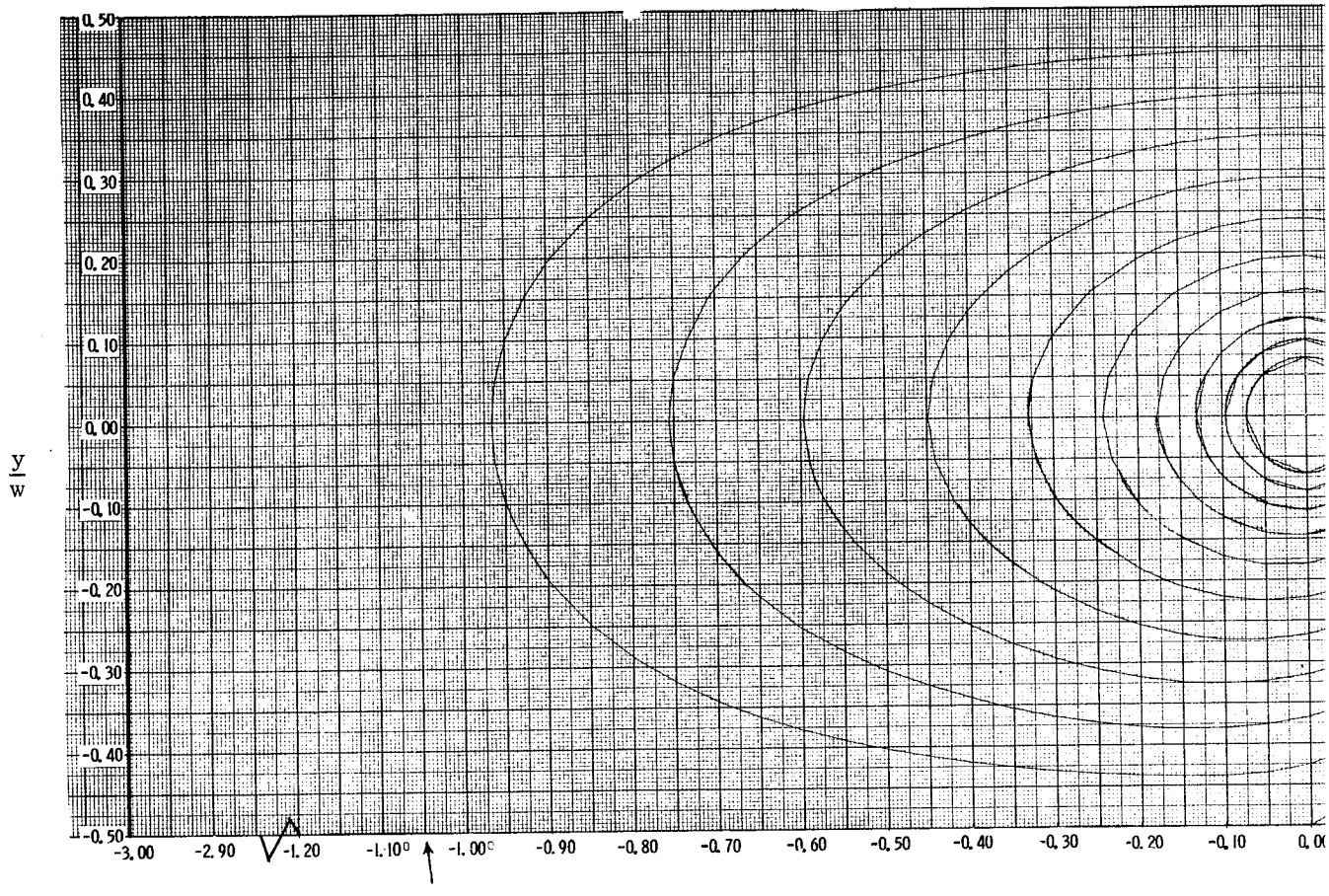

Figure 21 Roller

FOLDOUT FRAME

2

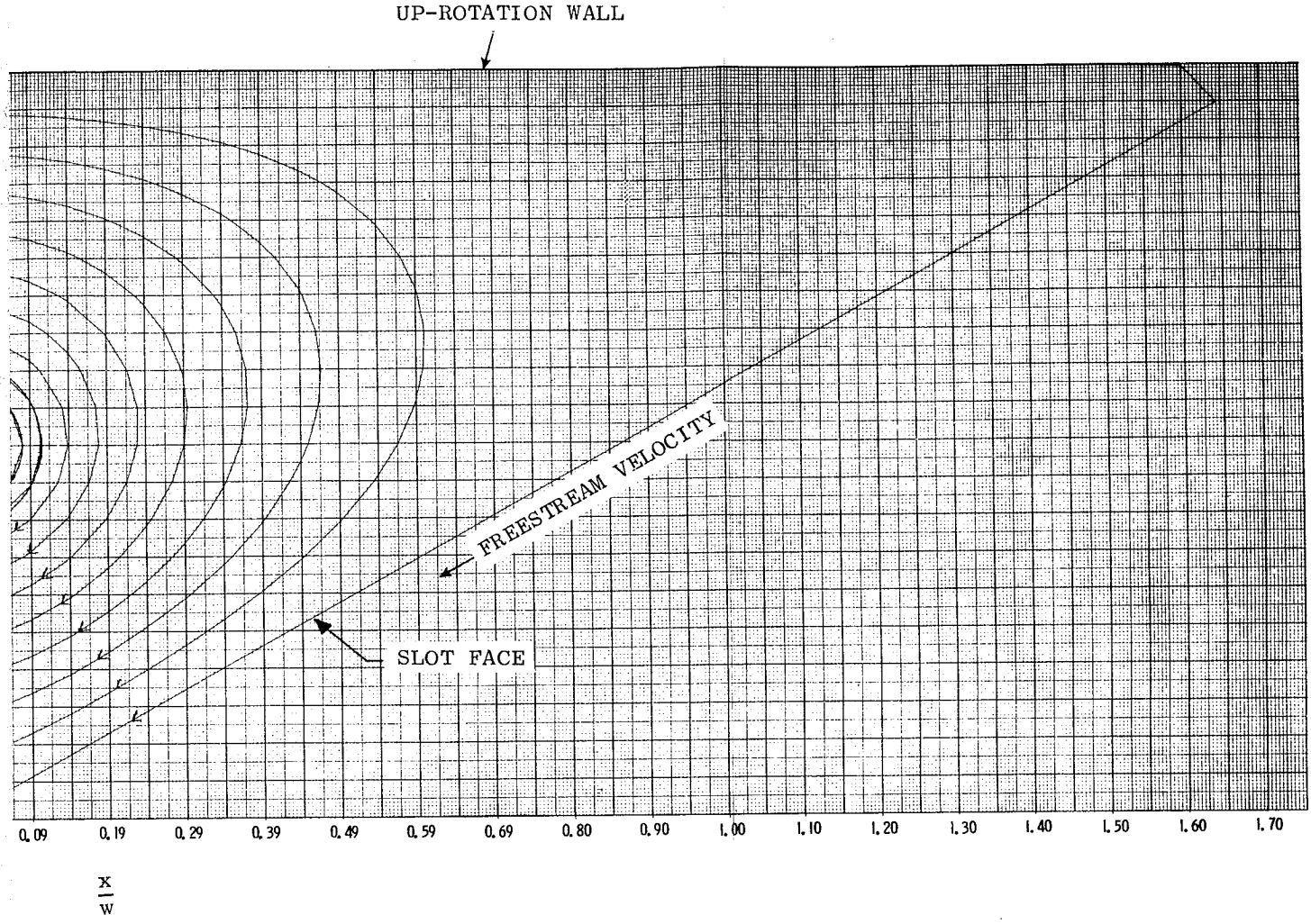

aring Flow Model in Axial Skewed Slot

Preceding page blank

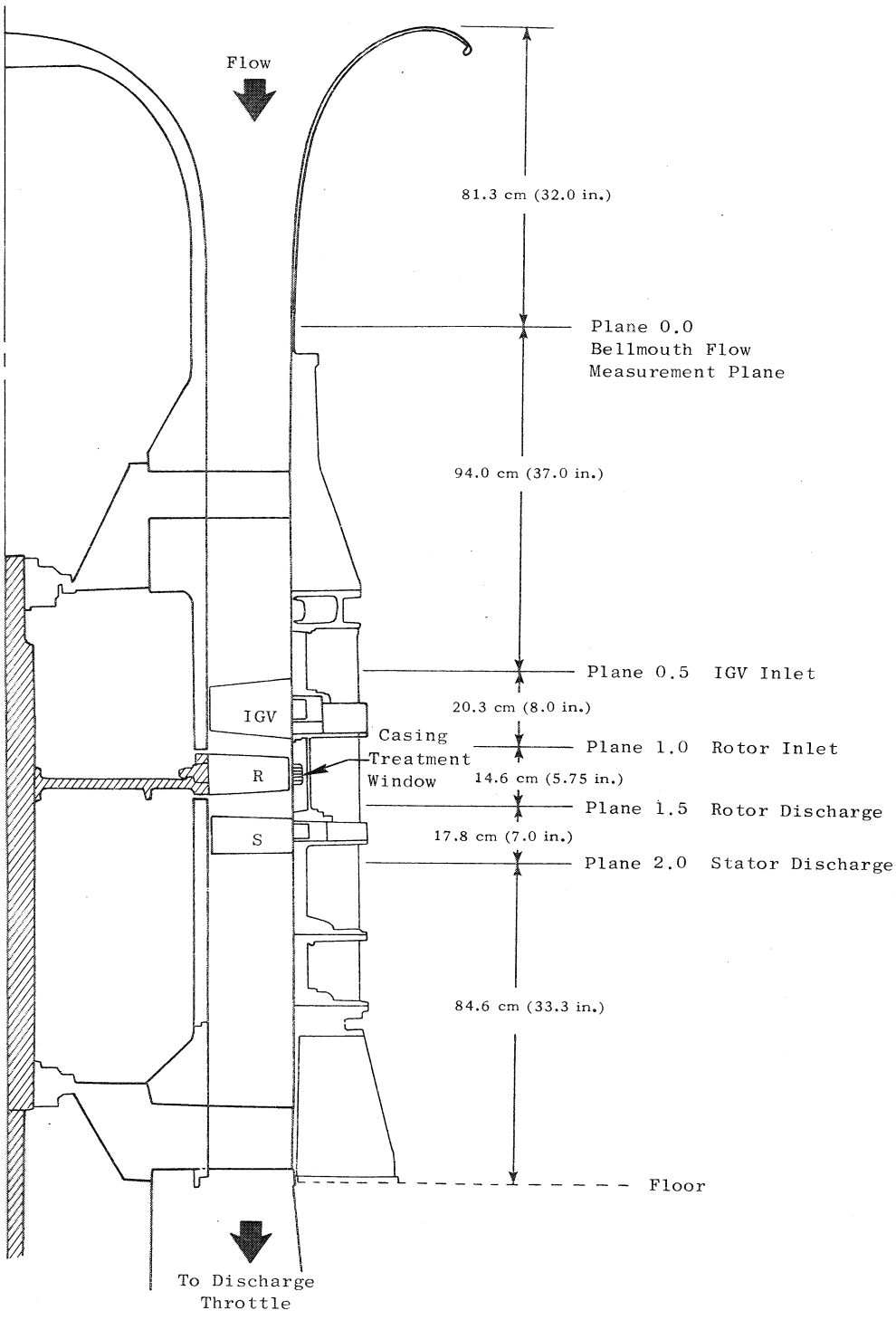

Figure 22 Cross Sectional Drawing of Low Speed Research Compressor

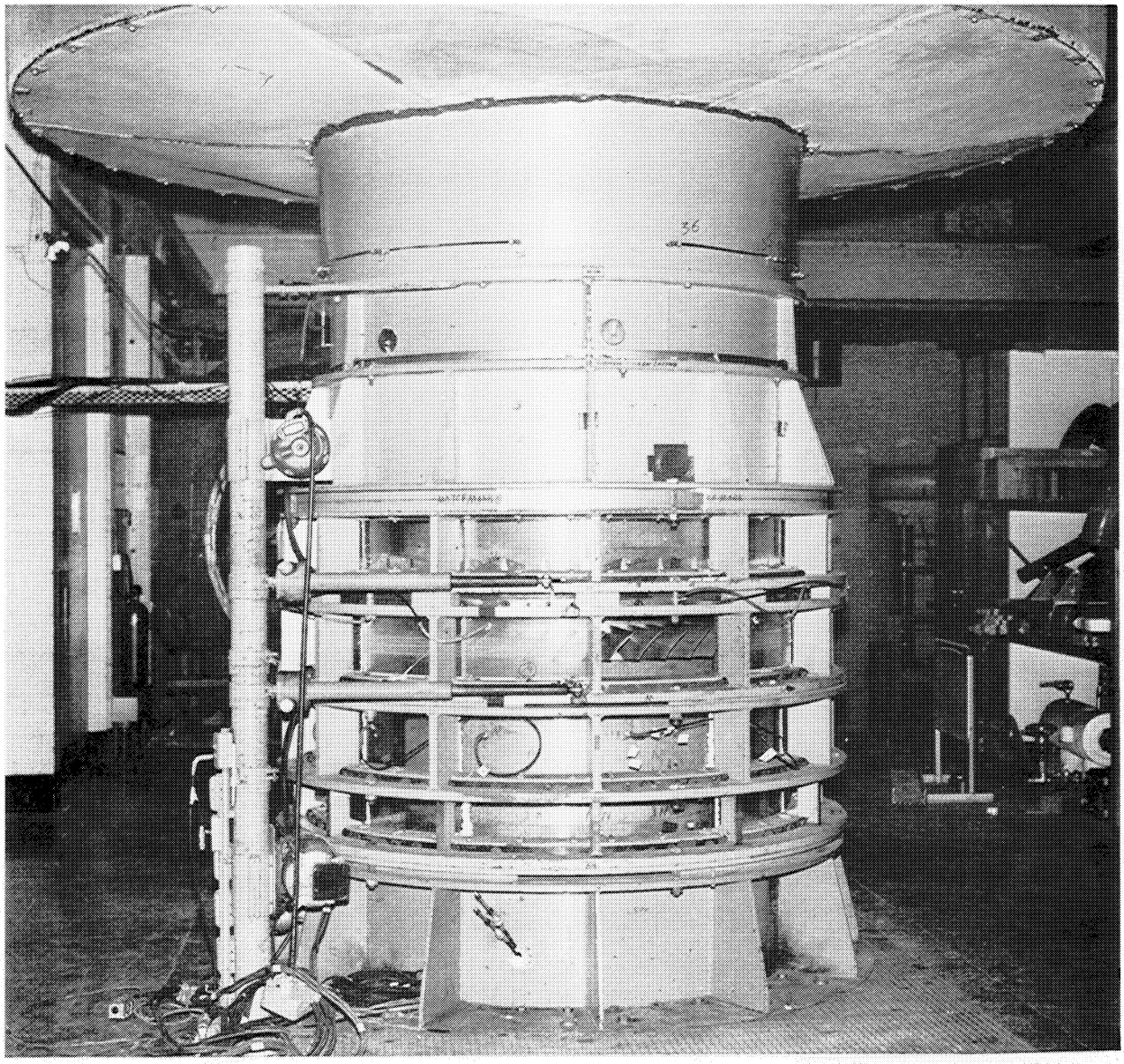

This page is reproduced at the back of the report by a different reproduction method to provide better detail.

Figure 23 Photograph of the Low Speed Research Compressor Buildup with Circumferential Grooved Windows Partially Installed

This page is reproduced at the back of the report by a different reproduction method to provide better detail.

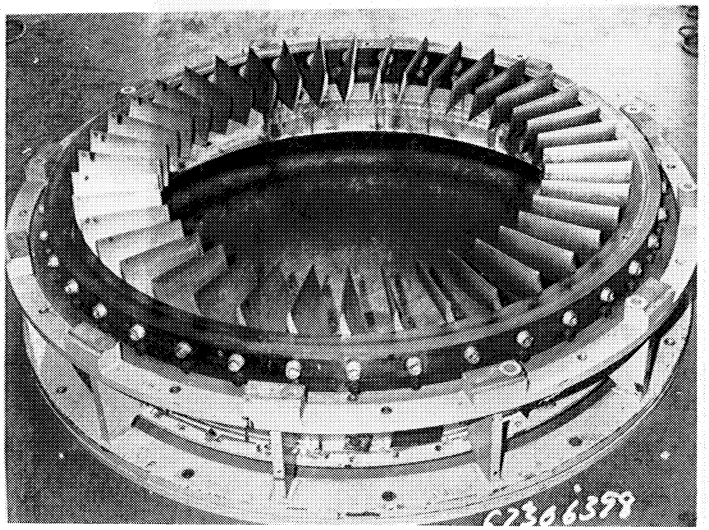

a. Inlet Guide Vanes

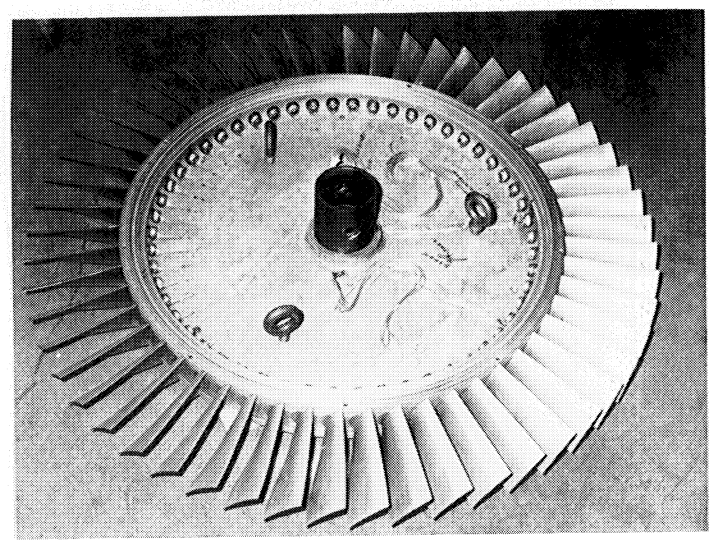

b. Rotor

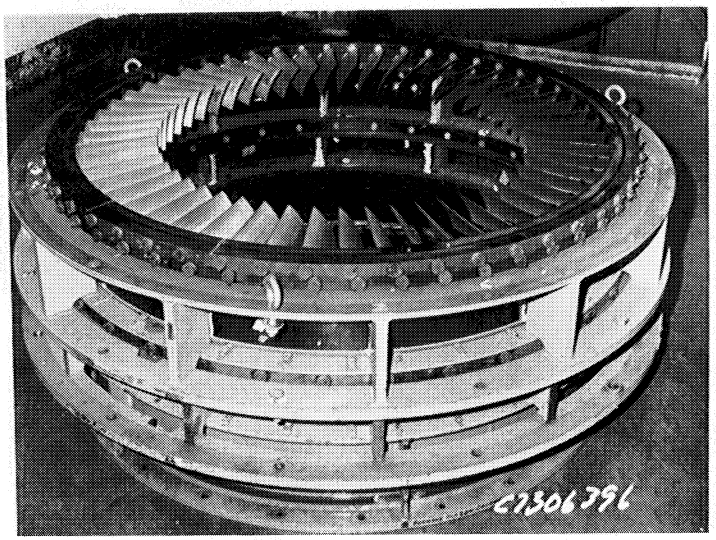

c. Stator

Figure 24 Blade Row Assemblies for Low Speed Research Compressor Casing Treatment Investigation

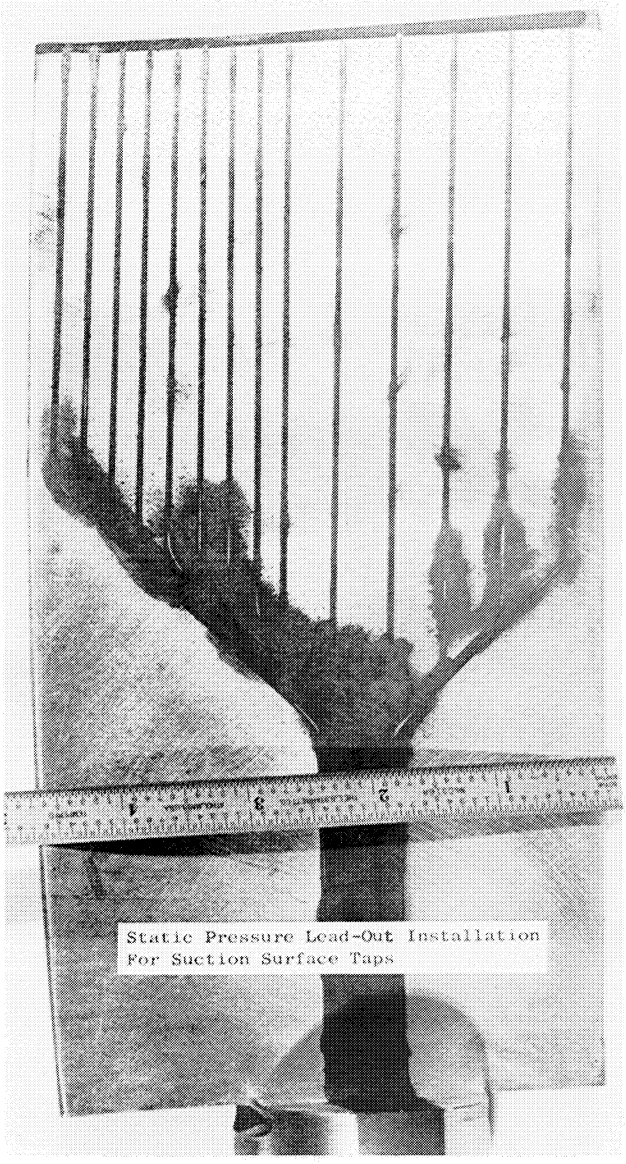

Static Pressure Lead-Out Installation
For Suction Surface Taps

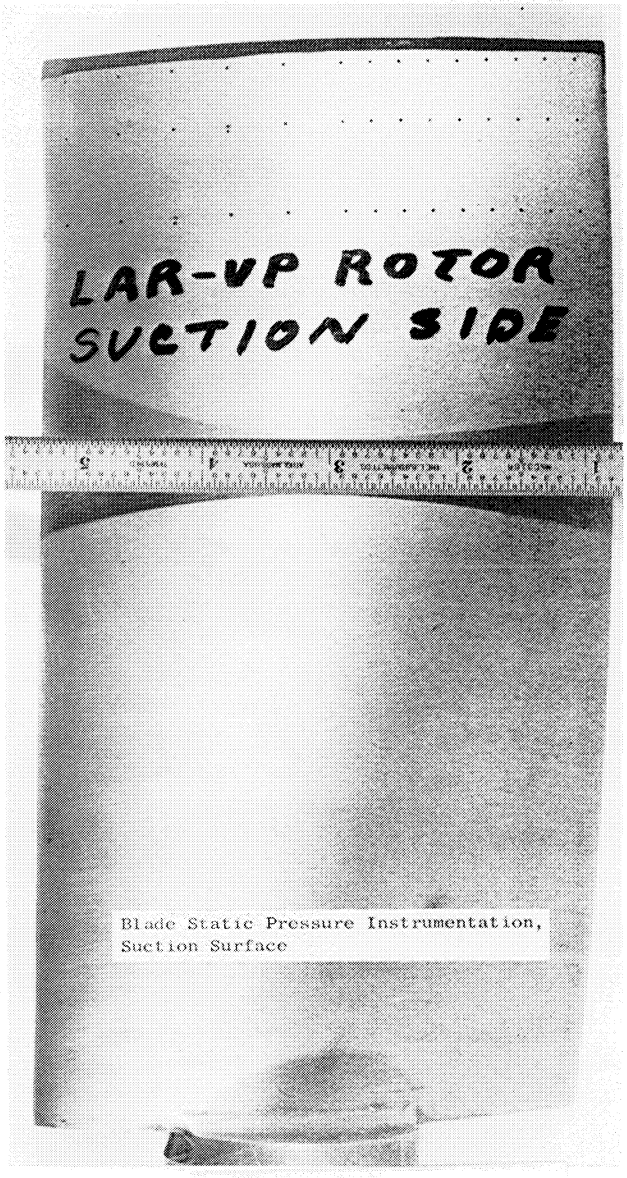

Blade Static Pressure Instrumentation,
Suction Surface

This page is reproduced at the back of the report by a different reproduction method to provide better detail.

Figure 25 Instrumentation for Blade Surface Static Pressure

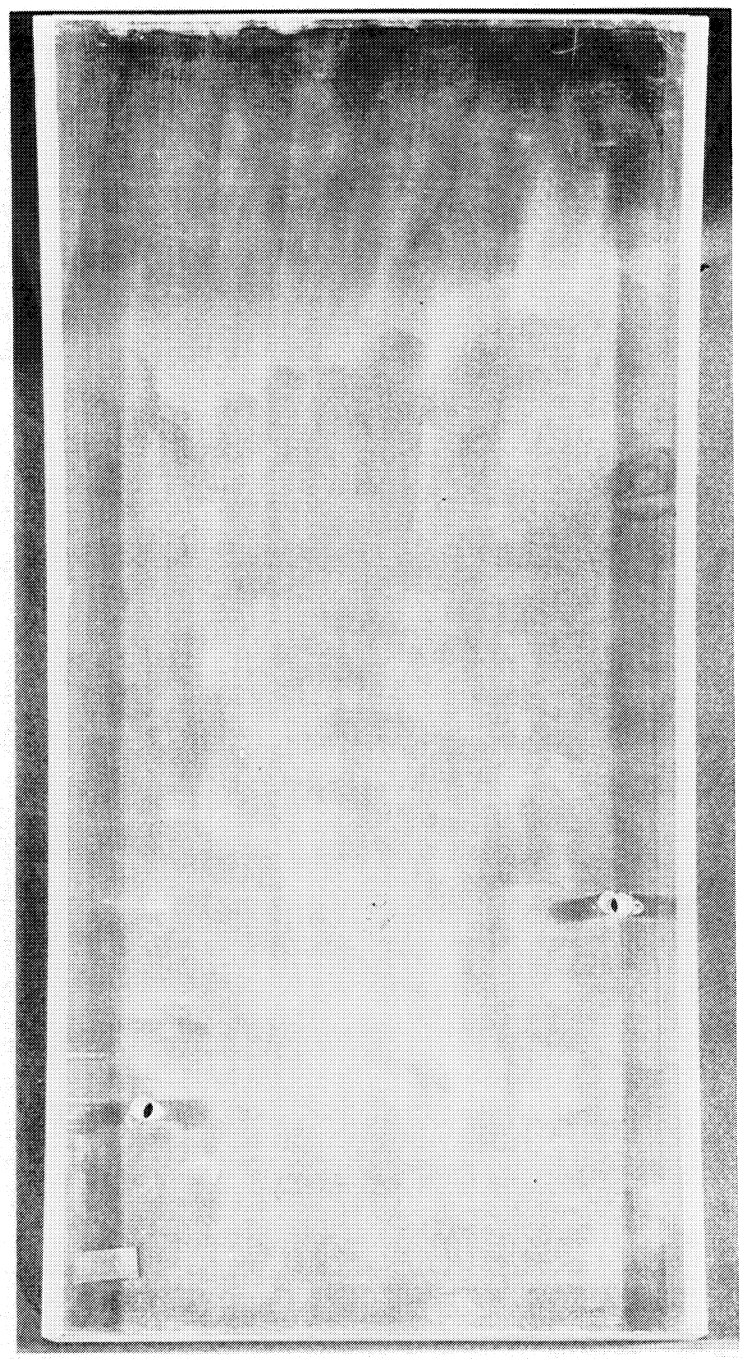

Figure 26 Smooth-Wall, Baseline Casing Treatment Configuration.

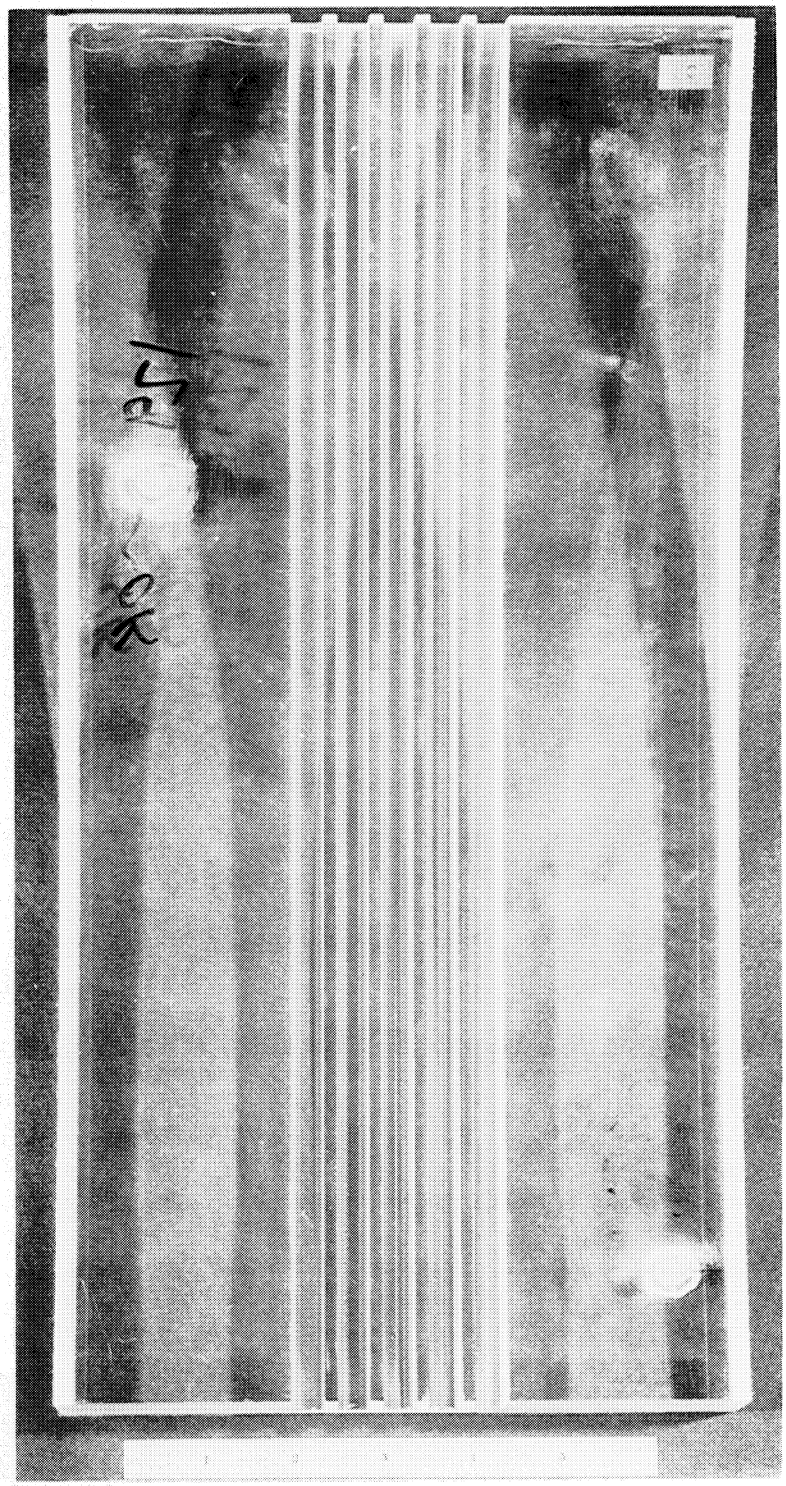

Figure 27 Circumferential Groove Casing Treatment Configuration.

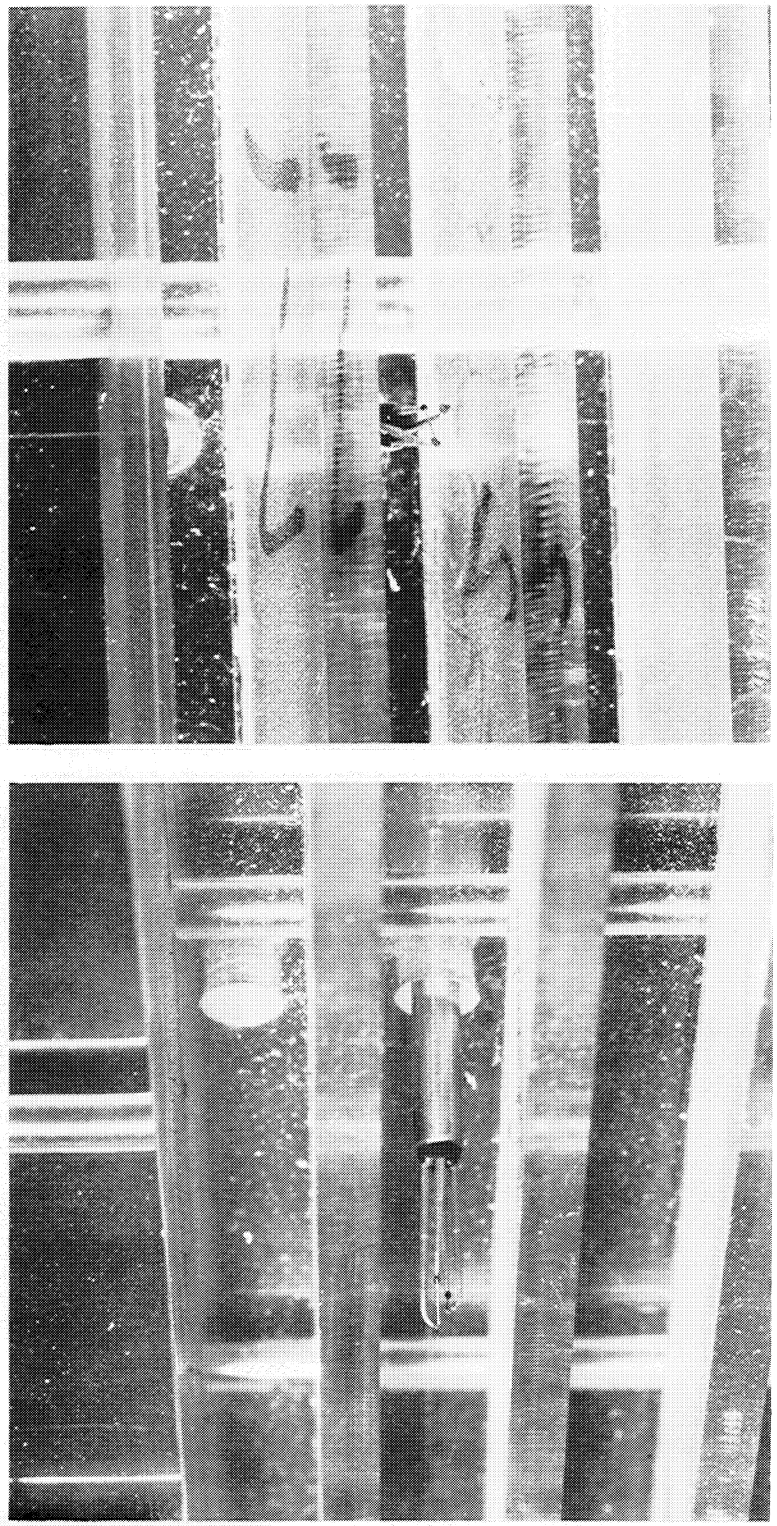

Figure 28 Installation of "Diagonal X" Hot Film Anemometer in Circumferential Groove

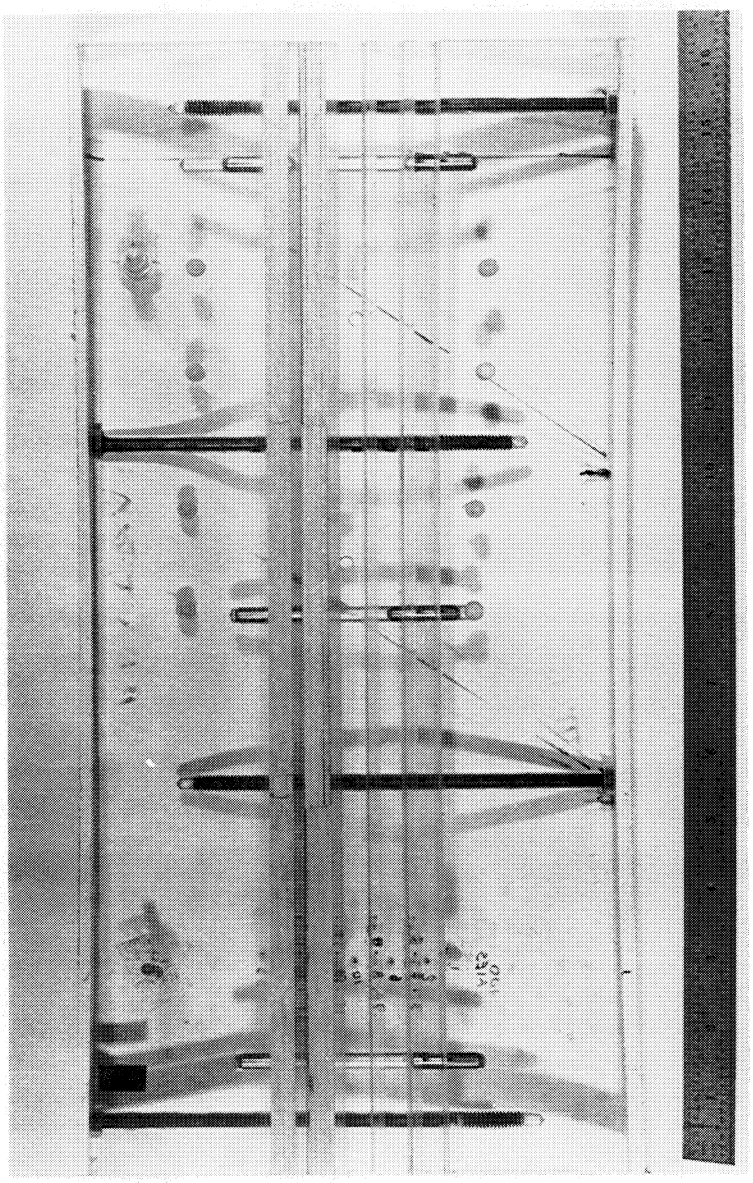

Figure 29 Circumferential Groove Casing Treatment With Three Open Grooves

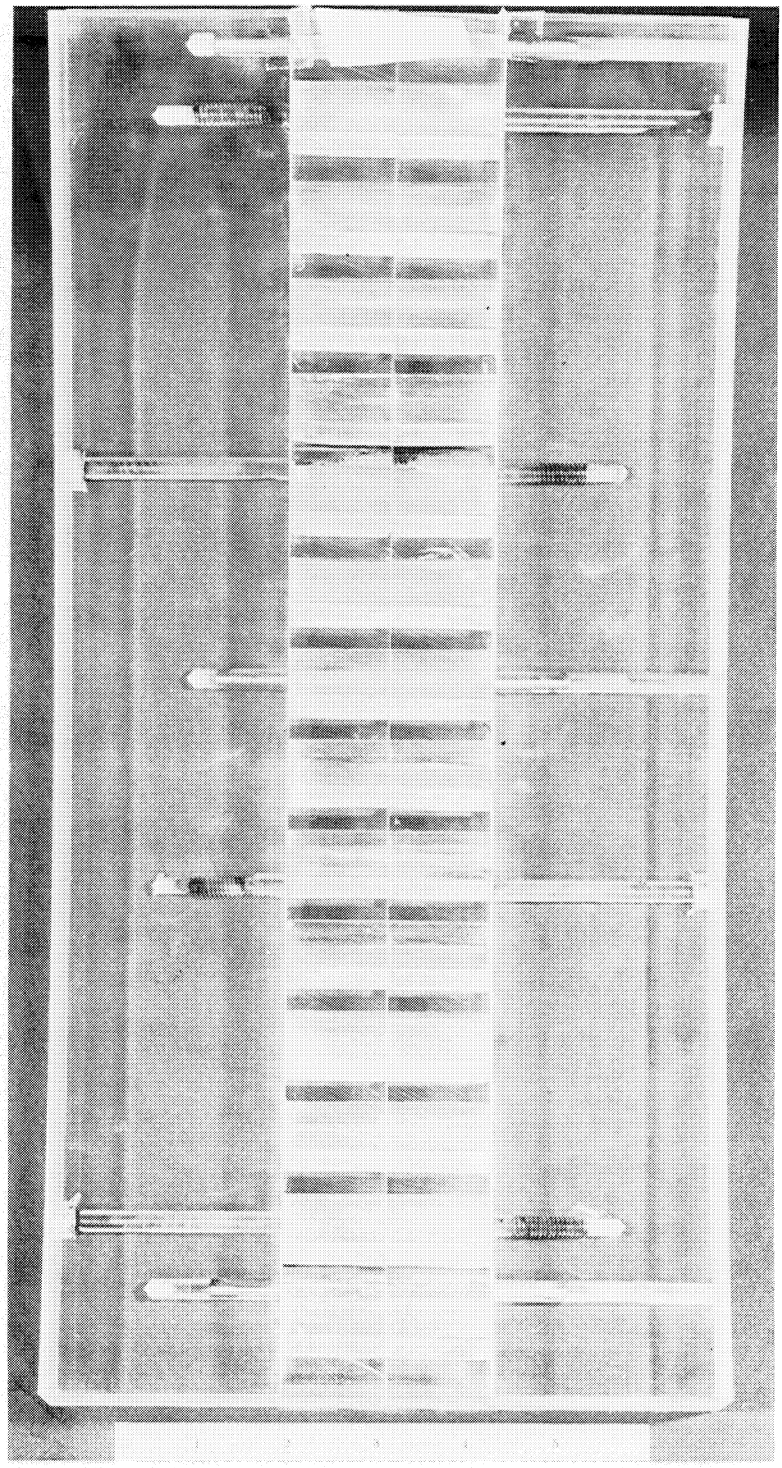

Figure 30 Axial Skewed Slot Casing Treatment Configuration.

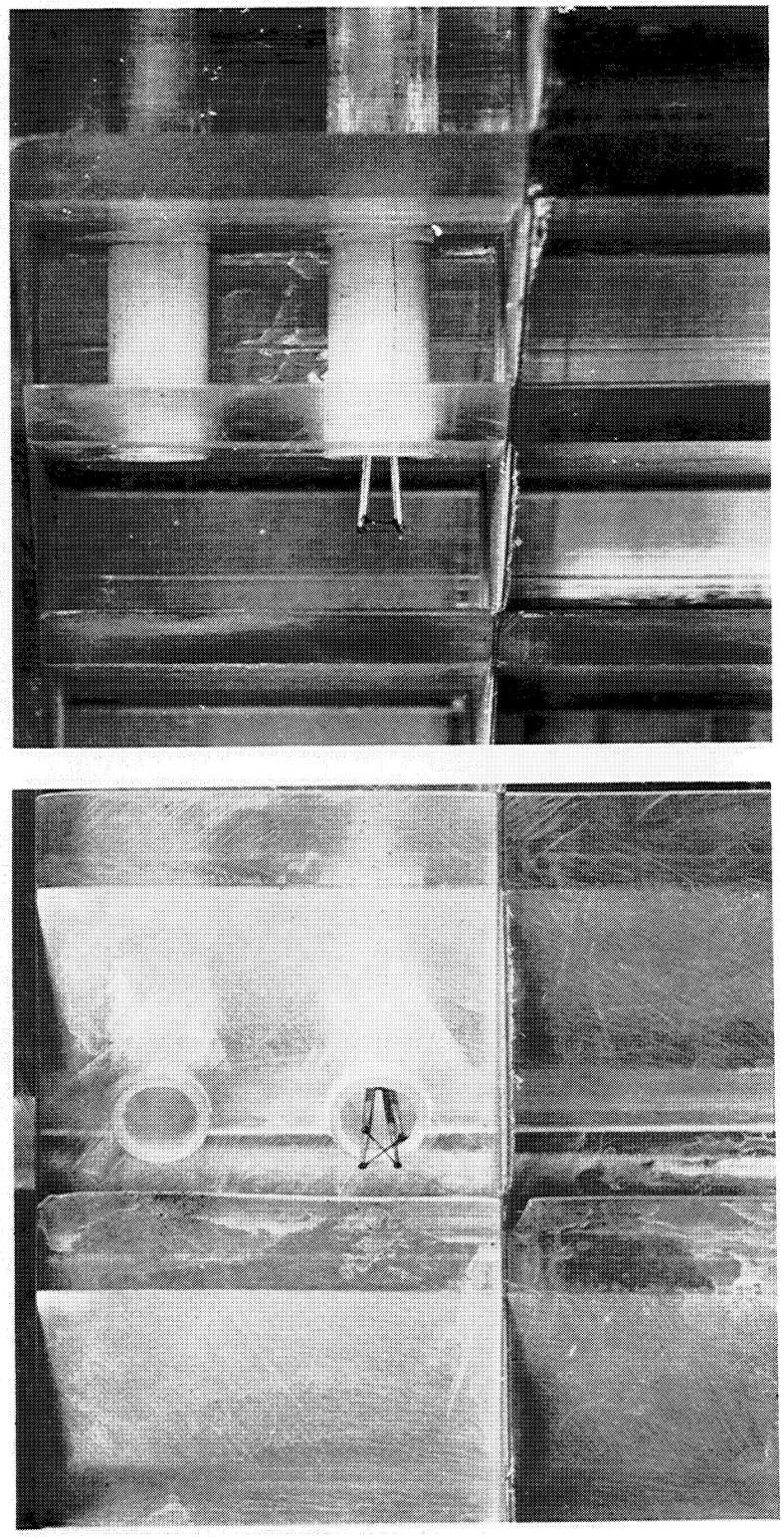

Figure 31 Installation of "Perpendicular X" Hot Film Anemometer in Axial-Skewed Slot

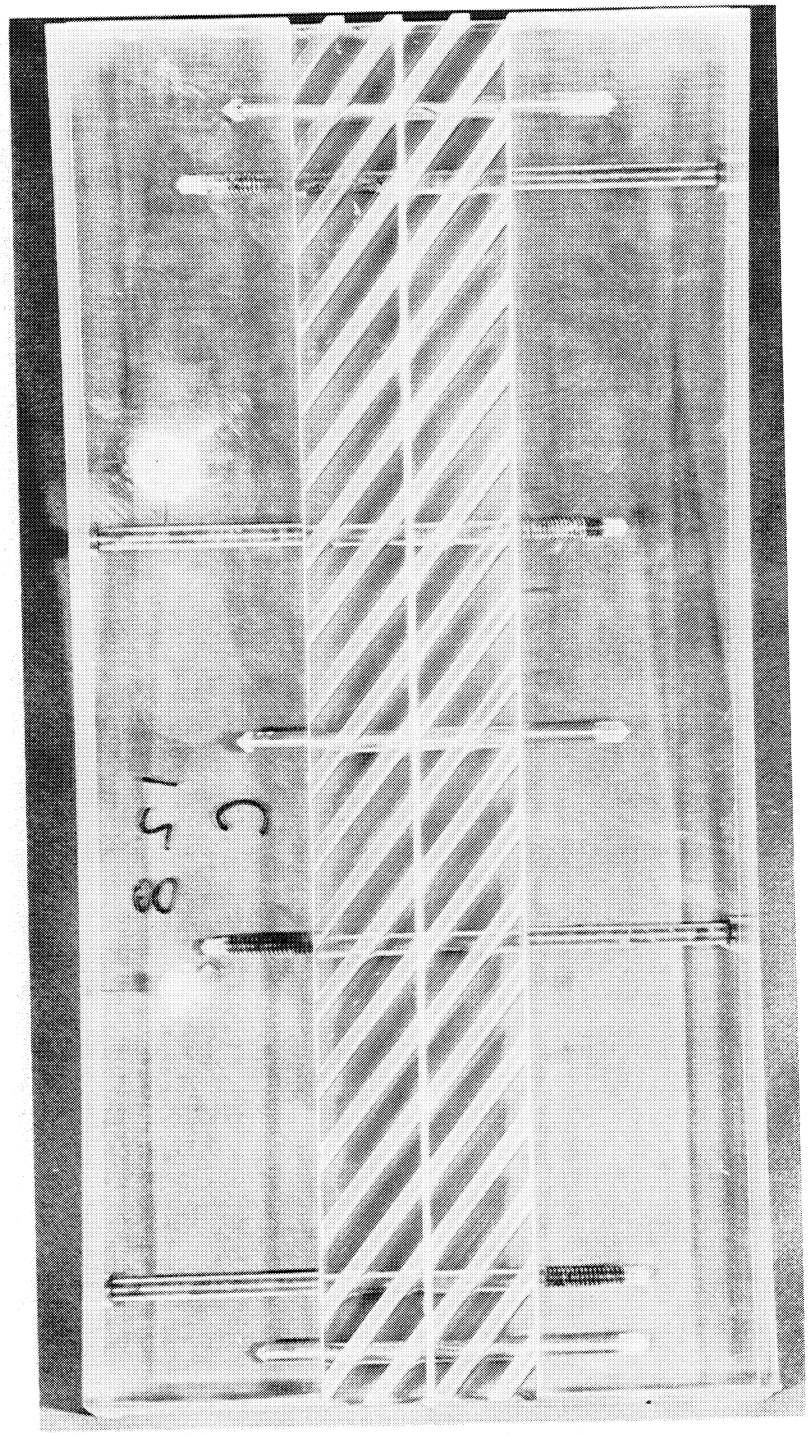

Figure 32 Wide Blade Angle Slot Casing Treatment Configuration.

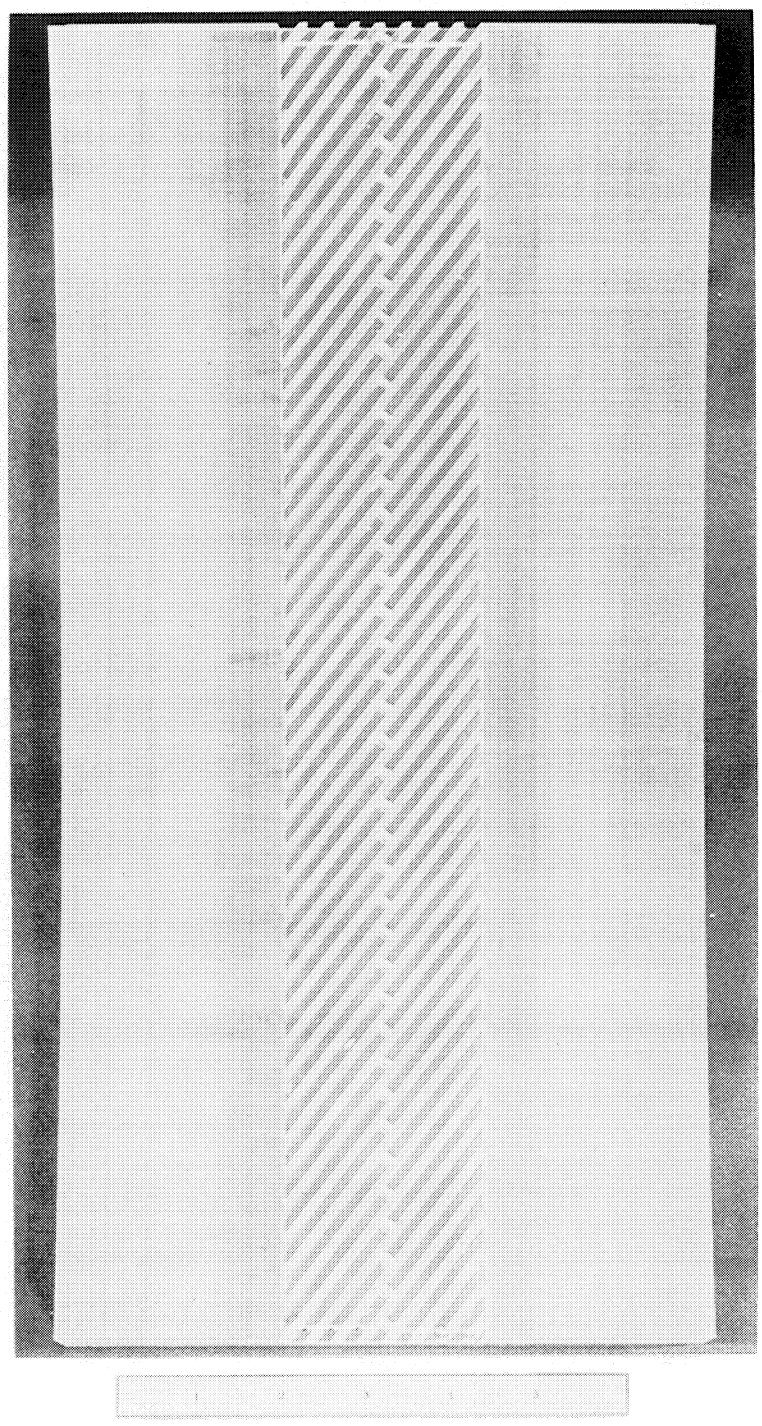

Figure 33 Narrow Blade Angle Slot Casing Treatment Configuration

This page is reproduced at the back of the report by a different reproduction method to provide better detail.

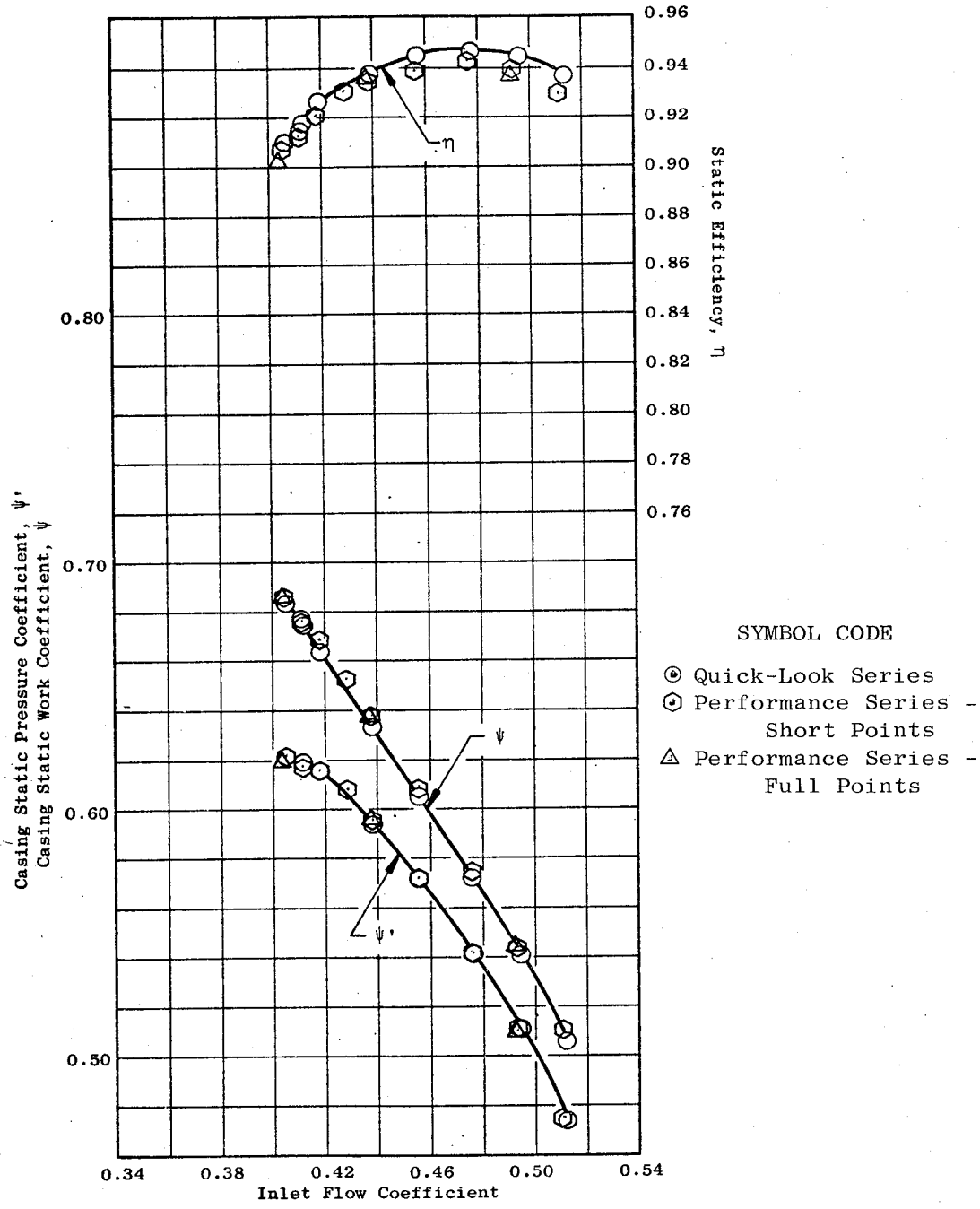

Figure 34 Overall Performance of the Baseline Configuration Based on Casing Static Pressure

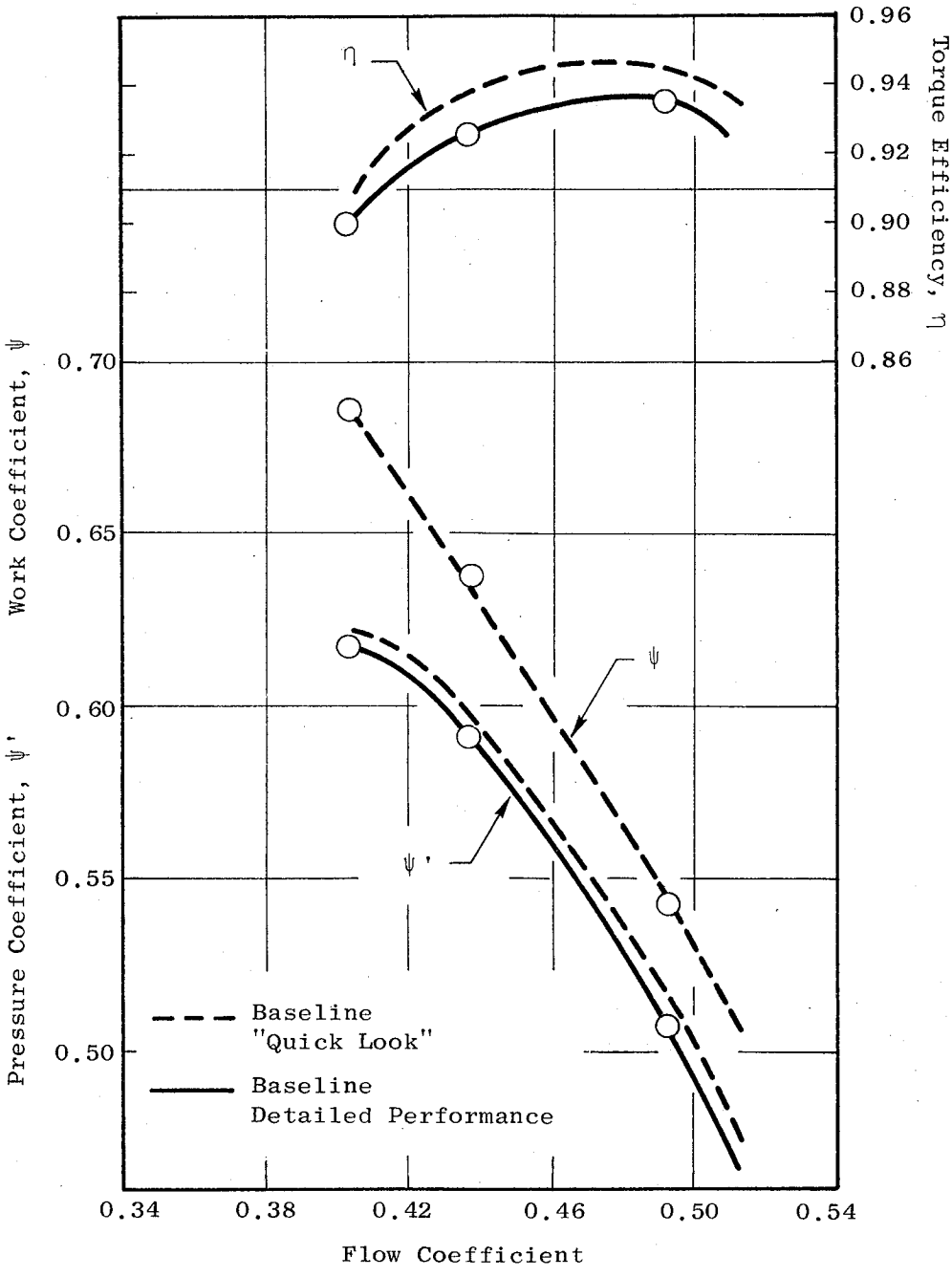

Figure 35 Overall Performance of the Baseline Configuration, Based on Mass-Averaged Total Pressure

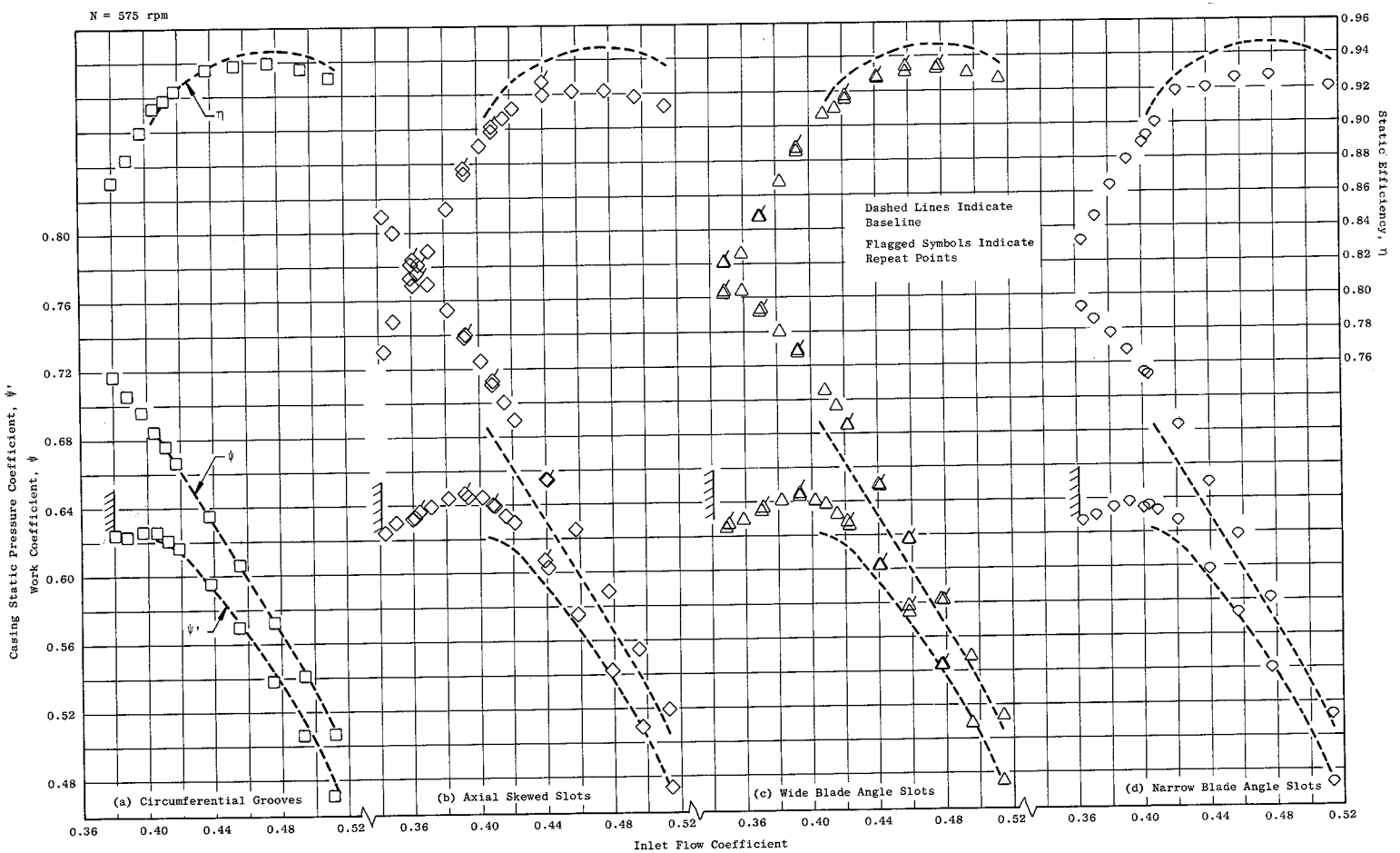

Figure 36 Overall Performance of the Various Casing Treatment Configurations Compared with the Overall Baseline Configuration Performance, Based on Casing Static Pressure

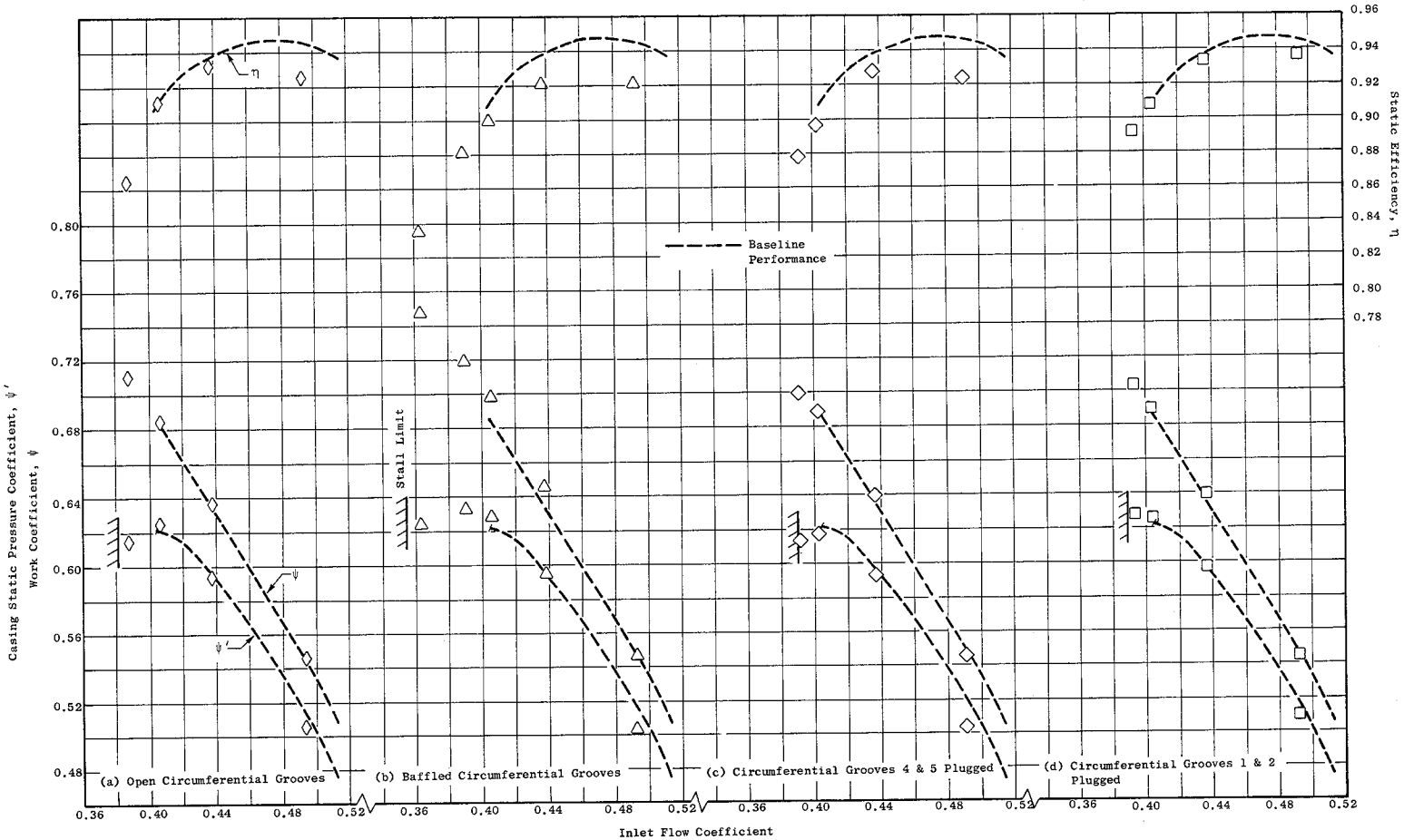

Figure 37 Overall Performance of Various Circumferential Groove Casing Treatment Configurations Compared with the Baseline Configuration Overall Performance, Based on Casing Static Pressure

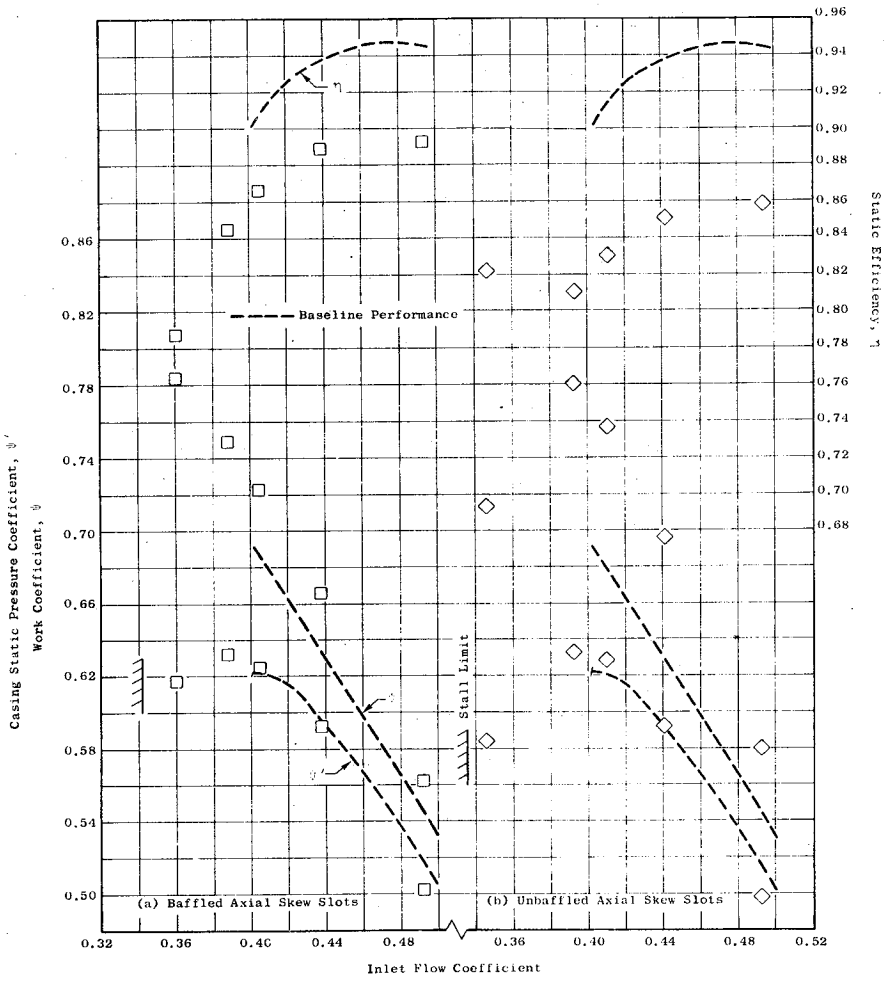

Figure 38 Overall Performance of Two Axial-Skewed Slot Casing Treatments Compared with Overall Baseline Configuration Performance, Based on Casing Static Pressure

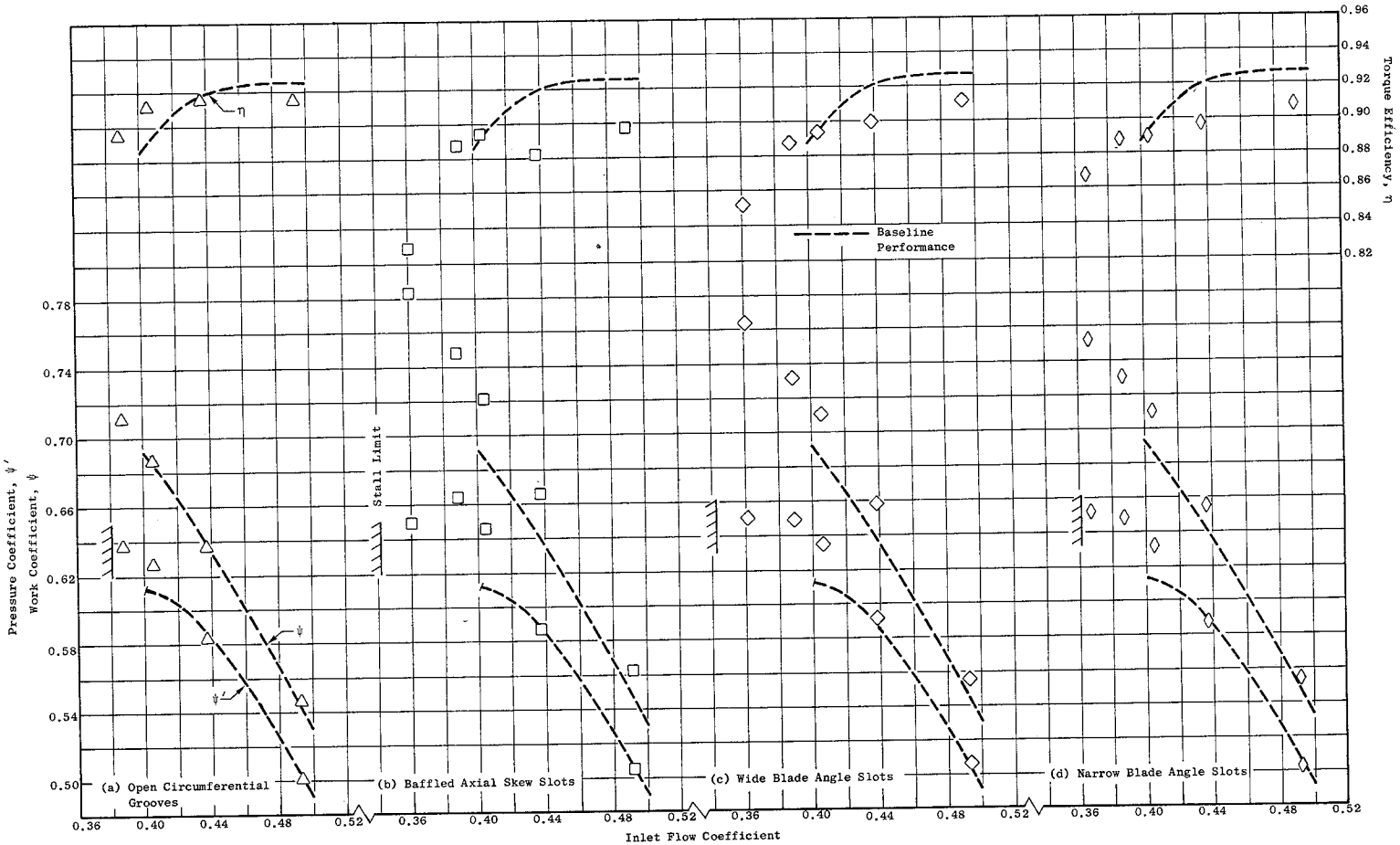

Figure 39 Overall Performance of Various Casing Treatment Configurations Compared with the Baseline Configuration Performance, Based on Mass-Averaged Total Pressures

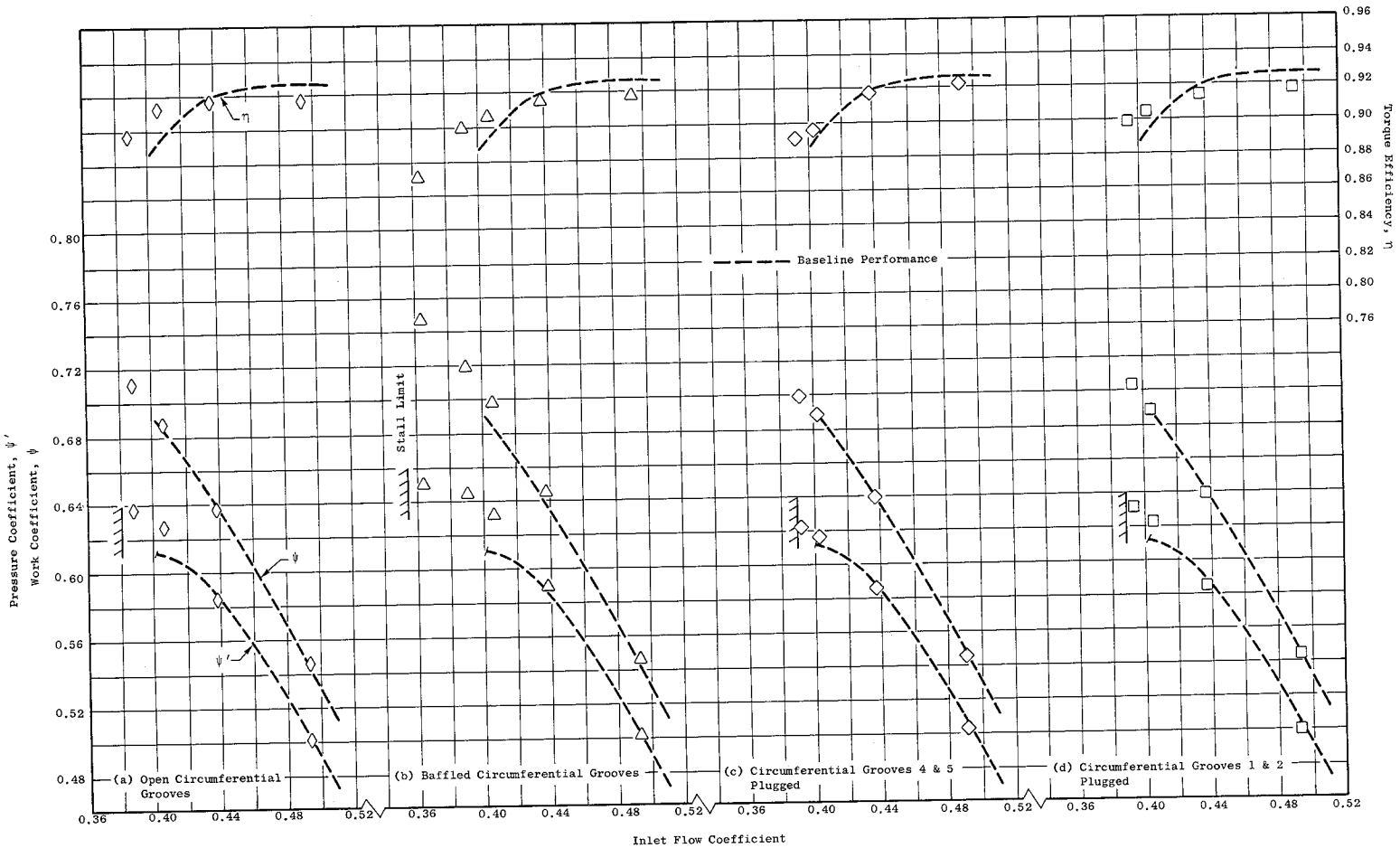

Figure 40 Overall Performance of Various Circumferential Groove Casing Treatment Configurations Compared with the Baseline Configuration Performance, Based on Mass-Averaged Total Pressure

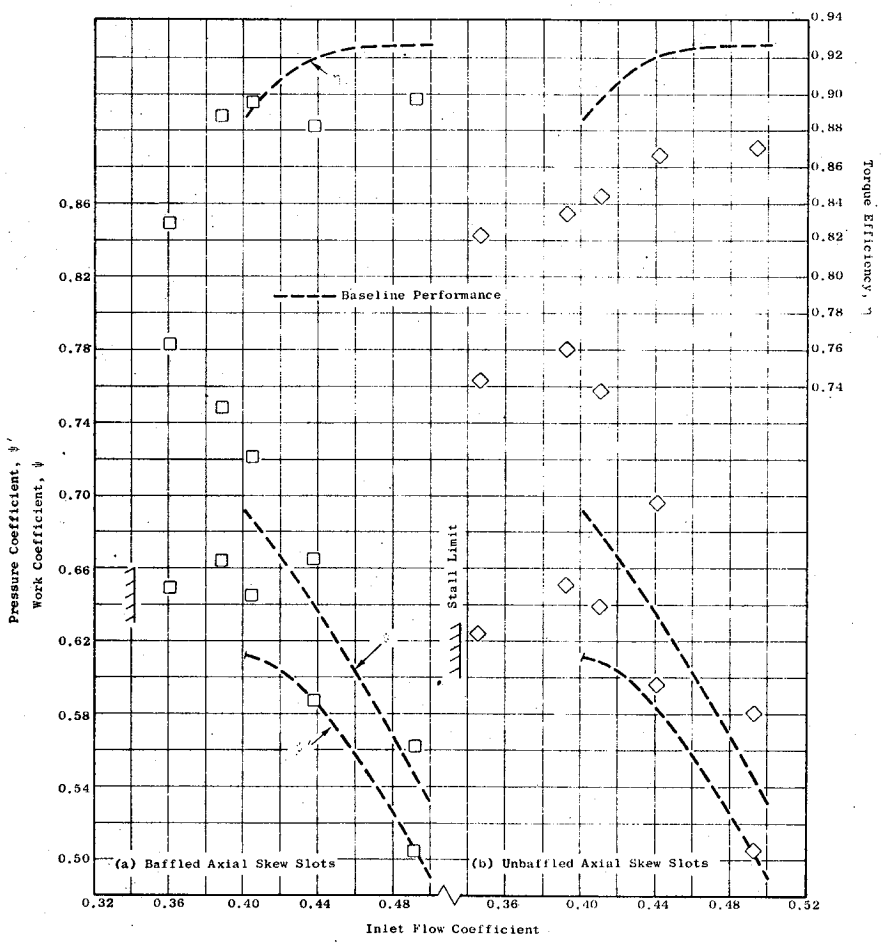

Figure 41 Overall Performance of the Two Axial-Skewed Slot Casing Treatments Compared with Detailed Baseline Configuration Performance, Based on Mass-Averaged Total Pressure

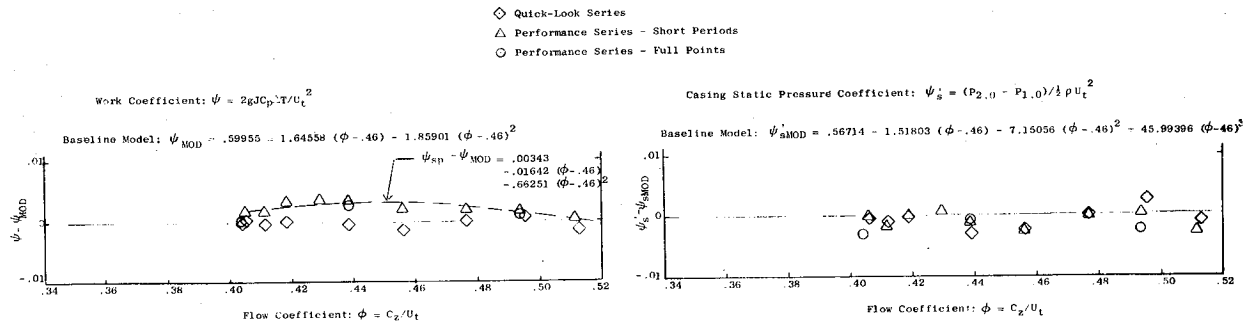

a. Baseline Configuration

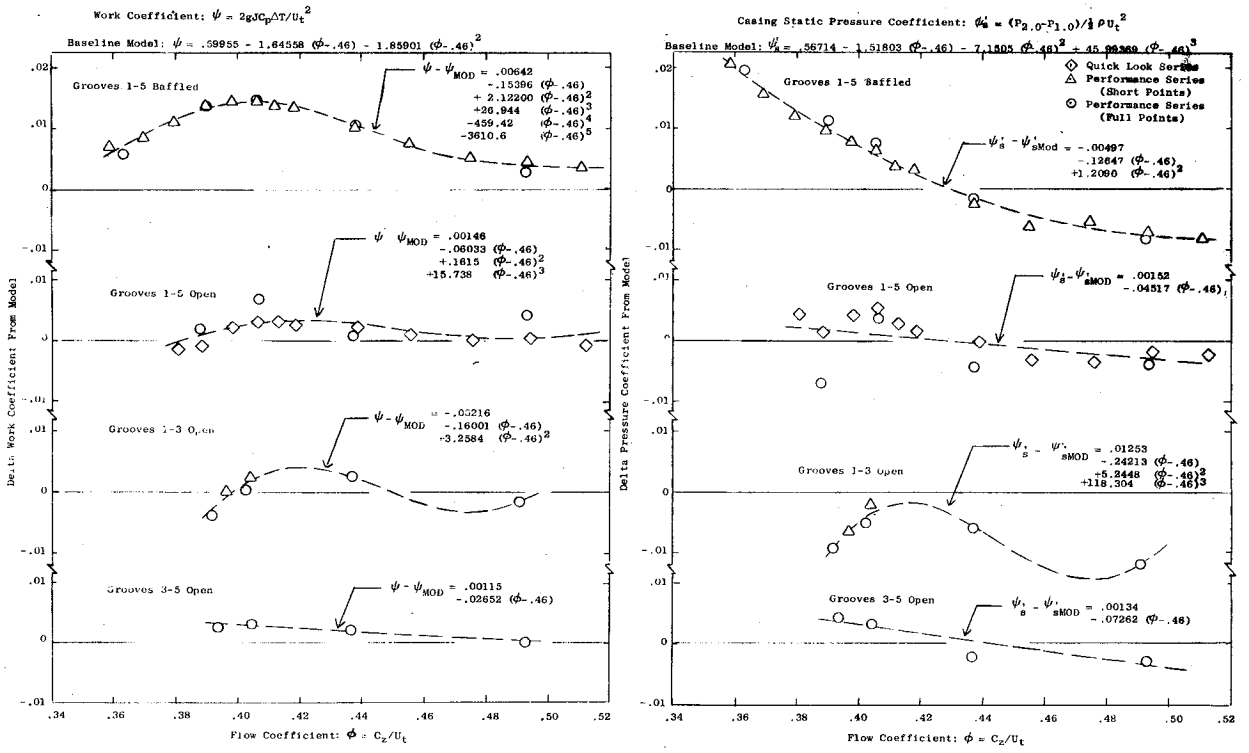

b. Four Circumferential Groove Configurations

Figure 42 Statistical Analysis of Experimental Data for Internal Consistency and Trends between Configurations

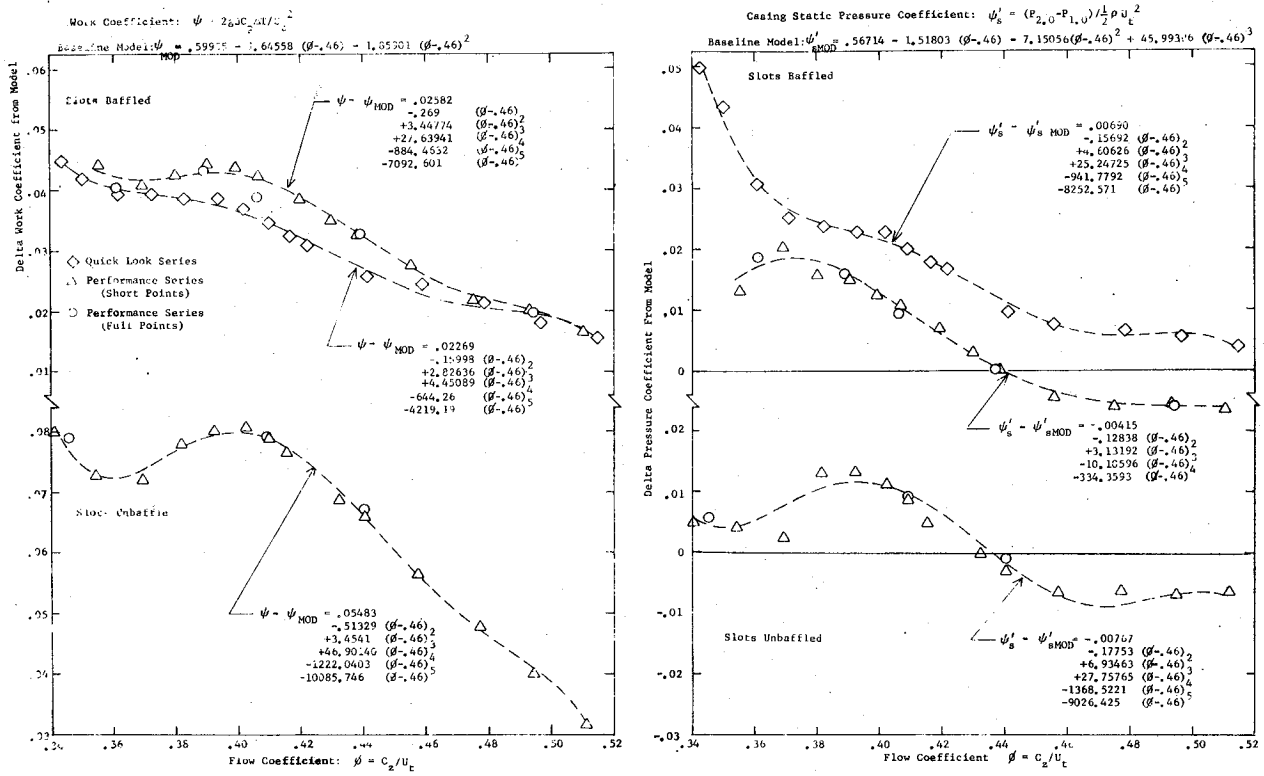

c. Two Axial-Skewed Slot Configurations

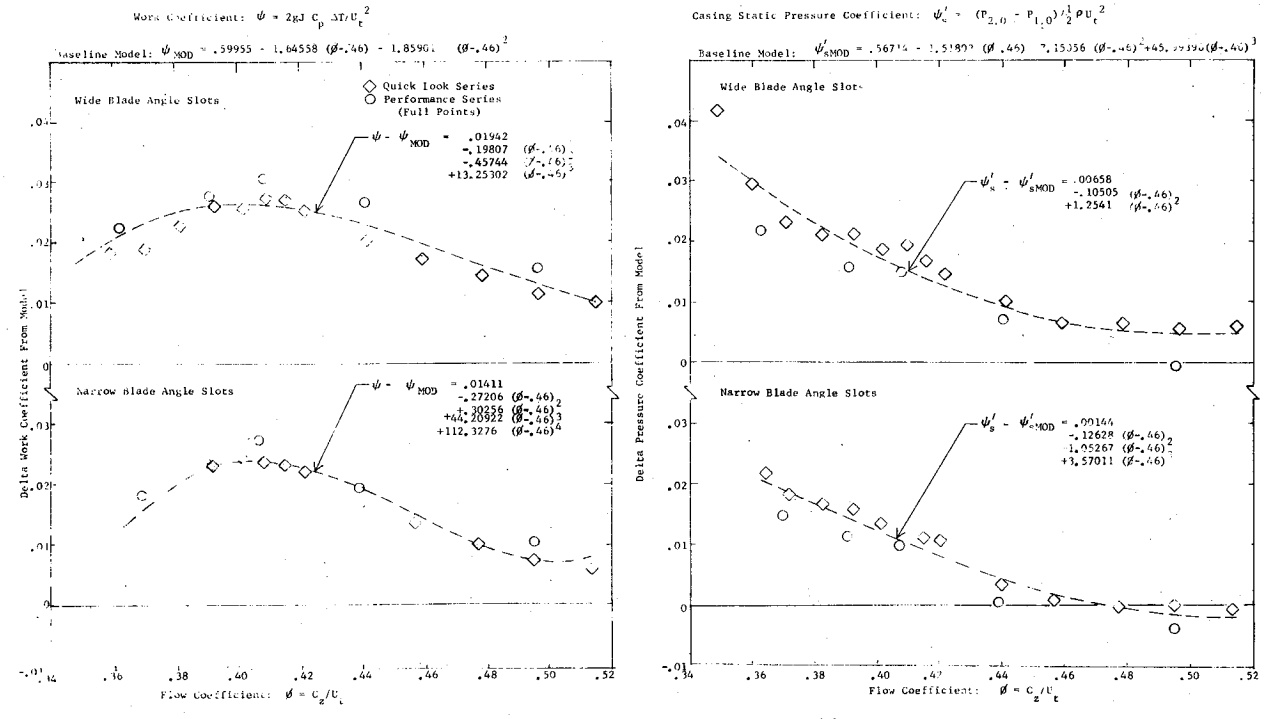

d. Two Blade Angle Slot Configurations

Figure 42 (Concluded)

FOLDOUT FRAME

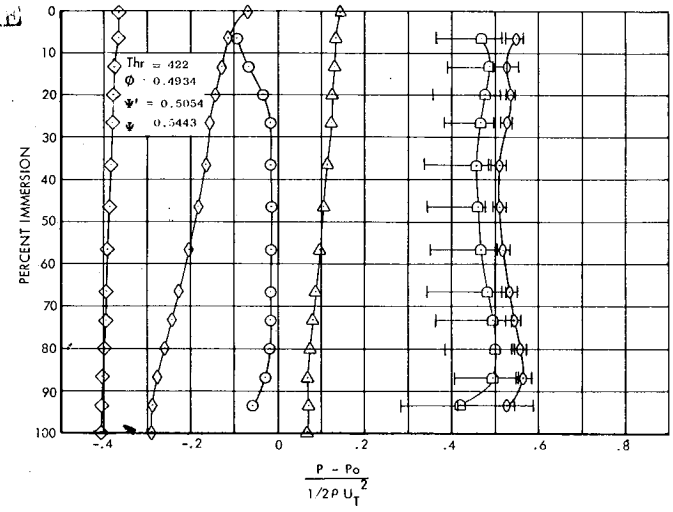

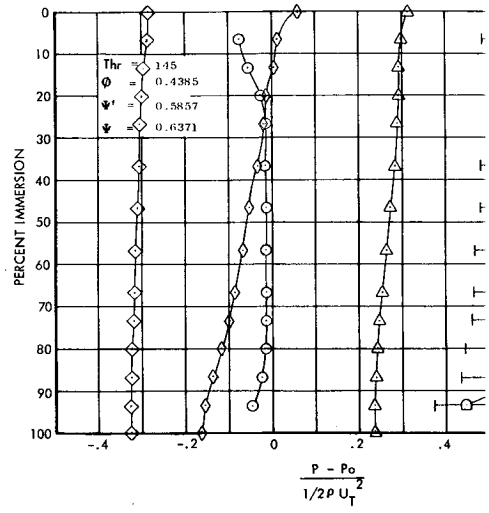

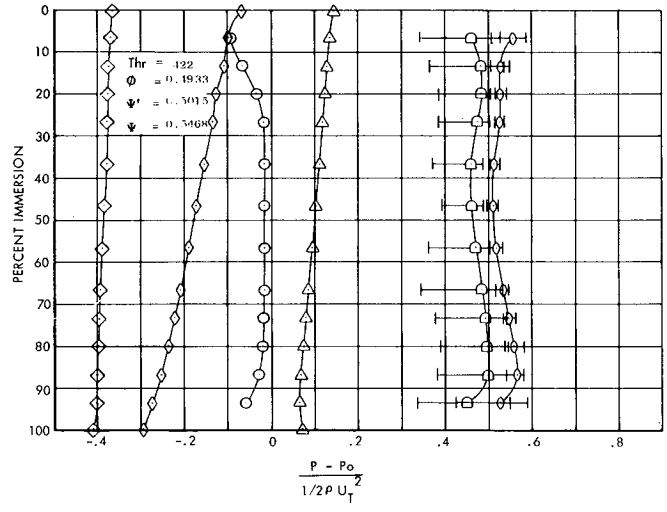

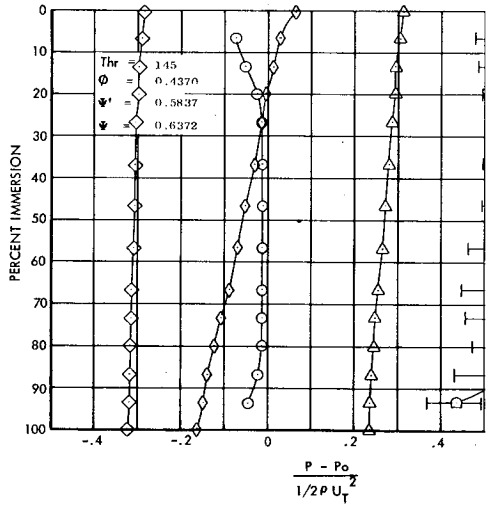

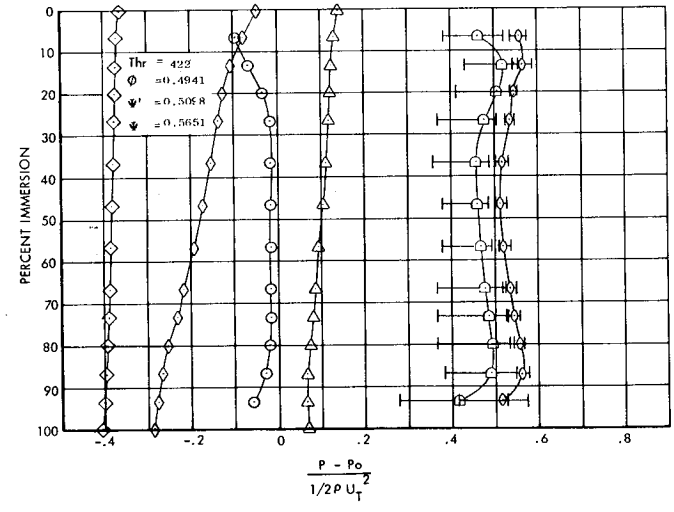

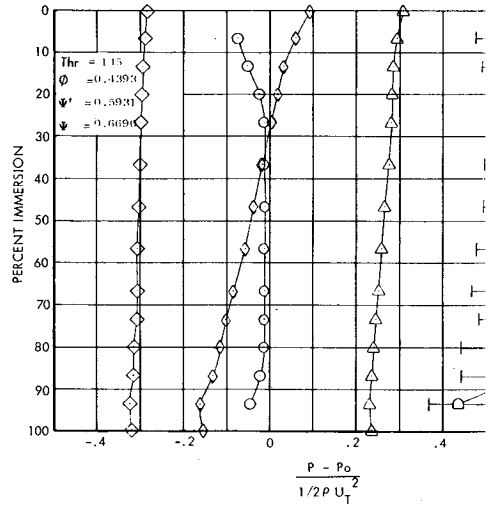

FOLDOUT FRAME

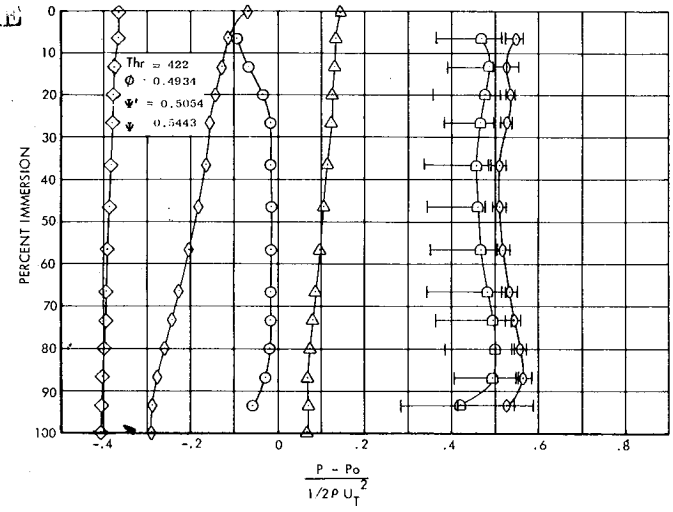

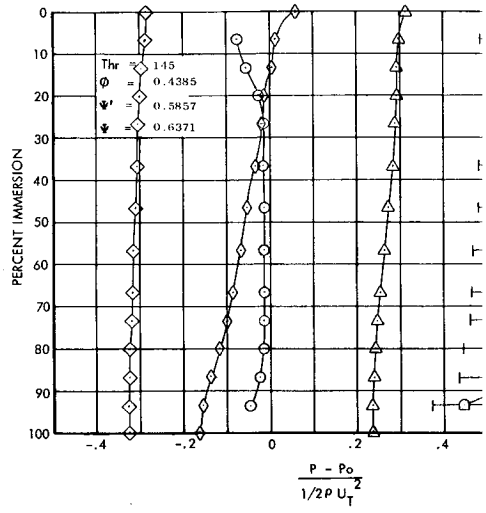

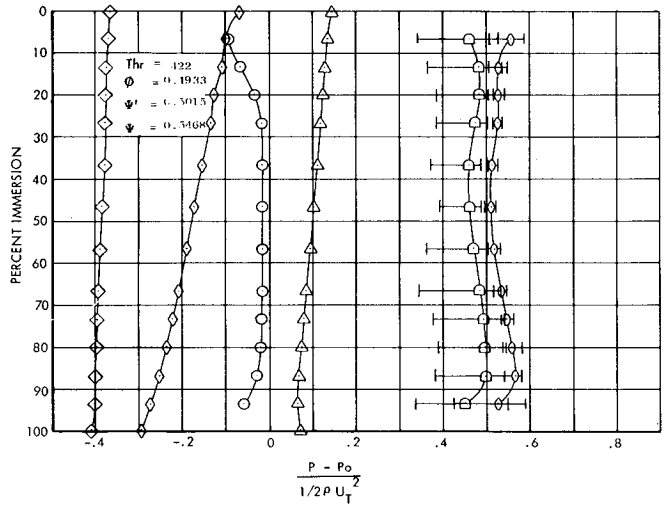

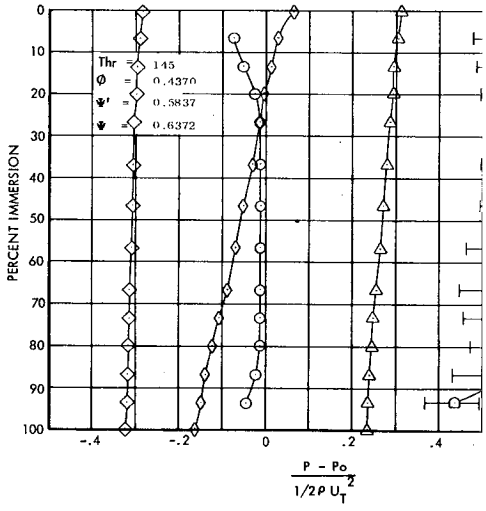

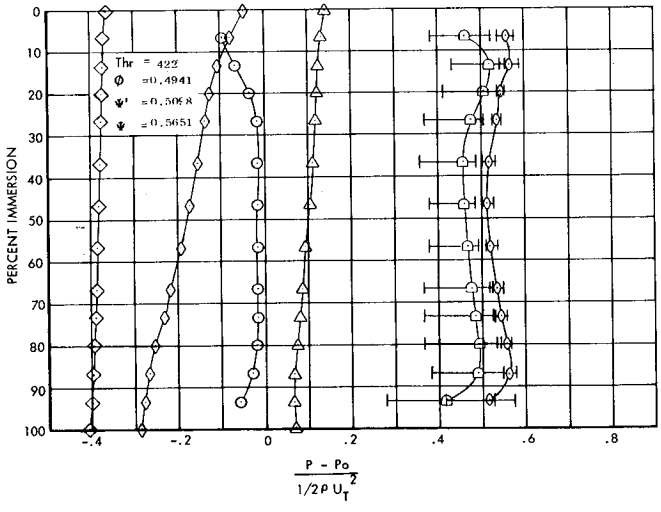

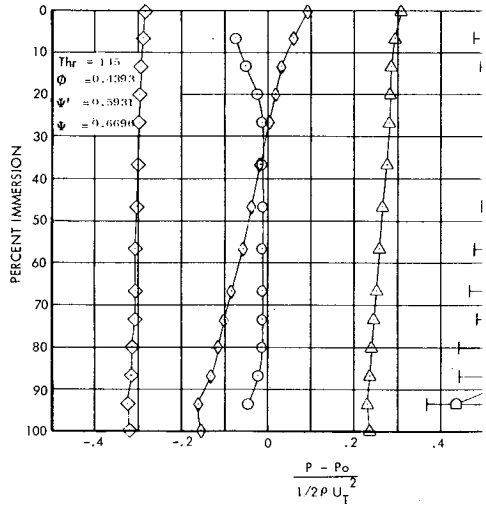

FOLDOUT FRAME

BASELINE CONFIGURATION

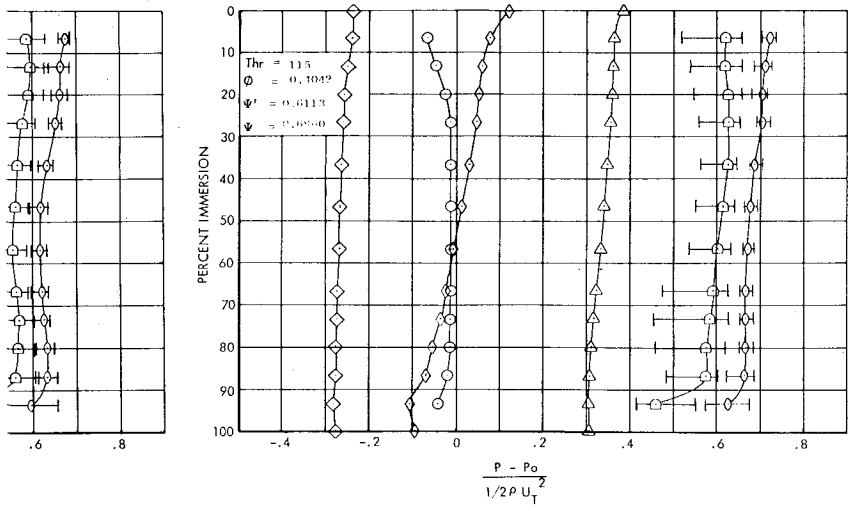

Note that horizontal line s
symbols for rotor exit and
pressure indicate range of
traversing of the movable s

CIRCUMFERENTIAL GROOVE TREATMENT

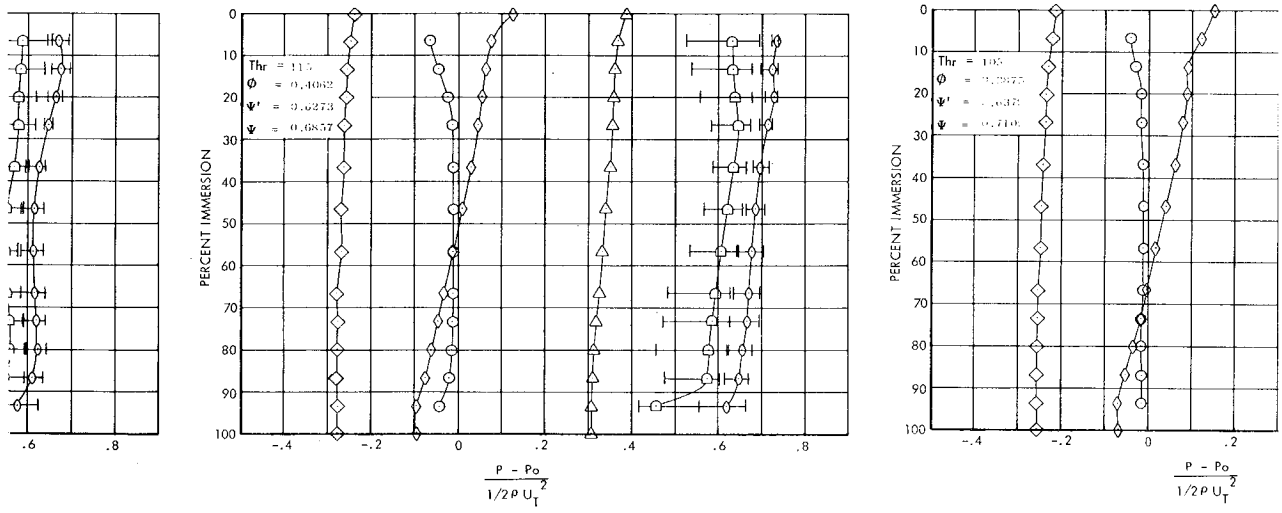

AXIAL-SKEWED SLOT TREATMENT

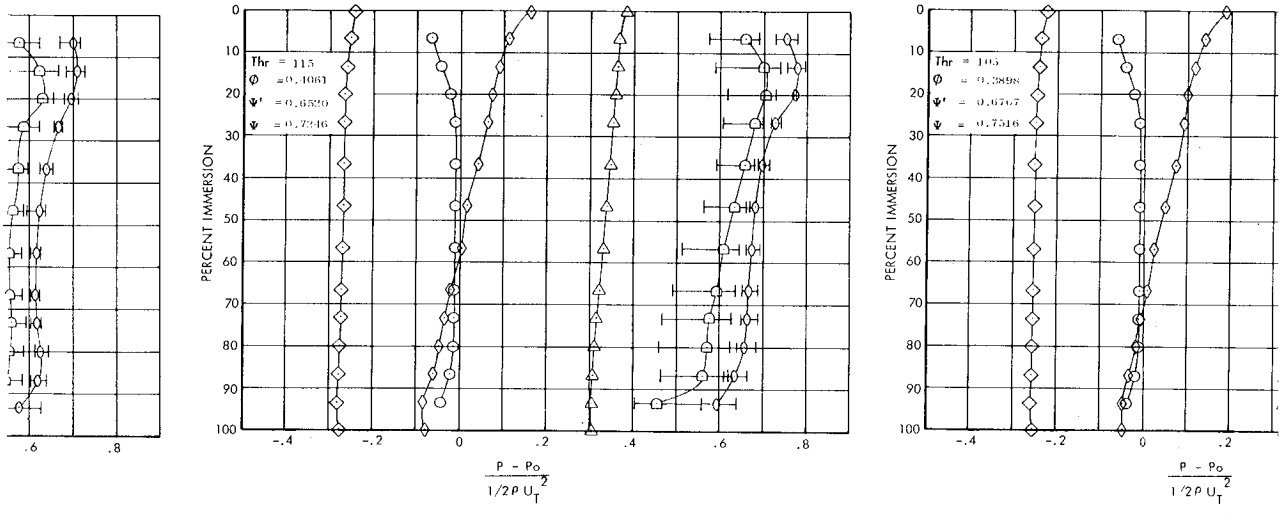

Figure 43

FOLDOUT FRAME

2

gments around
tator exit total
ata observed during
ator vane rings.

SYMBOL CODE

○ P_t	Plane 1.0 - Rotor Inlet
◇ P_s	
◊ P_t	Plane 1.5 - Rotor Exit
◊ P_s	
⌂ P_t	Plane 2.0 - Stator Exit
△ P_s	

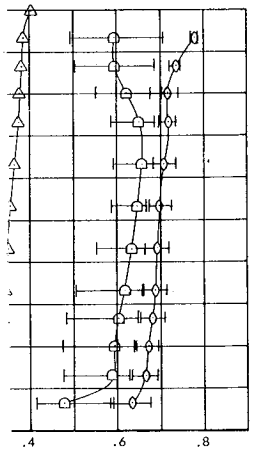

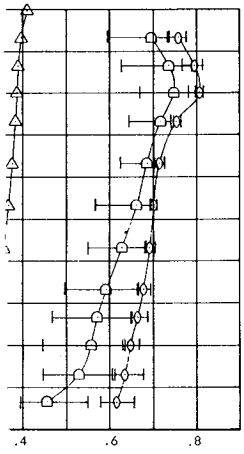

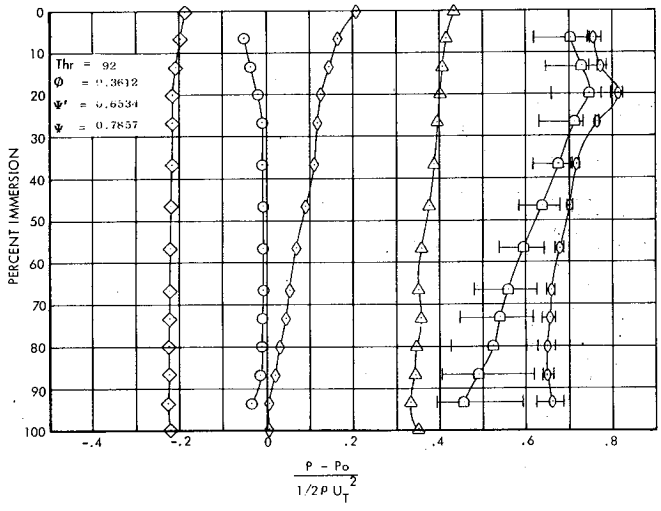

ıdial Profiles of Total and Static Pressure, Baseline,
.rcumferential Groove and Axial-Skewed Slot Configurations

FOLDOUT FRAME

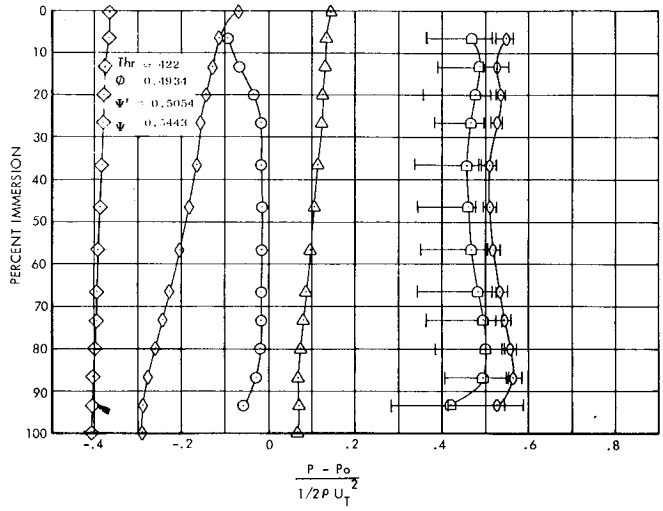

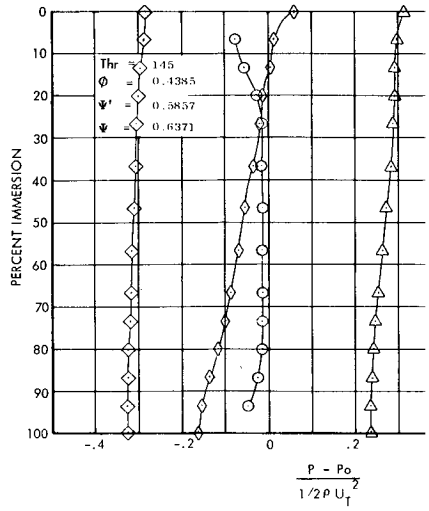

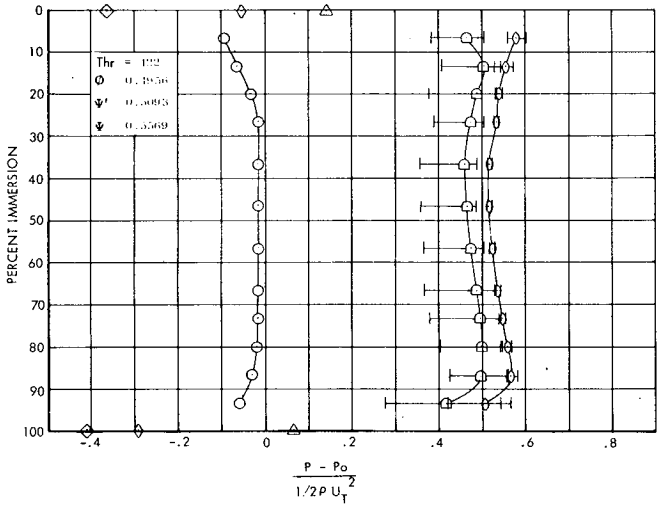

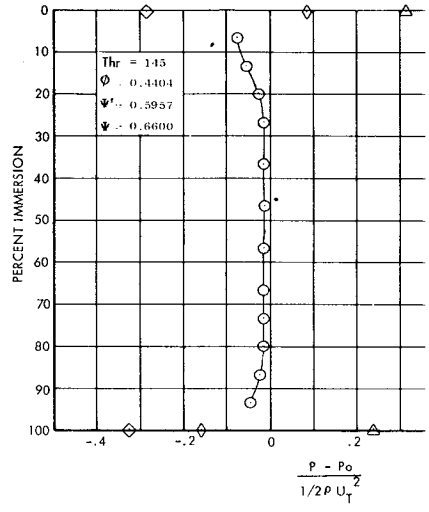

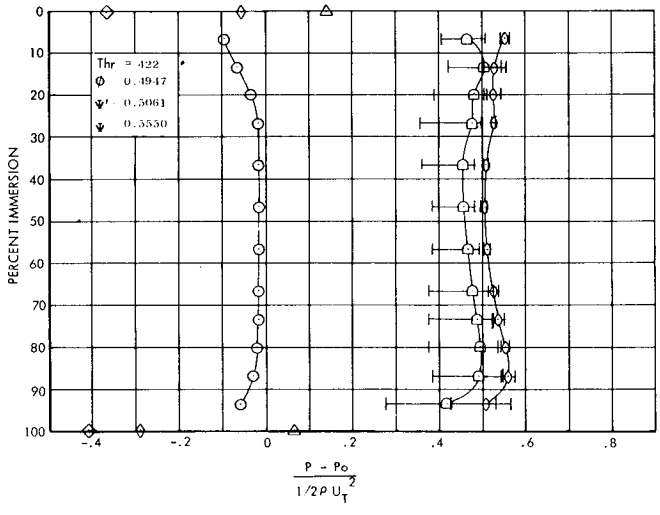

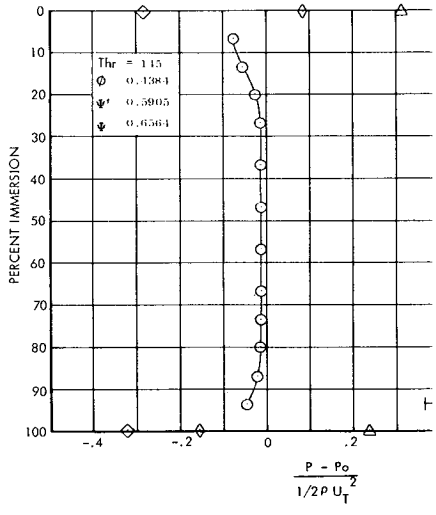

FOLDOUT FRAME

BASELINE CONFIGURATION

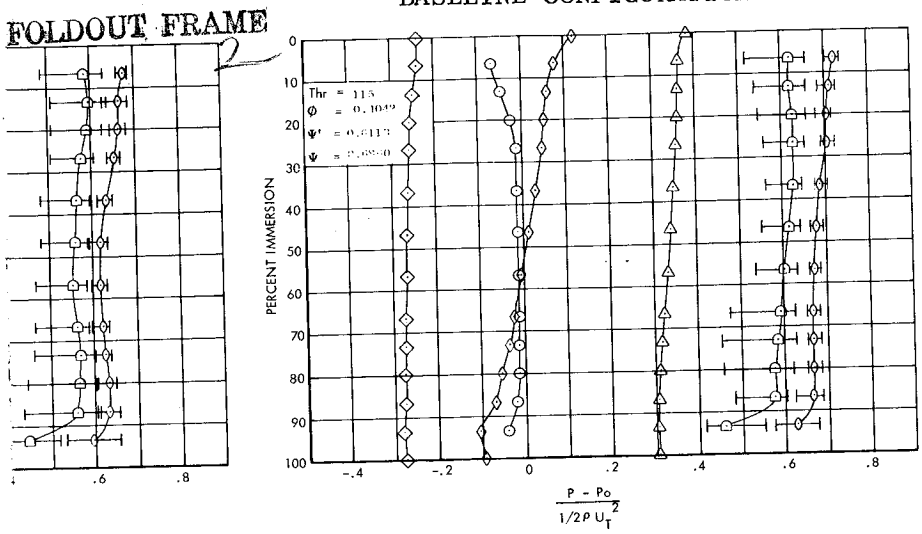

Note that horizont
symbols for rotor
pressure indicate
traversing of the

WIDE BLADE ANGLE SLOT TREATMENT

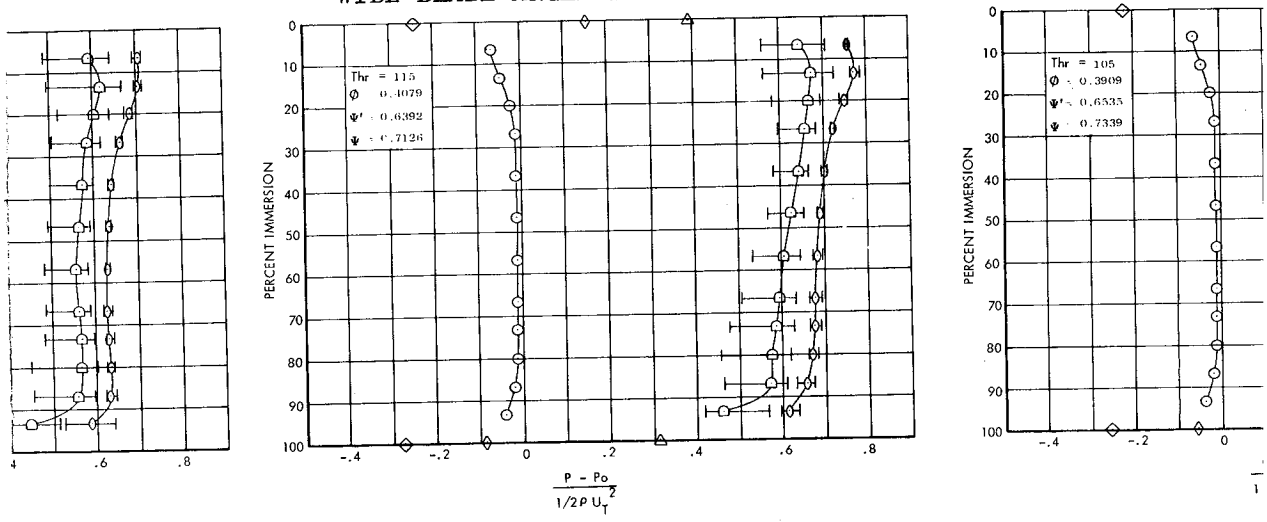

NARROW BLADE ANGLE SLOT TREATMENT

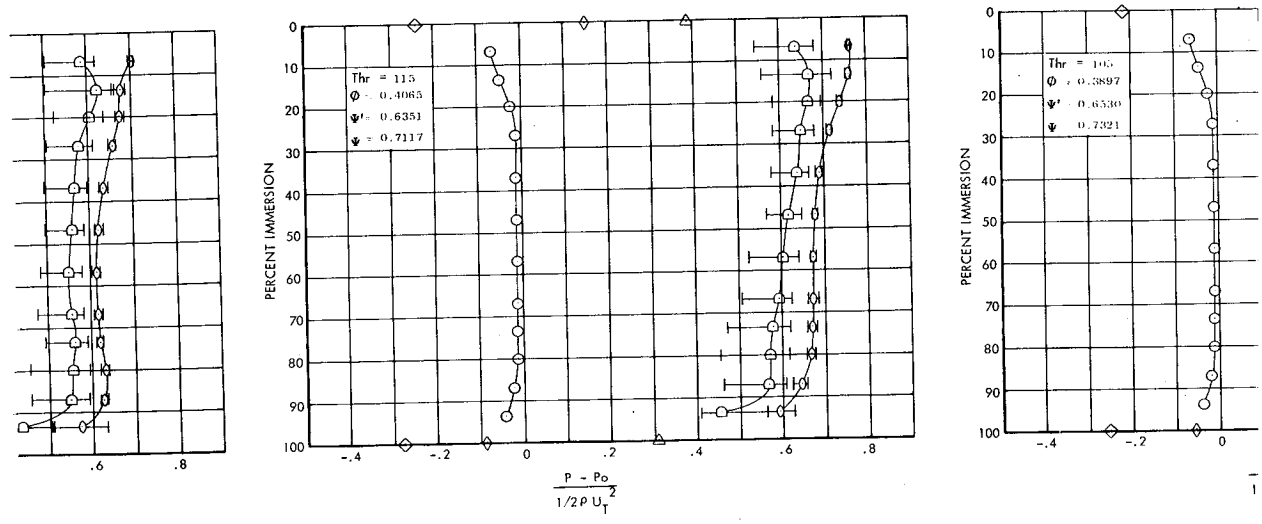

Figure 4

FOLDOUT FRAME

line segments around
it and stator exit total
nge of data observed during
vable stator vane rings.

SYMBOL CODE

○ P_t, ◇ P_s	Plane 1.0 - Rotor Inlet
◊ P_t, ◆ P_s	Plane 1.5 - Rotor Exit
⌂ P_t, △ P_s	Plane 2.0 - Stator Exit

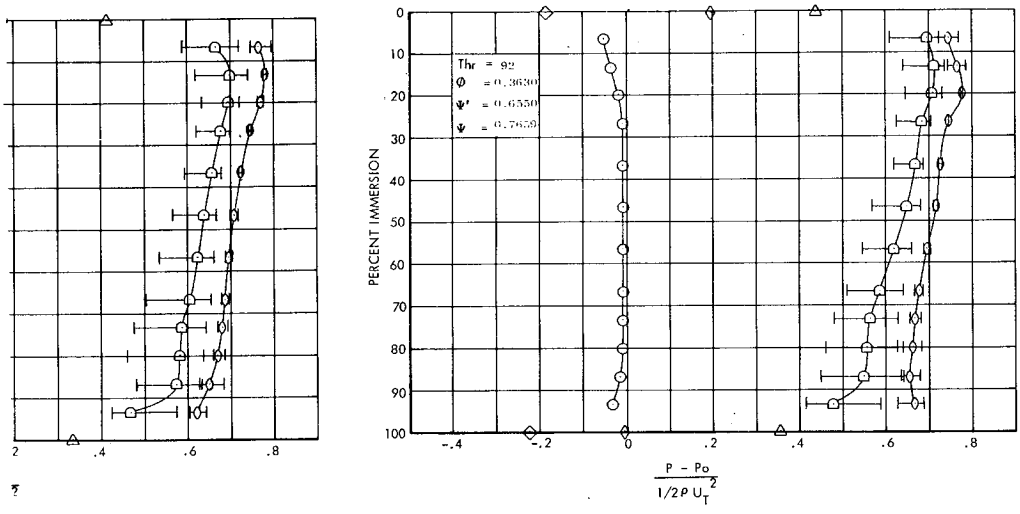

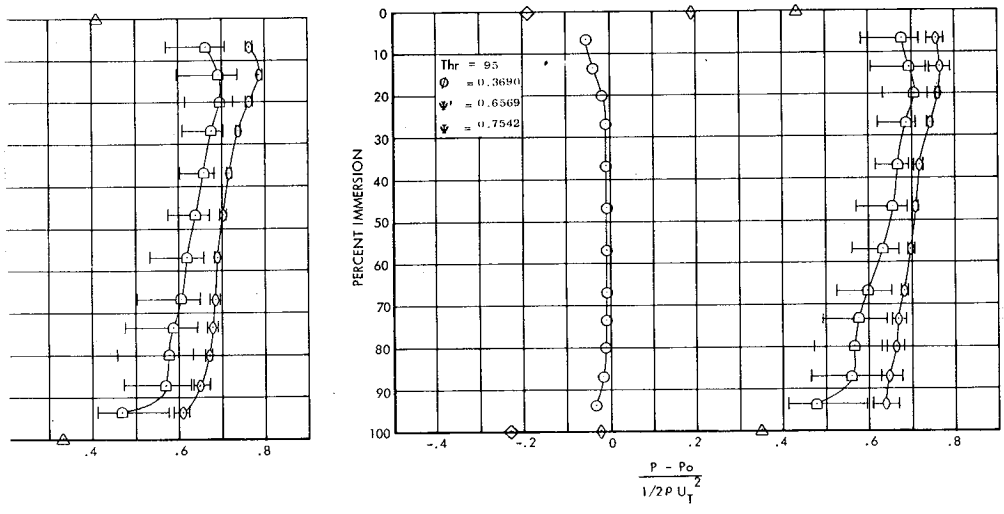

Radial Profiles of Total and Static Pressure; Baseline, Wide Blade Angle Slot and Narrow Blade Angle Slot Configurations

Preceding page blank

FOLDOUT FRAME

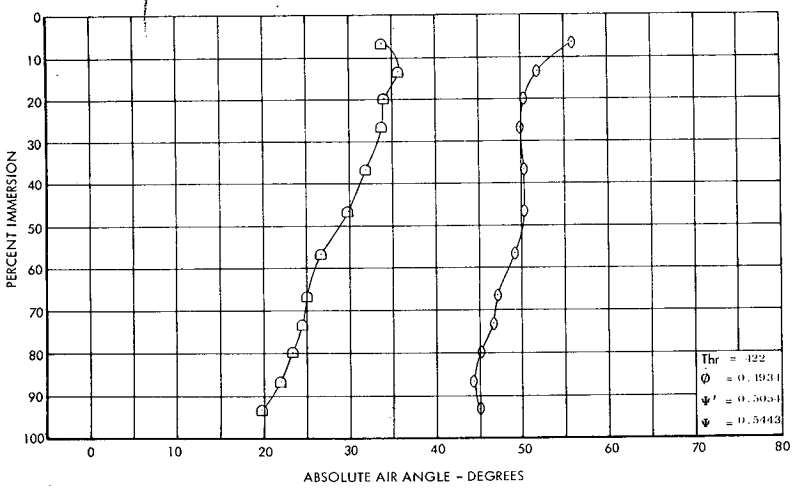

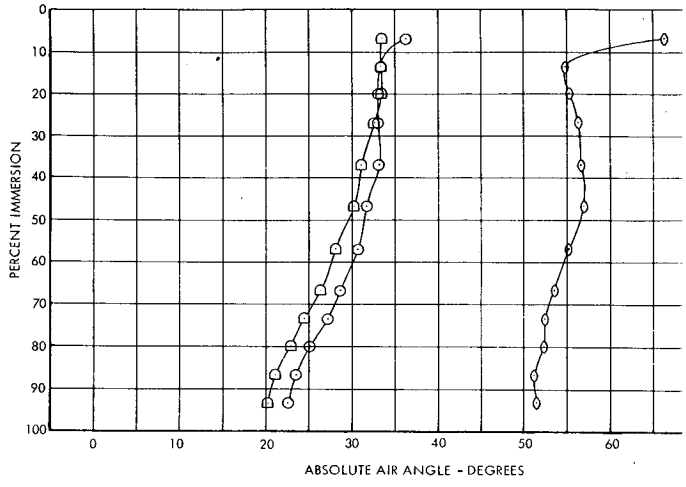

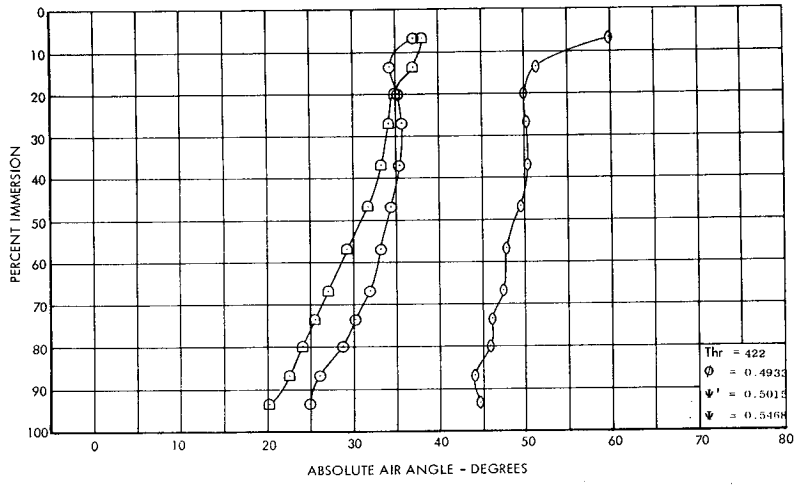

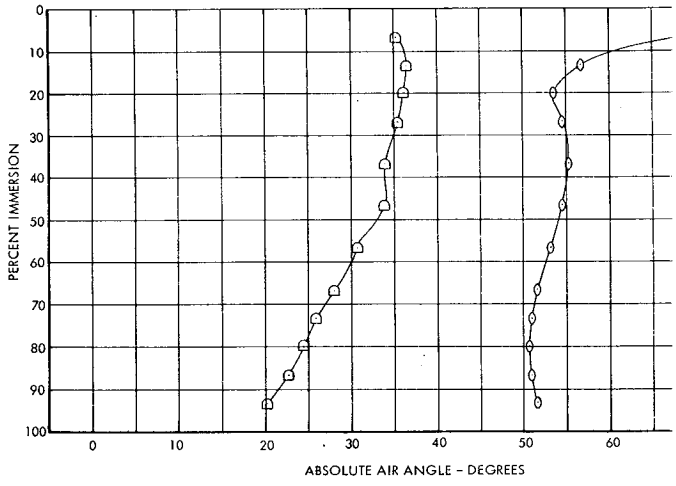

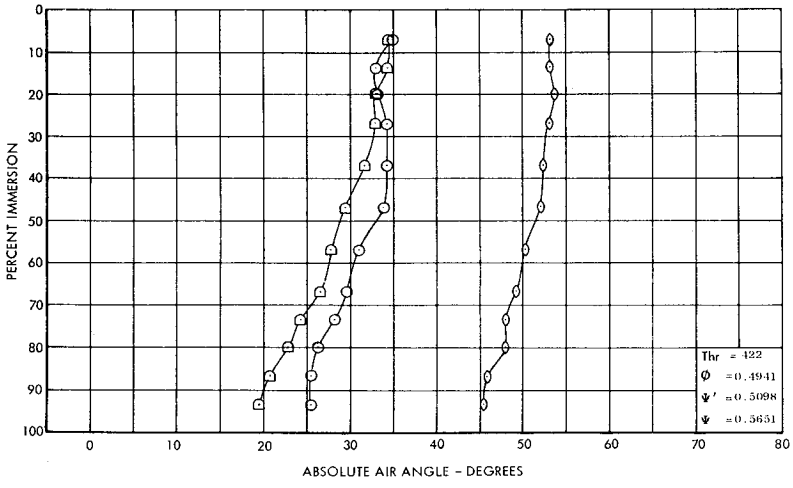

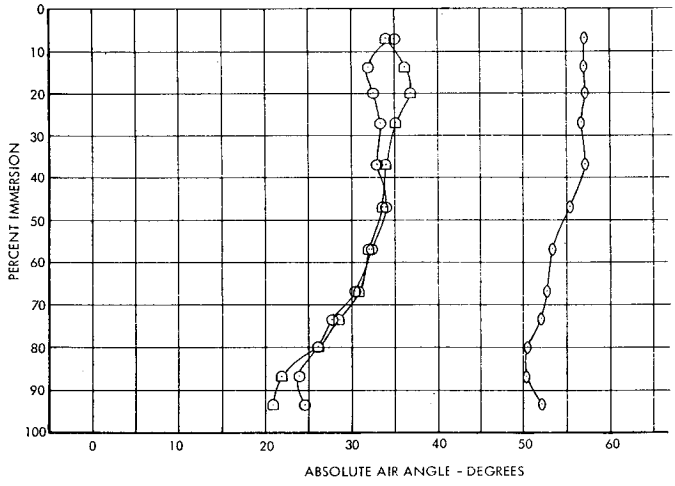

FOLDOUT FRAME

BASELINE CONFIGURATION

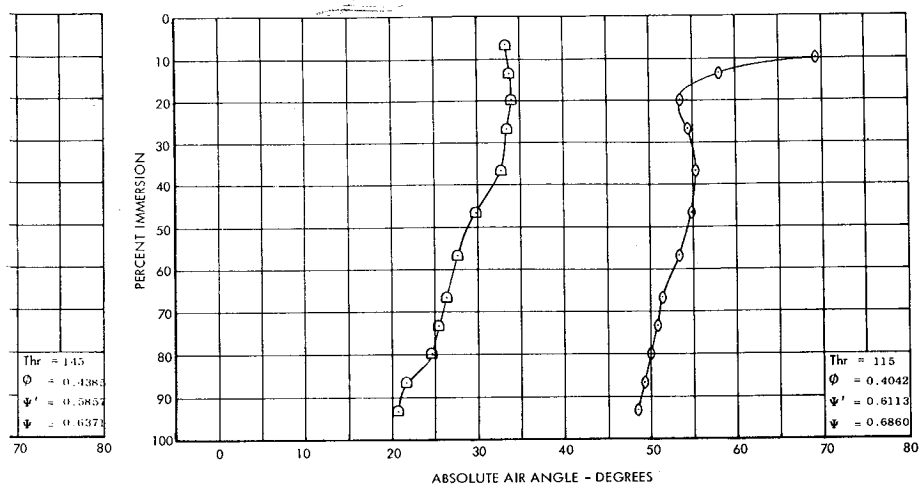

CIRCUMFERENTIAL GROOVE TREATMENT

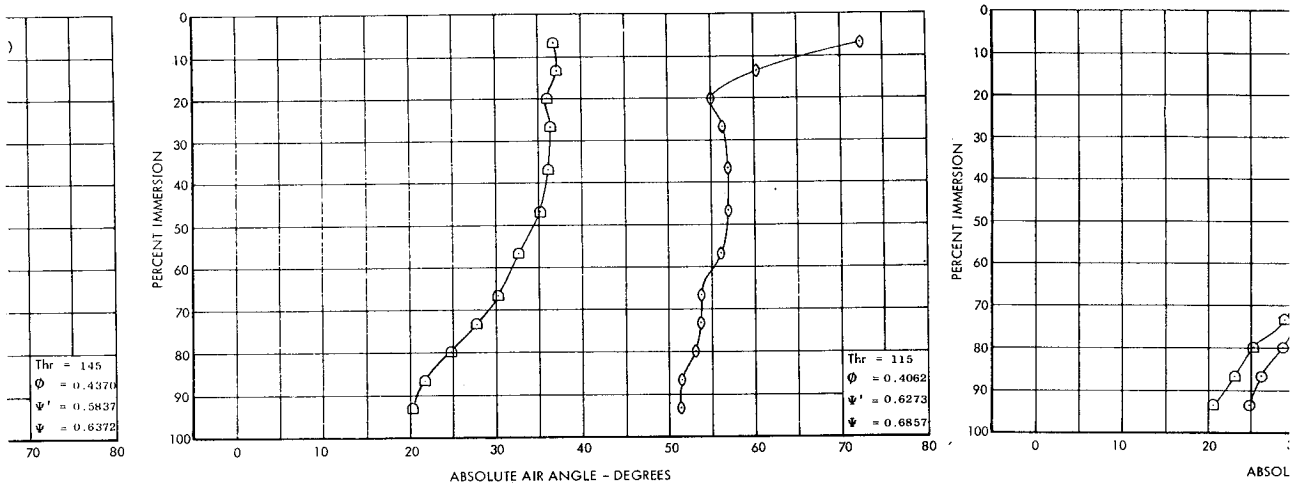

AXIAL-SKEWED SLOT TREATMENT

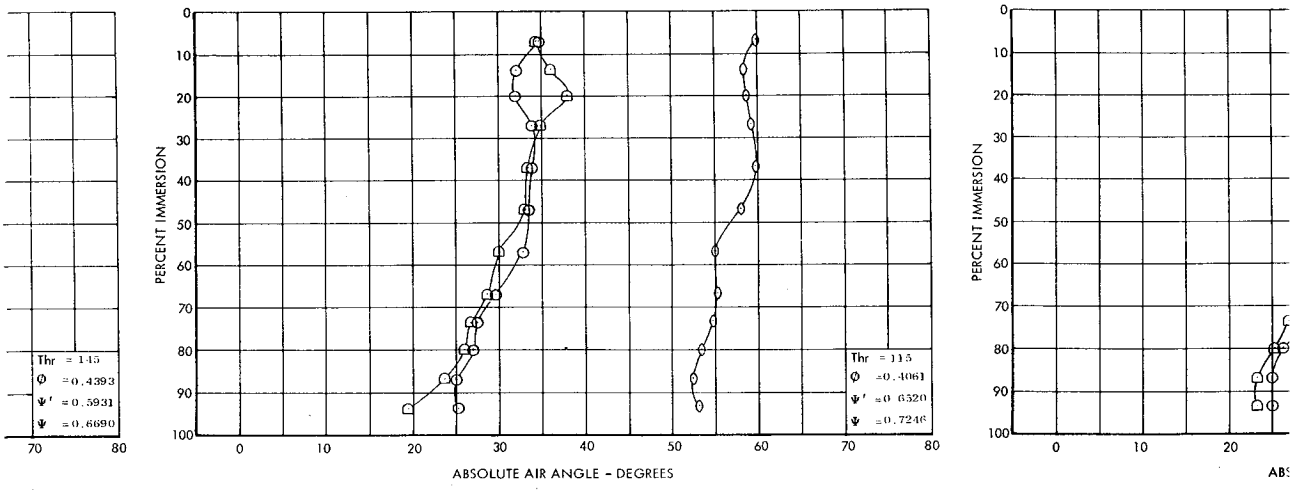

FOLDOUT FRAME

3

SYMBOL CODE

- O Plane 1.0 - Rotor Exit
- ◊ Plane 1.5 - Rotor Inlet
- Ω Plane 2.0 - Stator Exit

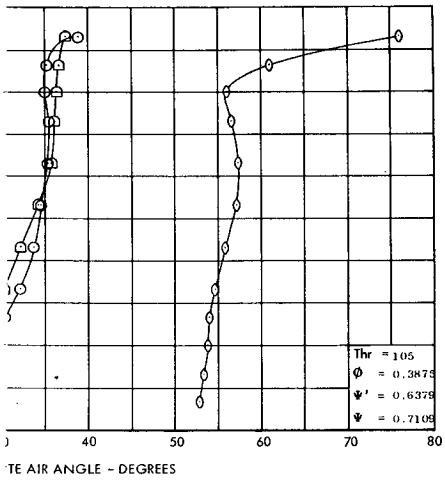

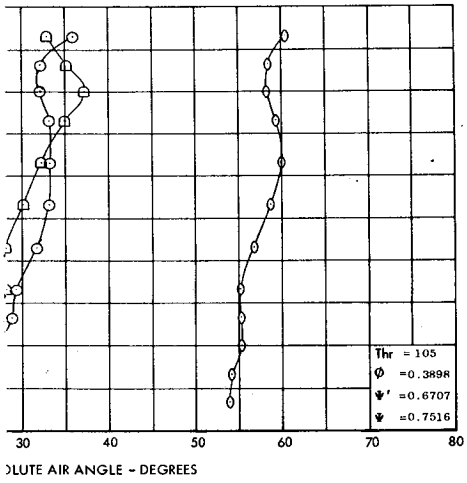

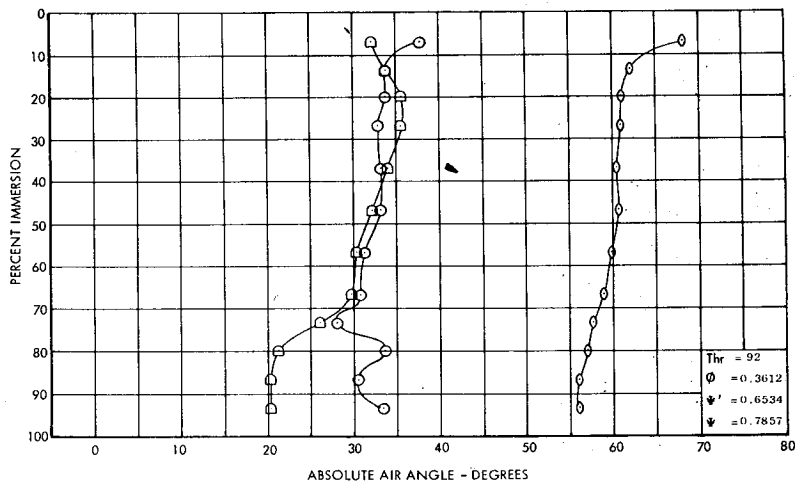

Figure 45 Radial Profiles of Absolute Flow Angle; Baseline, Circumferential Groove and Axial-Skewed Slot Configurations

Preceding page blank

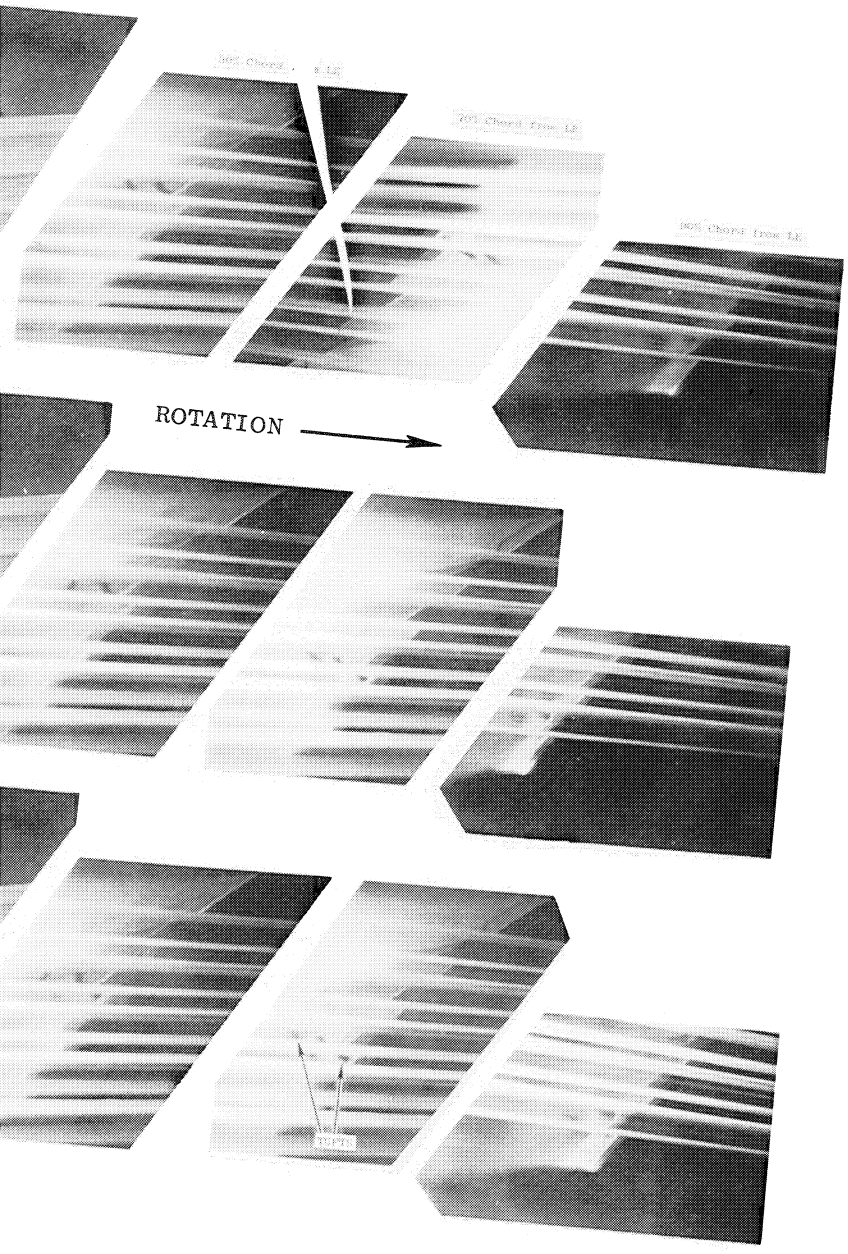

s Showing Tufts on Rotor Blades for Various
Circumferential Groove Casing Treatment
on

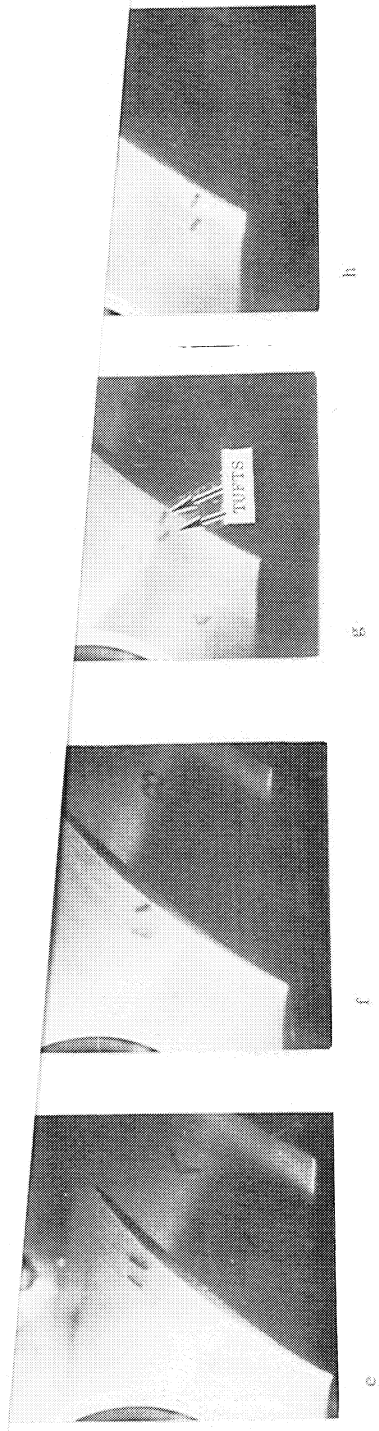

Figure 46 Photographs Showing Tufts on Rotor Blades for Various Throttles, Baseline Window (Plain Window) Configuration

Figure 46 (Concluded)

This page is reproduced at the back of the report by a different reproduction method to provide better detail.

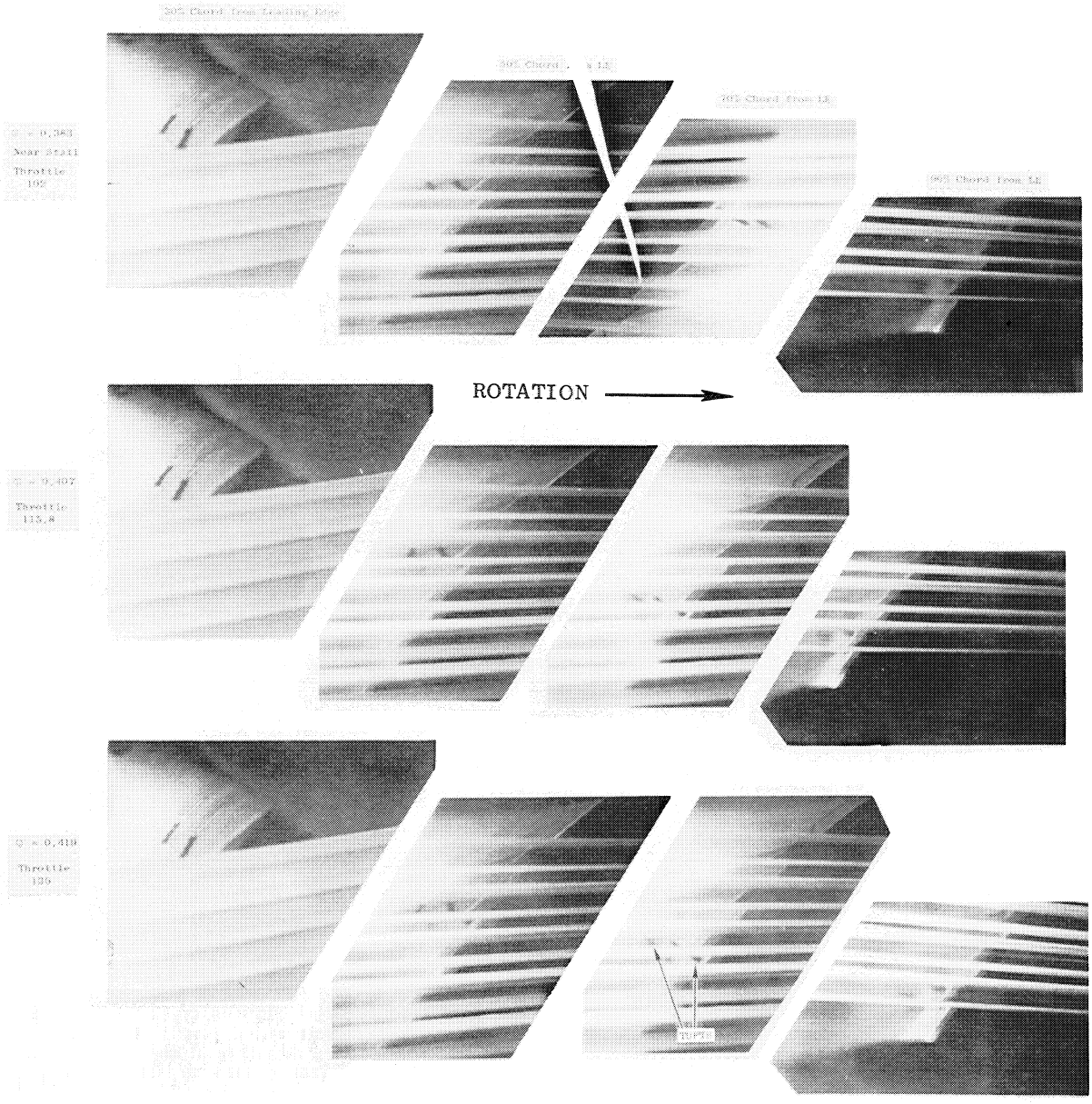

Figure 47 Photographs Showing Tufts on Rotor Blades for Various Throttles, Circumferential Groove Casing Treatment Configuration

This page is reproduced at the back of the report by a different reproduction method to provide better detail.

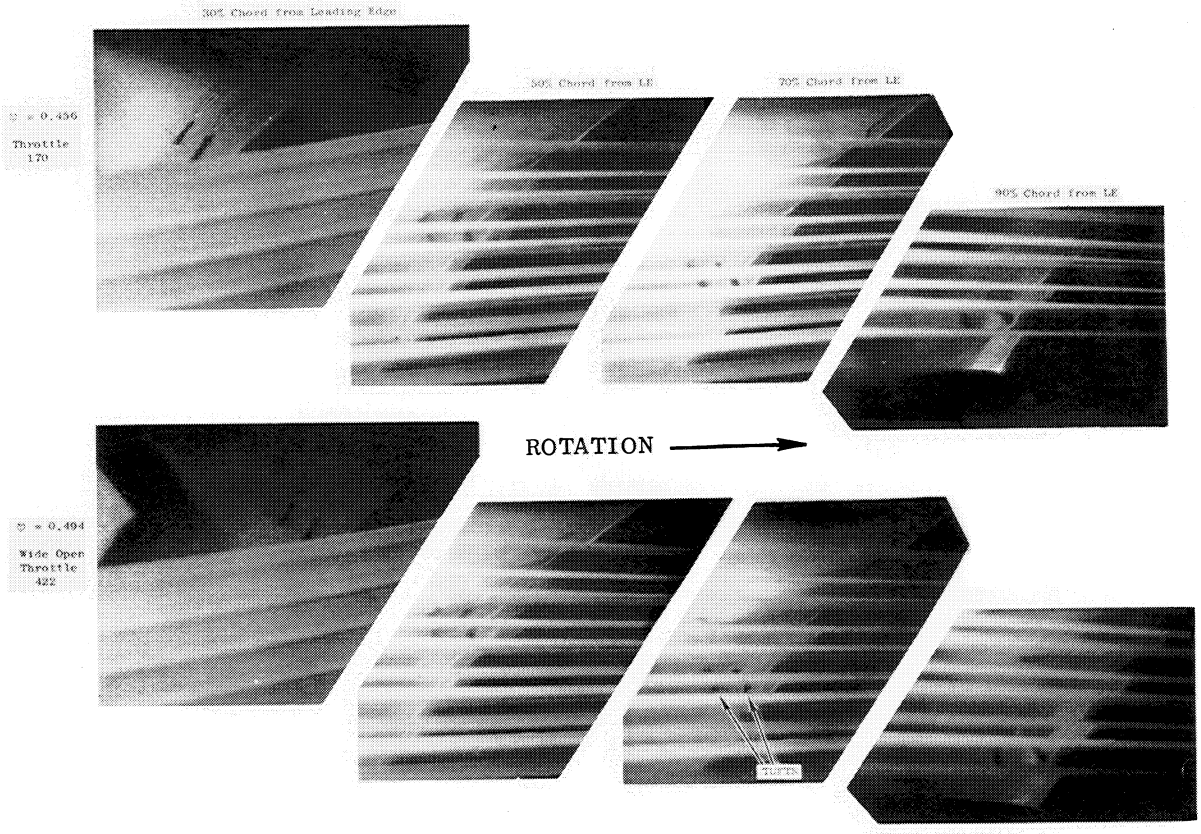

This page is reproduced at the back of the report by a different reproduction method to provide better detail.

Figure 47 (Concluded)

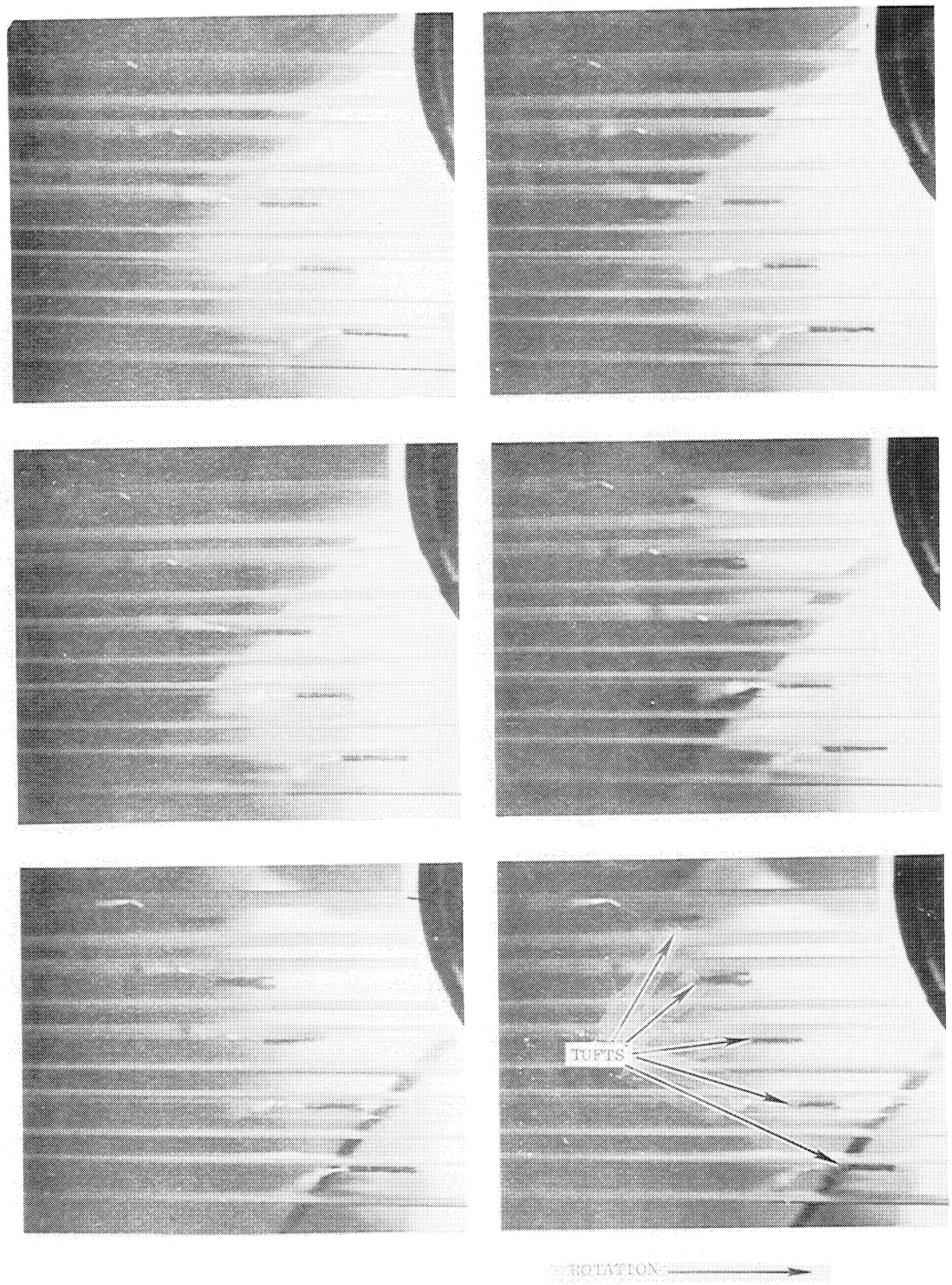

Figure 48 Photographs Showing Tufts in the Circumferential Grooves, Near Stall Throttle 102

This page is reproduced at the back of the report by a different reproduction method to provide better detail.

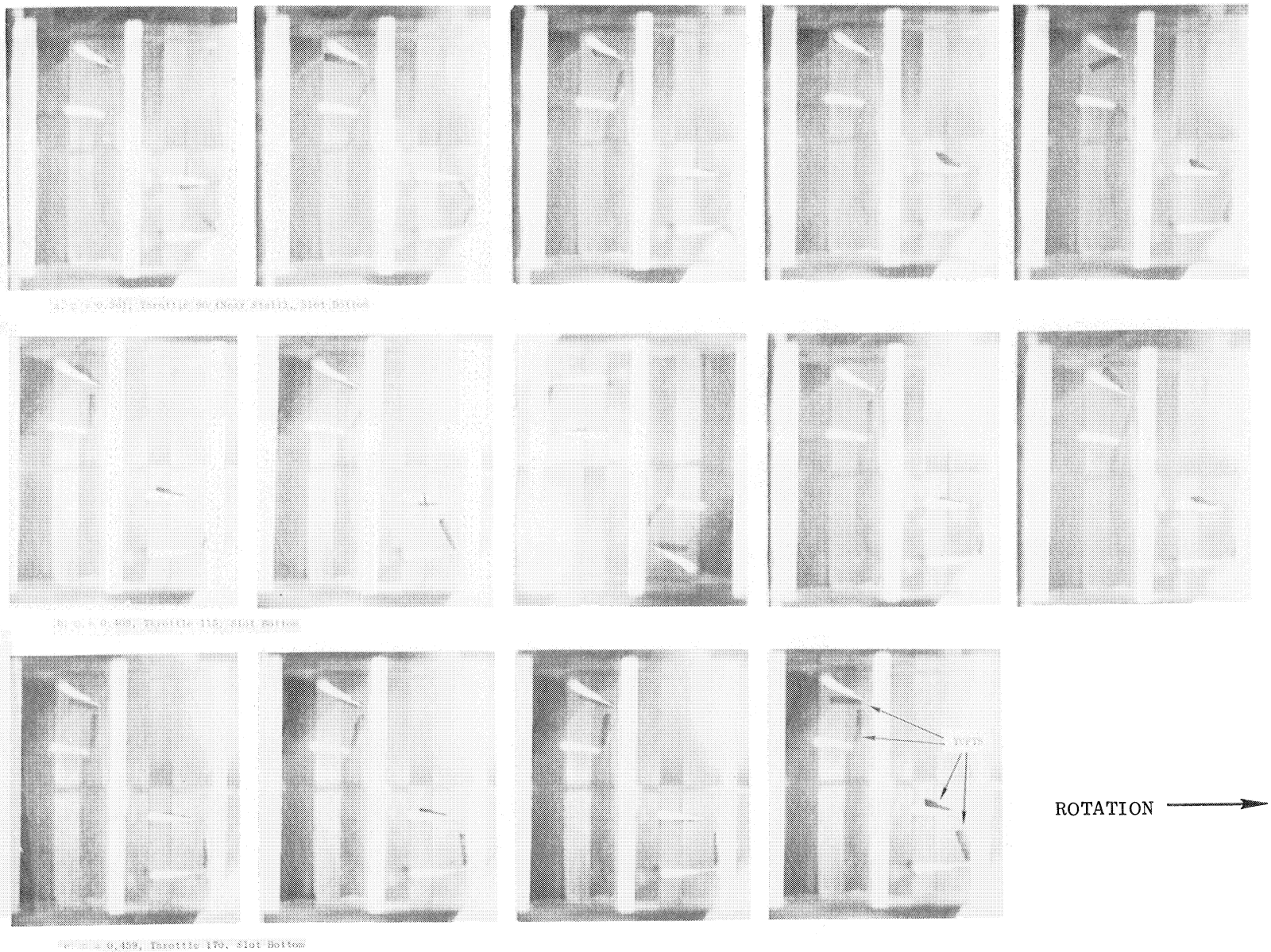

Figure 49 Photographs Showing Tufts Near Slot Bottom in the Axial-Skewed Slots

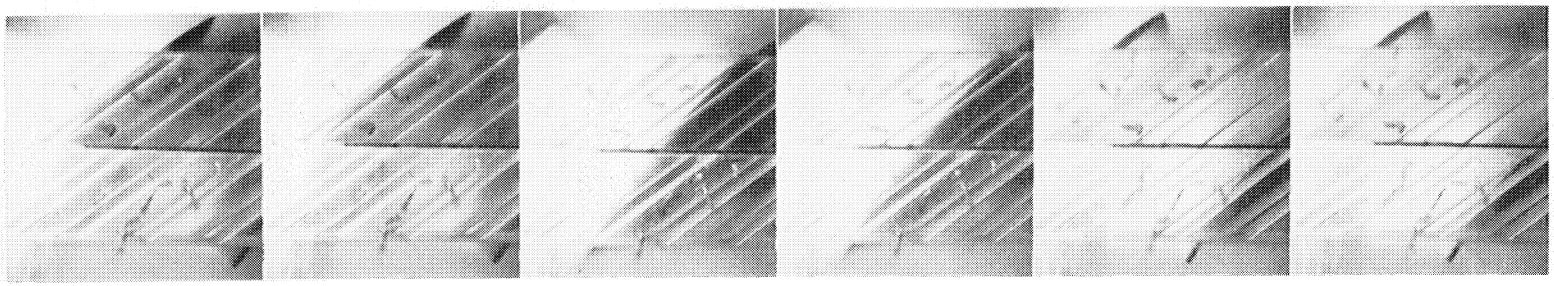

ROTATION →

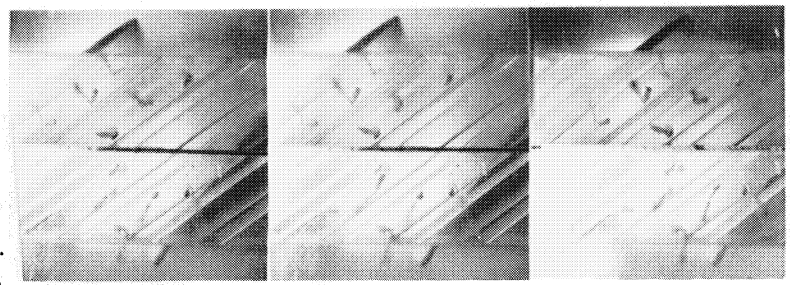

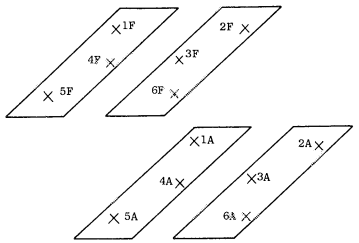

Schematic View of Slotted Tuft Locations

Figure 51 Photographs Showing Tufts in the Wide Blade Angle Slots Near Baseline Stall

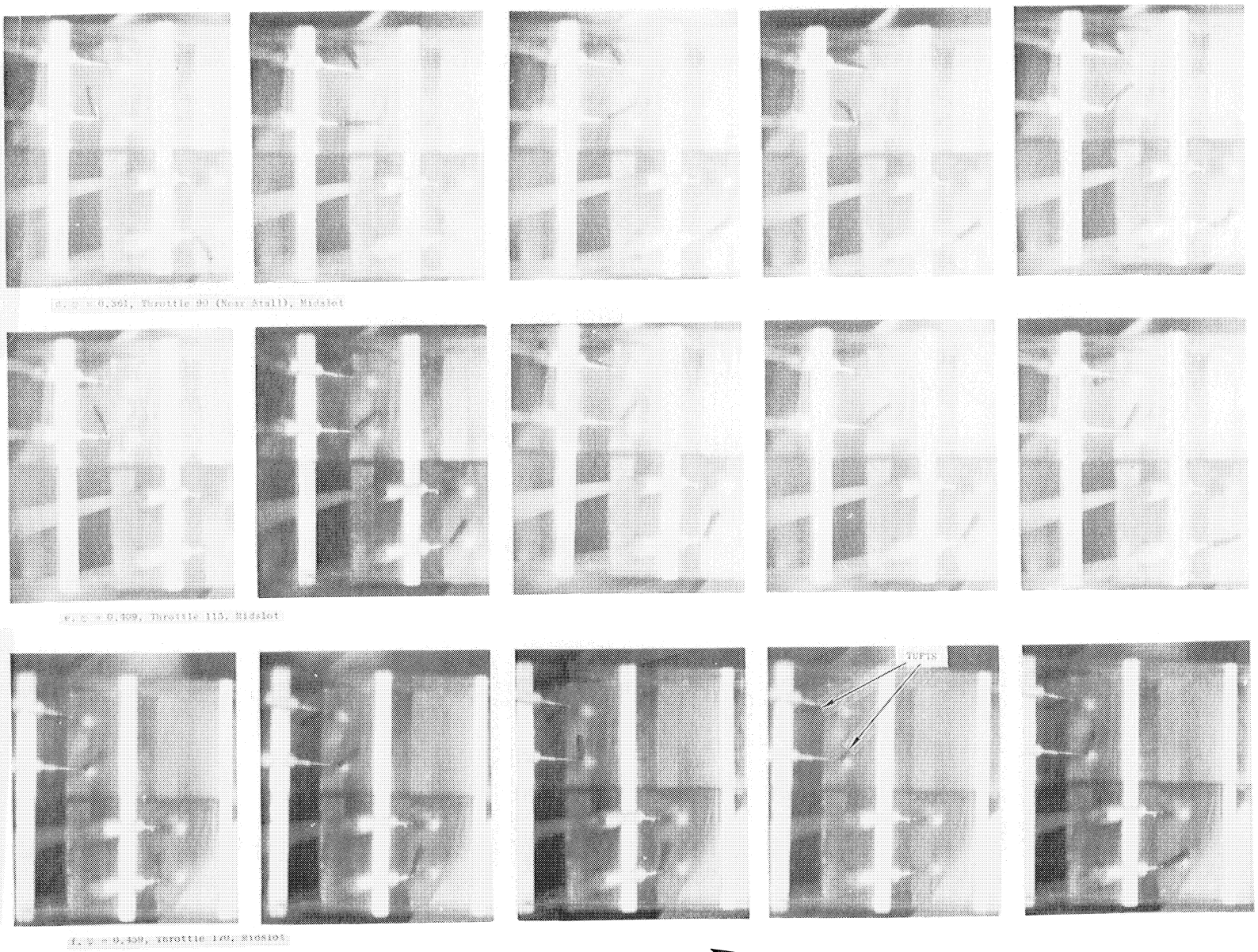

Figure 50 Photographs Showing Tufts at Mid-Depth in the Axial-Skewed Slots

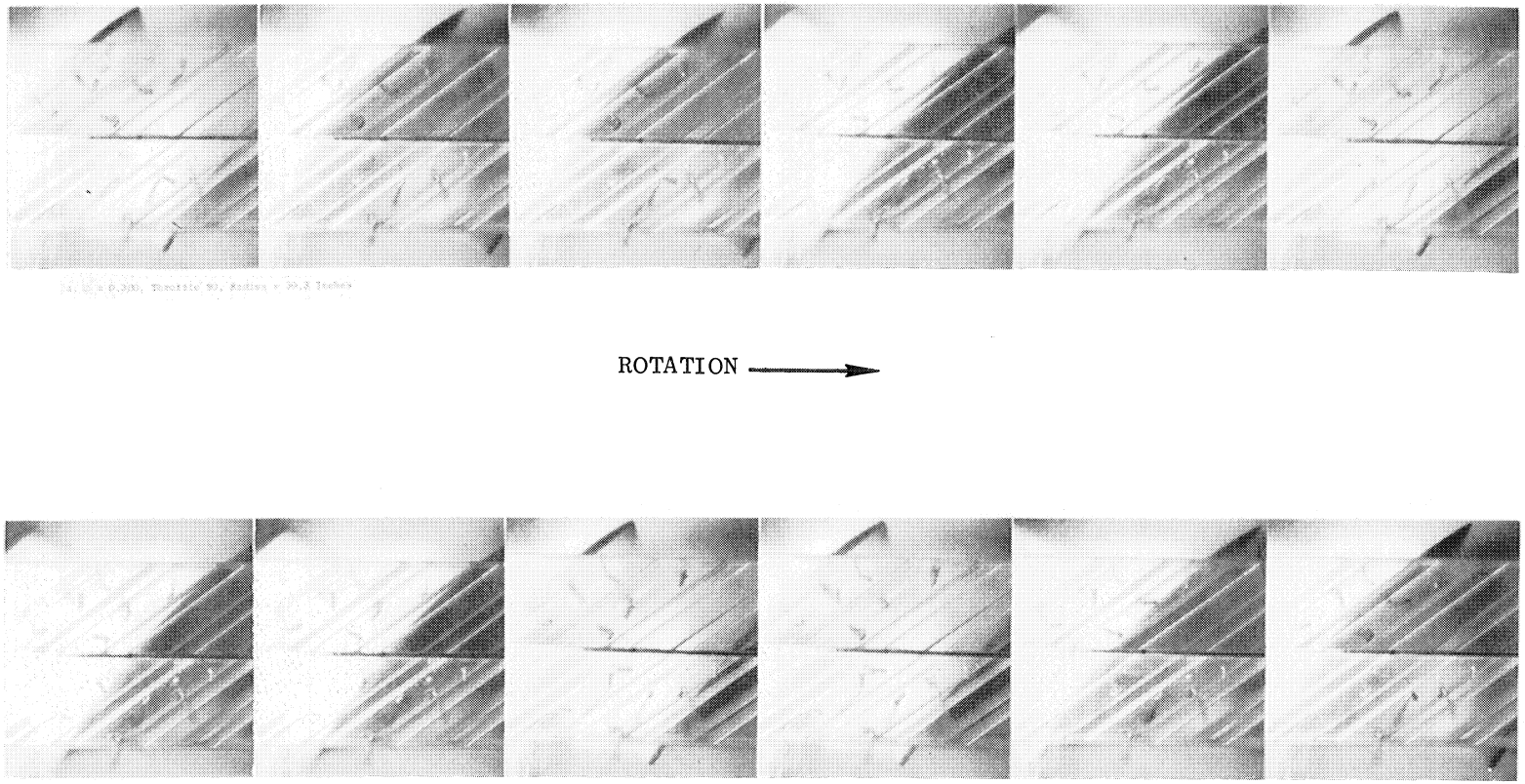

Figure 52 Photographs Showing Tufts in the Wide Blade Angle Slots Near Stall

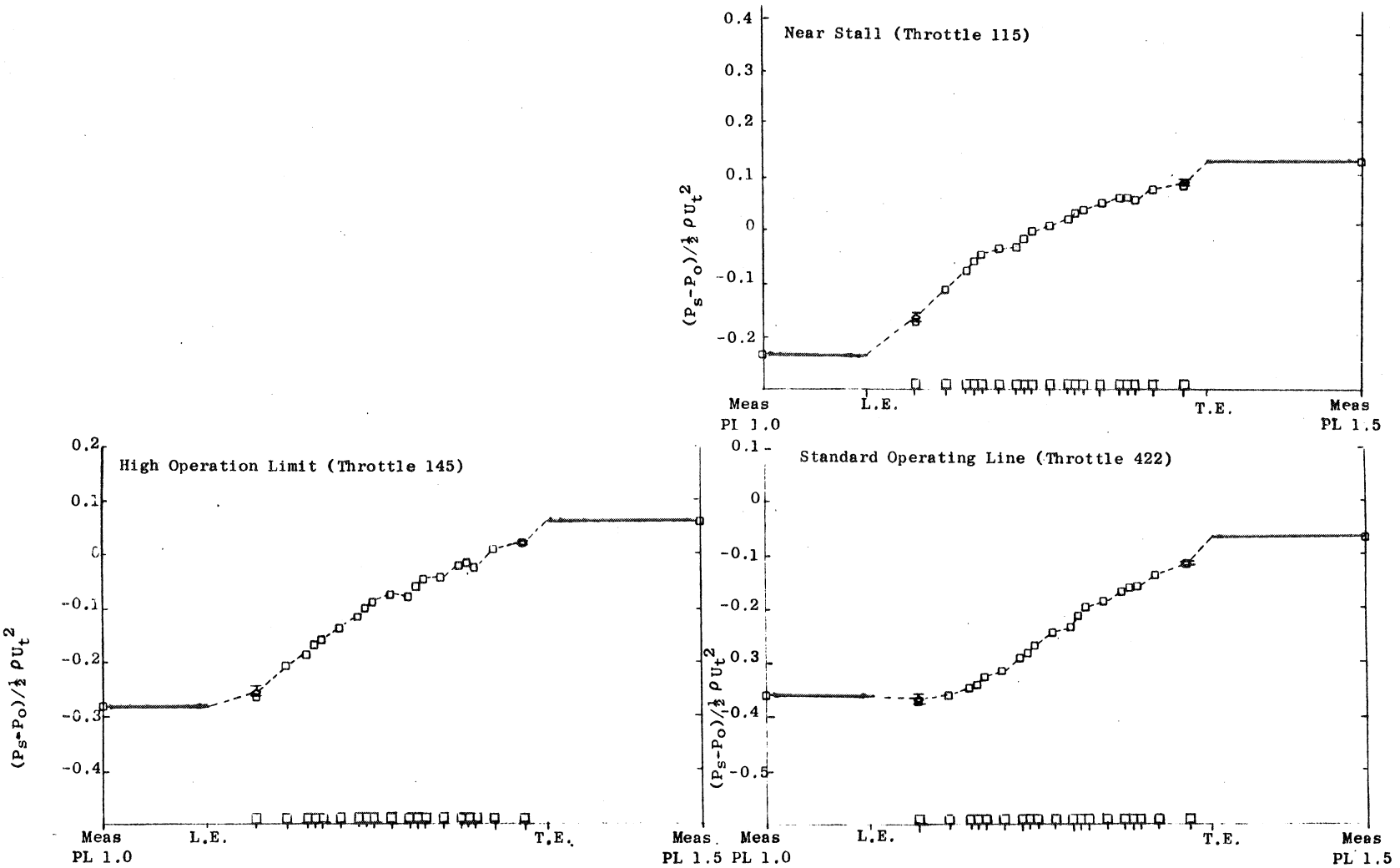

Figure 53 Annulus Wall (Casing) Static Pressure Distributions, Baseline Configuration

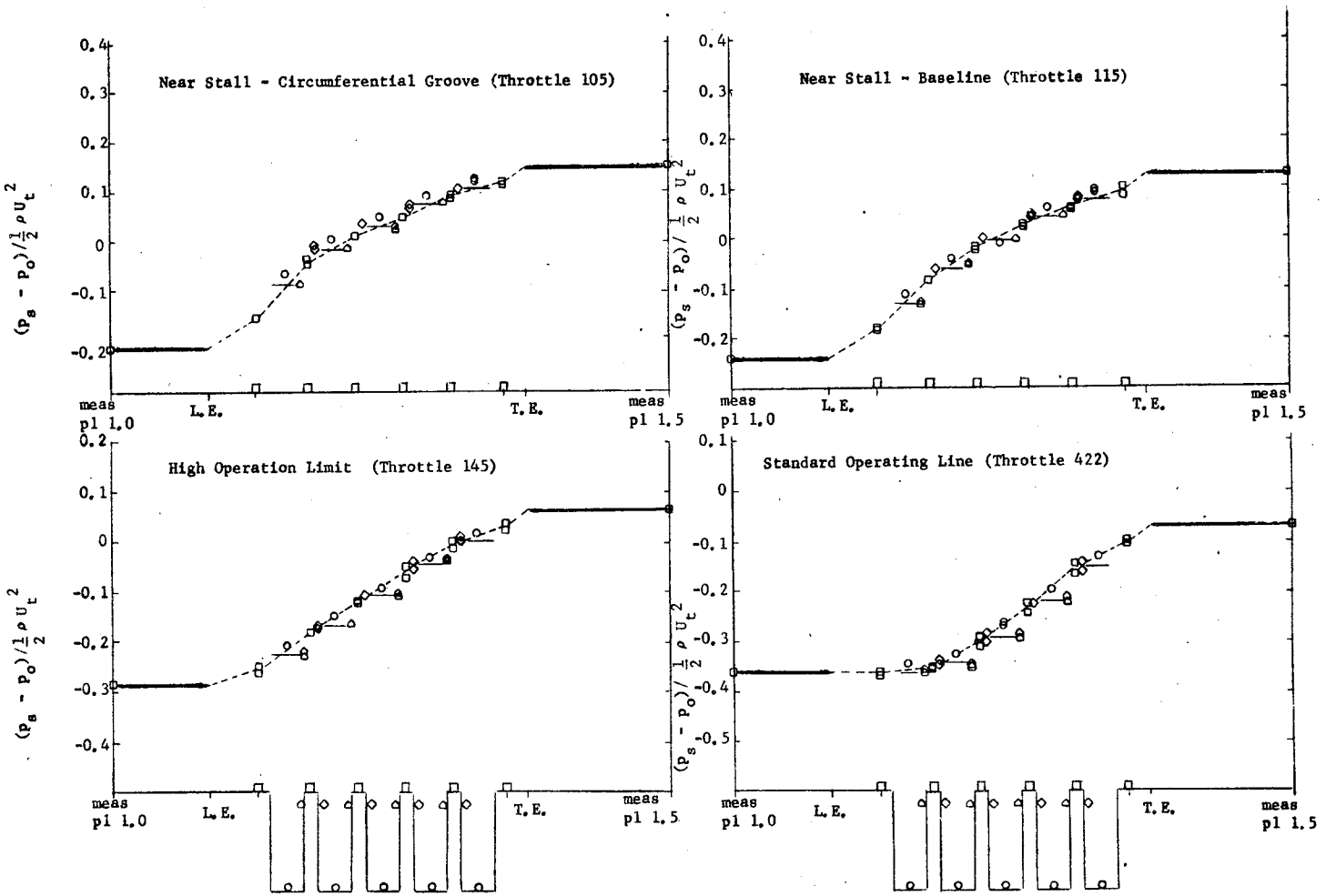

Figure 54 Annulus Wall and Cavity Statit Pressure Distributions - Open Circumferential Groove Configuration. Note that Multiple Symbols at One Axial Position Indicate Readings at Different IGV Wake Positions.

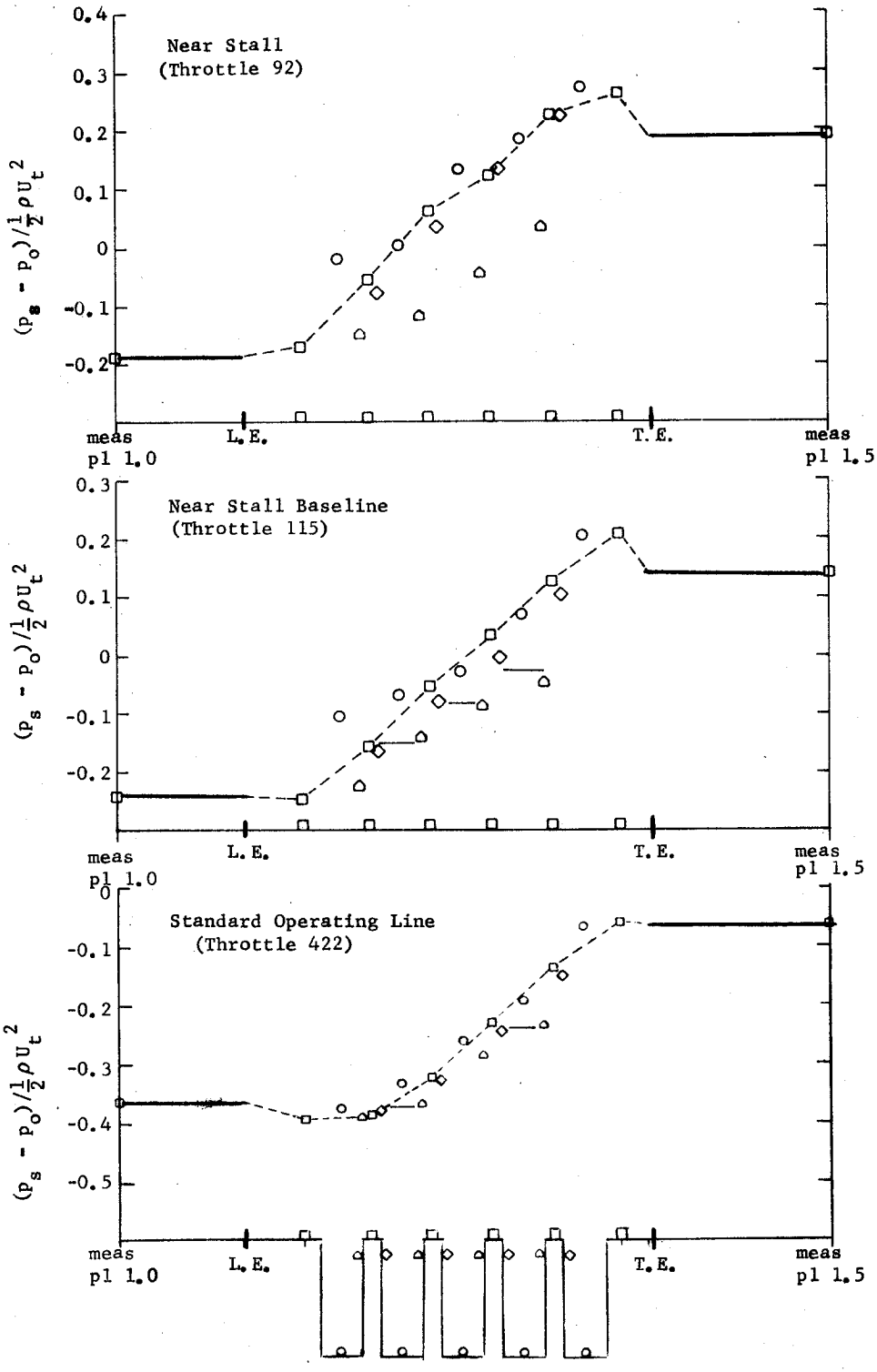

Figure 55 Annulus Wall and Cavity Static Pressure Distributions - Circumferential Groove Configuration - Grooves 1-5 Baffled

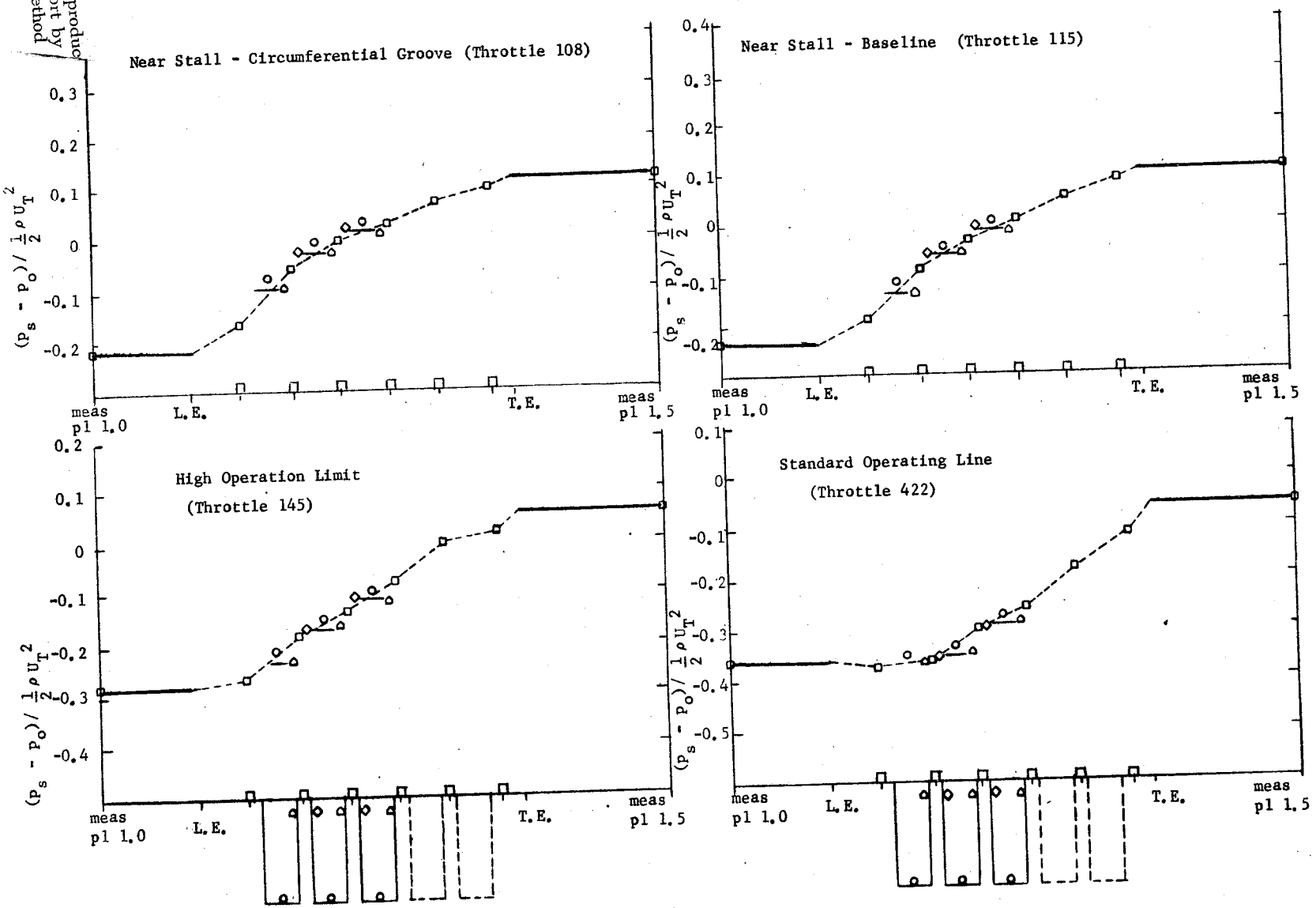

Figure 56 Annulus Wall and Cavity Static Pressure Distributions
Circumferential Groove Configuration - Grooves 1-3 Open

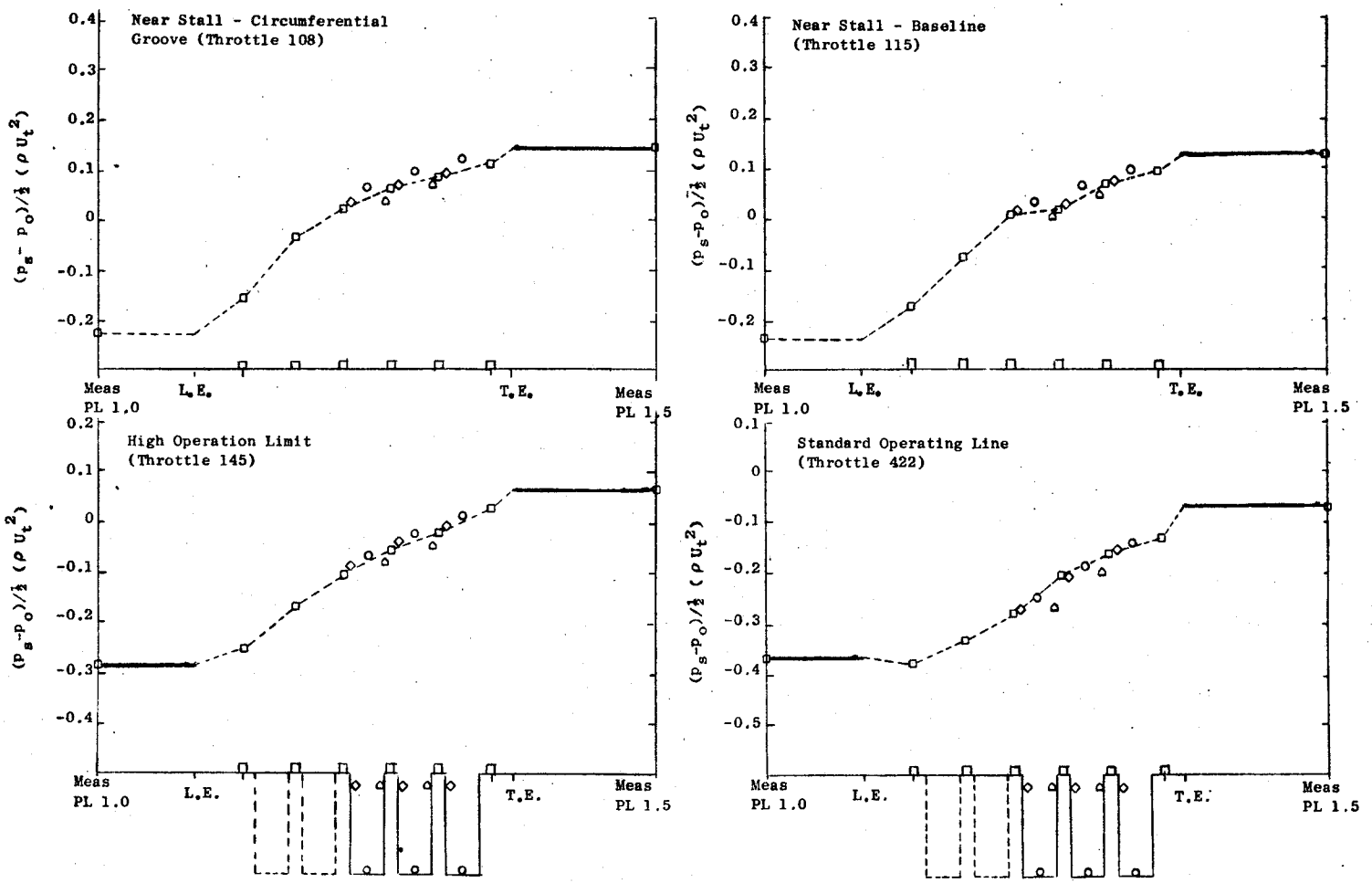

Figure 57 Annulus Wall and Cavity Static Pressure Distribution, Circumferential Groove Configuration - Grooves 3-5 Open

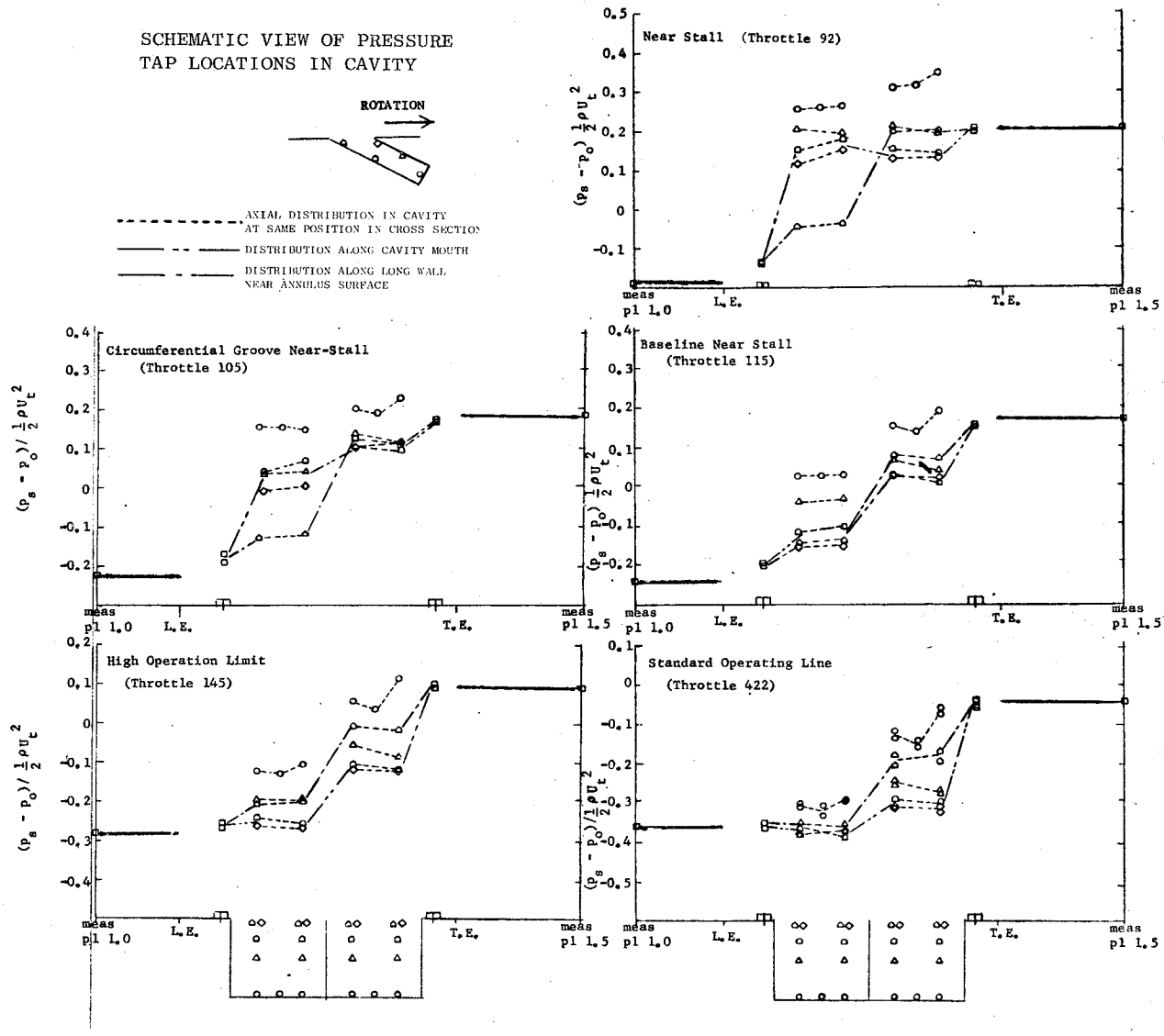

Figure 58 Annulus Wall and Cavity Static Pressure Distributions Axial-Skewed Slot Configuration - Baffled Slots. Note that multiple symbols at one axial position for throttle 422 indicate readings at different IGV wake positions.

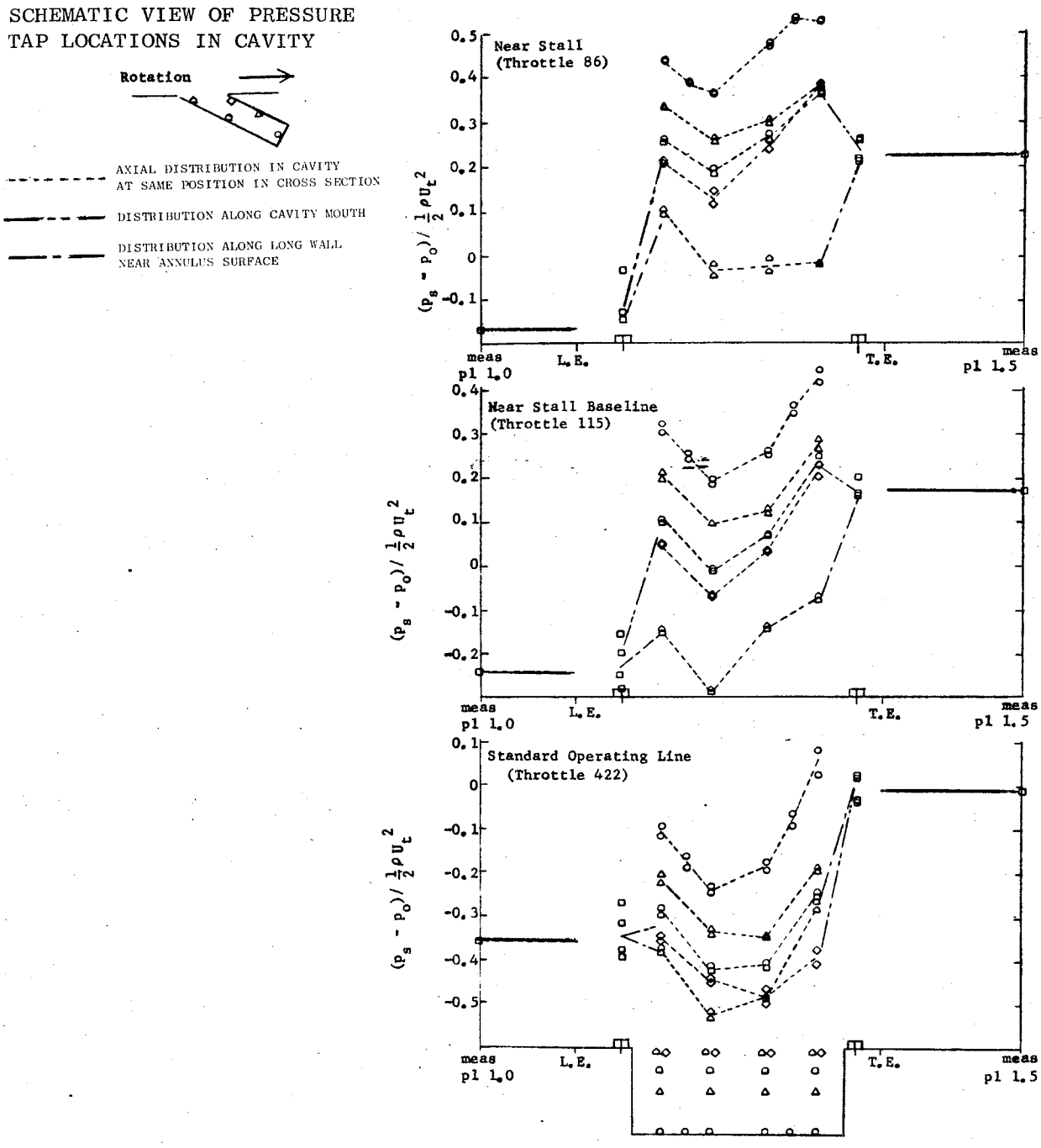

Figure 59 Annulus Wall and Cavity Static Pressure Distributions Axial-Skewed Slot Configuration - Slots Unbaffled. Note that Multiple Symbols at One Axial Position Indicate Readings with Different IGV Wake Positions.

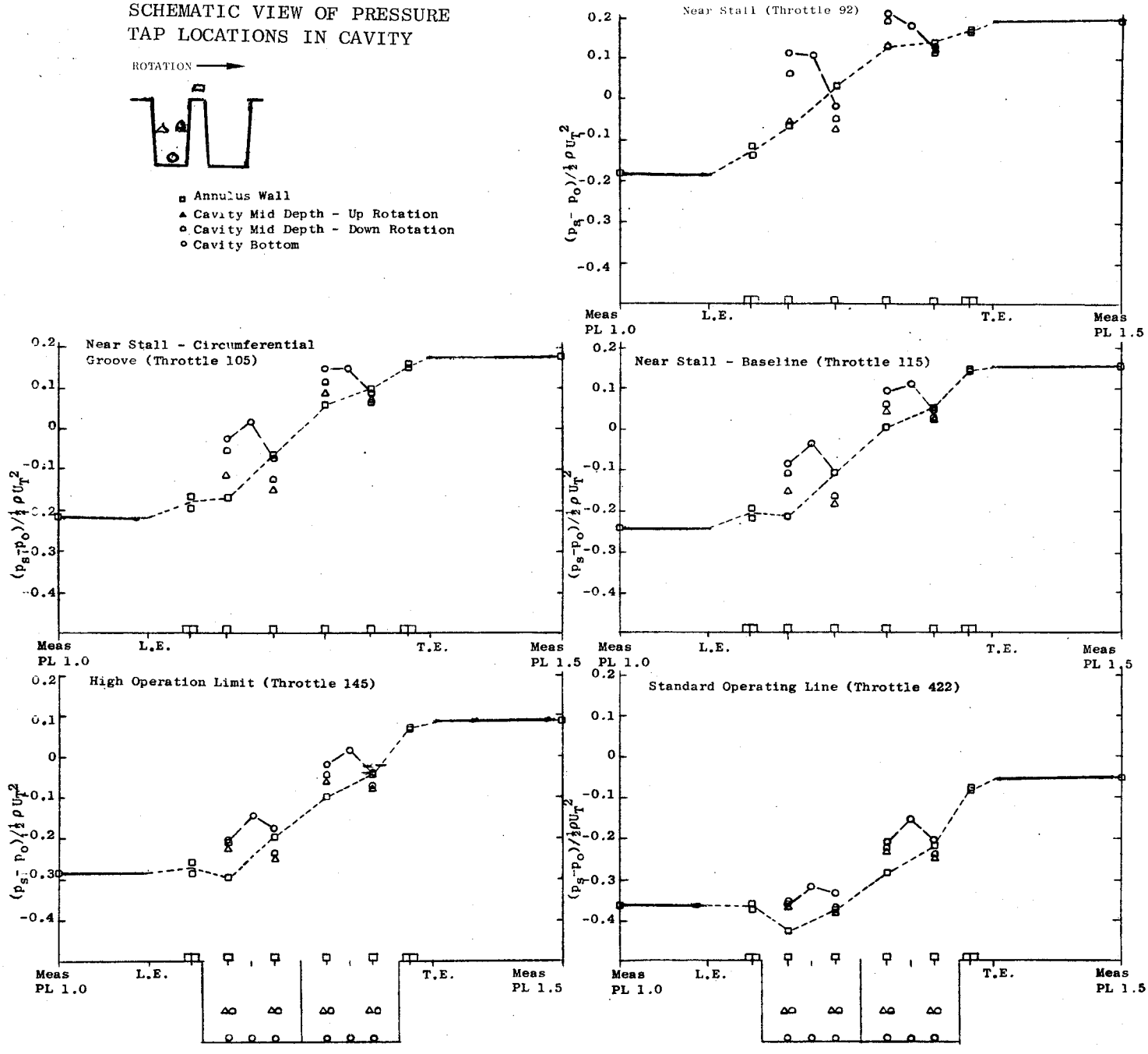

Figure 60 Annulus Wall and Cavity Static Pressure Distributions, Wide Blade Angle Slot Configuration

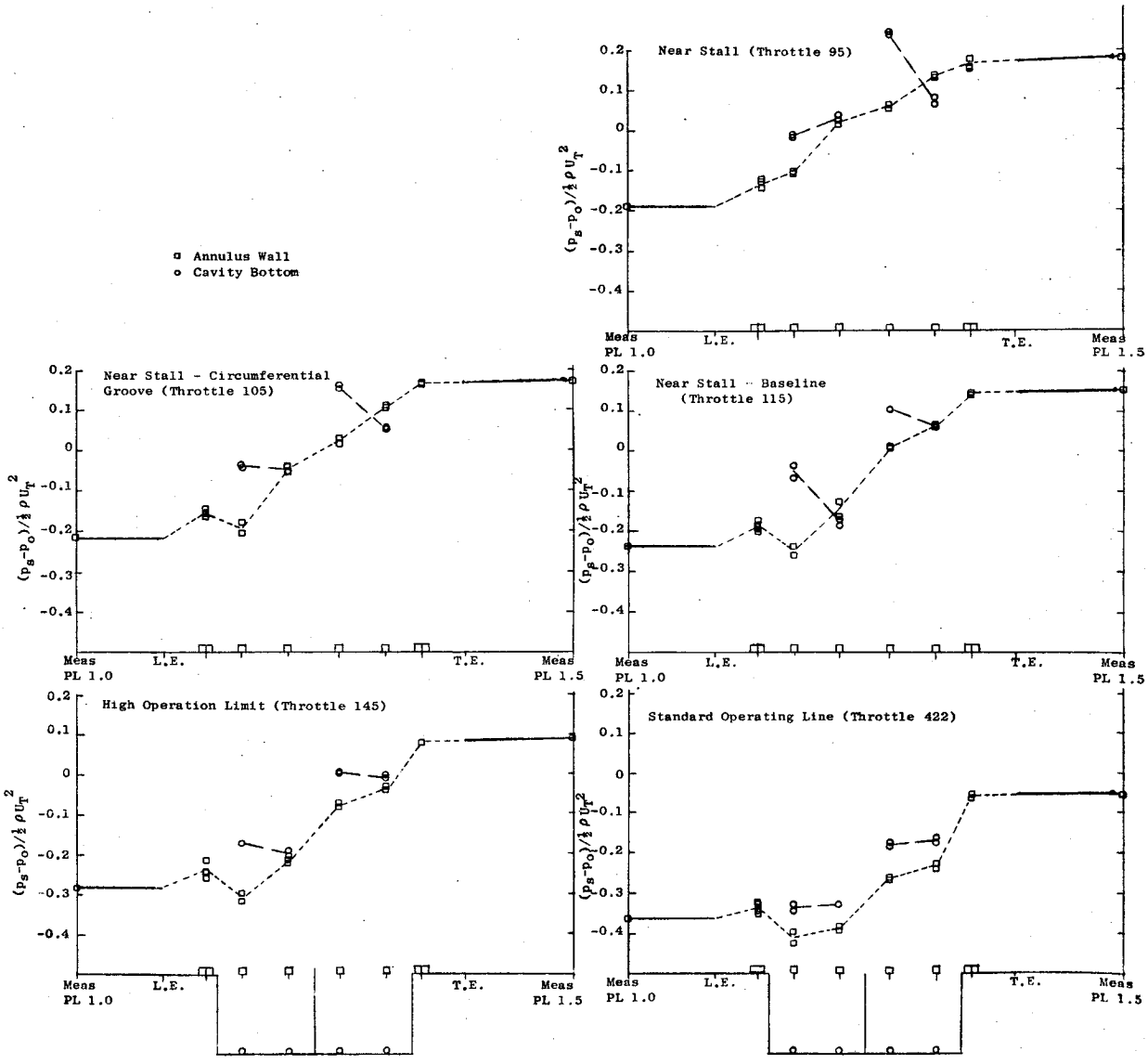

Figure 61 Annulus Wall and Cavity Static Pressure Distributions, Narrow Blade Angle Slot Configuration

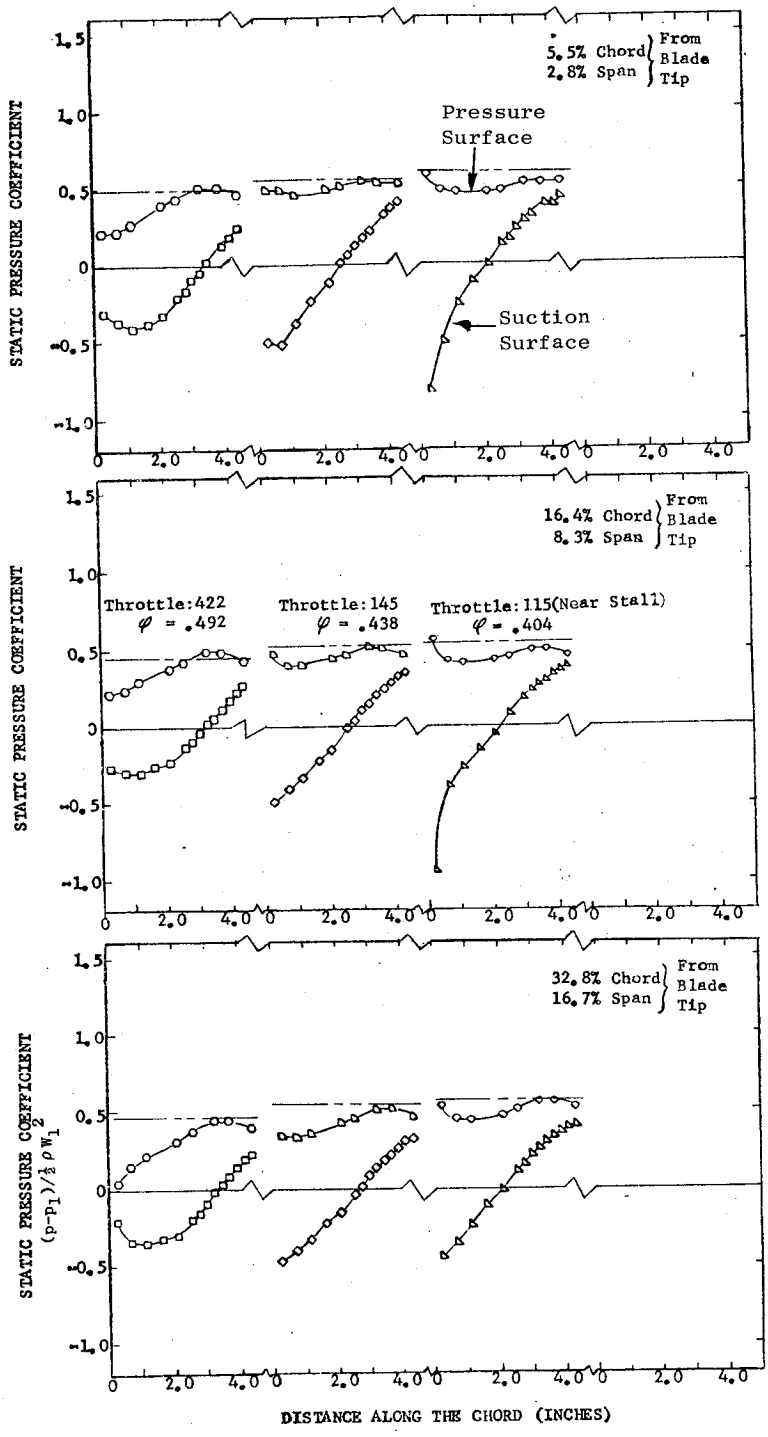

Figure 62 Blade Surface Static Pressures, Baseline Configuration

Long-short-long dash delineation indicates cascade discharge pressure.

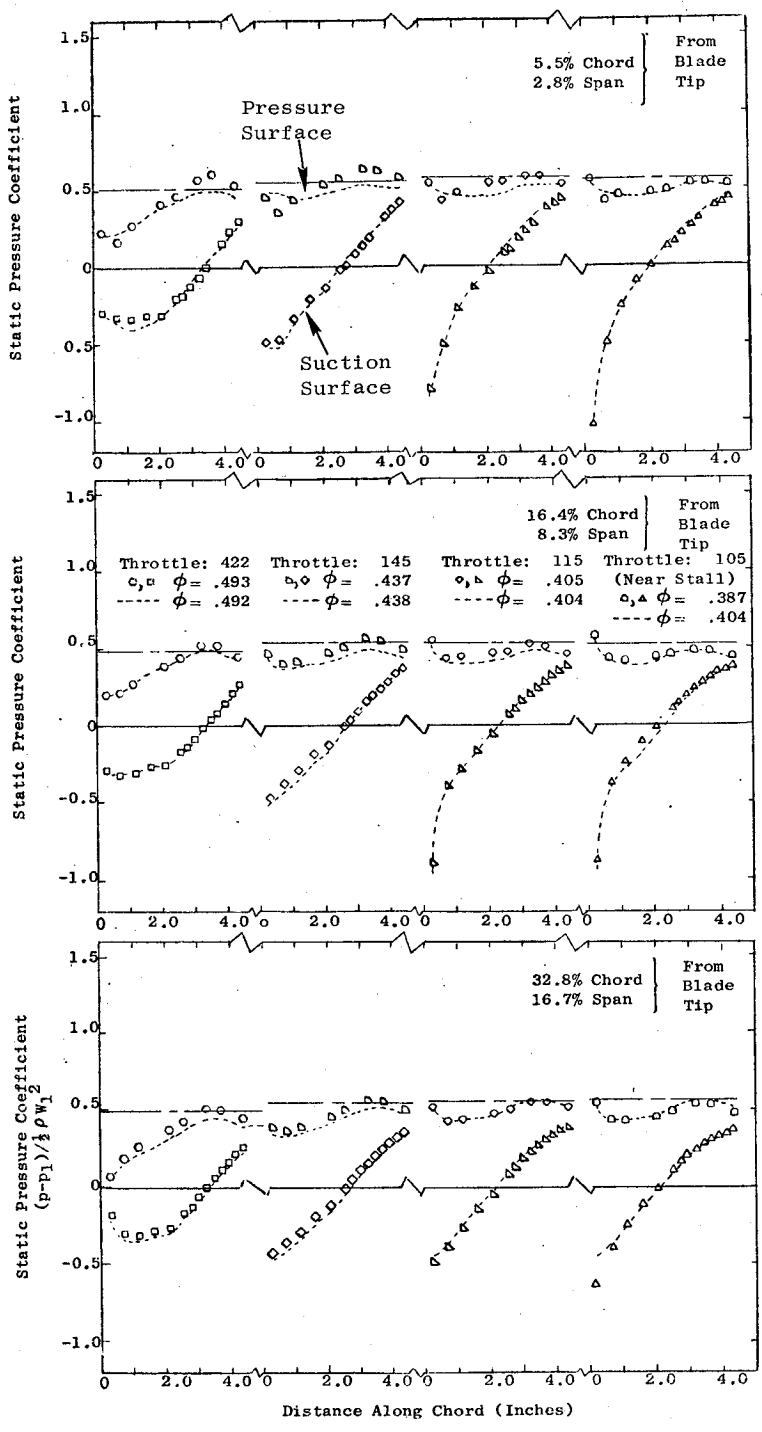

Figure 63 Blade Surface Static Pressures, Circumferential Groove Casing Treatment - Grooves 1-5 Open. Baseline Comparison Indicated by Dashed Lines

Long-short-long dash delineation indicates cascade discharge pressure.

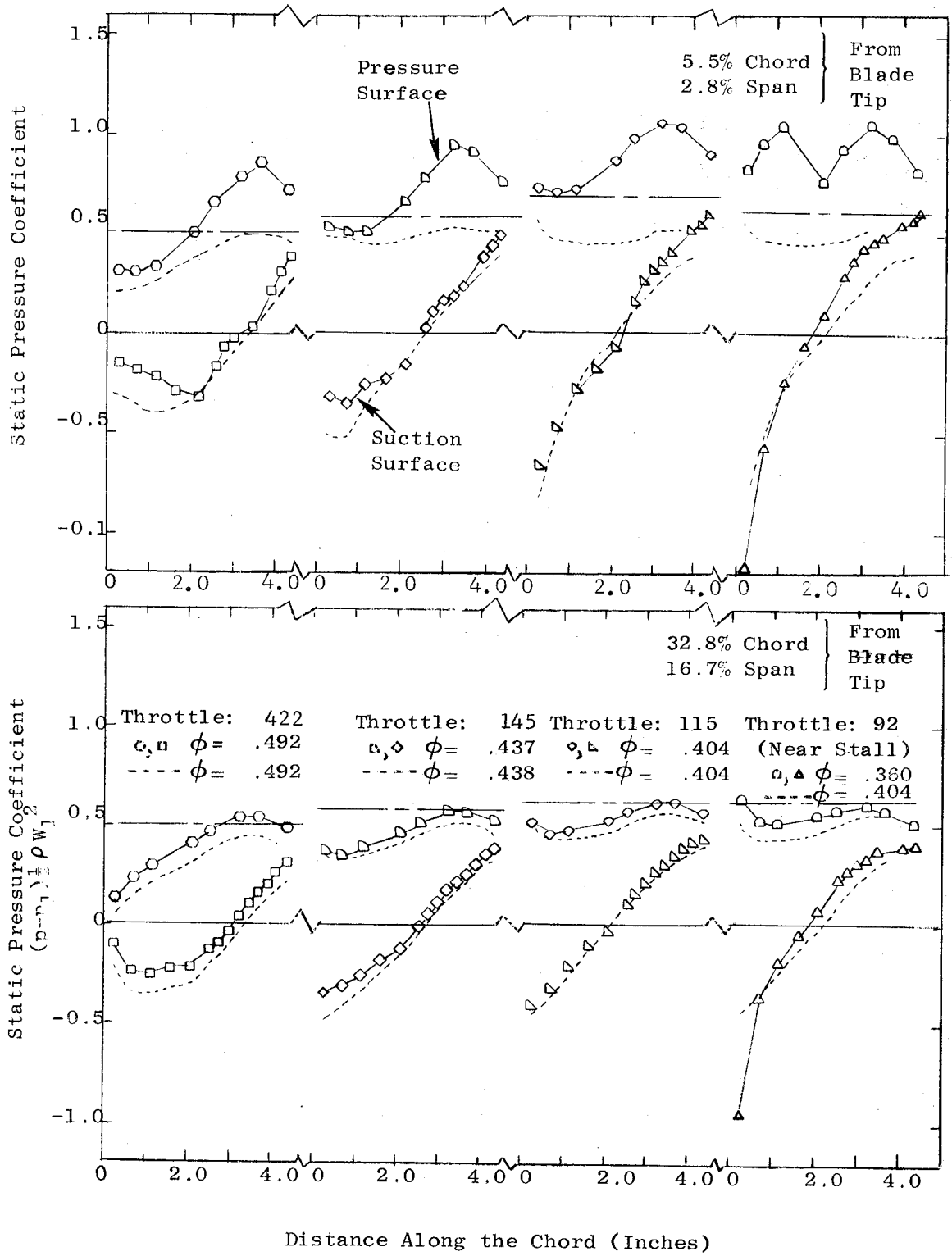

Figure 64 Blade Surface Static Pressures - Axial-Skewed Slot Configuration. Baseline Comparison is Indicated by Dashed Lines.

Long-Short-Long Dash Delineation Indicates Cascade Discharge Pressure.

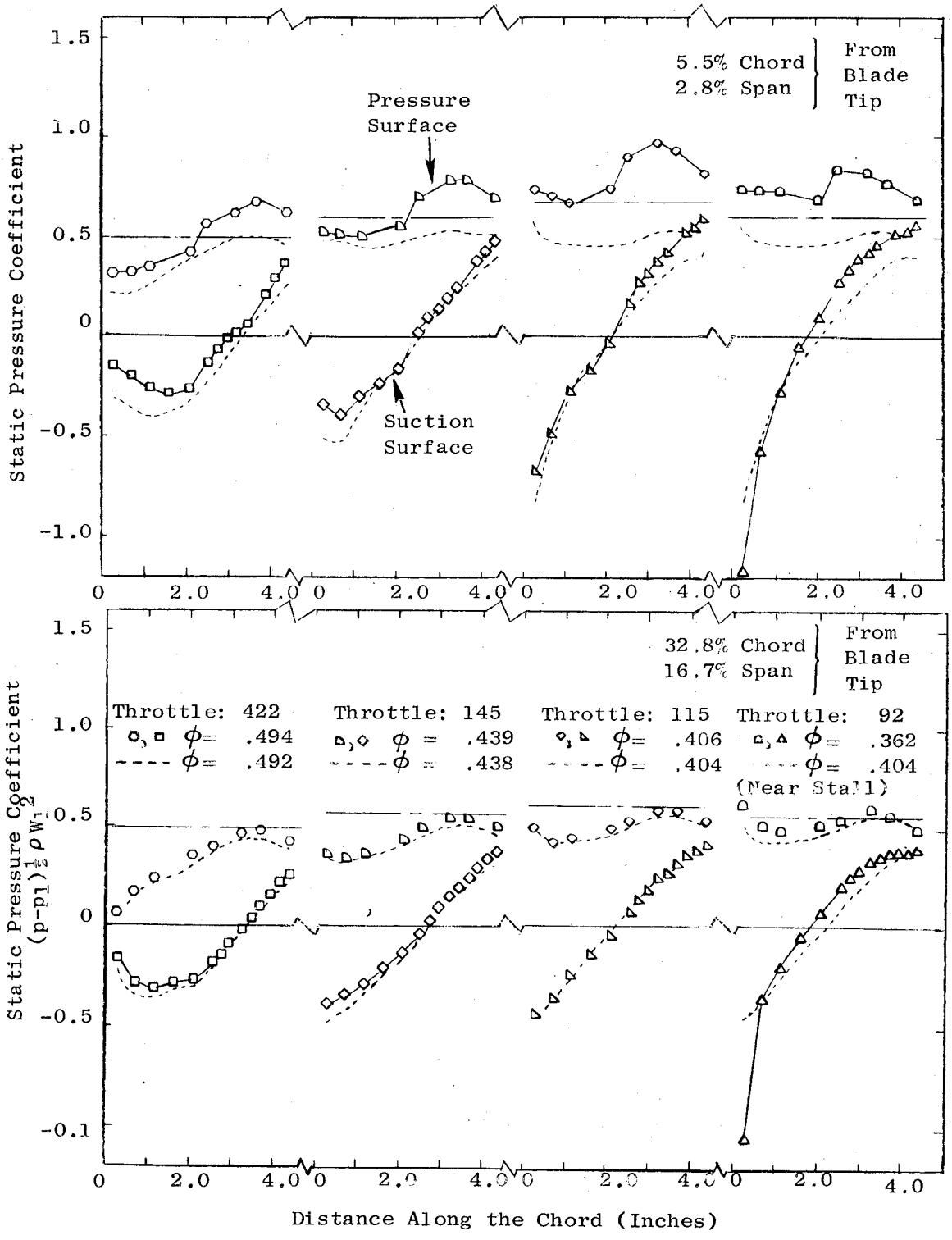

Figure 65 Blade Surface Static Pressures - Wide Blade Angle Slot Configuration. Baseline Comparison is Indicated By Dashed Lines.

Long-Short-Long Dash Delineation Indicates Cascade Discharge Pressure.

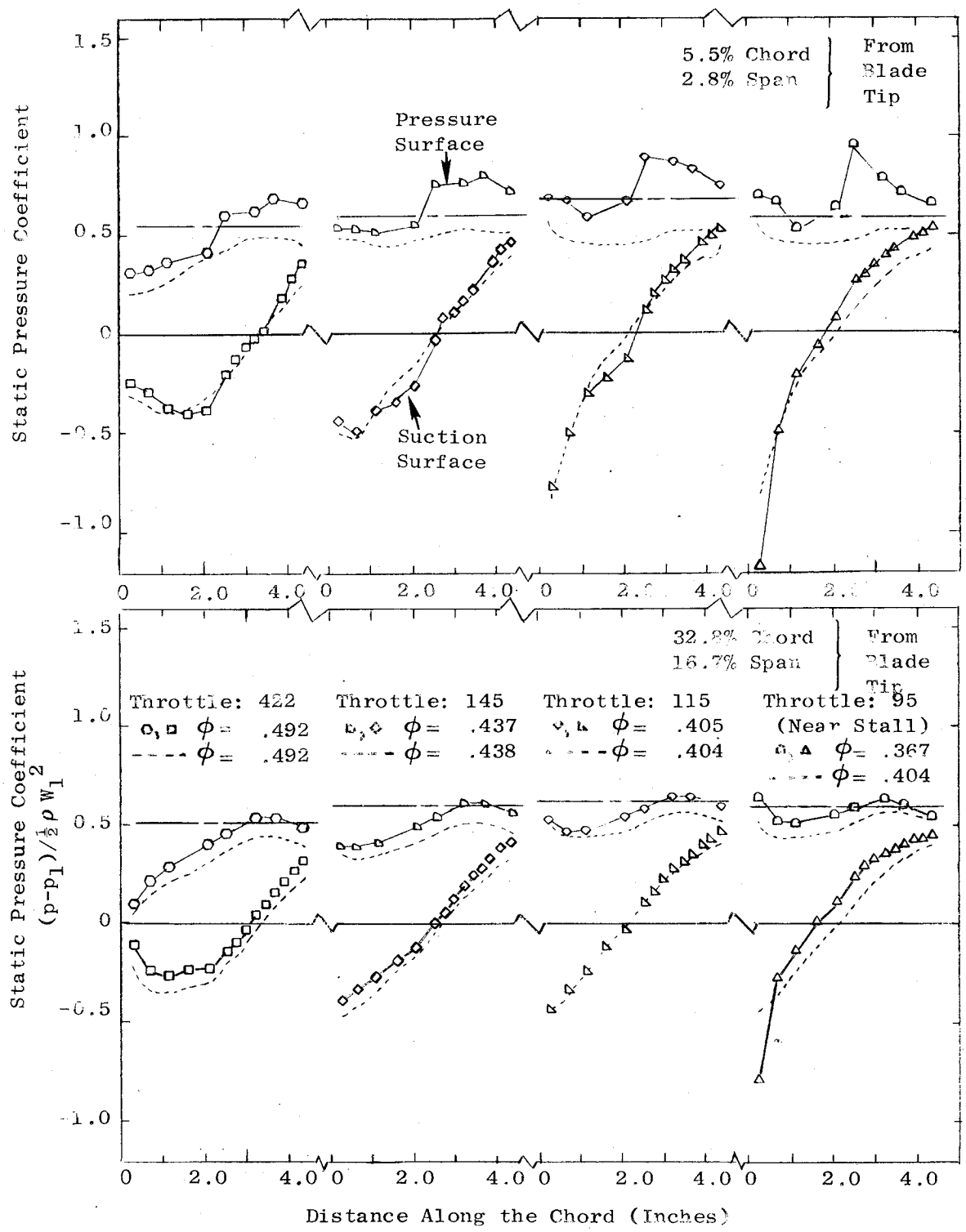

Figure 66 Blade Surface Static Pressures - Narrow Blade Angle Slot Configuration. Baseline Comparison is Indicated by Dashed Lines.

Long-Short-Long Dash Delineation Indicates Cascade Discharge Pressure.

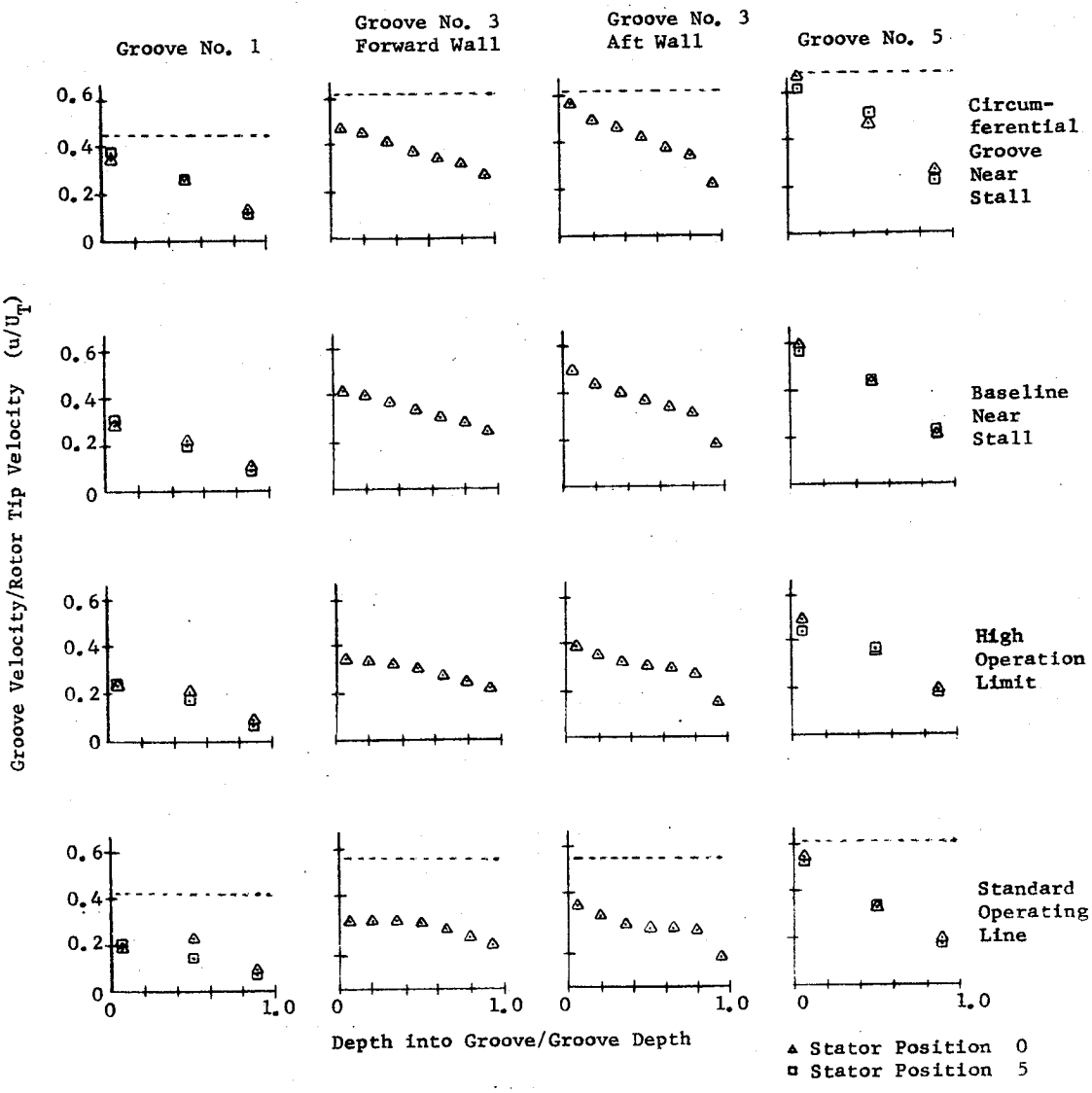

Figure 67 Velocity Measurements (Hot Film Anemometer) In Open Circumferential Grooves
Note: Dashed lines denote mean absolute circumferential velocities from cascade predictions.

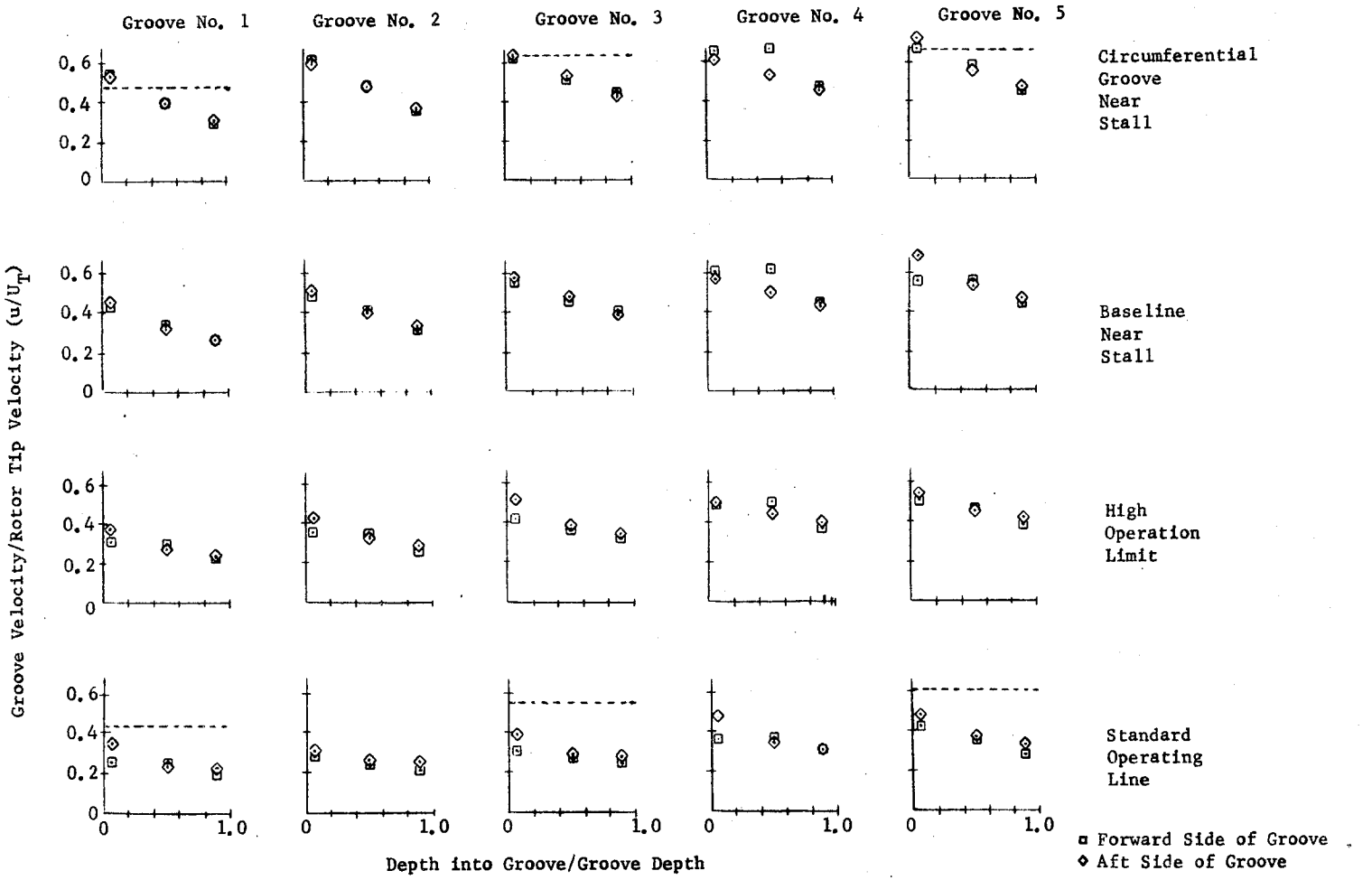

Figure 68 Velocity Measurements (Total and Static Pressure) In Open Circumferential Grooves
Note: Dashed lines denote mean absolute circumferential velocities from cascade predictions.

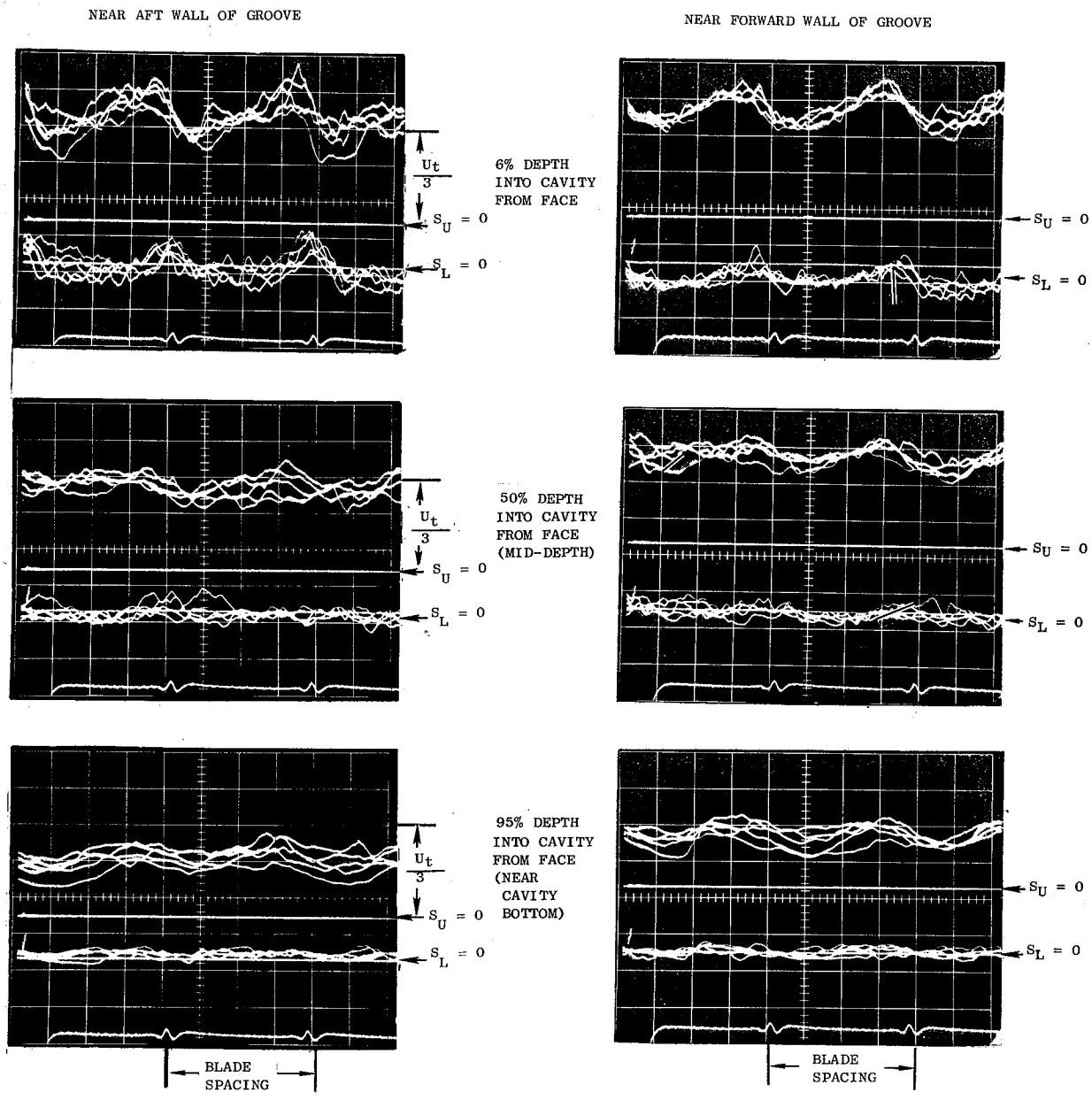

NOTE: To obtain flow angles from oscillograms, $\beta = 75\ (S_L/S_U)$, where S_L is the lower signal, S_U the upper signal. The calibration is valid from 40° into the groove to 20° out of the groove. $S_L > 0$ indicates flow into the groove.

Figure 69 Typical Oscillograms Showing the Output of a "Diagonal X Array" Hot Film Anemometer Located in Groove Number 3, $\phi = 0.438$, $\psi = 0.596$, Throttle = 145

FOLDOUT FRAME

FORWARD CAVITY

FORWARD POSITION

AFT POSITION

SLOT MID DEPTH

NEAR LONG WALL (UP ROTATION)

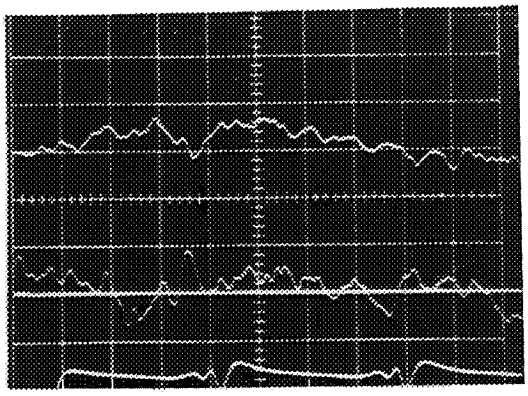

0.4 U_t RMS

$\lambda = 76°$

0.2 U_t

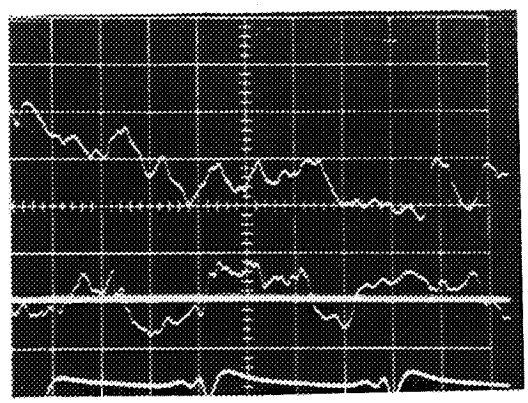

NEAR SHORT WALL (DOWN ROTATION)

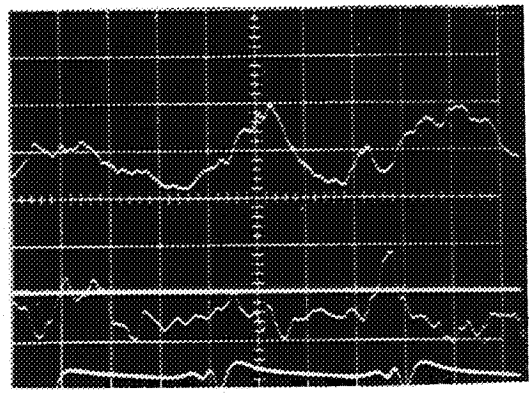

0.396 U_t RMS

$\lambda = 64°$

0.2 U_t

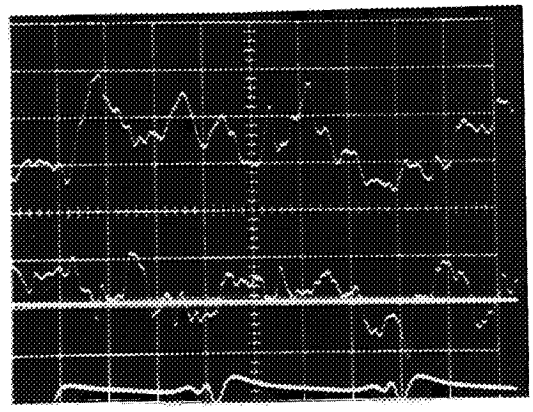

SLOT BOTTOM

NEAR LONG WALL (UP ROTATION)

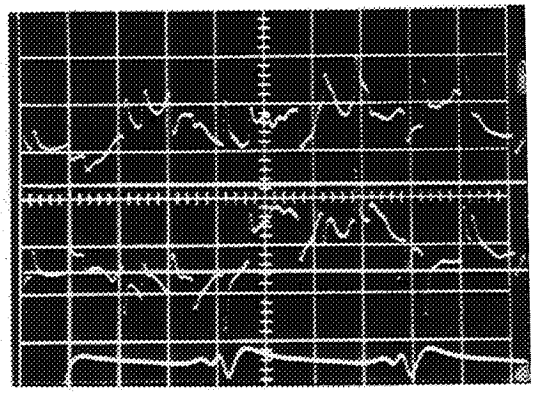

0.2 U_t

NEAR SHORT WALL (DOWN ROTATION)

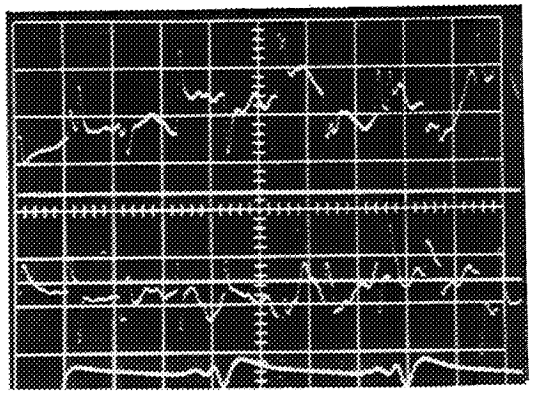

0.2 U_t

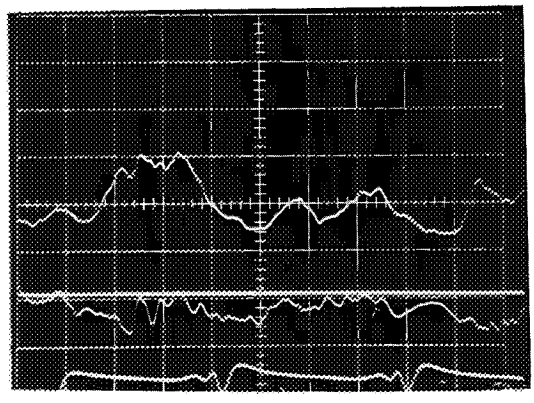

Note that null angles and RMS velocities were not record oscillograms, which have been included for most complete of irregular behavior.

FOLDOUT FRAME

FORWARD CAVITY

SLOT MID DEPTH

FORWARD POSITION

AFT POSITION

NEAR LONG WALL (UP ROTATION)

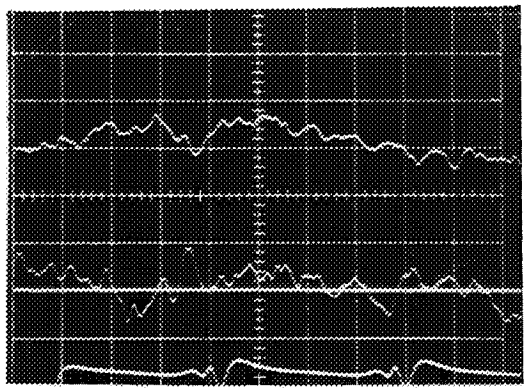

0.4 U_t RMS

$\lambda = 76°$

0.2 U_t

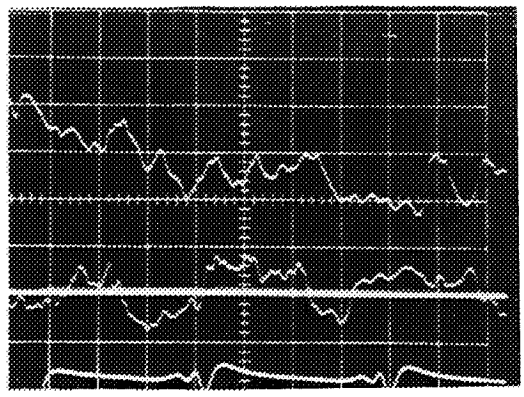

NEAR SHORT WALL (DOWN ROTATION)

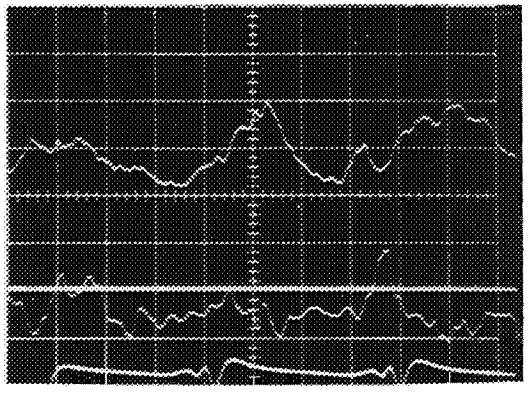

0.396 U_t RMS

$\lambda = 64°$

0.2 U_t

SLOT BOTTOM

NEAR LONG WALL (UP ROTATION)

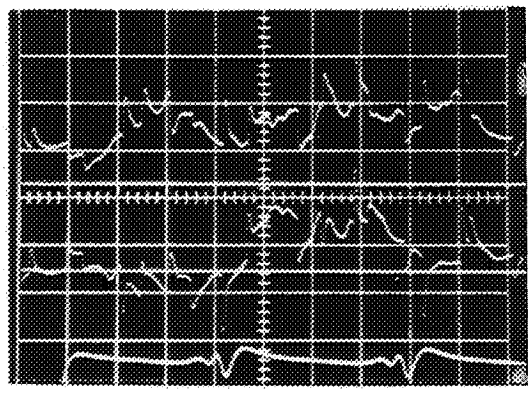

0.2 U_t

NEAR SHORT WALL (DOWN ROTATION)

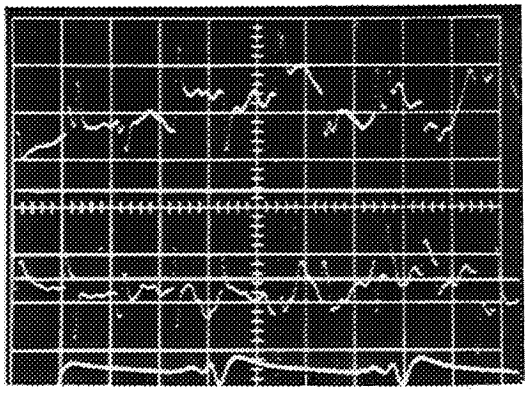

0.2 U_t

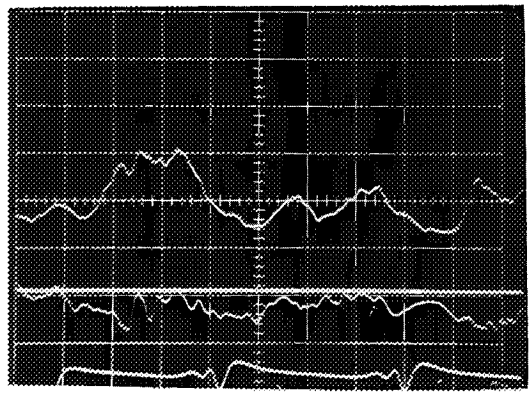

Note that null angles and RMS velocities were not recorded oscillograms, which have been included for most complete r of irregular behavior.

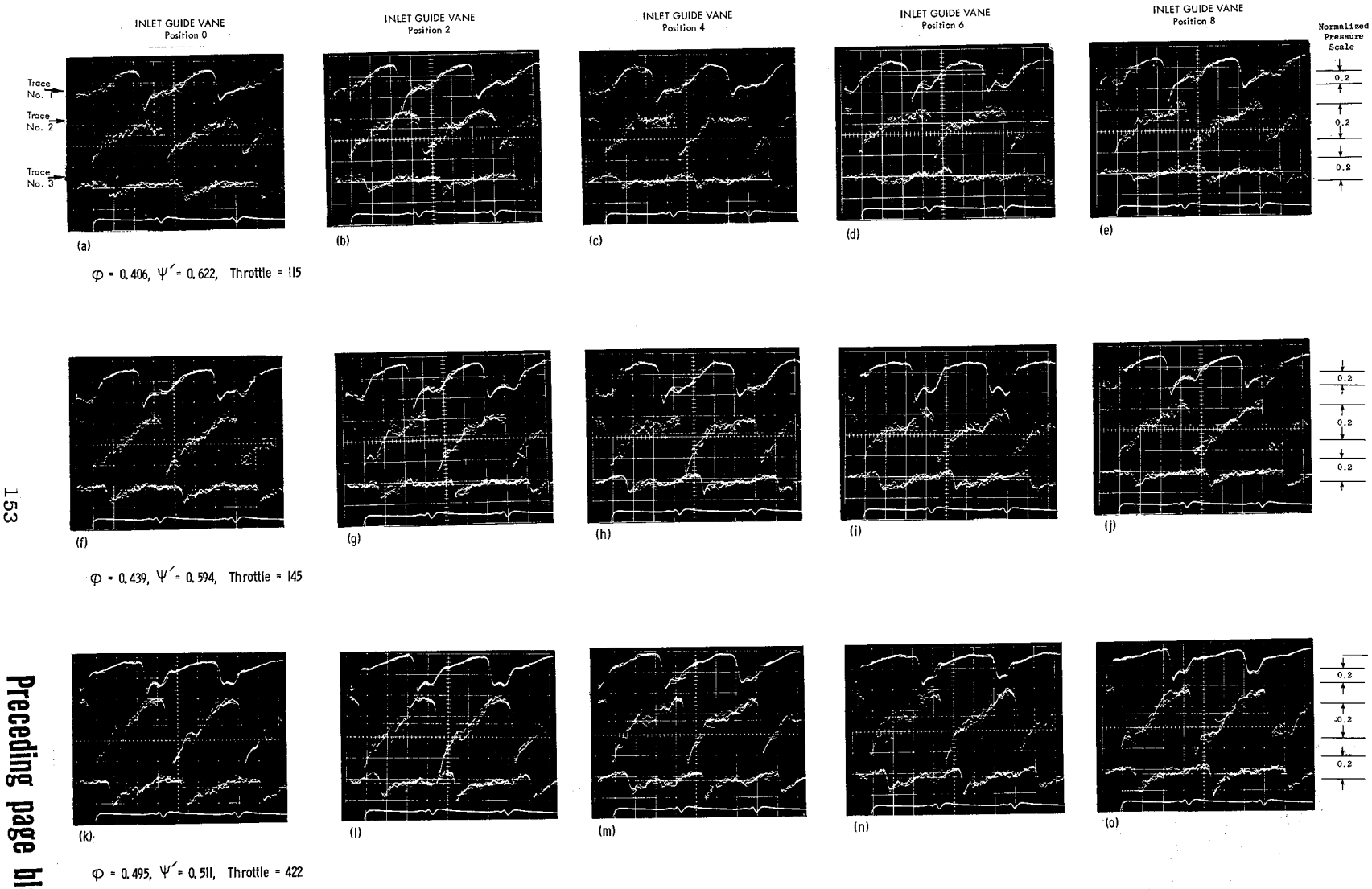

Figure 71 Typical Oscillograms Showing B and K Fluctuating Pressure Measurements on the Baseline Windows. B & K Locations: Trace No. 1 is 21% Axially Projected Chord from Leading Edge, Trace No. 2 is 51% C, Trace No. 3 is 81% C, Trace No. 4 Marks Blade Passing. Normalized Pressure Scale as Shown indicates $\Delta P / \frac{1}{2} \rho U_T^2$.

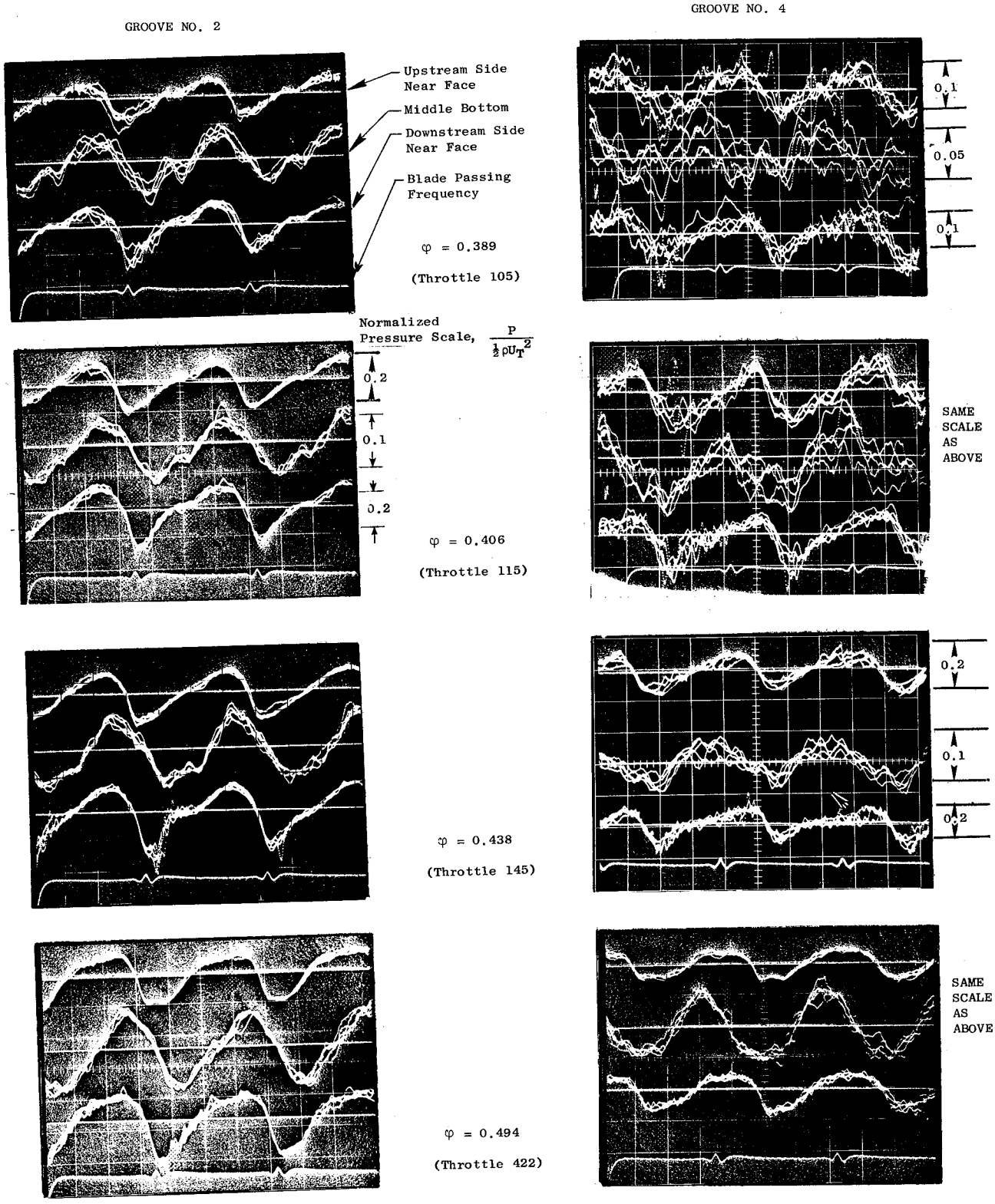

Oscillograms Showing B and K Pressure Measurements Within Circumferential Groove Number Two

Figure 72 Oscillograms Showing B and K Pressure Measurements within Circumferential Grooves

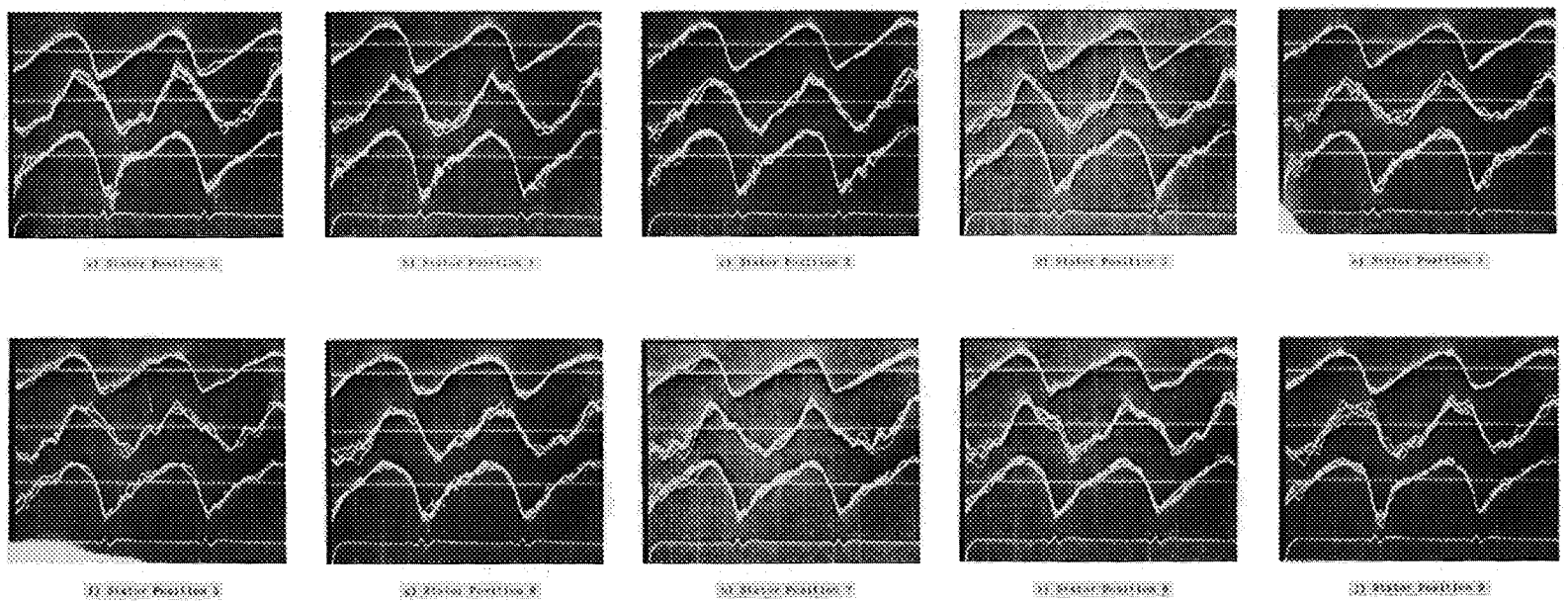

Figure 73 Typical Oscillograms Showing B&K Fluctuating Pressure Measurements in Groove Number 2 for Various Inlet Guide Vane Positions, $\phi = 0.438$, $\psi = 0.596$, Throttle = 145

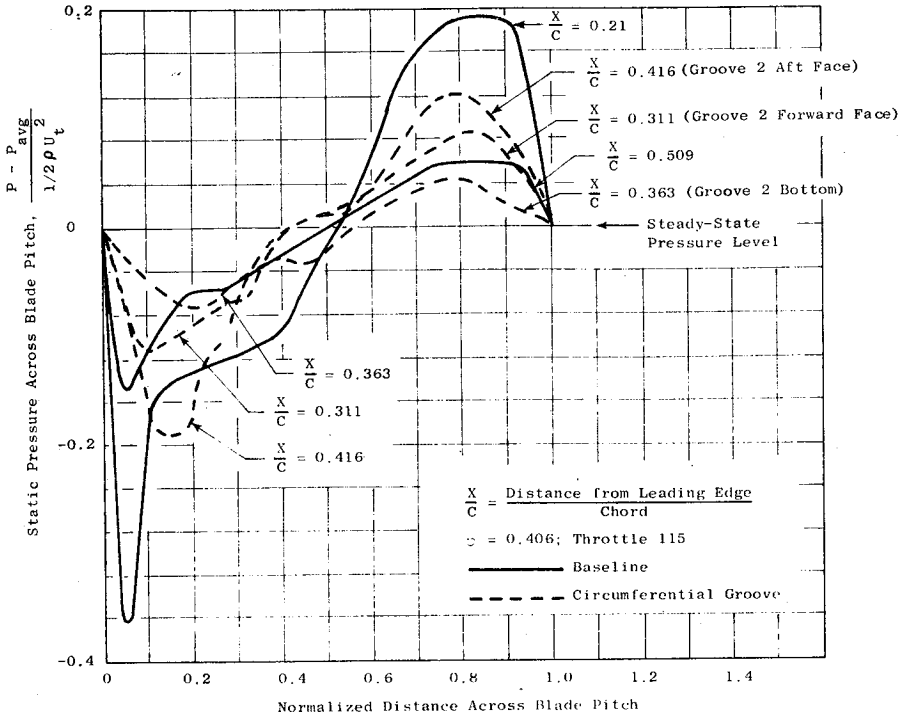

a. Near Baseline Stall

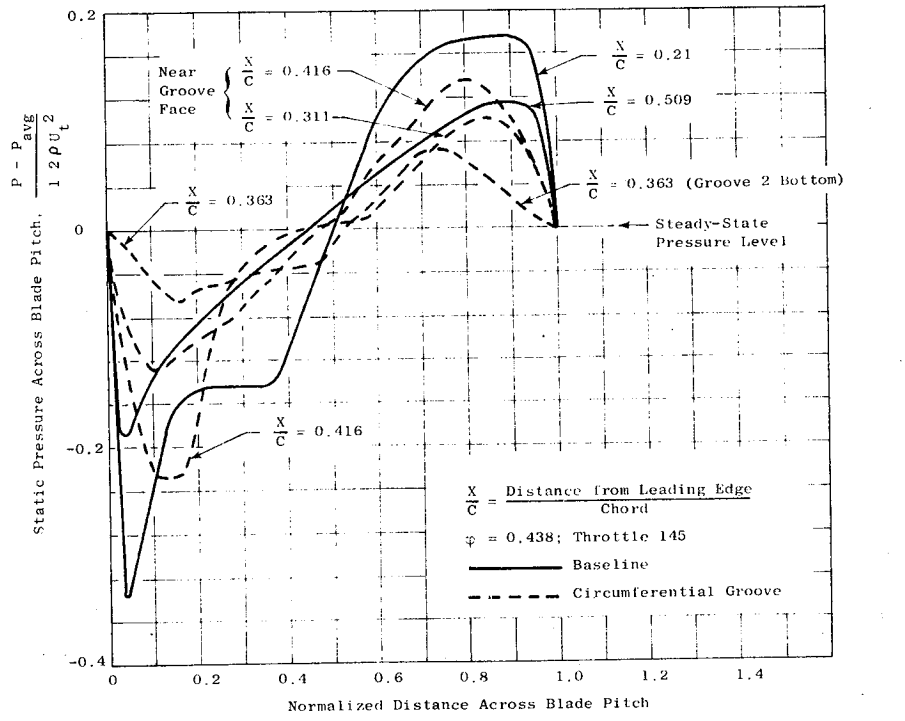

b. High Operation Limit

Figure 74 Pressure Distribution across Blade Pitch for Baseline and Circumferential Groove Configuration

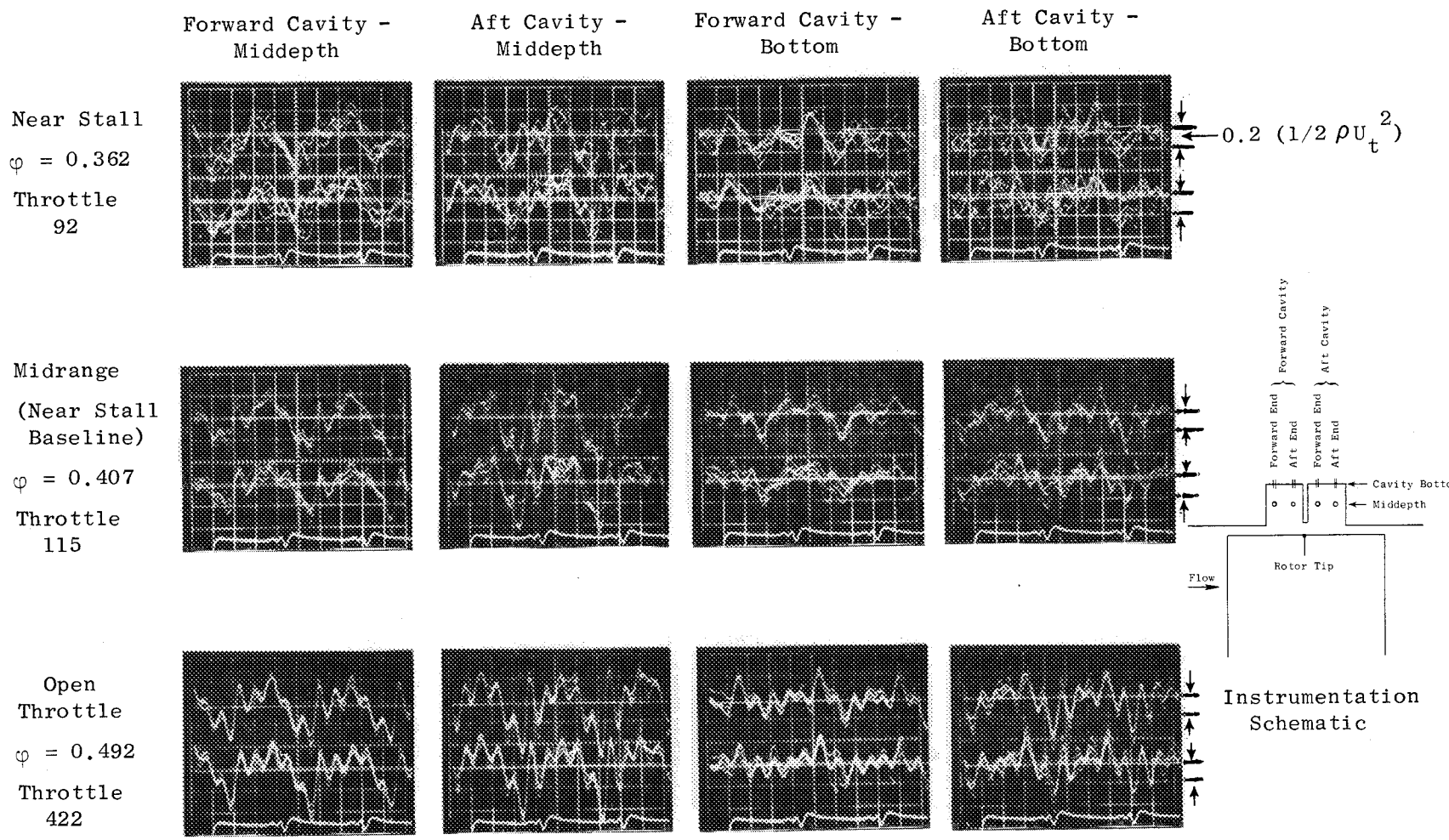

Figure 75 Axial-Skewed Slot Casing Treatment - Transient (B & K) Cavity Static Pressure.

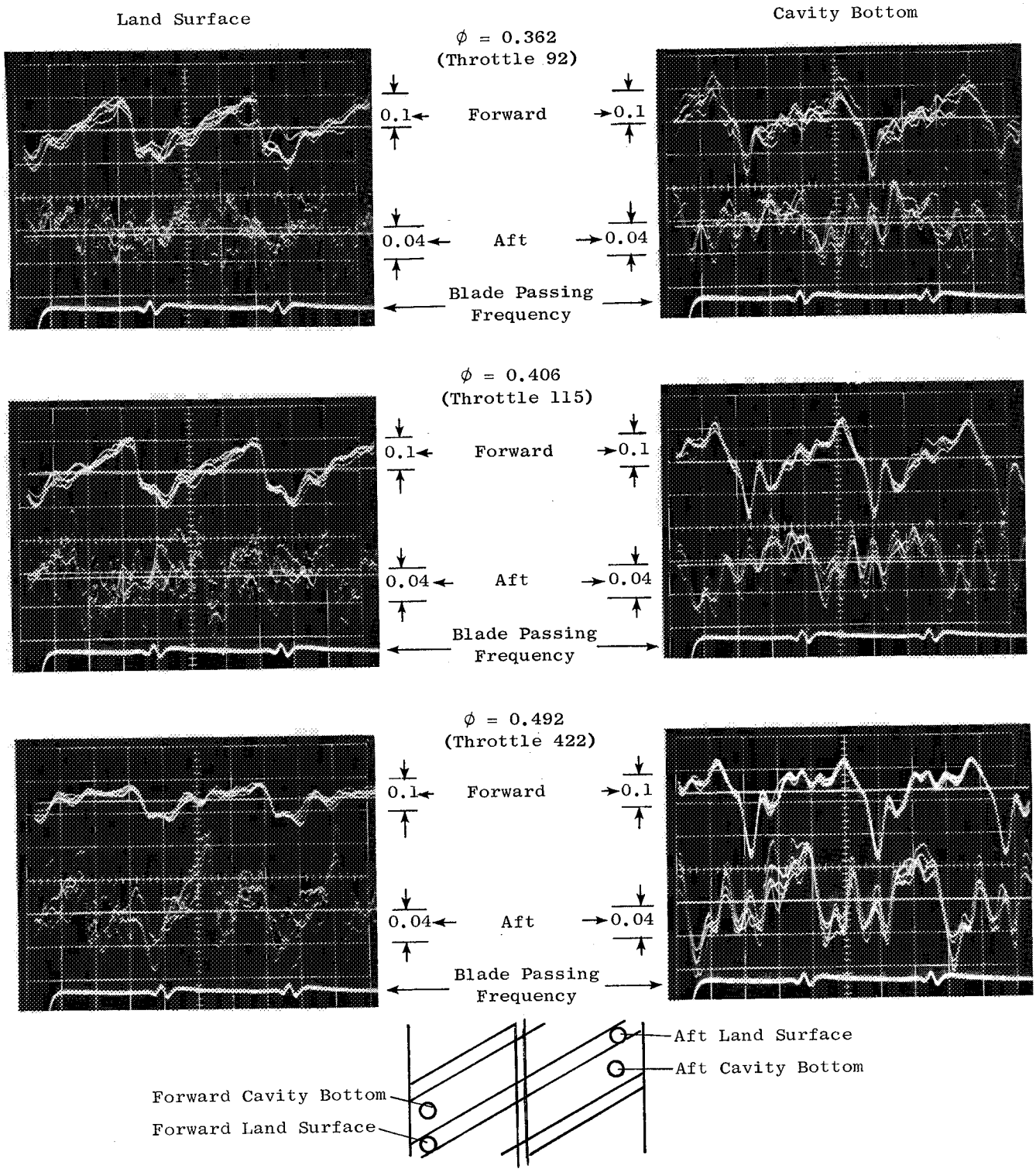

Figure 76 Oscillograms Showing B and K Pressure Measurements in Wide Blade Angle Slots. Normalized Pressure Scale Defines Pressure as $P/\frac{1}{2}\rho U_T^2$.

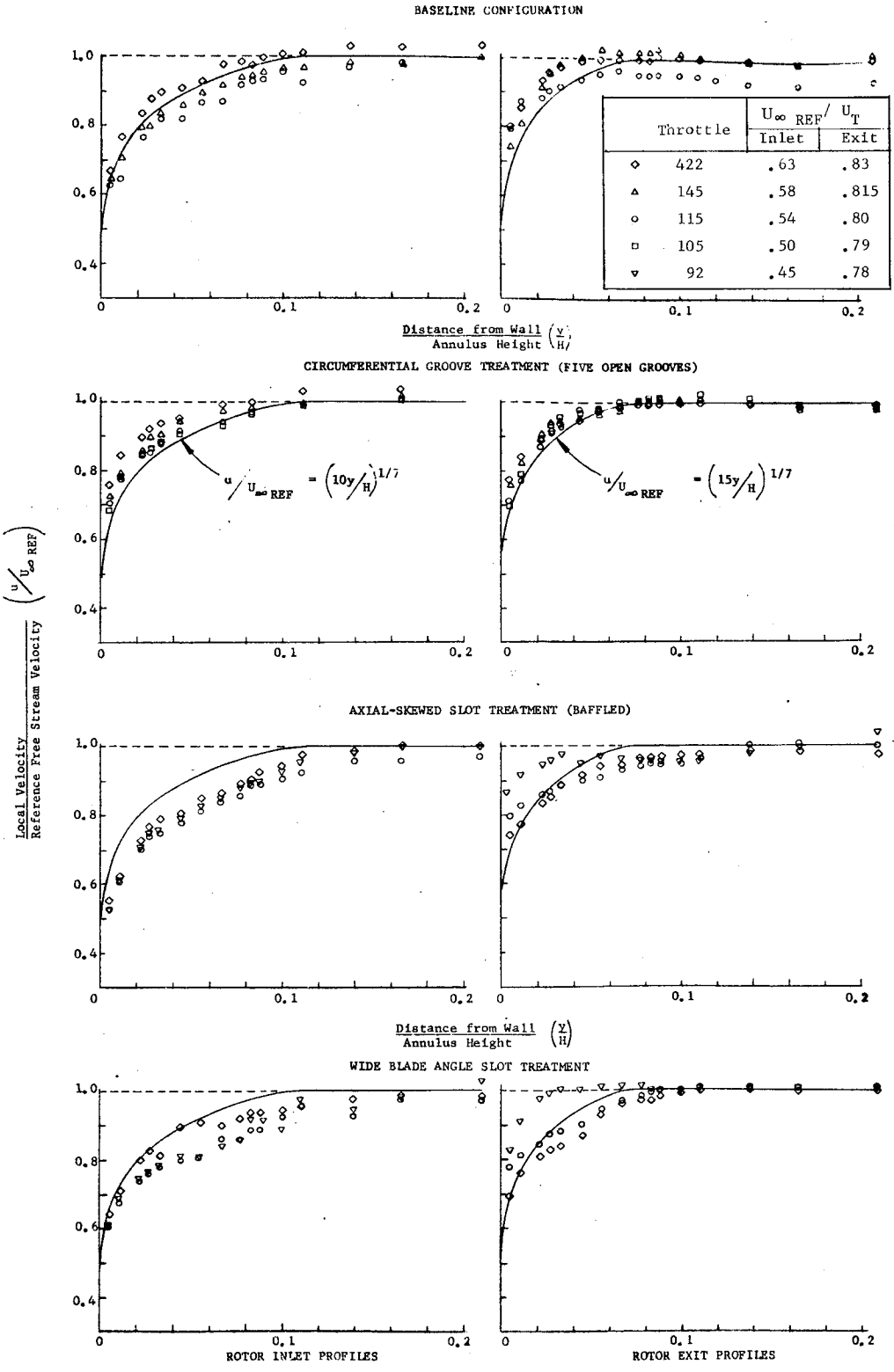

Figure 77 Annulus Wall Boundary Layer Profiles

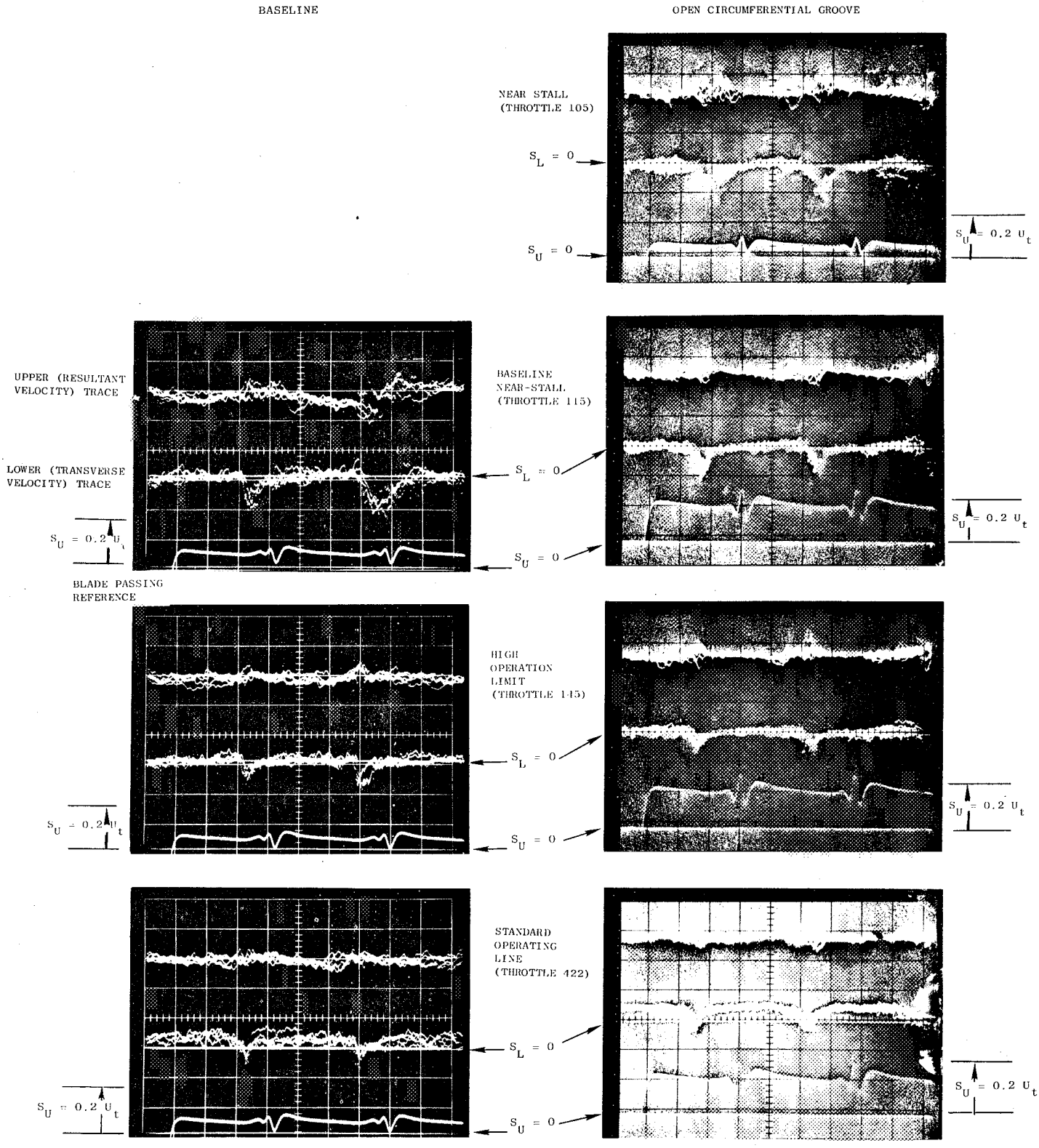

NOTE: To obtain flow angles from oscillograms, $\beta = 100\ (S_L\ S_U)$, where S_L is the lower transverse velocity signal. $S_L > 0$ indicates a flow angle more nearly axial than the nominal orientation.

Figure 78 Oscillograms Showing Rotor Blade Wake Profiles for Baseline and Open Circumferential Groove Configurations 17% Span from Tip

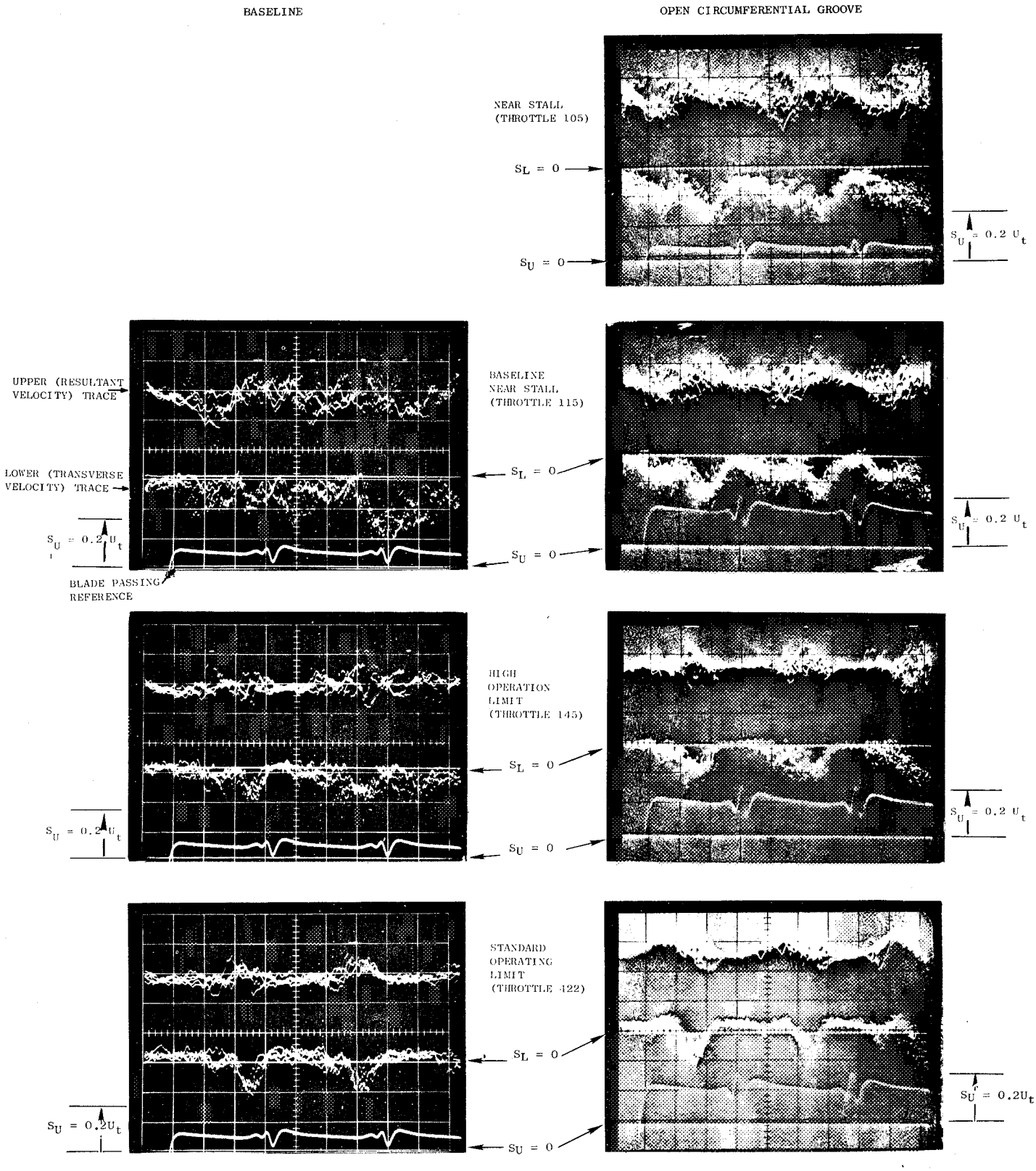

NOTE: To obtain flow angles from oscillograms, $\beta = 100\ (S_L/S_U)$, where S_L is the lower signal, S_U is the upper signal, $S_L > 0$ indicates a flow angle more nearly axial than the nominal orientation.

Figure 79 Oscillograms Showing Blade Wake Profiles for Baseline and Open Circumferential Groove Configurations 8% Span from Tip

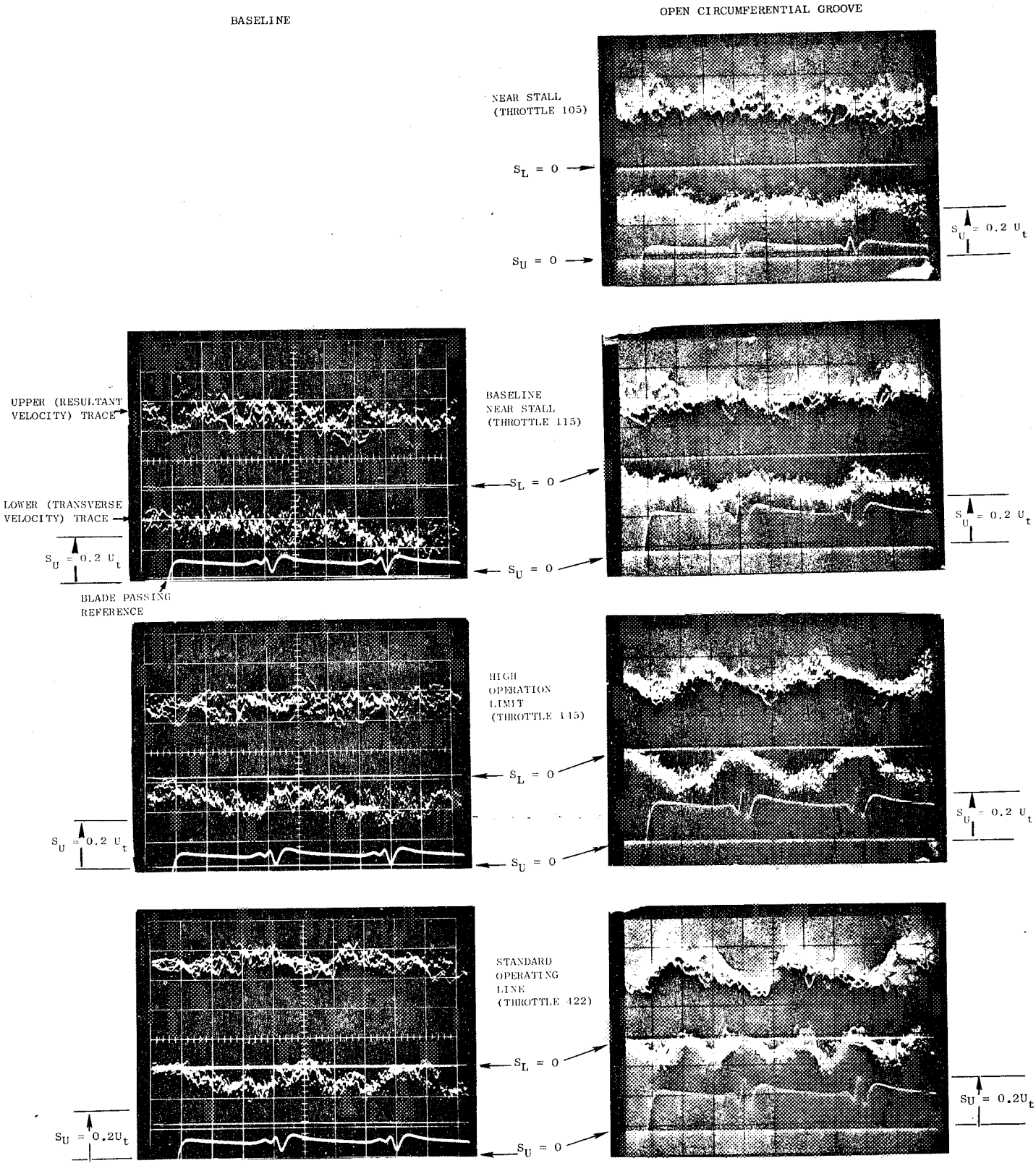

NOTE: To obtain flow angles from oscillograms, $\beta = 100\ (S_L/S_U)$, where S_L is the lower signal, S_U is the upper signal, $S_L > 0$ indicates a flow angle more nearly axial than the nominal orientation.

Figure 80 Oscillograms Showing Blade Wake Profiles for Baseline and Open Circumferential Groove Configurations 3% Span from Tip

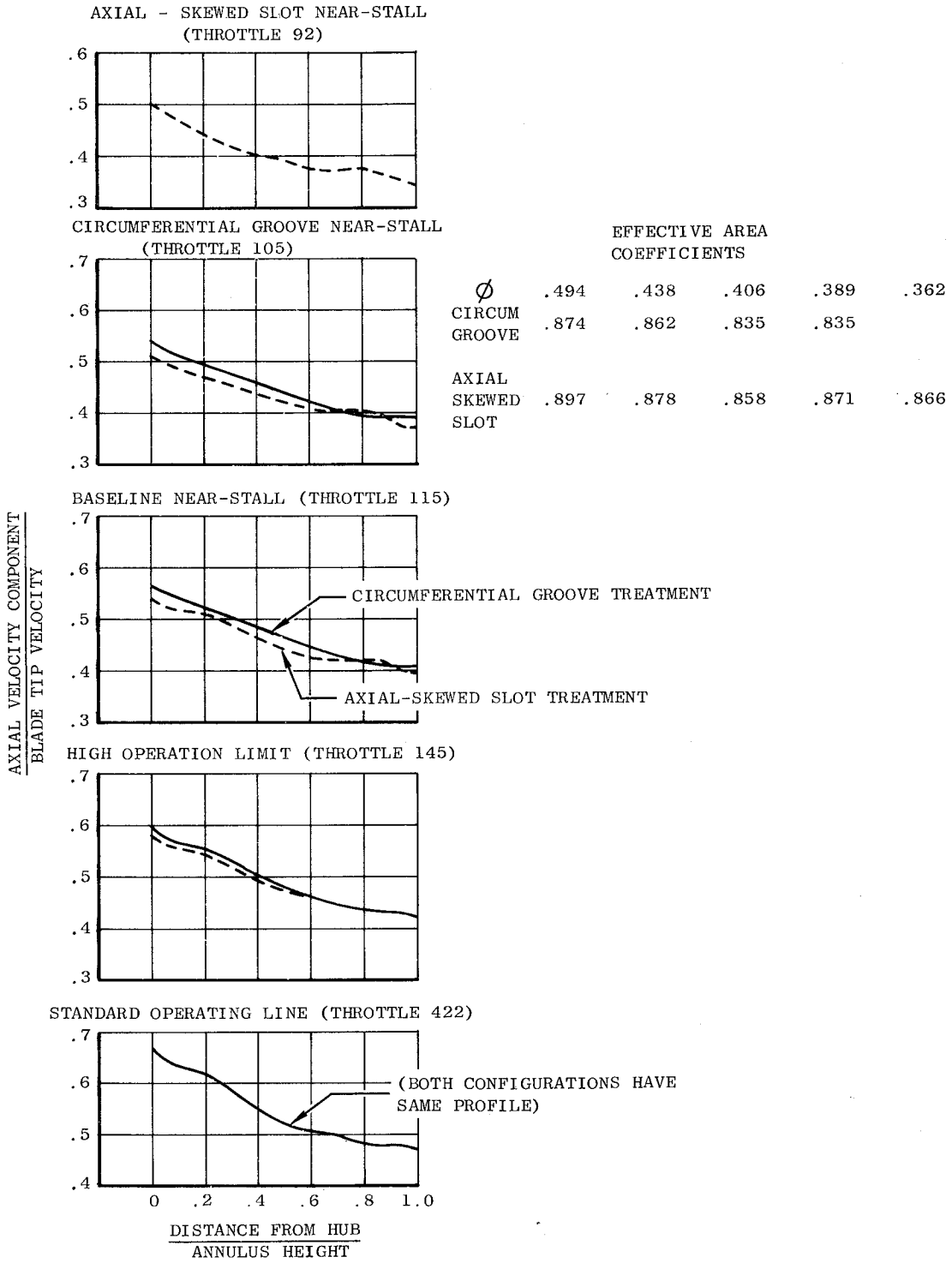

Figure 81 Profile of Axial Velocity Components at Rotor Exit from Vector Diagram Analysis

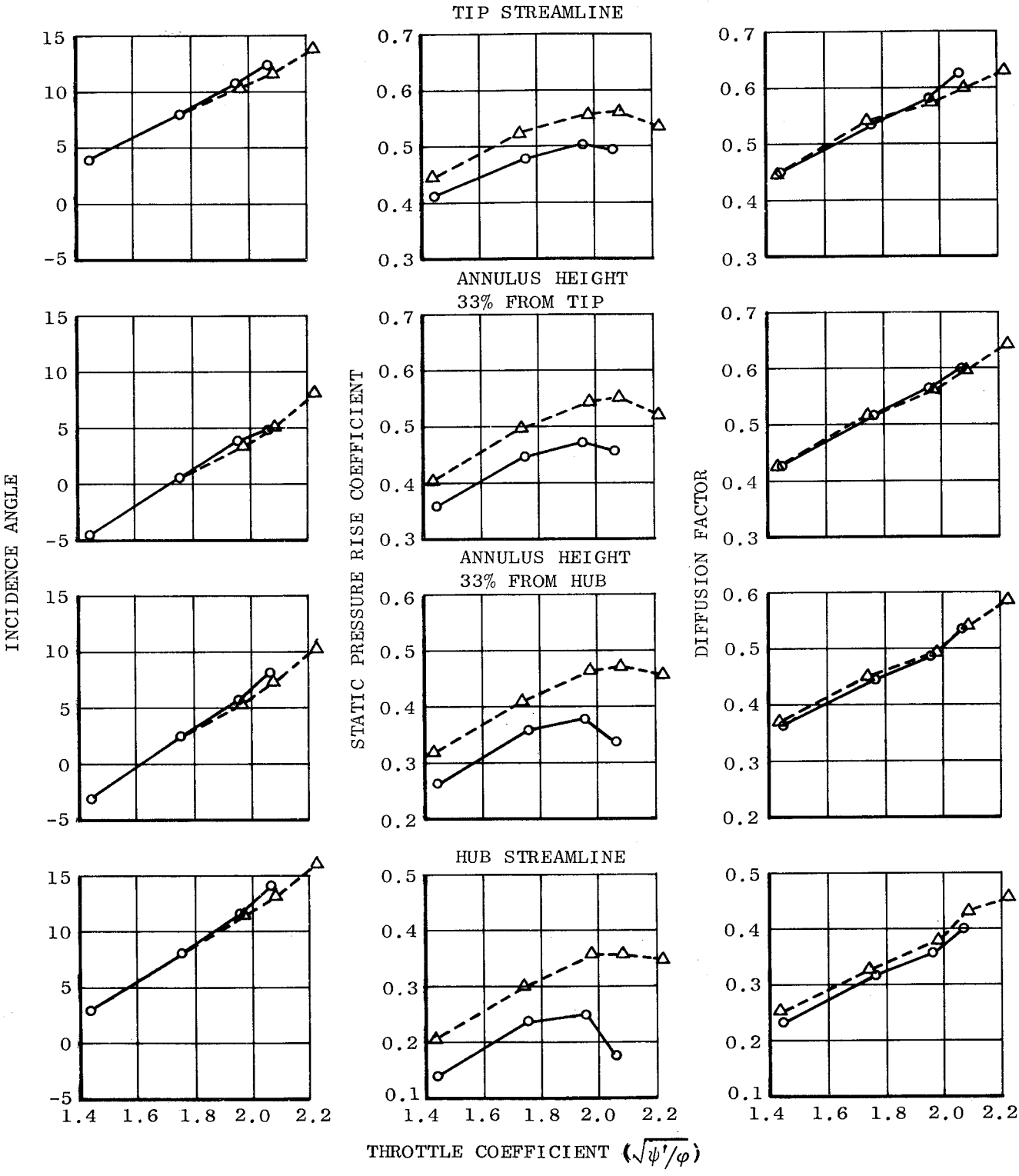

Figure 82 Rotor Blade Element Data from Vector Diagram Analysis

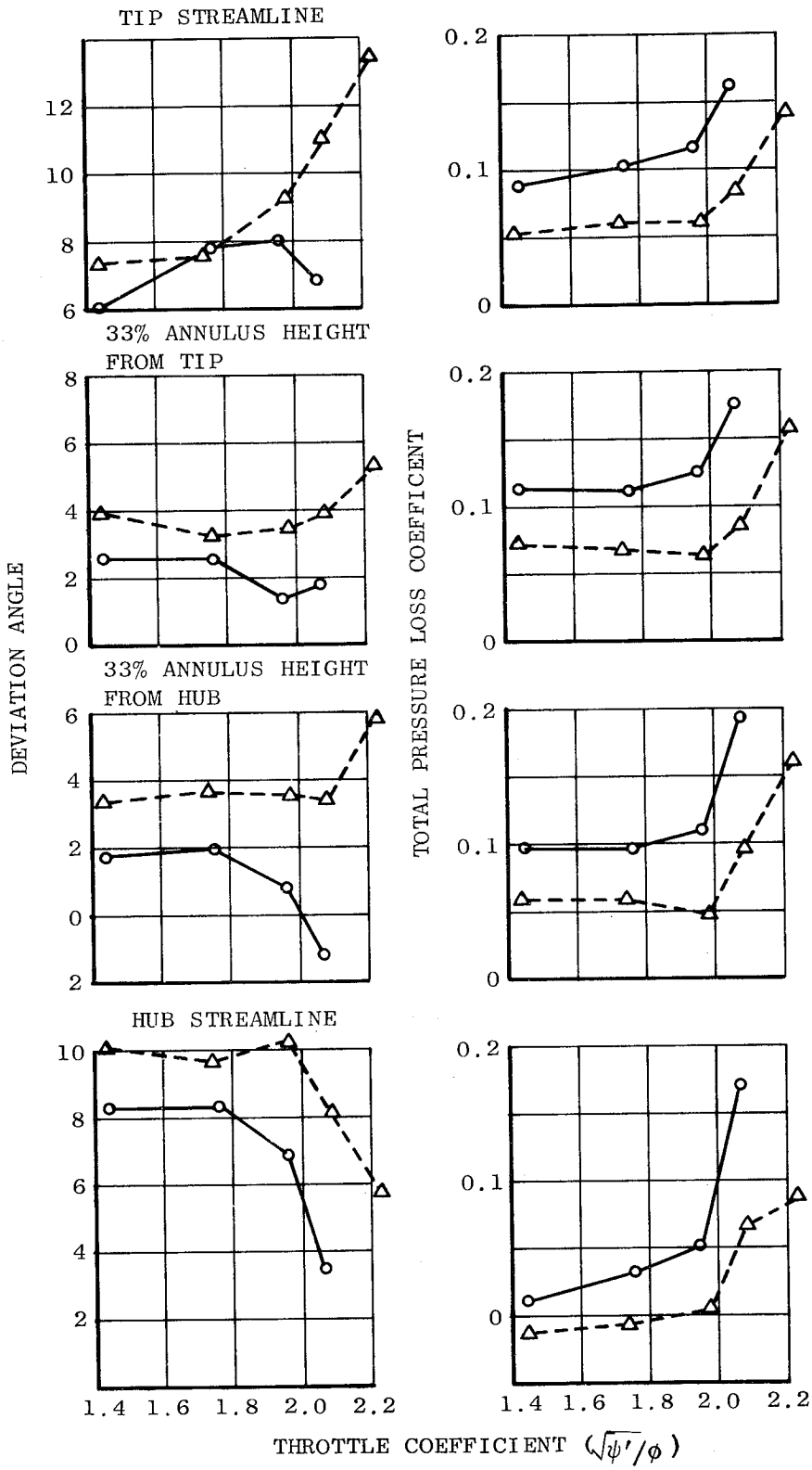

Figure 82 (CONCLUDED)

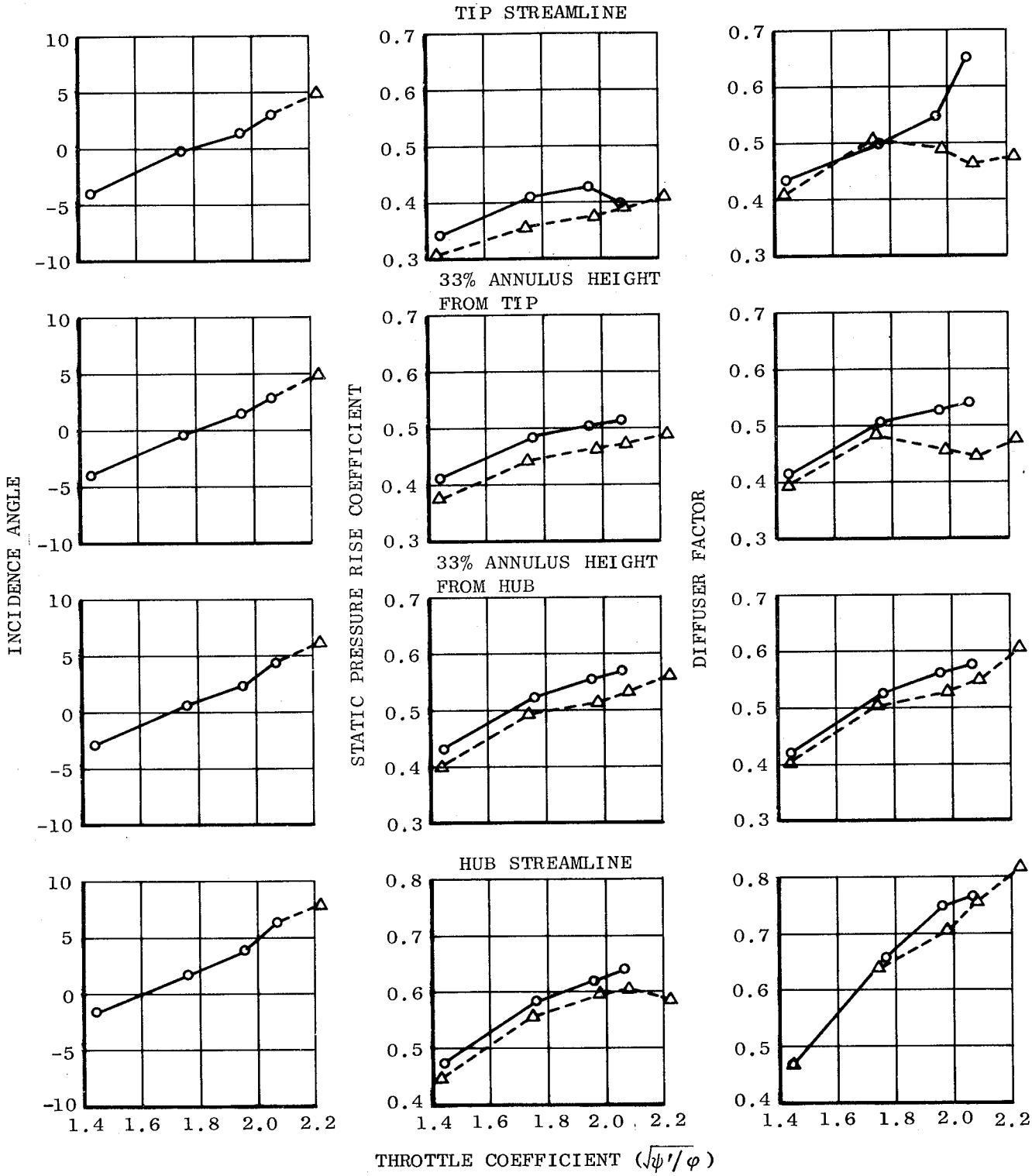

Figure 83 Stator Vane Element Data From Vector Diagram Analysis